UNIVERSITY OF SOUTH AFRICA

DOCTORAL THESIS

The search for a dark vector boson and a new scalar with the ATLAS detector

---

Author:
Diallo BOYE

Supervisors:
Prof. Lerothodi LEEUW
Prof. Simon CONNELL
Dr. Ketevi ASSAMAGAN
Dr. Loan TRUONG

A thesis submitted in fulfillment of the requirements for the degree of Doctor of Philosophy

in the

High Energy Physics Research Group of UNISA, UJ and BNL
Physics Department

June 26, 2020

Declaration of Authorship

I, Diallo BOYE, declare that this thesis titled, "The search for a dark vector boson and a new scalar with the ATLAS detector" and the work presented in it are my own. I confirm that:

- This work was done wholly or mainly while in candidature for a research degree at this University.
- Where any part of this thesis has previously been submitted for a degree or any other qualification at this University or any other institution, this has been clearly stated.
- Where I have consulted the published work of others, this is always clearly attributed.
- Where I have quoted from the work of others, the source is always given. With the exception of such quotations, this thesis is entirely my own work.
- I have acknowledged all main sources of help.
- Where the thesis is based on work done by myself jointly with others, I have made clear exactly what was done by others and what I have contributed myself.

Signed:

Date: June 26th, 2020

"If I have seen further than others, it is by standing upon the shoulders of giants."

Isaac Newton

UNIVERSITY OF SOUTH AFRICA

Abstract

College of Science, Engineering and Technology
Physics Department

Doctor of Philosophy

The search for a dark vector boson and a new scalar with the ATLAS detector

by Diallo BOYE

Hidden sector or dark sector states appear in many extensions to the Standard Model (SM), to provide particle mediators for dark matter in the universe or to explain astrophysical observations such as the positron excess in the cosmic microwave background radiation flux. A hidden or dark sector can be introduced with an additional $U(1)_d$ dark gauge symmetry. The discovery of the Higgs boson in 2012 during Run 1 by the Large Hadron Collider (ATLAS and CMS) opens a new and rich experimental program for Beyond Standard Model physics (BSM) based on the Higgs Portal. This exotic discovery route uses couplings to the dark sector at the Higgs level, which were not experimentally accessible before. This thesis presents the searches of possible exotic decays: $H \to Z_d Z_{(d)} \to 4\ell$ where Z_d is a dark vector boson. It had been initiated in the Run 1 period of the LHC using the ATLAS detector at CERN. The results showed (tantalizingly) two signal events where none were expected, so that in the strict criteria of High Energy Physics, the result was not yet statistically significant. The Run 1 analysis for a 8 TeV collision energy is further developed in Run 2 with a 13 TeV collision energy, to expand the search area, take advantage of higher statistics, a higher Higgs production cross section, and substantially better performance of the ATLAS detector. In this work, the search is further broadened and includes allowing the mass of the originating boson (the dark Higgs S) to vary from the SM value. This allows the search for the dark vector boson to also explore higher or lighter masses than the SM Higgs boson. This extended search is efficient and could include a more general class of models, with the mass constraint of the SM Higgs portal lifted. This thesis reviews the analysis results from Run 1 and Run 2, and presents its iteration in the full Run 2 search by focusing on its new channel where the additional scalar S (with $m_S \neq m_H$) decays to 4ℓ via two dark vector boson states Z_d. The case where the Higgs decays to 4ℓ via two Z_d ($H \to Z_d Z_d \to 4\ell$) and also called high mass channel, has been just unblinded. Nineteen data events are observed where 14 were predicted. In overall, the data are consistent with the Monte Carlo prediction. No evidence of deviation from the Standard Model expectations are observed.

Acknowledgements

First, I would like to summarize where everything started. In 2012, as master student in University Cheikh Anta Diop of Dakar (Senegal), my then supervisor, Prof Mamadou Faye advised me to apply to the African School of Physics in Ghana, where I got selected. During the school, I met many professors from all around the world (Switzerland, United States, France, England, Sweden ...), amongst them there were Dr. Ketevi Assamagan (from Brookhaven National Laboratory), Prof Simon Connell (from Johannesburg University) and Prof Ulrich Goerlach (from University of Strasbourg) who were organizers and also lecturers. It's also where I discovered High Energy Physics (HEP). After the school I continue an exchange with Prof Ulrich Goerlach who gave me the opportunity to enroll for a master's degree in HEP at the University of Strasbourg in France, after some online courses followed by a test. My studies in France contributed to building my skill in physics, especially in HEP. Three years after the ASP in Ghana, I met Prof Simon Connell again at CERN during my internship in CMS. That was a great moment, where he informed me about a PhD position where the successful candidate would be under the supervision of Prof Lerothodi Leeuw, Dr. Ketevi Assamagan, and him. I applied without hesitation and I got accepted. Today I am at the end of my PhD and I would like to deeply express my gratitude to these people: Prof Lerothodi Leeuw, Prof Simon Connell and Dr. Ketevi Assamagan. They always have been present; encouraging, teaching, helping, and advising to reach this great achievement. Their supervision was beyond physics actually; they have always been promoting me for any research field (hardware or software) or key position that would be beneficial to my career. As an example I was designated as contact person to this huge analysis I am presenting today thanks to their nomination. I am very grateful to work with them.

I would like also to express my gratitude to Prof Ulrich Goerlach for his great contribution to my career, and I feel very lucky to meet him, I am sure he would be very happy to read this thesis. Thank you very much Ulrich.

I would like to thank my late supervisor Prof Mamdadou Faye, who passed away just after I got back from Ghana. His memory will be always with me and I will be ever grateful for his support and his assistance.

I was very fortunate to work with a long list of colleagues, especially with Dr Loan Truong, as a post-doc in our team. I was working with her closely during my PhD, and I gained a lot from her experience, thank you very much Loan.

I acknowledge the support from SA-CERN. Their grant complemented by the Johannesburg University payment enabled me to be based 100% at CERN and work more efficiently on my thesis. I also acknowledge the support from the DOE (Department Of Energy) and ATLAS-US which enabled me to spend in total five months during my PhD at Brookhaven National Laboratory and work closely with Dr Ketevi Assamagan.

During my PhD I traveled a lot, for conferences or workshops and I always had to leave my wife, Maïmouna, alone for awhile. However, she always understood my situation and never complained, I would like to thank her a lot for her support and her love. I also would like to add to this list my mother, Issateuw Diop, my sister Mame Bourry and my parents who raised me, Ndiémé Fall and Ngor Diouf, for the education they gave me, for always believing in me and supporting me. Finally, I would like to thank all my relatives and friends who supported me in my career or in my education.

Contents

Declaration of Authorship iii

Abstract vii

Acknowledgements ix

1 Introduction 1
- 1.1 Four forces in the universe . . . 1
- 1.2 Symmetry breaking in particle physics . . . 2
- 1.3 Long quest of electromagnetic and weak force unification . . . 3
- 1.4 Is it the end of the physics journey ? . . . 3
- 1.5 Some words on Dark Matter . . . 5
- 1.6 Particle detections in particle physics . . . 5
  - 1.6.1 Scattering . . . 6
  - 1.6.2 Detectors . . . 7
- 1.7 Units . . . 7
- 1.8 Thesis plan . . . 8
- 1.9 The author's contributions . . . 8

I Theory 11

2 Standard Model (SM) of particle physics 13
- 2.1 The Standard Model successes . . . 13
- 2.2 The Standard Model limits . . . 16

3 Beyond the Standard Model 17
- 3.1 Hidden Abelian Higgs Model . . . 17
- 3.2 2HDM + Scalar . . . 21
- 3.3 Additional scalar (S) decaying to a Z_d . . . 24

II Detectors, Reconstruction, Identification 27

4 Large Hadron Collider: LHC 29
- 4.1 Motivation of building the LHC . . . 29
- 4.2 Designs parameters . . . 29
- 4.3 Luminosity . . . 32
- 4.4 Pileup . . . 33
- 4.5 Main detectors of the LHC . . . 34

5 ATLAS Detector 35
5.1 Coordinate system and nomenclature . . . 35
5.2 ATLAS detector overview . . . 35
5.3 ATLAS subsystems . . . 37
5.3.1 Magnet system . . . 37
5.3.2 Inner Detector . . . 37
5.3.2.1 Pixel detector . . . 38
5.3.2.2 Silicon Tracker (SCT) . . . 39
5.3.2.3 Transition radiation tracker (TRT) . . . 39
5.3.3 Calorimeters . . . 40
5.3.3.1 Electromagnetic calorimeter . . . 40
5.3.3.2 Hadronic calorimeters . . . 41
5.3.4 Muon spectrometer . . . 42
5.3.5 Trigger . . . 43

6 Event and Object Reconstruction 45
6.1 Track Reconstruction . . . 45
6.2 Electron reconstruction and identification . . . 46
6.2.1 Electron reconstruction . . . 46
6.2.2 Electron identification . . . 47
6.2.3 Reconstruction efficiency for electrons . . . 48
6.3 Muon reconstruction and identification . . . 49
6.3.1 Muon reconstruction . . . 49
6.3.1.1 Muon reconstruction in the MS . . . 50
6.3.1.2 Combined reconstruction . . . 50
6.3.2 Muons identification . . . 51
6.3.3 Reconstruction efficiency for muons . . . 51

III Analysis and interpretation 55

7 Dark vector boson (Z_d) and pseudo-scalar (a) search with ATLAS detector in Run1 and Run2 57
7.1 Z_d search in Run1: Results . . . 57
7.2 Z_d and a search in Run 2: Results . . . 61
7.3 Conclusion . . . 65

8 Dark vector boson (Z_d), pseudo-scalar (a) and dark Higgs (S) search with the ATLAS detector in full Run2 67
8.1 Object and event reconstruction . . . 67
8.1.1 Event preselection . . . 68
8.1.1.1 Trigger . . . 68
8.1.2 Baseline lepton selection . . . 70
8.1.3 Selection and ranking of quadruplets . . . 70
8.2 Event selection . . . 70
8.2.1 Invariant mass kinematic variables . . . 70
8.2.2 The E'_{ab} variable . . . 71
8.2.3 Requirements on leptons in the event selection . . . 71
8.2.4 Kinematic requirements in event selection . . . 71
8.3 Monte Carlo simulation . . . 75
8.3.1 Background and signal simulation . . . 75

8.4 Background estimation 77
8.4.1 Estimation of irreducible backgrounds 77
8.4.2 Estimation of reducible backgrounds 79
8.5 Systematics uncertainties 82
8.5.1 Experimental systematic uncertainties 82
8.5.2 Theoretical systematic uncerainties 82
8.6 Results 85
8.6.1 Additional Scalar results 85
8.6.2 ZX results 86
8.6.3 High mass results 86
8.6.4 Low mass results 86
8.7 Interpretation 93
8.7.1 Fiducial volume definition 93
8.7.2 Statistical model used for limit setting 93
8.7.3 Fiducial and total cross section limits 94
8.7.4 Limits on Higgs branching ratios and model parameters 96
8.7.4.1 Setting a limit on BR(H $\rightarrow$ XX) HM and LM 97
8.7.4.2 The limit on the Higgs mixing parameter κ 98
8.7.5 Limits in the ZX search 99
8.7.6 Limits in the AS search 100

9 Conclusion **103**

IV Appendix **107**

A Definition and derivation of cuts **109**
A.1 The Z veto cut definition for AS 109
A.2 Signal region re-optimization 111
A.3 E'_{ab}/m_{4l} variable 121

B m_{ab}, m_{cd} labeling used in additional scalar channel **125**

C Signal Modeling **129**
C.0.1 Shape of the $\langle m_{\ell\ell} \rangle$ observable for signal 129
C.0.2 Model-independent efficiency 129
C.0.3 Model-dependent acceptances 133
C.0.4 Mathematical derivation for the relation between fiducial cross section and efficiency 133
C.0.5 Mathematical derivation for the relation between total cross section and efficiency and acceptance 134

D kappa derivation **137**

E Report on my qualification task **139**
E.1 Introduction 139
E.2 The New Small Wheel (NSW) project 139
E.3 Micromegas detector technology 140
E.4 The quality control and quality assurance shifts 141
E.5 Pillar height measurements 143
E.6 Conclusion 150

Bibliography 151

List of Figures

1.1 Unification of the forces. Those enclosed in dashed lines are not yet established. Only the strong force changes its strength appreciably within currently available energy ranges or, equivalently, distances. This is why the distance of the strong force is specified. (Nagashima, 2009) 4

1.2 Rotation curve of spiral galaxy Messier 33 (yellow and blue points with error bars), and a predicted one from distribution of the visible matter (gray line). The discrepancy between the two curves can be accounted for by adding a dark matter halo surrounding the galaxy. (Wikipedia, 2019a) 5

1.3 A Livingston chart depicting progress in collision energy through 2010. The LHC is the largest collision energy to date, but also represents the first break in the log-linear trend. Plot from (Wikiwand, 2020) 6

2.1 The distribution of the four-lepton invariant mass, $m_{4\ell}$, for the selected candidates, compared to the background expectation in the 80–250 GeV mass range, for the combination of the $\sqrt{s}$ = 7 TeV and $\sqrt{s}$ = 8 TeV data. The signal expectation for a SM Higgs with m_H = 125 GeV is also shown. (Aad, 2012) 14

2.2 The measured value of m_W is compared to other published results, including measurements from the LEP experiments ALEPH, DELPHI, L3 and OPAL , and from the Tevatron collider experiments CDF and D0. The vertical bands show the statistical and total uncertainties of the ATLAS measurement, and the horizontal bands and lines show the statistical and total uncertainties of the other published results. Measured values of m_W for positively and negatively charged W bosons are also shown. (Aaboud, 2018b) 15

2.3 The hadronic cross-section as a function of centre-of-mass energy. The solid line is the prediction of the SM, and the points are the experimental measurements. Also indicated are the energy ranges of various e^+e^- accelerators. The cross-sections have been corrected for the effects of photon radiation. (Schael, 2006) 16

3.1 Constraints on ϵ versus m_{Z_d} for pure kinetic mixing (no additional source of mass mixing) for $m_{Z_d} \sim 10\ MeV$ GeV. The black dashed line separates prompt ($c\tau < 1\mu m$) from nonprompt Z_d decays. The three blue lines are contours of $Br(H \to ZZ_d)$ of 10^{-4}, 10^{-5}, and 10^{-6}, respectively. Plot from (Curtin et al., 2014) 18

3.2 Left: Mass plane in the SM + V model with different exotic Higgs decays for $\kappa \gg \epsilon$ (i.e., when the mixing between the Higgs and dark Higgs dominates over the kinetic mixing). The black contours are the values of $\kappa \times 10^3$ required for $Br(H \to Z_d Z_d, ss) = 10\%$. Region A covers the $H \to Z_d Z_d$ decay. Region C has no exotic Higgs decays. Region D covers the $H \to ss$ decay, and Region B has both the $H \to ss$ and $H \to Z_d Z_d$ decays, with the $H \to ss$ fraction of exotic decays shown on the right. In the upper left shaded region, $s \to Z_d Z_d$ is the dominant decay mode of the dark scalar. This allows the Higgs to decay to up to eight SM fermions (Curtin et al., 2014) 19
3.3 Exotic Higgs decays to four leptons induced by intermediate dark photons in HAHM. H is the Higgs boson, Z_d the dark vector boson, ϵ the kinetic mixing parameter, κ the Higgs mixing parameter, s the dark Higgs boson. Left: $H \to ZZ_d \to 4l$ via the hypercharge portal. Right: $H \to Z_d Z_d \to 4l$ via the Higgs portal. 20
3.4 Expected 95% CLs limits on the total exotic Higgs decay branching ratio, BR($H \to Z_d Z_d$). (Curtin et al., 2015) 20
3.5 Decay length of Z_d for different ϵ. The dashed lines indicate boundaries between qualitatively different experimental regimes: prompt decay for $c\tau \lesssim 1\mu m$ and likely escape from an ATLAS-size detector for $c\tau \gtrsim 20m$ (Curtin et al., 2015). 21
3.6 Branching ratios of a singlet-like pseudoscalar in the 2HDM+S for type-I Yukawa couplings. Decays to quarkonia likely invalidate our simple calculations in the shaded regions. (Curtin et al., 2014) 23
3.7 Branching ratios of a single-tlike pseudoscalar in the 2HDM+S for type-II Yukawa couplings. Decays to quarkonia likely invalidate our simple calculations in the shaded regions. (Curtin et al., 2014) 24
3.8 Branching ratios of a singlet like pseudoscalar in the 2HDM+S for type-III Yukawa couplings. Decays to quarkonia likely invalidate our simple calculations in the shaded regions. (Curtin et al., 2014) 25
3.9 Branching ratios of a singlet-like pseudoscalar in the 2HDM+S for type-IV Yukawa couplings. Decays to quarkonia likely invalidate our simple calculations in the shaded regions. (Curtin et al., 2014) 26

4.1 Cross section of the LHC dipole magnet. (Frontline, 2009) 30
4.2 List of current particle accelerators at CERN (Wikipedia, 2019b) 31
4.3 integrated luminosity reached in ATLAS and CMS from 2011 to 2018 (Rende Steerenberg, 2017) 33

5.1 Cut-away view of the ATLAS detector. The dimensions of the detector are 25 m in height and 44 m in length. The overall weight of the detector is approximately 7000 tonnes. (Aad et al., 2008) 36
5.2 Geometry of the ATLAS magnet system. 37
5.3 Cut-away view of the ATLAS inner detector. (Aad et al., 2008) 38
5.4 A cut-away view of the calorimeters. (Aad et al., 2008) 40
5.5 A sketch of the LAr geometry in an EMB module, showing the lateral and longitudinal segmentation in layers of radially coarser granularity. (Collaboration, 2020) 41

6.1 A schematic illustration of the path of an electron through the detector. The red trajectory shows the hypothetical path of an electron, which first traverses the tracking system (pixel detectors, then silicon-strip detectors and lastly the TRT) and then enters the electromagnetic calorimeter. The dashed red trajectory indicates the path of a photon produced by the interaction of the electron with the material in the tracking system (Aaboud, 2019b). 46
6.2 Measured combined reconstruction and identification efficiency for the various cut-based and LH selections as a function of E_T (A) and η (B) for electrons. ratios. The panel at the bottom shows the efficiency ratio between Data and MC. (The ATLAS Collaboration et al., 2017) . . 49
6.3 Muon reconstruction efficiencies for the Loose/Medium/Tight identification algorithms measured in $Z \rightarrow \mu\mu$ events as a function of the muon pseudorapidity for muons with $p_T > 10$ GeV. The prediction by the detector simulation is depicted as open circles, while filled dots indicate the observation in collision data with statistical errors. The bottom panel shows the ratio between expected and observed efficiencies, the efficiency scale factor. The errors in the bottom panel show the quadratic sum of statistical and systematic uncertainty. (Marchese, 2017) 52
6.4 Muon reconstruction efficiencies for the Medium identification algorithm measured in $J/\Psi \rightarrow \mu\mu$ and $Z \rightarrow \mu\mu$ events as a function of the muon momentum. The prediction by the detector simulation is depicted as empty circles (squares), while the full circles (squares) indicate the observation in collision data. Only statistical errors are shown in the top panel. The bottom panel reports the efficiency scale factors. The darker error bands indicate the statistical uncertainty, while the lighter bands indicate the sum of the statistical and systematic uncertainties in quadrature (Marchese, 2017) 53

7.1 The distribution of the mass of the second lepton pair, m_{34}, of the $\sqrt{s}$= 8 TeV data (filled circles with error bars) and the expected (pre-fit) backgrounds. The $H \rightarrow ZZ* \rightarrow 4\ell\ell$ expected (pre-fit) normalization, for a mass hypothesis of mH=125 GeV, is set by subtracting the expected contributions of the $ZZ*$, Z+jets and $t\bar{t}$ backgrounds from the total number of observed 4' events in the data (Aad et al., 2015b). 58
7.2 A) The 95% CL upper limits on the relative branching ratio, $R_B = \frac{BR(H \rightarrow ZZ_d \rightarrow 4\ell)}{BR(H \rightarrow 4\ell)}$ as a function of m_{Z_d}. The $\pm\sigma$ and $\pm 2\sigma$ expected exclusion regions are indicated in green and yellow, respectively. B) The 95% CL upper limits on the branching ratio of $H \rightarrow ZZ_d \rightarrow 4\ell$ as a function of m_{Z_d} using the combined upper limit on R_B and the SM branching ratio of $H \rightarrow ZZ^* \rightarrow 4\ell$ (Aad et al., 2015b). 58
7.3 A) The 95% CL upper limits on the gauge kinetic mixing parameter ϵ as a function of m_{Z_d} using the combined upper limit on the branching ratio of $H \rightarrow ZZ_d \rightarrow 4\ell$ and Table 2 of Ref.(Curtin et al., 2015).B) The 95% CL upper limits on the product of the mass-mixing parameter δ and the branching ratio of Z_d decays to two leptons (electrons, or muons), $\delta^2 \times \mathcal{B}(Z_d \rightarrow \ell\ell)$, as a function of m_{Z_d} using the combined upper limit on the relative branching ratio of $H \rightarrow ZZ_d \rightarrow 4\ell\ell$ and the partial width of $H \rightarrow ZZ_d$ (Aad et al., 2015b). 59

7.4 A) The 95% confidence level upper bound on the signal strength $\mu_d = \frac{\sigma \times BR(H \to Z_d Z_d \to 4\ell)}{\sigma \times BR(H \to ZZ^* \to 4\ell)}$ in the combined 4e, 2e2μ, 4μ final state, for m_H = 125 GeV. The $\pm\sigma$ and $\pm 2\sigma$ expected exclusion regions are indicated in green and yellow, respectively. B) The 95% CL upper limits on the branching ratio of $H \to Z_d Z_d \to 4\ell$as a function of m_{Z_d} in the combined 4e, 2e2μ, 4μ final state, for m_H = 125 GeV The $\pm\sigma$ and $\pm 2\sigma$ expected exclusion regions are indicated in green and yellow, respectively (Aad et al., 2015b). 60

7.5 The 95% confidence level upper bound on the Higgs mixing parameter $\kappa \times m_H^2 |m_H^2 - m_S^2|$ as a function of m_{Z_d} in the combined 4e, 2e2μ, 4μ final state, for m_H = 125 GeV. The $\pm\sigma$ and $\pm 2\sigma$ expected exclusion regions are indicated in green and yellow, respectively (Aad et al., 2015b). 61

7.6 Distribution of m_{34} for data and background events in the mass range $m_{4\ell} \in [115, 130]$ GeV after the $H \to ZX \to 4\ell$ selection. Three signal points for the $H \to ZZ_d \to 4\ell$ model are shown. The signal strength corresponds to a branching ratio $\mathcal{B}(H \to ZZ_d \to 4\ell) = \frac{1}{3}\mathcal{B}(H \to ZZ^* \to 4\ell)$ (with $\mathcal{B}(H \to ZZ^* \to 4\ell)$ corresponding to the SM prediction (Dittmaier, 2012)). The uncertainties include statistical and systematic contributions (The ATLAS collaboration et al., 2018). 62

7.7 (A) Upper limit at 95% CL on the branching ratio for the $H \to ZZ_d$ process. (B) Upper limits on the kinetic mixing parameter, ϵ, between the SM Z boson and Z_d. The limits on ϵ are obtained directly from the $BR(H \to ZZ_d \to 4\ell)$ (The ATLAS collaboration et al., 2018). 62

7.8 The branching ratio and the partial width of $H \to ZZd$ can be used to constrain as well the mass-mixing parameter, δ, of the model described, where the mass mixing between the Z_d and the SM Z boson is introduced. The limits are valid in the region where $m_{Z_d} < m_H - m_Z$, and are set on the product $\delta^2 \times B(Z_d \to 2\ell)$ since both δ and $B(Z_d \to 2\ell)$ are model-dependent (The ATLAS collaboration et al., 2018). 63

7.9 Distribution of (a) $\langle m_{\ell\ell} \rangle = \frac{1}{2}(m_{12} + m_{34})$ and (b) m_{34} vs m_{12}, for events selected in the $H \to XX \to 4\ell$ ($15 < m_X < 60$ GeV) analysis. The example signal distributions in (a) correspond to the expected yield normalized with $\sigma(pp \to H \to Z_d Z_d \to 4\ell) = \frac{1}{10}\sigma_{\mathrm{SM}}(pp \to) H \to ZZ^* \to 4\ell$(The ATLAS collaboration et al., 2018). 64

7.10 (A) Upper limit at 95% CL on the branching ratios for processes $H \to Z_d Z_d$. The step change at the $m_X = 15$ GeV boundary is due to the addition of sensitivity to 4e and $2e2\mu$ final states (lowering the limit). The shaded areas are the quarkonia veto regions. (B) The $H \to Z_d Z_d$ decay can be used to obtain the 95% CL upper bound on the effective Higgs mixing parameter $\kappa' = \kappa \times m_H^2/|m_H^2 - m_S^2|$ as a function of m_{Z_d}, for $m_H/2 < m_S < 2m_H$. κ is the size of the Higgs portal coupling and m_S is the mass of the dark Higgs boson, the relation can be achieved by using the partial width of $H \to Z_d Z_d$ as given in terms of κ. The limit is valid in the regime where the Higgs mixing parameter dominates ($\kappa \gg \epsilon$), $m_S > m_H/2, m_{Z_d} < m_H/2$ and $H \to Z_d Z* \to 4\ell$ is negligible. This would correspond to an upper bound on the Higgs portal coupling in the range $\kappa \sim (1-10) \times 10^{-4}$ (The ATLAS collaboration et al., 2018). 64
7.11 (A) Distribution of $\langle m_{\ell\ell} \rangle = \frac{1}{2}(m_{12} + m_{34})$, for events selected in the $H \to XX \to 4\mu (1 < m_X < 15$ GeV) analysis. (B) Upper limit at 95% CL on the branching ratios for processes $H \to aa$, for the 2HDM+S bench mark model studied. The limit is greater than 1 for $m_a > 15$ GeV. The shaded areas are the quarkonia veto regions (The ATLAS collaboration et al., 2018). 65

8.1 E'_{ab}/M_{4l} distributions for additional scalar signal hypotheses and the two leading SM background processes (normalized to unity). The dotted lines delimit the cut applied using this variable. 71
8.2 Width of dark Higgs mass (m_S) w.r.t to m_S. This plot is produced using the code available in (Contino et al., 2014) 77
8.3 The average di-lepton mass distribution $m_{\ell\ell} = \frac{m_{ab}+m_{cd}}{2}$ in VR1 is shown in Figure 8.3 for the three final states and all final states combined, all MC campaigns are also considered (mc16a, mc16d and mc16e). 78
8.4 The A, B, C, D regions defined by specific regions in the 2D plane of the two discriminating variables; the impact parameter d^0 (in the Y axis) and the isolation variable (on the X axis). 80
8.5 Feynman diagram of $Z^* \to 4\ell$ decay. 86
8.6 a), b), c) and d) are respectively the distributions of the average leading di-lepton mass $\langle m_{\ell\ell} \rangle$ for the $4e$, $2e2\mu$, 4μ, and combined channels in SR1 of the AS channel. The full MC campaigns are merged (mc16a+mc16d+mc16e). The signals are normalized by the gluon-gluon fusion Higgs cross-section. 87
8.7 a), b), c) and d) are respectively the distributions of the average leading di-lepton mass $\langle m_{\ell\ell} \rangle$ for the $4e$, $2e2\mu$, 4μ, and combined channels in SR2 of the AS channel. The full MC campaigns are merged (mc16a+mc16d+mc16e). The signals are normalized by the gluon-gluon fusion Higgs cross-section. 88
8.8 a), b), c) and d) are respectively the distributions of the scalar mass m_S $\langle m_{\ell\ell} \rangle$ for the $4e$, $2e2\mu$, 4μ, and combined channels in SR1 of the AS search from full MC merged (mc16a+mc16d+mc16e). The signals are normalized by the gluon-gluon fusion Higgs cross-section. 89

8.9 a), b), c) and d) are respectively the distributions of the the scalar mass m_S $\langle m_{\ell\ell}\rangle$ for the $4e$, $2e2\mu$, 4μ, and combined channels in SR2 of the AS search from full MC merged (mc16a+mc16d+mc16e). The signals are normalized by the gluon-gluon fusion Higgs cross-section. 90
8.10 Expected background m_{34} distribution in the ZX channel signal region with $H \to ZZ_d \to 4\ell$ signal templates. The kinematic variable m_{34} aims to reconstruct m_{Z_d} in the $H \to ZZ_d \to 4\ell$ process, and signal templates are shown for Z_d masses of $m_{Z_d} = 15, 30, 55$ GeV. The cross sections of the signal templates here are set to 1 fb. 91
8.11 HM search: 2015–8 with new Medium SR: distributions of $\langle m_{\ell\ell}\rangle$ in the signal region with the $4e$, 4μ, and $2e2\mu$ channels shown separately and combined. The predictions have been scaled separately to the integrated luminosity of each data-taken campaign and then combined. The total integrated luminosity is 140 fb^{-1}. The example signal distributions correspond to the expected yield normalized with $\sigma(pp \to H \to Z_d Z_d \to 4\ell) = \frac{1}{10}\sigma_{\mathrm{SM}}(pp \to H \to ZZ^* \to 4\ell)$. . . . 92
8.12 The total background expectation in low mass signal region as a function of $\langle m_{\ell\ell}\rangle$. The error band includes the systematic uncertainty on the heavy flavour background estimate and the statistical uncertainty. 93
8.13 95% CL upper bounds on the model-independent fiducial cross-sections corresponding to the fiducial phase spaces defined in Table 8.16 (separate phase spaces are defined for m_X above and below 15 GeV). 95
8.14 Expected 95% CL upper bounds on $\sigma_{fid}(H \to aa \to 4\ell)$ vs m_a for the LM search using the 2015–8 blinded 139 fb^{-1} dataset. The shaded areas are the quarkonia veto regions. 96
8.15 The expected and observed 95% confidence level upper bound on the total cross-section for the phase spaces covered by the benchmark models, $\sigma_H \mathrm{BR}(H \to XX \to 4\ell)$. 97
8.16 HM search: Observed and expected branching ratio limits on $H \to Z_d Z_d$ for the high-mass channel using the 2015–8 unblinded 140 fb^{-1} data set. 98
8.17 HM search: Observed and expected κ' limits on $H \to Z_d Z_d$ for the high-mass channel using the 2015–8 unblinded 140 fb^{-1} data set. . . . 99
8.18 Expected upper 95 % confidence level limits on σ_{ZZd} with the 139 fb^{-1} dataset. The limits are based on a binned maximum likelihood fit to 5000 background only Monte Carlo toys samples of the ZX signal region. 100
8.19 Signal-background efficiency versus (m_S, m_{Z_d}) in SR2 101
8.20 Signal-background efficiency versus (m_S, m_{Z_d}) in SR2 101

A.1 a) and b) are respectively the distributions of the leading (m_{ab}) and sub-leading (m_{cd}) di-leptons, c) and d) the distributions of the alternative leading (m_{ad}) and sub-leading (m_{cb}) di-lepton. All cuts are applied except Z-veto cut. Backgrounds are normalized by the theoretical cross section and signal by the SM Higgs boson production cross-section. 110
A.2 leading di-lepton (m_{ab}) distribution for each of the ten Z veto cut hypothesis 112
A.3 sub-leading di-lepton (m_{cd}) distribution for each of the ten Z veto cut hypothesis 113

A.4 leading di-lepton (m_{ad}) distribution for each of the ten Z veto cut hypothesis . . . 114
A.5 leading di-lepton (m_{cb}) distribution for each of the ten Z-veto cut hypothesis . . . 115
A.6 Significance vs Z veto cut hypothesis a) when the cuts are performed on the di-leptons pair and b) when the cuts are performed on the alternative di-lepton pairs. . . . 116
A.7 Average di-lepton mass of the signal and background MCs, all cuts are applied except the MSR cut. . . . 117
A.8 95% CL on μ_d for different signal mass points versus the size of the tested MSR cut. . . . 117
A.9 $< m_{ll} >$ distribution of the total background . . . 119
A.10 $< m_{ll} >$ distribution of the total background and modulating function 120
A.11 New and old signal region . . . 120
A.12 E'_{ab}/m_{4l} signal and background distributions. The dotted line indicates the cut applied using this variable. . . . 121
A.13 E'_{ab}/m_{4l} vs m_{cd}/m_{ab}. The mass of the Z_d is set to 50 GeV and the mass of the dark Higgs S varied from 150 to 800 GeV . . . 122

B.1 $E'_{l_1 l_2}/m_{4l}$ vs m_{34}/m_{12} for different mass points: s = 175 GeV, Z_d = 20 GeV, s = 250 GeV, Z_d = 70 GeV, s = 400 GeV, Z_d = 100 GeV,s = 800 GeV, Z_d = 250 GeV, the intensity bar on left hand refers to the signal, and the one on the right hand refers to the SMZZ background . . . 126
B.2 $E'_{l_1 l_2}/m_{4l}$ vs m_{34}/M_{12} for different mass points: s = 175 GeV, Z_d = 20 GeV, s = 250 GeV, Z_d = 70 GeV, s = 400 GeV, Z_d = 100 GeV,s = 800 GeV, Z_d = 250 GeV, the intensity bar on left hand refers to the signal, and the one on the right hand refers to the ggfh background . . . 126
B.3 $E'_{l_1 l_2}/m_{4l}$ vs m_{34}/m_{12} for different labeling with a child particle under Z boson mass: s = 175 GeV, Z_d = 20 GeV, the intensity bar on left hand refers to the signal, and the one on the right hand refers to the SMZZ background . . . 126
B.4 $E'_{l_1 l_2}/m_{4l}$ vs M_{34}/m_{12} for different labeling with a child particle under Z boson mass: s = 175 GeV, Z_d = 20 GeV, the intensity bar on left hand refers to the signal, and the one on the right hand refers to the ggfh background . . . 127
B.5 $E'_{l_1 l_2}/M_{4l}$ vs M_{34}/M_{12} for different labeling with a child particle above Z boson mass: s = 400 GeV, Z_d = 100 GeV, the intensity bar on left hand refers to the signal, and the one on the right hand refers to the SMZZ background . . . 127
B.6 $E'_{l_1 l_2}/M_{4l}$ vs M_{34}/M_{12} for different labeling with a child particle above Z boson mass: s = 400 GeV, Z_d = 100 GeV, the intensity bar on left hand refers to the signal, and the one on the right hand refers to the ggfh background . . . 127

C.1 Examples of Gaussian fits to the generated $H \to Z_d Z_d \to 4\ell$ signal samples in the medium SR (figure a, b, and c), and with the low-mass selection after the impact parameter requirement (figure d). The shaded regions in figure d indicate the regions where the loose SR and quarkonia veto cuts come into play and reduce the signal yield to zero. The signal model shape must be suppressed in these regions. 130

C.2 Parameters for a Gaussian signal model in the $\langle m_{ll} \rangle$ observable, $\langle \bar{m_{ll}} \rangle_c$ and $\sigma^c_{\langle m_{ll} \rangle}$, based on Gaussian fits to the generated $H \to Z_d Z_d \to 4\ell$ signal samples in the medium SR (figure a,b,c) and after the impact parameter cut low the low-mass selection (figure d). These extracted model parameters are assumed to be model independent for any narrow-width resonance model. The red line shows the relative mean of the fitted Gaussian: i.e. the mass scale is slightly miscalibrated (approximately 0.5% in the $\mu\mu$ channel and 2% in the ee channel, primarily due to final state radiative losses). The blue line shows the relative standard deviation of the fitted Gaussian (scaled by a factor of 100), which is consistent with $\frac{1}{2}\sqrt{\sigma^2_{ll1} + \sigma^2_{ll2}}$, where $\sigma_{ll1,2}$ are the mass resolutions in each dilepton channel (approximately 1.9% for $\mu\mu$ and 3.5% for ee). The effect of the constant term in the mass resolution can be seen by the rise is resolution for the smallest masses in figure d. The black line shows the goodness-of-fit for the Gaussian - while a Crystal Ball would be expected to provide a better model than a Gaussian, the Gaussian model is judged to be sufficient for the purposes for limit setting. . . . 131

C.3 Comparison of the efficiencies as measured with the two benchmark models used in this analysis. TODO: update this figure to release 21, currently use rel 20.7 old plots. 132

C.4 Efficiency with respect to the fiducial volumes defined in section 8.7.1: separate fiducial volumes are defined above and below $m_X = 15$GeV. The inner band of each curve is the MC-statistical uncertainty, and the outer band is the systematic uncertainty. The shaded regions in the low-mass region correspond to where the efficiency will drop to zero due to the quarkonia veto. The step-change in the 4μ efficiency at the $m_X = 15$GeV boundary is due to the differences in the fiducial volume definitions in the high and low mass regions: the additional ΔR requirement improves the signal efficiency. 132

C.5 Acceptance of each model into the fiducial volumes defined in section 8.7.1: separate fiducial volumes are defined above and below $m_X = 15$GeV. The shaded regions indicate where the effect of the quarkonia veto (which is part of the low-mass fiducial volume definition) invalidates the interpolated acceptance. The change in acceptance at 15 GeV is due to the change of fiducial phase space, with additional cuts applied above 15 GeV. The steep rise in acceptance in the high-mass selection in the 4μ and 4ℓ channels is due to the Z Veto, which is cutting on the alternative mass pairings m_{32} and m_{14}. This cut is not applicable to the $2e2\mu$ channel, which therefore has a higher acceptance. 134

E.1 Overall view of the New Small Wheel. Left: Views of the wheel highlighting the modules of the large sectors (LM1 and LM2) and the modules of the small ones (SM1 and SM2). Right: Enlarged view of a Large sector with two small-strip Thin Gap Chambers and two Micromegas quadruplets on both sides of the spacer frame (Manthos et al., 2019). 140

E.2 Left: Operating principle of a Micromegas detector (Alexopoulos et al., 2010). Right: Schematic of the New Small Wheel Micromegas anode board layers and dimensions of its main structures (Kuger, F. and Iengo, P., 2018). . . . 141
E.3 Taking shift at CERN building 188, this step corresponds to the pillar heights measurement. . . . 143
E.4 Pillar heights of each LS7 board superimposed. . . . 144
E.5 Pillar heights of all LS7 boards. . . . 145
E.6 Mean and standard deviation from the fit of each board. . . . 146
E.7 Pillar heights of all LS7 boards. . . . 146
E.8 Dividing the board in 2 equal parts, left and right in order to check any possible asymmetry regarding the pillar heights. . . . 146
E.9 Pillar heights of all LS7 boards. . . . 147
E.10 Left and right pillar heights superimposed. As expected no significant asymmetry is observed. . . . 148
E.11 Left: Pillar heights map of a given LS7 board. Right: Slices that I defined for checking any possible trend along the Y axis. . . . 148
E.12 Average of pillar heights vs slices. Most of the plots are flat which means no trend along th Y axis is observed. . . . 149

List of Tables

4.1 Nominal LHC parameters for the injection and collision energy 31
4.2 The main parameters for ATLAS, CMS, ALICE and LHCb 34

5.1 Parameters of the Inner Detector. The resolutions quoted are typical values (the actual resolution in each detector depends on the impact angle) (Airapetian, 1999) 38

7.1 Expected and observed events for mass $m_{Zd} = 25\,GeV$ (Aad et al., 2015b) 59
7.2 Expected and observed events for mass $m_{Zd} = 20.5\,GeV$ (Aad et al., 2015b) 60
7.3 Expected and observed of events at $36.1 fb^{-1}$ (The ATLAS collaboration et al., 2018). 61
7.4 Expected and observed of events at $36.1 fb^{-}1$ (The ATLAS collaboration et al., 2018) 63
7.5 Expected and observed events at $36.1 fb^{-1}$ (The ATLAS collaboration et al., 2018). 65

8.1 Triggers used in the 2015–8 analysis. Triggers are only used when they are unprescaled. Prescaled triggers are not included because of their low thresholds. 69
8.2 Summary of the event selection of SR1 and SR2 for the AS search. . . . 73
8.3 Cut-flow two in SR1 and SR2 for the mass points $((m_{Zd}, m_S) = (70, 250)$ and $((m_{Zd}, m_S) = (35, 80)$ GeV , and their efficiencies respectively. 74
8.4 Signal samples generated for the AS channel, with variation of the dark Higgs mass (m_S) , the dark vector boson mass (m_{Z_d}) and the dark Higgs width (Γ) with respect to the dark Higgs mass (m_S). 76
8.5 The total expected and the total observed number of events in the validation regions. The uncertainties on the total expected number of events include only MC-statistical components. The predictions do not include Z+jets, because of the unreliability of the MC prediction (negative event yields). 77
8.6 The correlation coefficient for the isolation and the impact parameter variables of the different channels, 4e, 2e2μ, 4μ for data1516 and data17 80
8.7 Estimation of the $t\bar{t}$ background in HM and AS search for the 2015–16 data (with mc16a MC) and the 2017 data (with mc16d MC), by channel. 81
8.8 Estimation of the $Z +$ jets background in HM and AS search for the 2015–16 data (with mc16a MC) and the 2017 data (with mc16d MC), by channel. 81
8.9 Highest QCD and PDF uncertainties of signals and our main background ZZ^*. 83

8.10 AS search: Relative systematic uncertainties in percent on the yield for mc16a signal in SR1 for the mass points $(m_{Zd}, m_S) = (20, 175)$, $(70, 250)$, and $(150, 750)$ GeV. 83
8.11 AS search: Relative systematic uncertainties in percent on the yield for mc16a signal in SR2 for the mass points $(m_{Zd}, m_S) = (35, 80)$, $(40, 90)$, and $(45, 100)$ GeV. 84
8.12 AS search: Relative systematic uncertainties in percent on the yield for the $ZZ^* \to 4\ell$ backgrounds in SR1 for mc16a+d+e (2015–8) simulation. 84
8.13 AS search: Relative systematic uncertainties in percent on the yield for the $ZZ^* \to 4\ell$ backgrounds in SR2 for mc16a+d+e (2015–8) simulation. 85
8.14 Background yields in SR1 and SR2 of the AS channel with the full MC campaign merged, mc16a+mc16d+mc16e 86
8.15 The total expected background yields in the low mass signal region for the full Run 2 luminosity. 91
8.16 Summary of the fiducial definitions used in this analysis, appropriate for processes of the form $H(125) \to XX \to 4\ell$ where X is a promptly-decaying, on-shell, narrow resonance. 94
8.17 Limit setting on the total cross section ratio of $S \to Z_d Z_d \to 4\ell$ and $H \to Z_d Z^* \to 4\ell$ processes XS ratio $= \frac{\sigma^{tot}_{(S \to Z_d Z_d \to 4l)}}{(\sigma_{(ggFH)} \times BR(H \to ZZ^* \to 4l))_{SM}}$ 100
8.18 Limit setting on the total cross section ratio of $S \to Z_d Z_d \to 4\ell$ and $H \to Z_d Z^* \to 4\ell$ processes XS ratio $= \frac{\sigma^{tot}_{(S \to Z_d Z_d \to 4l)}}{(\sigma_{(ggFH)} \times BR(H \to ZZ^* \to 4l))_{SM}}$ 102

A.1 Additional scalar scalar signal samples 109
A.2 The ten Z veto cut hypothesis 111
A.3 Statistics of the signal MC events for different signal mass points with respect to the tested MSR cut. 118
A.4 Statistics of the background MC events differentially with respect to bins in di-lepton mass with respect to the tested MSR cut. 118
A.5 Ratio of efficiencies between signal and background computed by applying either m_{cd}/m_{ab} or $E'_{ab}/m_{4\ell}$ for different signal mass points, $(m_S, m_{Z_d}) = (125, 50), (400, 50)$ and $(755, 65)$ 123
A.6 Events surviving from m_{cd}/m_{ab} or E'_{ab}/m_{ab} cuts, for different signal mass point hypothesis and the two main backgrounds, gluon-gluon fusion (ggF) and SM $ZZ*$ to 4ℓ. 124

This thesis is dedicated to my late supervisor Prof. Mamadou Faye from University Cheikh Anta Diop of Dakar (Senegal). His memory will be always with me.

Chapter 1

Introduction

1.1 Four forces in the universe

In its long quest to understand the physical world in which it lives and of which it is a part, humanity has always thought that to be exact the answer to its questions must be simple. This research has two aspects. One aspect is the search for the elementary entities of which all matter is made, this aspect continues the tradition of Democritus' approach where he postulated the existence of the atom (Berryman, 2016). The other aspect is the search for common features that tend to unify our understanding of the forces acting between the elementary constituents, this second aspect is close to Archimedes' approach, for example.

Some physicists assign the unification to Al-Biruni, a great physicist who lived in the year 1000 in Afghanistan. He seems to be the first to speak about the universality of the laws of physics, a subject which 600 years later was approached experimentally by Galileo (Pitt, 1988). Then came Newton who unified the forces of gravity: the celestial gravity, the force that keeps the earth in orbit around the sun, and the Earth's gravity, the force responsible for the fall of the apples (if we believe the famous anecdote on this subject) (Butterfield, 1984). This was, it seems, the first great unification of physical phenomena.

One hundred and fifty years after Newton, Faraday and Ampere achieved a fundamental unification by linking the phenomenon of magnetism to the movement of electric charges. Thus the two forces of electricity and magnetism became one: electromagnetism. 50 years later, Maxwell developed a complete mathematical framework of electromagnetism (Chilton, 1964) and showed that accelerated charges emit radiation: the electromagnetic radiation he identified with light. This was a milestone in the development of a unified description of physical phenomena. Hence, optics, as a distinct branch of classical physics, becomes part of electromagnetism.

Then Einstein unified the concepts of space and time (Einstein, Podolsky, and Rosen, 1935). Even more he realized that, treating space-time as a dynamic system, its curvature could be associated with the gravitational force postulated by Newton. This leads to an understanding of cosmology as an expression of a space-time dynamic, to the idea of the "Big Bang". The "Big Bang" theory suggested by the observation of the expanding universe and confirmed by cosmic microwave background (CMB) is considered as remnant from an early stage of the universe, known as a relic of the "Big Bang".

Thus, by the 1920s, these two forces, gravity and electromagnetism, described virtually everything we knew about nature at that time. Einstein then cultivated a dream: if one could explain all the phenomena of nature in terms of these two forces, these two forces could be unified as aspects of a single force. His long years of effort were unsuccessful especially because he neglected nuclear forces, which were not well known at this time. All that was known in this field at the beginning of the twentieth century was the atom in the point of view of Democritus.

In 1911, Rutherford, through his scattering of particles, showed the existence of the nucleus (Todd, 2012). Then came Bohr who suggested the planetary model of the atom in 1913 (Wolfgang and Pauli, 1955). From this moment, it became very difficult to attribute the responsibility of the different stages in the description of nature to a given person. In 1935, Yukawa proposed an explanation of nuclear forces as the constant exchange of particles, between the nucleons (Yukawa, 1935). He called the particles exchanged between nucleons, pion (meson) , which are supposed to be "force carrier particles". It turns out that mesons are not elementary particle, hence can't be "force carrier" however his idea remains valid.

Meanwhile, Fermi was developing the theory of β decay (Brown and Rechenberg, 1988). He is the one who made the first step in the theory of weak interaction. In 1933 he published the theory of β-ray emission based on the assumption of the existence of the neutrino. Finally, studying the allowed transitions, Fermi derives an estimate of G_F, the coupling constant which will be shown later to be the universal coupling constant of the weak interaction in 1947. Hence in early 1940 all the 4 fundamental forces in nature were known:

- Gravitational forces: it enables the cohesion of planets, stars, planetary systems, and galactic systems. Compared to the other forces, Its affect is very negligible and becomes sensitive only at Planck scale (at very small scale $\sim 10^{-35}$) which is not reachable by our current tools. We refer to it as a long-range force.

- Electromagnetic forces: it's the more experienced force in our daily life. It explains the attraction (repulsion) between two particles with different (same) charges. For instance it's responsible for the binding between electrons and nuclei, which enables the existence of atom. It's very well described by the quantum electrodynamics (QED) which is on of the most tested theory ever.

- Strong nuclear force: it enables cohesion nucleus in atoms. The mathematical framework used to describe strong interaction is called QCD (Quantum chromodynamic)

- Weak nuclear force: it explains β decay and the energy production in the sun

1.2 Symmetry breaking in particle physics

During the development of particle physics it became essential to introduce a mechanism capable of symmetry breaking. Especially the moment where physicists were conceptualizing the unification of the electromagnetic and weak forces, where the questions which needed to be answered were how these two forces with long and short ranges can have a common description which becomes the same under certain conditions. The mechanism invented then was the "spontaneous breaking" of symmetry. This is a concept that had already been invented by physicists studying the solid state, and they had given it the name of "order" rather than that of "spontaneously broken symmetry"; it was therefore necessary to introduce the phenomenon of "order" into particle physics.

Hence Englert and Brout (Englert and Brout, 1964) demonstrated that gauge bosons, abelian or not, acquire a mass during a spontaneous symmetry breaking. Although observing that the zero mass scalar meson played the role of maintaining gauge invariance in the vector meson propagator, they did not make explicit that it was the only role of the Goldstone bosons, and as a result of which they were in fact unobservable in this type of theory. This aspect of the theory was the dominant aspect of Higgs' work.

1.3 Long quest of electromagnetic and weak force unification

After the unsuccessful attempt of Einstein to unify the electromagnetic and gravitational interactions, there appeared in the 50's the first attempts at unifying the weak and electromagnetic interactions.

When Fermi published his paper on β decay, little was known in the field of the weak interaction. In 1938, following the example of Yukawa, Klein suggested the existence of a new field B_k as the mediator of the interaction responsible for β decay. His work appears as a natural generalization of the theories of currents; indeed it obtains equations of the type of those of Dirac (Bell and Ruegg, 1975), but with terms, in addition to those containing the electromagnetic field A_k, new field B_k describing the action of the charged fields on particles with spin. He introduces a doublet of isospin (proton, neutron) from the Lagrangian L^0, which verifies a local gauge invariance, and obtains neutral and charged fields interacting each other. So, the Lagrangian L^0 can be decoupled in two parts, one part describing heavy particles, and the one for light particles with spin.

The complete Lagrangian would then describe an interaction of light particles with spin and heavy particles not only via the electromagnetic field A_k but also via the B_k field. This interaction is responsible for the β decay process anticipating the existence of intermediate bosons proposed many years later as mediators of weak interaction.

Then, in 1964, Salam and Ward proposed a structure SU(2)$\times$U (1) without introducing a spontaneous breaking of symmetry as a mass generator. Finally, in 1967, using the Higgs mechanism, Weinberg (Weinberg, 1967) introduced the spontaneous breaking of symmetry as a mechanism to give mass to vector mesons and leptons.

1.4 Is it the end of the physics journey ?

Of course, it is not the end of the physics journey. After the unification of electromagnetic and weak interaction, there have been various attempts to unify the strong and electroweak interaction, such as the "Great Unification" theories, for instance. More generally we have witnessed attempts to unify these last three forces and gravitational forces, as part of some string or other types of theories. It is currently believed that beyond a certain threshold of energy for particle interactions, a domain impossible to reach today in a laboratory, the strong, weak and electromagnetic interactions become of the same strength and appear as a single force. The energy domain within which such unification would be observable would be greater than 10^{15} GeV. With regard to gravitational interaction, the problem is that we do not yet have an acceptable quantum theory for gravity; it is not even demonstrated that gravity is of a quantum nature. Figure 1.1 shows the historical progress of this unification. Quantum Chromodynamic and the electroweak theory collectively named Standard Model (SM) of elementary

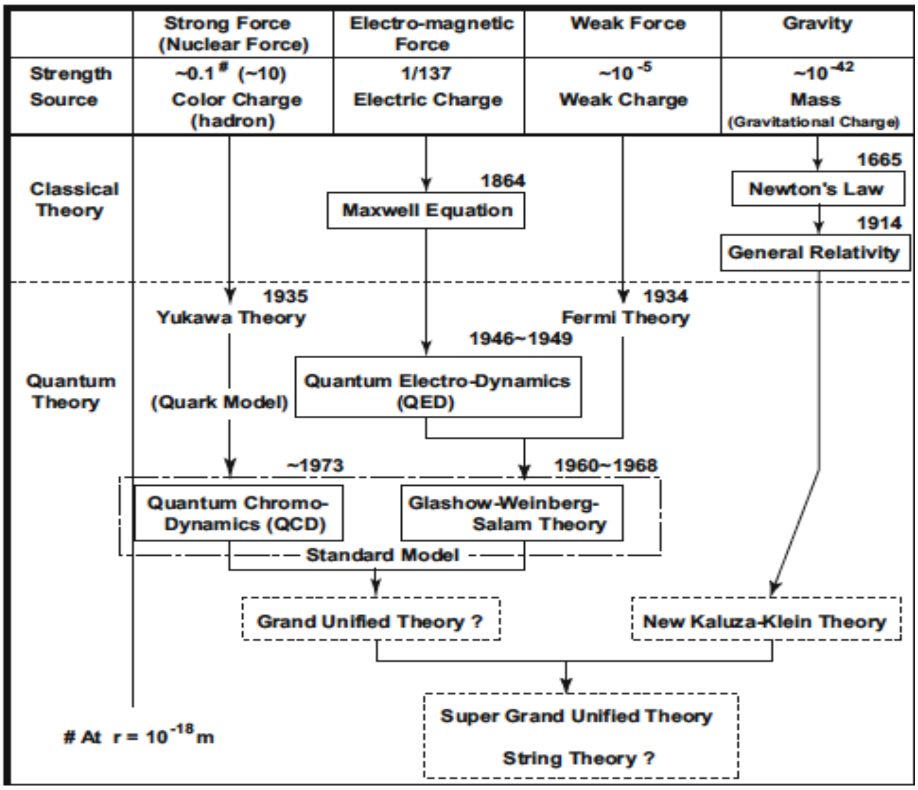

FIGURE 1.1: Unification of the forces. Those enclosed in dashed lines are not yet established. Only the strong force changes its strength appreciably within currently available energy ranges or, equivalently, distances. This is why the distance of the strong force is specified. (Nagashima, 2009)

particle is experimentally very well established. It's very powerful and has demonstrated huge successes in providing experimental predictions.

However, the SM has some limits in the sense that there are many others phenomena that can't be explained by the SM. Hence, physicists are persuaded that there is new physics which would be then Beyond Standard Model (BSM), and are an extension of SM and may be able to explain some enigmas that puzzle the physics community. One of these is the presence of dark matter (DM) in the universe for instance, which accounts for approximately 85% of the matter in the universe. The benchmark models used in this thesis are BSM. These models deal competently with all aspects of the currant DM conundrum, as posed by Astrophysics. They predict particles which could be DM mediators and also fermionic candidates for DM. The Dark Mediator can kinetically mix with the SM equivalent Mediator, and thereby provides the route for DM cooling, as required by Astronomical observations, as this mixing would play the role of the residual interaction that astrophysics requires. Hence, this thesis contributes to the DM study, and in the next section some aspect of DM is discussed.

1.5 Some words on Dark Matter

Dark matter is a kind of matter whose existence is claimed by astrophysicists. It accounts for approximately 85% of the matter in the universe. Many observations are in favor of the existence of dark matter, such as gravity effects which cannot be explained by accepted theories of gravity (General Relativity) unless more matter is present than can be seen. Dark matter is called so because it doesn't interact with observable electromagnetic radiation, and is invisible to the entire electromagnetic spectrum.

Zwicky is one of the first who suggested the existence of dark matter in 1933 (Hubble, Humason, and L., 1931). He obtained evidence of missing mass when he applied the virial theorem to the Coma clusters he was studying. He called the missing mass dark matter. Then Rubin and Ford came up with the same conclusion by observing the rotational curves of spiral galaxies (Rubin and Ford, 1970) in the 1970s. By comparing the rotational velocity of spiral galaxies observed with the expectation based on the visible matter as shown in Figure 1.2, they found the former far greater. This is consistent with the existence of dark matter. Dark matter

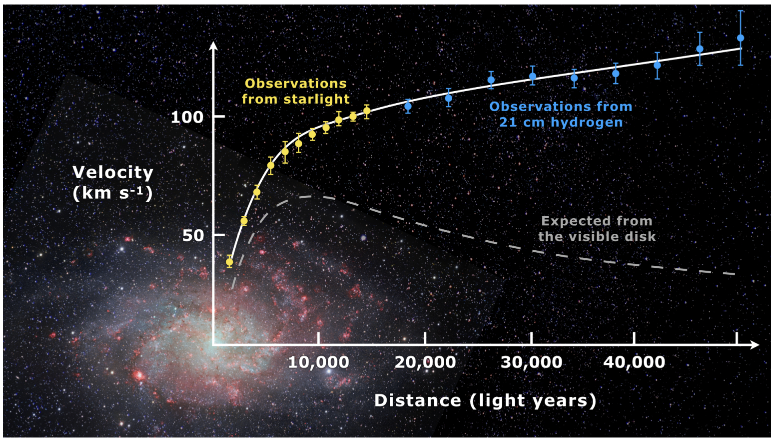

FIGURE 1.2: Rotation curve of spiral galaxy Messier 33 (yellow and blue points with error bars), and a predicted one from distribution of the visible matter (gray line). The discrepancy between the two curves can be accounted for by adding a dark matter halo surrounding the galaxy. (Wikipedia, 2019a)

must be electrically neutral (no electromagnetic interaction), and it must gravitate. It must also be cold (low relative motion compared to the average motion), so in order to cool, it should have at least a weak residual interaction with normal matter. There are no particles in the standard model that could be candidates of dark matter. However, models with physics content Beyond the Standard Model (BSM) such us supersymmetry or string theory or the dark / hidden sector or other models predict some particles which could be dark matter constituents.

1.6 Particle detections in particle physics

A particle accelerator is one of the powerful tools used to investigate the microscopic structure of matter. The dual wave/particle nature of matter predicts a wavelength for particles which is given by the De Broglie equation $\lambda = h/p$. Therefore, the resolution is directly proportional to the inverse momentum of the incoming particle. The smaller the length scale, the higher the particle energy.

Therefore, to explore elementary particle interactions, the highest energy technologically realizable at the era is required. Nowadays the particle accelerator with the highest energy ever is the LHC (Large Hadron Collider) located at the border between France and Geneva. In this thesis we are using the data collected from the ATLAS experiment at the LHC. The development and constructions of accelerators through the years shown in Figure 1.3, enabled the discovery of more

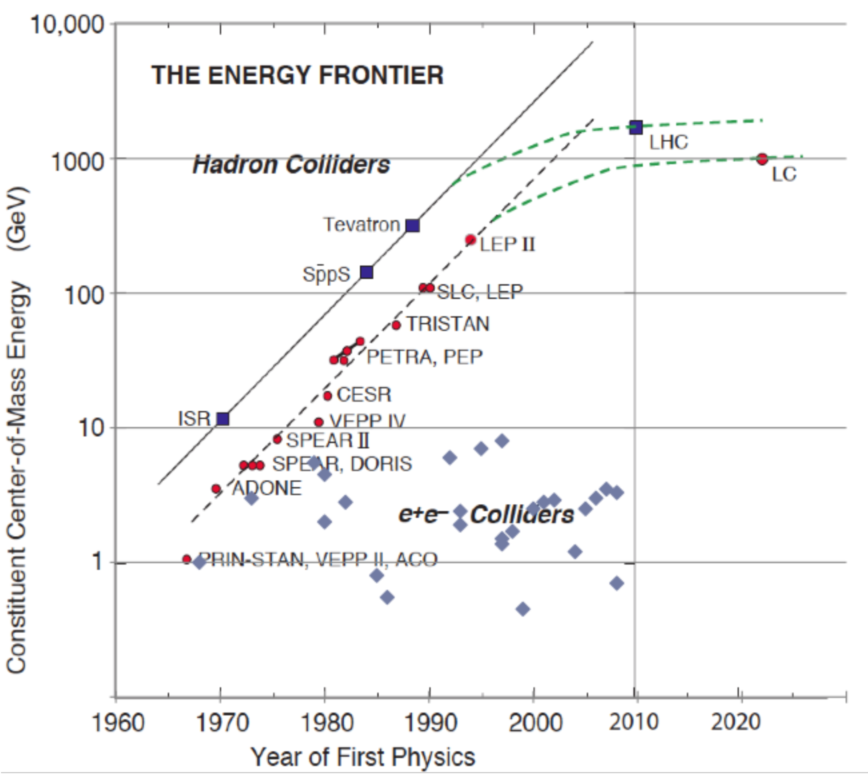

FIGURE 1.3: A Livingston chart depicting progress in collision energy through 2010. The LHC is the largest collision energy to date, but also represents the first break in the log-linear trend. Plot from (Wikiwand, 2020)

and more elementary particles, as higher Center of Mass (CoM) energies became available. In particle physics the experiments can be classified as scattering, spectroscopy and detectors.

1.6.1 Scattering

In a scattering experiment we have a beam of particles of a given energy and momentum directed towards a target. Through this process we can learn about the beam-target or particle-particle interactions by exploiting the changes on the kinematic quantities. Electron scattering is an example of a scattering process, which enables the measuring of the nuclear radii in nuclear physics. The structure of the nuclei in the target become visible via diffraction only when the De Broglie wavelength of the electron is comparable to the target nucleus's size. Therefore, we can extract the size of the nucleus from the diffraction pattern of the scattered particles.

1.6.2 Detectors

Particles can interact with matters in the form of gases, liquids, amorphous solids and crystals. These interactions produce electrical or optical signals which betray the passage of the charged particles. For particles without electric charge the detection is done indirectly, through secondary particles: For example the photon produces free electrons, by the photoelectric or Compton effects, and it produces electron-positron pairs by pair production. Neutrons and neutrinos produce charged particles through reactions with nuclei. Here are the different categories of particles detectors:

- Scintillators: they provide fast timing information, but have only moderate spatial resolution.
- Gaseous detectors: they cover large areas and provide good spatial resolution, used in combination with a magnetic field to measure momentum.
- Semiconductor detectors: they have a very good energy and spatial resolution.
- Cherenkov detectors: they can image the Cherenkov light and can be used for particle identification and also velocity measurement.
- Calorimeters: they are of several types and used to measure the total energy deposited by particles with very high energies.
- Transition Radiation Detectors : use the emission of lower energy photons at the boundaries between stratified materials with some active material (gas or silicon detector) between the strata to measure the particle energy.

1.7 Units

The units for length and energy commonly used in particle and nuclear physics are the femtometer (fm or Fermi) and electron volt (eV) respectively. One fm corresponds to 10^{-15} m which is a standard SI-unit and corresponds to the size of a proton. By definition an electron volt is the energy gained by a particle with charge 1e by traversing a potential difference of 1 volt, so one eV correspond to 1.602×10^{-19} J.

keV, MeV, GeV... are used, which are specific decadal metric prefix scale multipliers to the units of eV. From the equation

$$E = mc^2 \leftrightarrow m = E/c^2.$$

MeV/c^2, GeV/c^2 is used as unit of the particles masses. A useful approximation to remember is also the relation between the Plank constant and the speed of life relation: $\hbar \times c = 197.3269631(49)$ MeV fm. The fine structure constant is also another quantity often used, it is the coupling constant for electromagnetic interactions and defined by:

$$\alpha = \frac{e^2}{4\pi\epsilon_0\hbar c} \sim \frac{1}{137}.$$

It is convenient in particle physics to set $\hbar$ and c equal to 1 and to chose $\epsilon_0 = \mu_0 = 1$ so that Maxwell's equations have the Standard International form known as Heaviside units.

1.8 Thesis plan

In this thesis, the search for a dark vector boson and a new scalar with the ATLAS detector is carried out and it's structured as following:

- the theory part,
- detector, reconstruction and identification part,
- analysis and conclusion part.

In the theory part, the Standard Model (SM) and the Beyond Standard Model (BSM) theories motivating the search are reviewed. In the detector, reconstruction and identification part, the Large Hadron Collider (LHC), the ATLAS detector, and the reconstruction of events and object are described. In the analysis and conclusion part, the results of Run 1 and Run 2 analysis performed with the ATLAS detector at the Large Hadron Collider are reviewed. The Run 1 (Run 2) analysis uses data from proton-proton collision corresponding to an integrated luminosity of about 20.3 fb^{-1} (36.2 fb^{-1}) at the center-of-mass energy of $\sqrt{s}$ = 8 TeV (13 TeV). These two previous searches are iterated and extended in the full Run 2 analysis corresponding to an integrated luminosity of 139.1 fb^{-1}. They are presented in the last part before the conclusion.

1.9 The author's contributions

The ATLAS[1] experiment is a huge collaboration with more than 3,000 physicists. Publishing a paper using the ATLAS detector requires a lot of effort, dedication and man power; from data taking, including all the components, MC simulation, Editorial Board for approval, to publication. The long authors list in the published papers is just to give credit to each single person who somehow participates in the achievement. However, to be authored, an authorship qualification task is required. Hence, my first year of PhD was mostly focused on my qualification task in the New Small Wheel experiment. I was supporting the quality control/quality assurance (QCQA) activity of the Micromegas Read Out (RO) Printed Circuit Boards (PCBs). After a dedicating training I joined the shift crew taking regular QCQA shifts. In parallel, I developed software tools to perform statistical analysis of the measurements performed during the QCQA shifts which include in particular, statistics for the pillar heights measurement and the board dimension measurements. The qualification task is described in Appendix E.

In parallel to my qualification task I was also involved in our analysis. The analysis is performed in Run 1 with the ATLAS detector in proton-proton collision data at $\sqrt{s}$ = 8 TeV with an integrated luminosity of 20 fb^{-1}. It's iterated in Run 2 where the center-of-mass energy and the integrated luminosity increased to 13 TeV and 36.1 fb^{-1} respectively. Now it's being performed in the full Run 2, where the integrated luminosity became 139.0 fb $^{-1}$. The Run 2 analysis searches for a Higgs boson decaying to 4 leptons (electrons or muons) via two dark vector bosons states Z_d or pseudo scalars a, and has 3 sub-analysis or channels as follows:

1. $H \to ZZ_d \to 4\ell$ (ZZ_d channel)
2. $H \to Z_d Z_d \to 4\ell$ (high mass channel)

[1] It's described in the Chapter 5.2

3. $H \to aa \to 4\mu$ (low mass channel)

My main contribution in Run 2 is on high mass channel. I performed cut flow comparisons for validation, I also participated in the limit setting on the branching ratio $H \to Z_d Z_d$ and on the model parameters that control the mixing between the SM Higgs and the Dark Higgs. I validated the model interpretation of the low mass ($H \to aa \to 4\mu$) results in the 2HDM+Singlet used as bench mark model. I also participated in the paper drafting process. In the full Run 2 these 3 channels have been extended and two new channels have been added:

1. $S \to Z_d Z_d \to 4\ell$ (additional scalar channel)
2. $H \to Z_d Z_d/aa \to 4\ell$ (tau channel: including tau) [2]

The additional scalar channel searches for a dark Higgs (S with $m_S \neq m_H$) decaying two four leptons via two Z_d. The tau channel includes τ in the final states of the $H \to Z_d Z_d/aa \to 4\ell$ search. In the full Run 2 iteration I am the main analyzer of the additional scalar channel, from MC simulation at truth level to limit setting. I also participated in the high mass channel, especially in the signal region re-optimization and the data driven method used to estimate the reducible backgrounds. I am also editor of the support note and the main editor of the additional scalar section. As a contact person of the analysis I also have to monitor and look after all the 5 channels even thought I don't have a direct contribution in the ZZ_d and tau channels.

During these three years I also participated in many workshops, conferences and seminars:

- International Conference on Neutrinos and Dark Matter, in Egypt, 11-14th January, 2020 (from an official invitation from ATLAS, as ATLAS speaker).
- Johns Hopkins University Seminar, October 25th 2019 (as speaker).
- Higgs and Diboson Searches (HDBS) workshop in Naples June 11th-14th 2019 (as speaker).
- International Workshop on Discovery Physics at the LHC (Kruger 2018) in South Africa, 3-7th December, 2018 (presenting a poster).
- African conference of physics (ACP) in Namibia, July 2nd, 2018 (as speaker).
- Dark Interaction workshop at BNL, USA, October 4th 2018 (as speaker).
- South African Institute of Physics (SAIP) in South Africa, June 27th, 2018 (as speaker).
- Annual Interdisciplinary Academy 2018 at the University of South Africa (UNISA), in South Africa, November 6th, 2018 (as speaker).

where some of them led to a proceedings and published articles (Boye and Mapekula, 2019).

During my PhD period I also participated a lot in the data taken by doing shifts (day or night) in the ATLAS control room especially in the run and trigger desks.

[2] The tau channel is not discussed in this thesis

Part I

Theory

Chapter 2

Standard Model (SM) of particle physics

The SM describes the three forces (the electromagnetic force, the weak force and the nuclear force) known in the universe and their interactions with the elementary particles. The electromagnetic force is mediated by the photons, the weak interaction by the W boson and the Z boson, and the strong force by the gluons. Fermions appear as leptons and quarks in exactly three matching generations of pairs and participate in the $SU(3)_C \times SU(2)_L \times U(1)_Y$ gauge interactions. The $SU(2)_L \times U(1)_Y$ symmetry is spontaneously broken at a scale of $v \sim 0.25$ TeV leaving $SU(3)_C$ and $U(1)_{em}$ symmetries unbroken. A Non-abelian gauge symmetry underlies the universality of the couplings of fermions with gauge fields. The condensation of quarks into hadrons is also a consequence of non-Abelian gauge symmetry. The SM is the most precise mathematical model ever tested by measurements of its prediction, most of its which have been approved by experiments. In this thesis the SM is not used as a benchmark, instead Beyond Standard Models are used. Therefore, the SM is not derived here, however it's successes and limitations are recalled. For more details about the SM the following references can be consulted: (Hollik, 2010; Fritzsch and Gell-Mann, 1972; Cottingham and Greenwood, 2007; Eidelman et al., 2004; Gaillard et al., 1999).

2.1 The Standard Model successes

The SM successes started from its basic construction and continue to amaze physicists by the accuracy of its predictions. Some of its successes are recalled in this section as follows:

- Already in 1969 Gell-Mann was awarded a Nobel Prize for his "contributions and discoveries concerning the classification of elementary particles and their interactions" (Lütkebohle, 1969).
- In 2013 Englert and Higgs received the Nobel Prize for their contributions on the model for the mass generation mechanism of gauge bosons, predicted around 1964. The predicted particle (associated with this mechanism), named as Higgs boson, was discovered in 2012 by the two experiments ATLAS and CMS at the Large Hadron Collider at CERN (Aad, 2012; Chatrchyan, 2012). Figure 2.1 shows the $m_{4\ell}$ distribution of the signal and the backgrounds, where the bump around 125 GeV indicates the Higgs boson decaying to 4 leptons through the process: $H \rightarrow ZZ^* \rightarrow 4\ell$. This is one of the biggest successes of particle physics. It had been considered by many physicists as the missing piece of the SM.

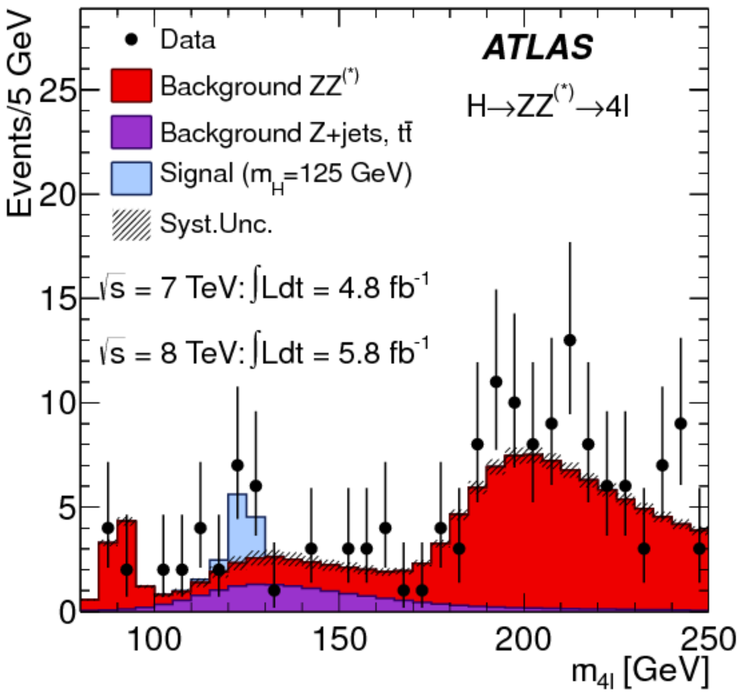

FIGURE 2.1: The distribution of the four-lepton invariant mass, $m_{4\ell}$, for the selected candidates, compared to the background expectation in the 80–250 GeV mass range, for the combination of the $\sqrt{s}$ = 7 TeV and $\sqrt{s}$ = 8 TeV data. The signal expectation for a SM Higgs with m_H = 125 GeV is also shown. (Aad, 2012)

.

- Glashow, Salam and Weinberg merged the electroweak interaction and the BEH (Brout-Englert-Higgs) mechanism into a renormalizable gauge theory, where the gauge bosons $W^{\pm}$ and Z^0 were predicted. These 2 bosons were discovered in 1983 at the Super Proton Synchrotron (SPS) at CERN (Arnison et al., 1983; Banner et al., 1983). They were awarded the 1979 Nobel Prize for their contributions. Since their discovery, the $W^{\pm}$ and Z^0 boson have always been studied and one of the recent results is presented in this article (Aaboud, 2018b). Figure 2.2 shows for instance the measurements of the $W^{\pm}$ boson mass by the ATLAS experiment compared to the previous measurements by LEP experiments ALEPH, DELPHI, L3 and OPAL , and by the Tevatron collider experiments CDF and D0. The measured W boson mass is $m_W = 80370 \pm 19$ MeV, where the the statistical uncertainty, the experimental uncertainty and the physics modeling uncertainty are included. Figure 2.3 shows the hadronic cross-section for the production of Z, as a function of centre-of-mass energy, where an excellent agreement between the SM prediction (in line) and the data (in dots) is observed. This is a good example of the SM accuracy. It also worth mentioning that the experimentalists Carlo Rubbia and Simon Van der Meer were awarded the 1984 Nobel Prize for the discoveries of the $W^{\pm}$ and Z^0 particles.
- In 1970 the Glashow-Iliopoulos-Maiani mechanism known as GIM mechanism postulated the existence of a fourth quark on top of the ones already known (u, d and s). This quark (charm) was discovered in 1974

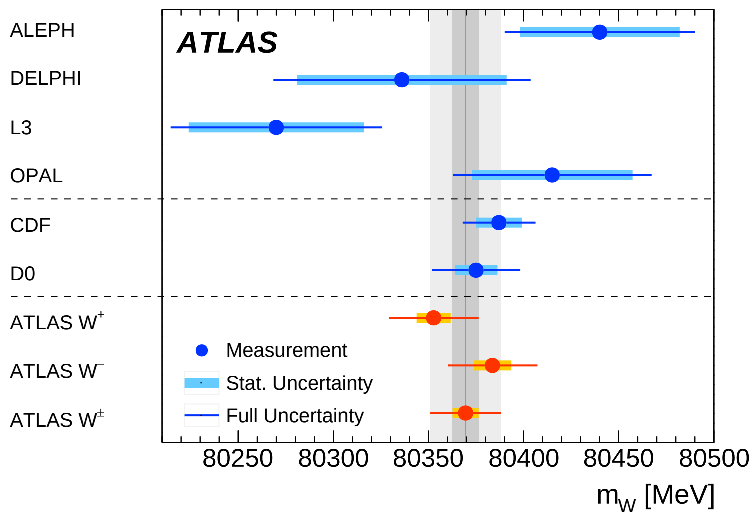

FIGURE 2.2: The measured value of m_W is compared to other published results, including measurements from the LEP experiments ALEPH, DELPHI, L3 and OPAL , and from the Tevatron collider experiments CDF and D0. The vertical bands show the statistical and total uncertainties of the ATLAS measurement, and the horizontal bands and lines show the statistical and total uncertainties of the other published results. Measured values of m_W for positively and negatively charged W bosons are also shown. (Aaboud, 2018b)

.

through the measurement of the J/Ψ meson production and decay by the Stanford Linear Accelerator Center (SLAC), in an experiment led by Burton Richter, and also at the Brookhaven National Laboratory (BNL), in an experiment led by Samuel Ting (Khare, 1999) which enabled them to each win the 1976 Nobel Prize.

- Asymptotic freedom explains the interactions between particles which become asymptotically weaker as the energy scale increases and the corresponding length scale decreases. This key feature of QCD was discovered in 1973 by Gross, Politzer, and Wilczek (Gross, 2005) and enabled them to get the 2004 Nobel Prize. In the same year the high-p_T particles, the CERN ISR and 3 years later in 1978, the gluons, predicted by QCD were discovered at the PETRA, e^+e^- collider at DESY in Hamburg.
- In 1975 the third charged lepton τ was discovered by the SPEAR (Perl, 2004) team led by Per,.Hence, he got the 1995 Nobel Prize for this discovery.
- In 1977 the fifth quark, b was discovered at Fermilab. In 1995 and 2000, Tevatron and Fermilab discovered the top and τ neutrino quarks respectively which complete the third family of the SM.

The successes of the SM listed above and ordered by chronological predictions, is non-exhaustive, nevertheless they show how this model work so perfectly. It is very predictive in terms of new particles and phenomena, and also in terms of the precision at which some parameters can be calculated. However, the SM appears to be unable to explain some physics phenomena, hence has some limits or deficiencies.

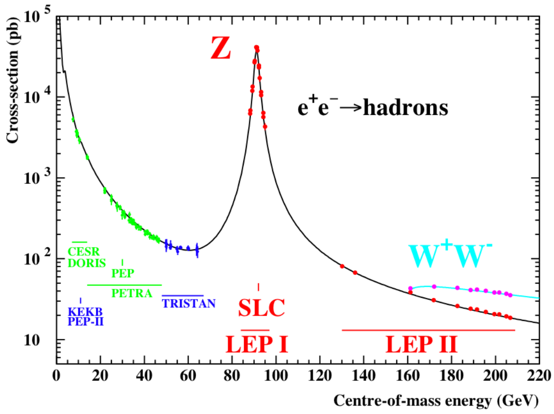

FIGURE 2.3: The hadronic cross-section as a function of centre-of-mass energy. The solid line is the prediction of the SM, and the points are the experimental measurements. Also indicated are the energy ranges of various e^+e^- accelerators. The cross-sections have been corrected for the effects of photon radiation. (Schael, 2006)

.

2.2 The Standard Model limits

Beyond its successes listed above, the SM does not explain the number of fermions, the number of fermion generations, the number and type of gauge interactions, it does not constrain the coupling constants, it does not explain the source of P, C, and T violation, and the origin of spontaneous symmetry breaking. It is unsatisfactory that there are many free parameters (gauge couplings, vacuum expectation value, mass of the Higgs boson, fermion masses, CKM matrix elements), which are not predicted but have to be taken from experiments. The theory also fails to explain the pattern that occurs in the arrangement of the fermion masses, the quantization of the electric charge, or the values of the hypercharge. A very important deficiency is the missing connection to gravity. There are also no answers provided about the nature of dark matter that constitutes the largest fraction of matter in the universe, the presence of dark energy, and also the origin of the baryon asymmetry in the universe. In order to give answers to these questions, new physics which goes beyond the standard model must be discovered.

Conclusion: Despite being the most successful theory of particle physics to date, in describing a large variety of phenomena, at a high level of accuracy on both the theoretical and the experimental side, the Standard Model is not perfect. A large share of the published output of theoretical physicists consists of suggestions for various forms of "Beyond the Standard Model" new physics proposals that would modify the Standard Model in ways subtle enough to be consistent with existing data. In the next chapter some Beyond Standard Models physics is discussed.

Chapter 3

Beyond the Standard Model

The well known theoretical attempts beyond the SM include supersymmetry, string theory, loop quantum gravity, amongst other. Amongst the BSM theories, two of them used in this thesis as benchmarks will be considered in more detail which are: the HAHM (Hidden Abelian Higgs Model) and the 2HDM+s (Two-Higgs-doublet model+singlet). These two models predict particles (named Z_d or a) which can be candidate for the dark matter (Clowe et al., 2006) and by decaying to leptons such as electrons or muons, they could also explain astrophysical observations of positron excesses (Chang et al., 2008; Adriani, 2009; Aguilar et al., 2013).

3.1 Hidden Abelian Higgs Model

The SM can be extended by adding a $U(1)_d$ gauge symmetry to its Lagrangian, which is theoretically well motivated. Several possibilities exist to connect the $U(1)_d$ gauge symmetry to the SM (Langacker, 2009; Jaeckel and Ringwald, 2010; Hewett, 2012; Essig, 2013), in the literature the $U(1)_d$ vector boson is referred to as A', Z', γ_D, or Z_d. The model predicts a Higgs decay to A', with a mass range between $\sim$ MeV to 60 GeV. A' is a good candidate to explain the anomalies related to the dark matter and the discrepancy between the calculated and measured muon anomalous magnetic moment. It also could give explanation of astrophysical observations of positron excesses.

In a renormalizable interaction the $U(1)_d$ vector boson can couple to the SM via a small gauge kinetic mixing term $\frac{1}{2}\epsilon F'_{\mu\nu}B^{\mu\nu}$ (Holdom, 1986) between the dark photon and the hypercharge gauge boson, which can be generated at a high scale in a grand unified theory or in the context of string theory with a wide range of the kinetic mixing parameter $\epsilon \sim 10^{-17} - 10^{-2}$ (Holdom, 1986; Abel and Schofield, 2004). A "dark Higgs" S with a nonzero vacuum expectation value can give a nonzero mass to A'. That can be probed in beam dumps and colliders, and with measurements of the muon anomalous magnetic moment, supernova cooling, and rare meson decays, in sub-GeV mass range.

The $U(1)_d$ can be broken and this leads to exotic Higgs decays, where we also have a mixing between S and H (the Standard Model Higgs), and we note the corresponding vector field as Z_d. Only prompt Z_d decays are considered, which requires $m_{Zd} \gtrsim 10\,\text{MeV}$ given the current constraints shown in Figure 3.1.

The kinetic terms of the hypercharge and $U(1)_d$ are

$$\mathcal{L}_{gauge} = -\frac{1}{4}\hat{B}_{\mu\nu}\hat{B}^{\mu\nu} - \frac{1}{4}\hat{Z}_{d\mu\nu}\hat{Z}_d^{\mu\nu} + \frac{1}{2}\frac{\epsilon}{\cos\theta_W}\hat{B}_{\mu\nu}\hat{Z}_d^{\mu\nu} \tag{3.1}$$

with $\hat{B}_{\mu\nu} = \partial_\mu\hat{B}_\nu - \partial_\nu\hat{B}_\mu$, $\hat{Z}_{d\mu\nu} = \partial_\mu\hat{Z}_{d\nu} - \partial_\nu\hat{Z}_{d\mu}$ and $\cos\theta_W = g/\sqrt{g^2+g'^2}$ is the usual Weinberg mixing angle. The hatted quantities are fields before diagonalizing

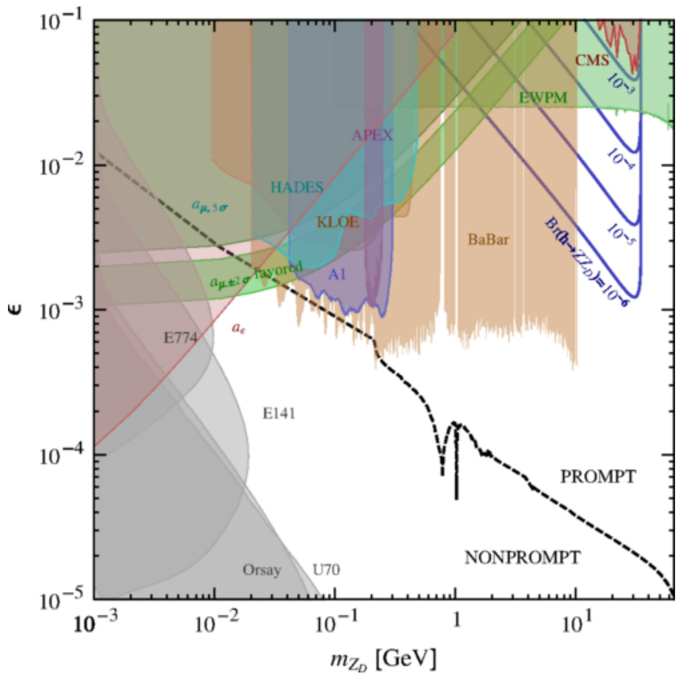

FIGURE 3.1: Constraints on ϵ versus m_{Z_d} for pure kinetic mixing (no additional source of mass mixing) for $m_{Z_d} \sim 10\ MeV$ GeV. The black dashed line separates prompt ($c\tau < 1\mu m$) from nonprompt Z_d decays. The three blue lines are contours of $Br(H \to ZZ_d)$ of 10^{-4}, 10^{-5}, and 10^{-6}, respectively. Plot from (Curtin et al., 2014)

the kinetic term. The Higgs potential is

$$V_0 = -\mu^2|H|^2 + \lambda|H|^4 - \mu_d^2|S|^2 + \lambda_d|S|^4 + \kappa|S|^2|H|^2. \tag{3.2}$$

Z_d obtains its mass m_{Z_d} from the dark Higgs S that acquires a vacuum expectation value. The connection between the dark and the standard model sector are the gauge kinetic mixing ϵ and the Higgs mixing κ, where the phenomenology depends on which one dominates. Another scenario that can also occurs is where on has a mass-mixing between the SM Z boson and a Z_d through a coupling proportional to the mass mixing parameter δ.
The mass terms of Z_d and Z are

$$\mathcal{L}_{mass} = \frac{1}{8}w^2 g_d^2(\hat{Z}_{d\mu})^2 + \frac{1}{8}v^2(-g\hat{W}_\mu^3 + g'\hat{B}_\mu)^2. \tag{3.3}$$

Three cases can be considered for the relevant limits of this theory:

Gauge kinetic mixing dominates: For $\epsilon \gg \kappa$ the dominant exotic Higgs decay is $H \to ZZ_d$. To leading order in $m_{Z_d}^2/m_Z^2$ the partial width is

$$\Gamma(h \to ZZ_d) = \frac{\epsilon^2 \tan^2\theta_W}{16\pi}\frac{m_{Z_d}^2(m_h^2 - m_Z^3)^3}{m_H^3 m_Z^2 v^2}. \tag{3.4}$$

This is in agreement at $\sim 10\%$ to the full analytical expression for $m_H - m_Z - m_{Z_d} >$ 1 GeV. Figure 3.1 shows contours of $BR(H \to ZZ_d) = 10^{-4}, 10^{-5}, 10^{-6}$. The largest branching ratio allowed by indirect electroweak precision constraints is $\sim 3 \times 10^{-4}$.

Higgs mixing dominates: In case Higgs mixing dominates ($\kappa \gg \epsilon$), then $H \to Z_d Z_d$ and ss are both possible, depending on the mass spectrum of the dark sector. The partial decay widths to the leading order in κ are

$$\begin{aligned}\Gamma(H \to Z_d Z_d) =& \frac{\kappa^2}{32\pi} \frac{v^2}{m_H} \sqrt{1 - \frac{4m_{Z_d}^2}{m_H^2}} \frac{(m_H^2 - 2m_{Z_d}^2)^2 - 8(m_H^2 - m_{Z_d}^2)m_{Z_d}^2}{(m_H^2 - m_s^2)^2}, \\ \Gamma(h \to ss) =& \frac{\kappa^2}{32\pi} \frac{v^2}{m_h} \sqrt{1 - \frac{4m_s^2}{m_h^2}} \frac{(m_h^2 + 2m_s^2)^2}{(m_h^2 + m_s^2)^2}.\end{aligned} \tag{3.5}$$

Figure 3.2 shows the different regions of the (m_{Z_d}, m_s) mass plane, along with the size of the Higgs mixing $\kappa \sim 10^{-3} - 10^{-2}$ required for $Br(H \to Z_d Z_d, ss) = 10\%$ and the relative rates of $H \to ss$ versus $H \to Z_d Z_d$ decays when both are allowed. The

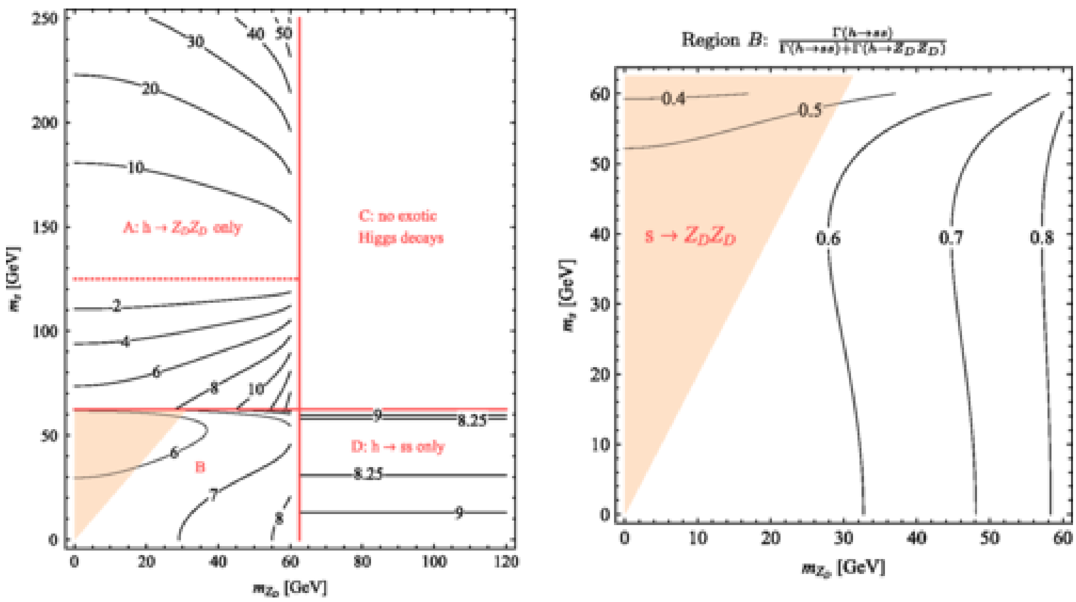

FIGURE 3.2: Left: Mass plane in the SM + V model with different exotic Higgs decays for $\kappa \gg \epsilon$ (i.e., when the mixing between the Higgs and dark Higgs dominates over the kinetic mixing). The black contours are the values of $\kappa \times 10^3$ required for $Br(H \to Z_d Z_d, ss) = 10\%$. Region A covers the $H \to Z_d Z_d$ decay. Region C has no exotic Higgs decays. Region D covers the $H \to ss$ decay, and Region B has both the $H \to ss$ and $H \to Z_d Z_d$ decays, with the $H \to ss$ fraction of exotic decays shown on the right. In the upper left shaded region, $s \to Z_d Z_d$ is the dominant decay mode of the dark scalar. This allows the Higgs to decay to up to eight SM fermions (Curtin et al., 2014)

.

region A ($m_s > m_H/2; m_{Z_d} < m_H/2$) allows only the Higgs decaying to two Z_d to four leptons ($H \to Z_d Z_d \to 2\ell 2\ell'$ with $\ell, \ell' = e$ or μ), where the reconstruction of the Z_d resonance is above the τ or b thresholds. Region B allows the two cases where the Higgs decays to $Z_d Z_d$ or ss. The presence of two resonances $< m_H/2$ corresponds to a rich exotic-decay phenomenology. The branching ratios of $H \to ss \to 4Z_d$ and $H \to Z_d Z_d$ are roughly equal and lead up to eight leptons in the final state. In this simplified model, there is no corresponding $Z_d \to ss$ decay in the lower right corner of that mass plane. However, a (pseudo)scalar pair could be produced from dark vector decay in, e.g., a 2HDM+V framework, resulting in final states with as many

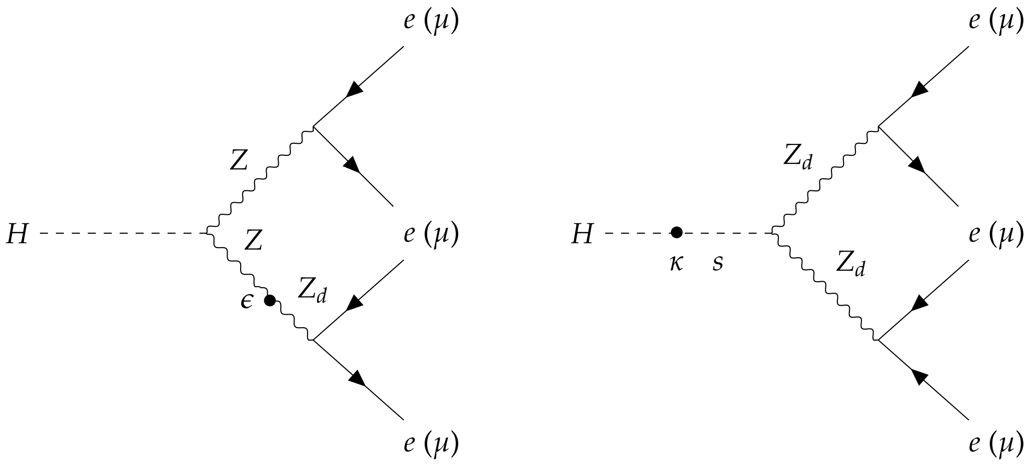

FIGURE 3.3: Exotic Higgs decays to four leptons induced by intermediate dark photons in HAHM. H is the Higgs boson, Z_d the dark vector boson, ϵ the kinetic mixing parameter, κ the Higgs mixing parameter, s the dark Higgs boson. Left: $H \rightarrow ZZ_d \rightarrow 4l$ via the hypercharge portal. Right: $H \rightarrow Z_dZ_d \rightarrow 4l$ via the Higgs portal.

as eight b quarks. The upper bond limit of the $BR(H \rightarrow Z_dZ_d)$ with the current data is $\lesssim 10^{-4}$.

Figure 3.3 shows the two Feynman diagrams corresponding to the two regimes ($\epsilon \gg \kappa$ and $\kappa \gg \epsilon$) that are considered in this thesis. The left-hand side of Figure 3.3 corresponds to the $H \rightarrow ZZ_d$ process which probes the parameter space of ϵ and the mass of dark vector boson m_{Z_d}, or δ and m_{Z_d}. The right-hand side corresponds to $H \rightarrow Z_dZ_d$ process and covers the parameter space of κ and m_{Z_d}. For a heavy singlet scalar but non-negligible singlet-Higgs mixing, this decay is by far the most sensitive test of the $U(1)_d$ hidden sector if $\epsilon \lesssim \mathcal{O}(10^{-3})$ and while production of the Z_d pair occurs through the Higgs portal, Z_d decay has to proceed through the hypercharge portal. Therefore, observation of $H \rightarrow Z_dZ_d$ requires a non-zero value for ϵ.

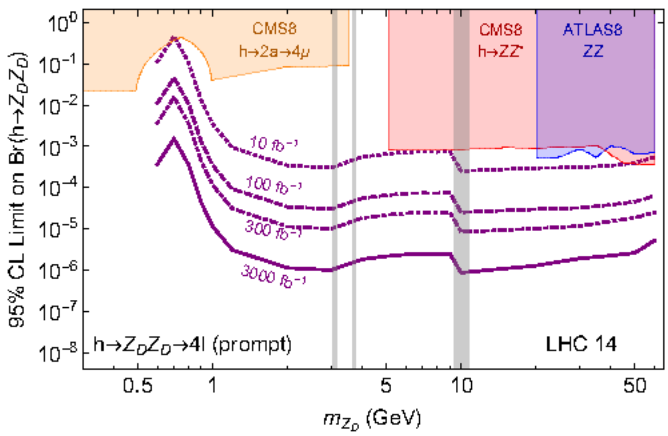

FIGURE 3.4: Expected 95% CLs limits on the total exotic Higgs decay branching ratio, BR($H \rightarrow Z_dZ_d$). (Curtin et al., 2015)

Only Z_d produced on-shell is considered, as otherwise the Higgs decay will be suppressed by ϵ^2 and thus unobservable. They also are assumed to decay promptly as shown in Figure 3.4, which correspond to $\epsilon \gtrsim 10^{-5} - 10^{-3}$ (Figure 3.5). This is in order to not have a displaced vertex or significant lifetime, which would mean a different experimental search program.

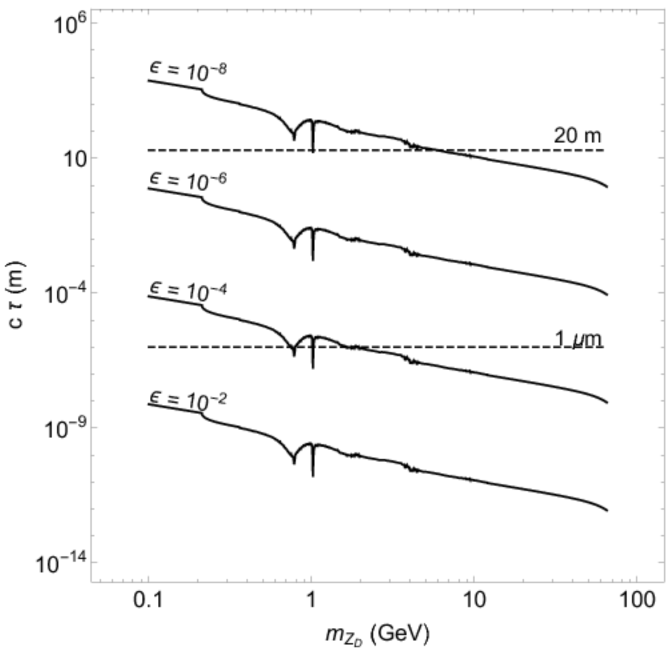

FIGURE 3.5: Decay length of Z_d for different ϵ. The dashed lines indicate boundaries between qualitatively different experimental regimes: prompt decay for $c\tau \lesssim 1\mu m$ and likely escape from an ATLAS-size detector for $c\tau \gtrsim 20m$ (Curtin et al., 2015).

Intermediate regime: The intermediate regime corresponds to the case where the kinetic mixing ϵ and the Higgs mixing parameters are similar κ. As shown in Figure 3.1, the region for $\epsilon \sim 10^{-2}$ and $m_{Z_d} > 10$ GeV is not excluded, this allows $Br(H \to ZZ_d) \lesssim 10^{-4}$, which is similar to $Br(H \to Z_d Z_d; ss)$ if $\kappa \sim 10^{-4}$.

In summary, many kinds of exotic Higgs decays are allowed by the HAHM scenario , including $H \to ZZ_d$, $H \to Z_d Z_d$, $h \to ss$ with $Z_d \to f\bar{f}$ and $s \to f\bar{f}$ or $s \to Z_d Z_d \to (f\bar{f})(f\bar{f})$. This leads to final states of $Z + (f\bar{f})$, $(f\bar{f})(f\bar{f})$, and $((f\bar{f})(f\bar{f}))((f\bar{f})(f\bar{f}))$ where parentheses around a set of particles denotes a resonance (all final-state particles combined will form the Higgs resonance). Since the Z_d (although not the s) couples to the fermions' gauge charges, final states with several light leptons have sizable branching fractions over the entire kinematically permitted mass range.

3.2 2HDM + Scalar

Another way to go beyond the SM is by simply adding a doublet to its single $SU(2)_L$ doublet H with hypercharge $Y = +\frac{1}{2}$. This Higgs sector extension is known as the 2HDM (2 Higgs doublet model) and should be compatible with a ρ parameter close to 1. It is well motivated and flourishes in the literature such as in articles on supersymmetry (Haber and Kane, 1985) and on axion models (Kim, 1987; Peccei and Quinn, 1977), where holomorphy and the Peccei-Quinn symmetry, respectively, necessitate an additional doublet; it also appears in some theories of electroweak baryogenesis, which might be made viable with additional doublets (Trodden, 1998); and in some grand unified models.

The most general 2HDM+scalar Higgs potential is given by

$$\begin{aligned} V = & m_1^2|H_1|^2 + m_2^2|H_2|^2 + \frac{\lambda_1}{2}|H_1|^2 + \frac{\lambda_2}{2}|H_2|^2 + \frac{\lambda_3}{2}|H_1|^2|H_2|^2 + \frac{\lambda_4}{2}|H_1^\dagger H_2|^2 \\ & + \frac{\lambda_5}{2}[(H_1H_2)^2 + c.c.]m_{12}^2(H_1H_2 + c.c.) \\ & + [\lambda_6|H_1|^2(H_1H_2) + c.c.] + +[\lambda_7|H_2|^2(H_1H_2) + c.c.]. \end{aligned} \tag{3.6}$$

To ensure that fermions with the same quantum numbers all couple to only one Higgs field, $\mathbb{Z}_2$ symmetry is required, this enables one to avoid the most general Yukawa couplings to fermions that would result in large flavor-changing neutral currents. It also results in four types of fermion couplings commonly discussed in the literature: type I (all fermions couple to H_2), type II (MSSM-like, d_R and e_R couple to H_1, u_R to H_2), type III (lepton-specific, leptons and quarks couple to H_1 and H_2, respectively) and type IV (flipped, with u_R; e_R coupling to H_2 and d_R to H_1).

The 2HDM predicts the Higgs particle (denoted as H or H^0 with 125 GeV state) decaying to exotic particles: $H \to AA$, $H^0 \to HH, AA$ or $H \to ZA$, which could then decay to SM fermions or gauge bosons. This phenomenology is very constrained by the current data (Gunion et al., 1997; Bélanger et al., 2013), however there is still some region in the parameter space which is not yet excluded.

To avoid these restrictions, the 2HDM is assumed to be near or in the decoupling limit,

$$\alpha \to \pi/2 - \beta. \tag{3.7}$$

β is a rotation angle defined by $\tan\beta = \frac{v_2}{v_1}$ ($v_{1,2}$ are the vacuum expectation values of $H_{1,2}$). In the 2HDM, H is the observed 125 GeV state which is the lightest state, the fermion couplings of H also become identical to the SM Higgs, while for $\tan\beta \gtrsim 5$ the gauge boson couplings are very close to SM-like . The properties of H and the type of fermion couplings are determined by $\tan\beta$ and α. The parameters related to the Higgs spectrum and its phenomenology, are very constrained by the measured production and decay of H, but some viable parameter space exist in the decoupling limit.

Another way of avoiding the restrictions is to add to the 2HDM one complex scalar singlet,

$$S = \frac{1}{\sqrt{2}}(S_R + iS_I). \tag{3.8}$$

This assumption is known as the 2HDM+S. This singlet may attain a vacuum expectation value that we implicitly expand around. It only couples to $H_{1,2}$ in the potential, and do not have Yukawa couplings, instead it couples to SM fermions through its mixing with $H_{1,2}$. In order to maintain the SM-like nature of H, this mixing is required to be small.

These two assumptions imply exotic Higgs decays of the form

$$H \to ss \to X\overline{X}Y\overline{Y} \quad \text{or} \quad H \to aa \to X\overline{X}Y\overline{Y}, \tag{3.9}$$

as well as

$$H \to aZ \to X\overline{X}Y\overline{Y}, \tag{3.10}$$

where $s(a)$ is a (pseudo)scalar mass eigenstate mostly composed of $S_R(S_I)$ and X, Y

are SM fermions or gauge bosons.

Let's discuss now the branching ratios of different types that can be considered in the 2HDM+S mentioned earlier:

Type I: The branching ratios are independent of $\tan\beta$ since all fermions couple only to H_2. The pseudoscalar couplings and the SM Higgs couplings to fermions are proportional, with the same proportionality constant. The branching ratios are also comparable to those of the SM+S as discussed in the reference (Curtin et al., 2014)) with a complex S and a light pseudoscalar a.

type II: The exotic-decay branching ratios depend on $\tan\beta$ unlike type-I models, with decays to down-type fermions suppressed (enhanced) for down-type fermions for $\tan\beta < 1(\tan\beta > 1)$.

type III: The branching ratios are $\tan\beta$ dependent. For $\tan\beta < 1$, pseudoscalar decays to leptons are more probable than its decays to quarks.

type IV: The branching ratios are $\tan\beta$ dependent. For $\tan\beta < 1$ and compared to the NMSSM (Ellwanger, Hugonie, and Teixeira, 2010), the pseudoscalar decays to up-type quarks and leptons are privileged over its decays to downtype quarks, which leads so a similar branching ratio decays to $b\bar{b}$, $c\bar{c}$ and $\tau^+\tau^-$. This allows the possibility to test this model in the following final states: $2b2\tau$ or $2c2\tau$.

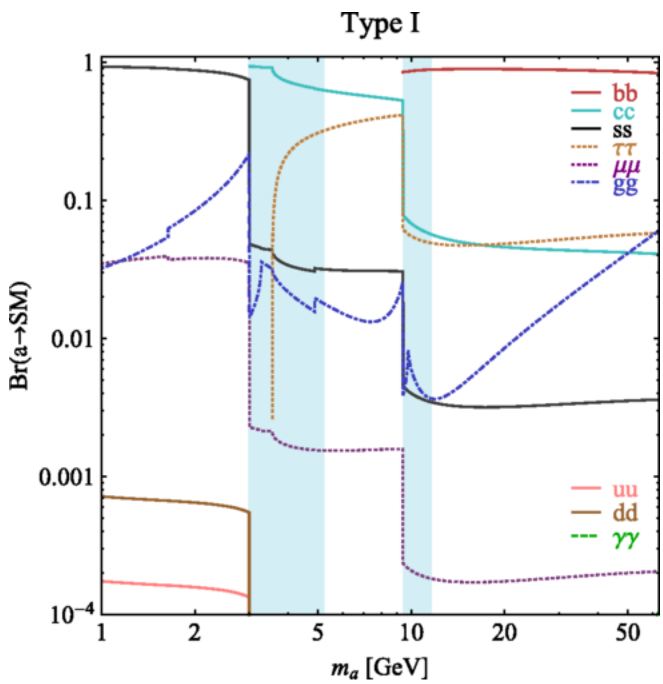

FIGURE 3.6: Branching ratios of a singlet-like pseudoscalar in the 2HDM+S for type-I Yukawa couplings. Decays to quarkonia likely invalidate our simple calculations in the shaded regions. (Curtin et al., 2014)

.

Several searches for a Higgs boson decaying to electrons, muons, τ leptons or b-jets

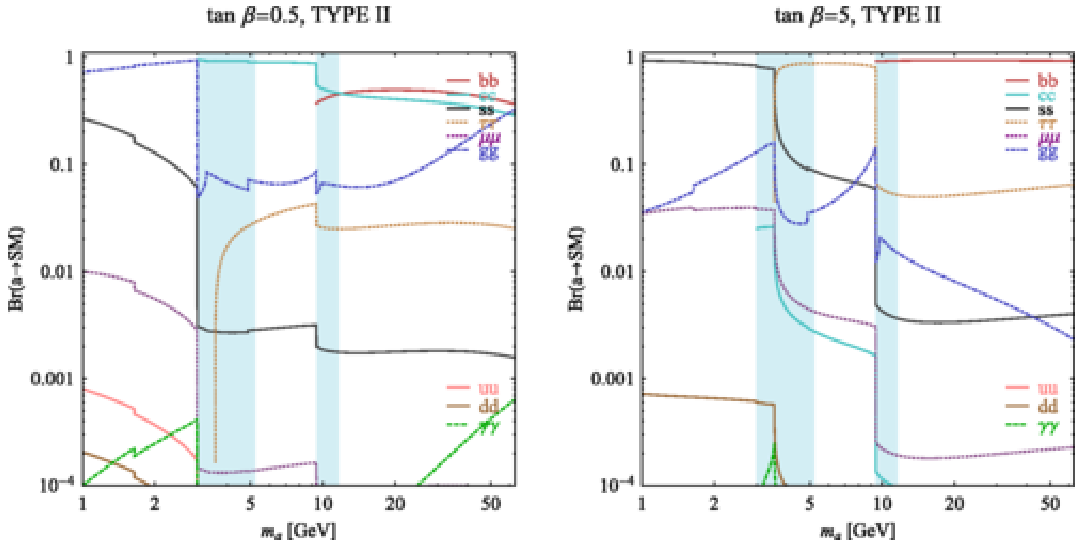

FIGURE 3.7: Branching ratios of a single-tlike pseudoscalar in the 2HDM+S for type-II Yukawa couplings. Decays to quarkonia likely invalidate our simple calculations in the shaded regions. (Curtin et al., 2014)

.

via two pseudoscalars have been performed at both the LHC and the Tevatron. The DØ and ATLAS collaborations have searched for a signal of $H \to aa \to 2\mu 2\tau$ in the a boson mass ranges $3.7 \leq m_a \leq 19$ GeV and $3.7 \leq m_a \leq 50$, respectively (Abazov et al., 2009; Aad et al., 2015a). The DØ and CMS collaborations have searched for the signature $H \to aa \to 4\mu$ in the range $2m_\mu \leq m_a \leq 2m_\tau$ (Abazov et al., 2009; Khachatryan et al., 2016). The CMS collaboration has additionally searched for $H \to aa \to\to 4\tau, 2\mu 2\tau, 2\mu 2b$ in the range $5\ GeV \leq m_a \leq 62.5$ GeV (The CMS collaboration et al., 2017) and the ATLAS collaboration for $H \to aa \to\to 4b$ in the range$20\ GeV \leq m_a \leq 60$ GeV. These searches have led to limits on the branching ratio of the Higgs boson decaying to aa, scaled by the ratio of the production cross-section of the Higgs boson that is searched for to that predicted by the SM, $\sigma(H)/\sigma_{SM} \times \mathcal{B}(H \to aa)$. Those limits are between 1-3% for pseudoscalar-boson masses between 1 GeV and 3 GeV and between 10-100% for masses larger than 5 GeV, assuming a 2HDM+S Type-II model with $\tan\beta = 5.0$.

In summary, The 2HDM+S allows for a large variety of Higgs decay phenomenologies: $H \to aa \to X\bar{X}Y\bar{Y}$, $H \to ss \to X\bar{X}Y\bar{Y}$ and $H \to Za \to X\bar{X}Y\bar{Y}$, by coupling the SM-like Higgs H to a singletlike scalar s or pseudoscalar a. The singlet's couplings within each fermion "family" are ranked by their Yukawa couplings and the relative coupling strength to each family can be adjusted, and arbitrarily so in the scalar case.

3.3 Additional scalar (S) decaying to a Z_d

In this thesis the Higgs decaying to a Z_d is extended and an additional scalar is considered. This extension searches for a dark Higgs (S) decaying to four leptons (e or μ) through a Z dark boson: ($S \to XX \to 4\ell$), where S is different in mass from the discovered SM Higgs boson, its mass could be from 20 GeV to 1 TeV, but

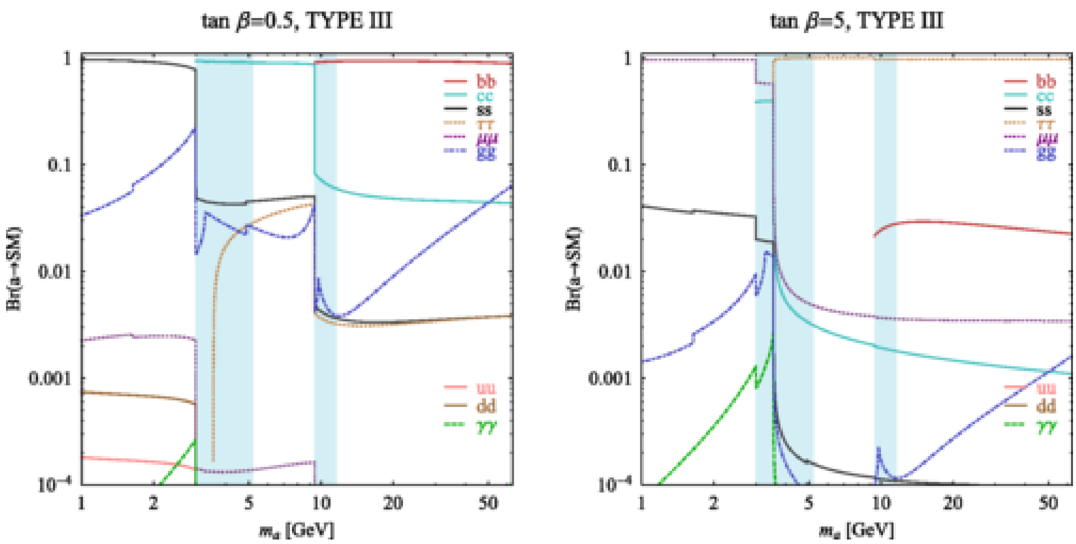

FIGURE 3.8: Branching ratios of a singlet like pseudoscalar in the 2HDM+S for type-III Yukawa couplings. Decays to quarkonia likely invalidate our simple calculations in the shaded regions. (Curtin et al., 2014)

.

excluding the SM Higgs window $115 < m_{4\ell} < 130\ GeV$. This lower limit of 20 GeV arises because for Z_d lighter than 10 GeV, corresponds to the low mass regime where leptons are boosted and the isolation cut fails.

This search channel scenario exists implicitly in many of the references previously mentioned in chapter 7, but where it is neither discussed further nor excluded as a new search. Once again we have the dark Higgs S mixing with the SM Higgs with coupling constant κ. This mixing allows all the same processes which can create the SM Higgs to also create the dark Higgs. We have then opened the dark Higgs portal. The dominant production process will be the gluon fusion process, and the resulting dark Higgs can also decay to two dark vector bosons, just as in the previously discussed searches.

Once the dark Higgs has the possibility to be heavier, then so too does the dark vector boson. A heavier Z_d would very likely have other decay channels open to it. It could therefore decay predominantly into other dark sector states, thus becoming invisible. To still have the searched process $Z_d \to \ell\ell$, we would need to assume that the additional Z_d is the lightest state in the dark sector so that only SM decays are open. Another consideration is that such an additional Z_d might be produced directly in the process $pp \to Z_d$. LEP data with $ee \to \ell\ell$ (Z^* in the intermediate state) would have a contribution analogous to Drell-Yan $pp \to Z_d \to \ell\ell$.

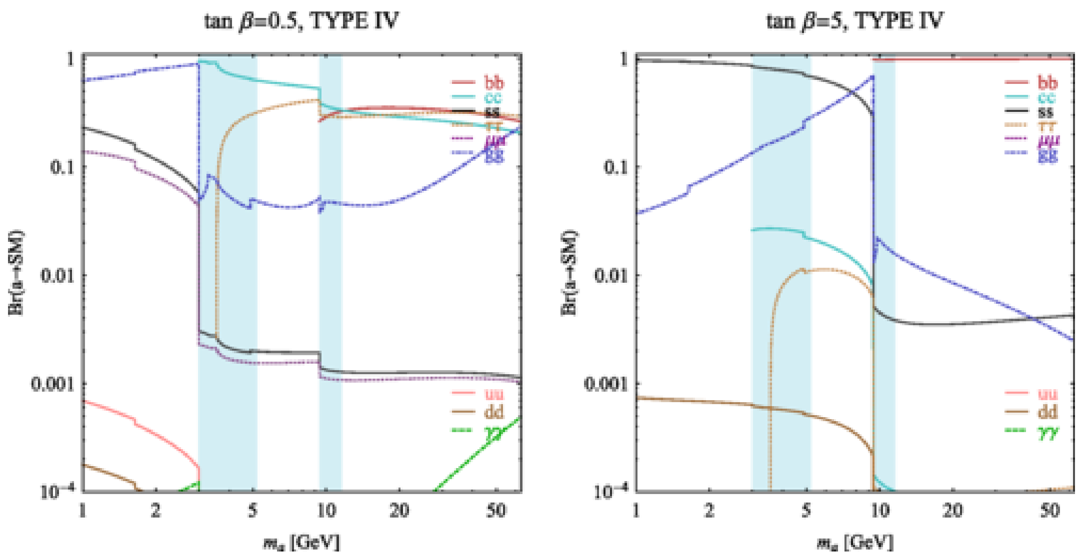

FIGURE 3.9: Branching ratios of a singlet-like pseudoscalar in the 2HDM+S for type-IV Yukawa couplings. Decays to quarkonia likely invalidate our simple calculations in the shaded regions. (Curtin et al., 2014)

.

Conclusion: The field on BSM theories is very wide and well motivated in the literature. Two of them, the HAHM and the 2HDM are used as benchmark models in this thesis. The are described here in sufficient detail for this search. An model independent which is not ruled out by any of the currents BSM theories is considered in this thesis. It suggests a dark Higgs S with mass heavier or lighter than the discovered Higgs particle, decaying to four leptons via two Z_d bosons. Hopefully the LHC experiments may soon shed light on our unanswered questions, or may also surprise us by raising new questions that physicists didn't ask.

In the next chapters the LHC and the ATLAS detectors is discussed.

Part II

Detectors, Reconstruction, Identification

Chapter 4

Large Hadron Collider: LHC

4.1 Motivation of building the LHC

The main arguments for building the Large Hadron Collider were: to search for the Higgs boson (theoretically established by the Brout-Englert-Higgs (BEH) mechanism), to understand the mechanism of the electroweak symmetry breaking, to search for supersymmetry at a scale of 1 TeV (or below), to investigate b and t quarks and a new form of matter, to potentially study the quark gluon plasma among others. Scientists were persuaded that to achieve this goal the tool would be a proton-proton collider of a center of mass energy between 10 and 20 TeV with a luminosity of up to 10^{34} $\mathrm{cm}^{-2}\mathrm{s}^{-1}$. Such an ambitious machine with a maximum magnetic field of 10 T required a well established R&D program.

4.2 Designs parameters

The LHC consists of two anti-parallel rings of superconducting accelerator structures with several intersections where collisions are possible; its center of mass collision energy is up to 14 TeV. Located at the border between France and Switzerland, it has a 27 km of circumference and is installed about 100 m underground. The superconducting magnets of the two rings are located in a common return yoke and cryostat, hence they constitute a compact design. The two anti-parallel rings have to be operated in a synchronized way during particle injection, acceleration and luminosity operation mode.

To maintain the orbits of the two beams of oppositely charged particles, but each rotating in opposite directions, magnetic dipole fields are required. Hence, 1232 dipole magnets, 15 meters in length (Figure 4.1) keep the beams on their near circular paths, while an additional 392 quadrupole magnets, 5-7 meters long enable to keep the beams focused. Stronger quadrupole magnets close to the intersection points are also used to squeeze the particles close together and maximize the chance of interaction where the two beams cross. In order to correct the small imperfections in the field geometry, magnets with higher multi-pole orders are used. In total, about 10,000 superconducting magnets are installed, with the dipole magnets having a mass of over 27 tonnes. The super conducting magnets operate at a temperature of 1.9 K (-271.3°C) which makes the LHC the largest cryogenic system in the world and one of the coldest places on Earth. To produce a magnet field of 8.3 T and maintain the particles circular trajectory along the 27 km, require supplying a current of 11850 A to the coils of the LHC main magnets. To achieve these values a superconducting material (niobium-titanium, NbTi) is used, and 120 t of liquid helium to keep the NbTi wires at their operational temperature. Table 4.1 gives the main parameters of the machine for the injection and collision energy.

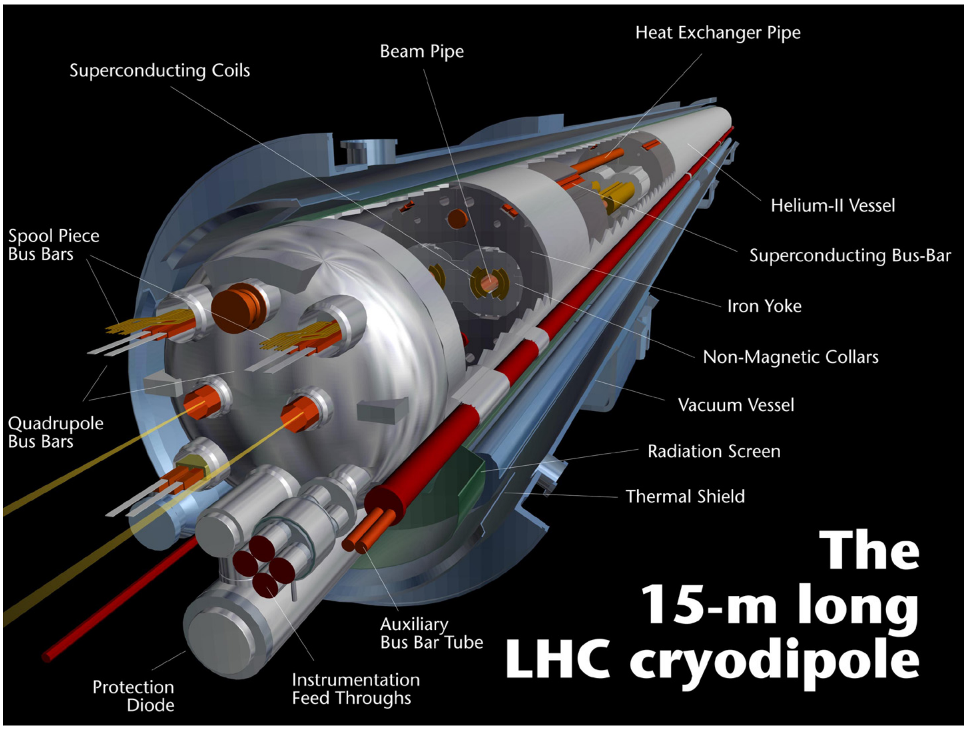

FIGURE 4.1: Cross section of the LHC dipole magnet. (Frontline, 2009)

.

The beam is not continuous, instead the protons which form the beam are bunched[1] together into up to 2808 bunches, with 115 billions protons in each bunch. The interactions between the beams take place in four interactions points (IPs) surrounded by the detectors in one of the four main experiments: ATLAS, CMS, ALICE and LHCb. The bunches have discrete intervals of 25 ns apart with a bunch collision rate of 40 MHz.

Before reaching the main LHC accelerator, particles pass through a series of systems which increase their energy successively. These systems are:

1. The primary linac particle accelerator LINAC 2 which generates 50 MeV protons;
2. The proton synchrotron booster (PSB) which accelerates the protons up to 1.4 GeV;
3. The proton synchrotron (PS) which increases the proton energy up to 26 GeV;
4. The super proton synchrotron (SPS) which increases the proton energy up to 450 GeV and injects them into the main ring.

Figure 4.2 gives a list of some accelerators at CERN.

[1] A bunch is a number or groups of particles captured within one radio-frequency bucket, that can be carried in the machine.

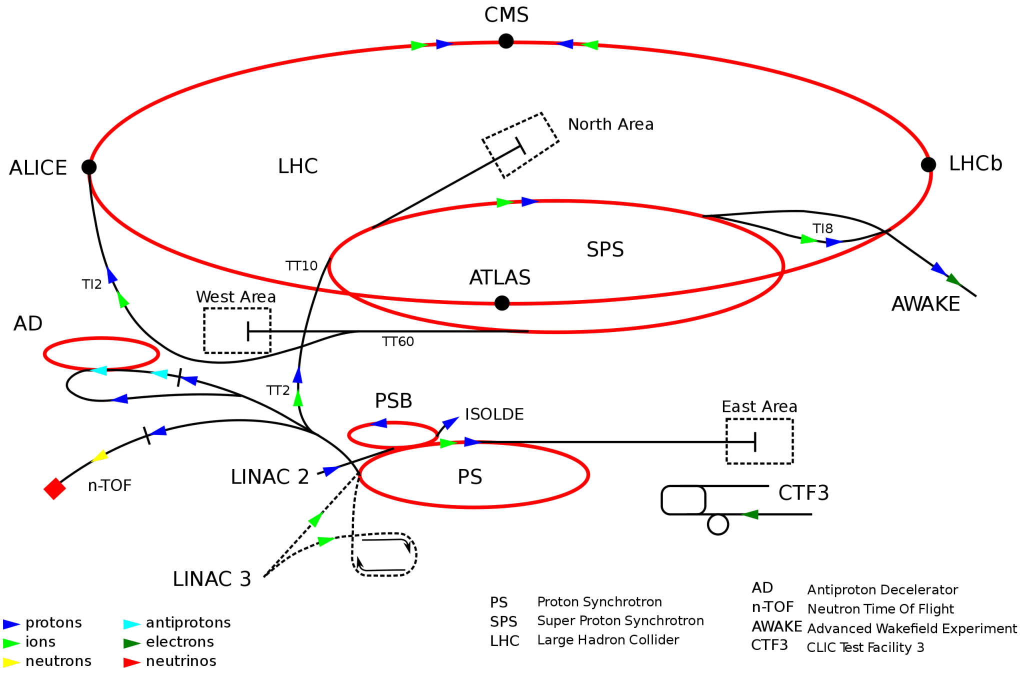

FIGURE 4.2: List of current particle accelerators at CERN (Wikipedia, 2019b)

.

	Injection	Collision
Proton energy	450	7000
Circumference (m)	26658.883	
Particle/bunches (10^{11})	1.15	
Number of bunches	2808	
Bunch distance (ns)	25	
Beam current (mA)	584	
Norm.emittance (x and y)(μmrad)	3.5	3.75
Stored energy per beam (MJ)	23.3	362
Rms beam size at IP1 and IP5 (μm)	375	17
Rms beam size at IP2 and IP8 (μm)	280	71
Peak luminosity ($cm^{-2}s^{-1}$)		1.0×10^{34}

TABLE 4.1: Nominal LHC parameters for the injection and collision energy

4.3 Luminosity

The time integrated luminosity is defined as the ratio between the numbers of events generated in particle collisions, N_{event}, and the cross section of the event category considered, σ_{event}:

$$\mathcal{L} = \frac{N_{event}}{\sigma_{event}}. \tag{4.1}$$

For a Gaussian transverse particle distribution, it can be obtained from the instantaneous luminosity written as:

$$L = \frac{N_1 N_2 f_{rev} n_b}{2\pi\sqrt{\sigma_{1x}^2 + \sigma_{2x}^2}\sqrt{\sigma_{1y}^2 + \sigma_{2y}^2}} \cdot F \cdot W, \tag{4.2}$$

where N_1 an N_1 are the numbers of particles in the n_b colliding bunches, f_{rev} describes the revolution frequency in the ring and σ stands for the transverse beam size at the interaction point in the horizontal (x) and vertical (y) directions for beam 1 and 2. F and W are the luminosity reduction factors, which describe the effect of the final crossing angle of the two beams (F) and the transverse offset at the collision point (W), which are ideally set to be equal to 1.

The large number of stored bunches and the resulting small bunch temporal distance of 25 ns create unwanted collisions every 3.75 m. If ignored, at least 34 of these collision points are obtained upstream and downstream of the interaction points. This would affect the beam stability and the quality of the detector data analysis. To avoid these unwanted collisions, a crossing angle 2×142 μrad in IPs 1 and 5 is needed. Hence, the bunches do not collide anymore head on at the IPs and that the geometrical reduction factor F becomes less than 1. F can be written as

$$F = \frac{1}{\sqrt{1 + 2\frac{\sigma_s^2}{\sigma_{1x}^2 + \sigma_{2x}^2}\tan^2\frac{\phi}{2}}}, \tag{4.3}$$

which depends on the bunch length σ_s, on the transverse beam size in the plane of crossing, and on the size of the crossing angle ϕ.

The large multi-purpose detectors at two of the IPs ATLAS and CMS, are capable of analyzing an enormous number of events per brunch crossing created in the LHC collision with high luminosity. In contrast, the ALICE (IP 8) and LHCb (IP 2) detectors are optimized for more specific purposes and cannot be operated with the highest luminosity. The different running conditions is a challenge. Therefore, the luminosity delivered to the IP 8 and IP 2 should be reduced to a tolerable level. Typical values of $L = 10^{32}\text{cm}^{-2}\text{s}^{-1}$ in IP 8 and $L = 10^{27}\text{cm}^{-2}\text{s}^{-1}$ in IP 2 have been established, during LHC operation in Run 1. These numbers were achieved by setting the beam collision conditions up with different beam optics at these interactions points, with a transverse offset between the beams that corresponds to about 2-3 σ of the transverse beam size. W depends on the offset distance $d_{1,2}$ and the beam sizes $\sigma_{1,2}$ in the direction of the beam offset and is written as:

$$W = e^{\frac{-(d_1 - d_2)^2}{2(\sigma_1^2 + \sigma_2^2)}}, \tag{4.4}$$

and provides the necessary event rate reduction.

The luminosity performance is an indicator by which the effectiveness of a collider is measured. The bigger the value of $\mathcal{L}$, the larger the number of collisions.

Through the years the LHC underwent many upgrade phases, where the luminosity was increased. Figure 4.3 shows the integrated luminosity in ATLAS and CMS from 2011 to 2018. Many ways can be used to increase the luminosity; the

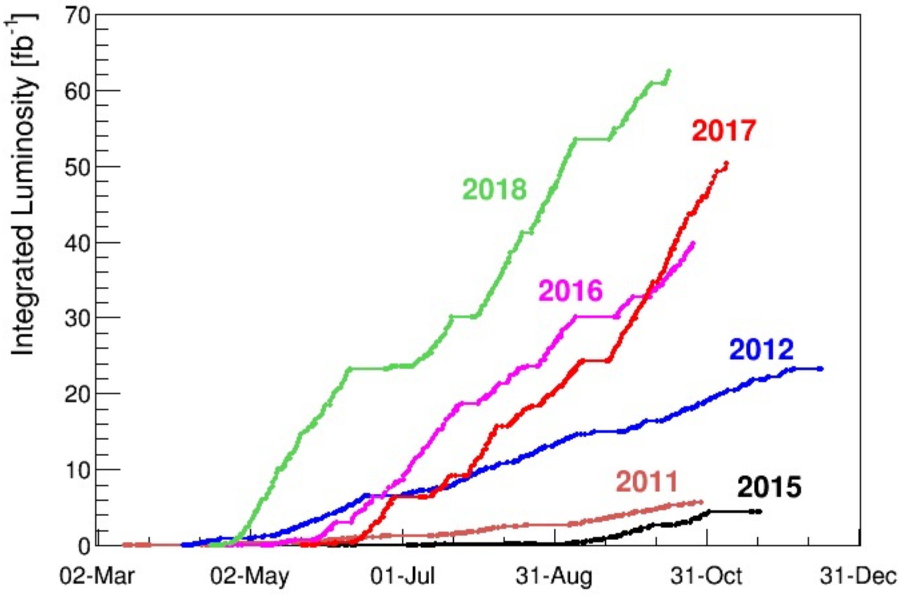

FIGURE 4.3: integrated luminosity reached in ATLAS and CMS from 2011 to 2018 (Rende Steerenberg, 2017)

most direct one is to focus the beam more tightly at the collision point. Increasing the number of bunches or the number of protons per bunch can be considered, but there are limitations to how these parameters should be pushed such as the beam-beam limit, the long range intra beam interactions, the electron cloud effect, the implications of collimation and machine protection, pileup of events in the experiments and so on.

4.4 Pileup

Increasing the number of protons per bunch and improving the beam optics, lead to a higher rate of collisions to a point where several quark/gluon collisions occur simultaneously, causing the effect known as pileup. When the LHC experiments are keen to study a hard (rare) process from a high energy collision, a number of other simultaneous collisions will occur during the same bunch crossing. The overall final-state of the collision, observed in the detectors, is therefore not only the products of the one hard collision we are interested in, but the superposition of these products with those of all the simultaneous soft collisions, which will make the reconstruction very challenging.

Given the time separation between two bunches (25 ns), a luminosity of around $2.10^{34}\text{cm}^{-2}\text{s}^{-1}$ and a total proton-proton cross-section of order 100 mb, the average pileup multiplicity $\langle N_{PU} \rangle$ is around 50. The pileup issue was already present at the Tevatron but with a much lower multiplicity (around 5), so that a simple technique was sufficient to address its effect. With the large luminosity in the LHC, pileup becomes a serious problem. For instance the pileup multiplicity in Run 1 was

$\langle N_{PU} \rangle \sim 20$ and 30 at the beginning of Run 2. For the coming high-luminosity LHC (HL-LHC) one expects an average pileup multiplicity between 140 and 200.

Probably the most typical situation where pileup impacts the ability to properly reconstruct the objects in the final-state of a hard collision is the case of jets, which is not the case for this thesis (jets are not considered here) so its effect is negligible for our analysis.

4.5 Main detectors of the LHC

The interaction points of the large hadron collider are located in the four main detectors: ALICE, ATLAS, CMS and LHCb. These experiments are the most complex, advanced detectors ever built for particle physics, involving thousands of scientists, engineers and technicians. They were optimized for their respective specific physics requirements and experimental conditions, which differ from experiment to experiment. The main parameters of the four detectors are summarized in Table 4.2. Let's review briefly the physics goal of each detector:

Parameter	ATLAS	CMS	ALICE	LHCb
Total weight (tons)	7000	12500	10000	5600
Overall length (m) (μm)	46	20	26	21
Overall diameter (m)	22	15	16	–
Width $\times$ eight (m $\times$m)	–	–	–	13×10
Magnet	Toreoid/solenoid	Solenoid	Solenoid/dipole	Dipole
Magnet filed for tracking (T)	1/2	3.8	0.5/0.67	1.1

TABLE 4.2: The main parameters for ATLAS, CMS, ALICE and LHCb

- ALICE: which stands for A Large Ion Collider Experiment, studies the physics of strongly interacting matter and of the quark-gluon plasma at extreme values of energy and temperature in nucleus-nucleus collisions;

- LHCb: which stands for Large Hadron Collider beauty, is dedicated to measure heavy flavour physics by studying the CP violation and decay rates of beauty and charm hadrons;

- ATLAS: which stands for A Toroidal LHC ApparatuS, aims to investigate a wide range of physics, including the search for the Higgs boson (already discovered), extra dimensions, and particles that could make up dark matter;

- CMS: which stands for Compact Muon Solenoid, has the same physics goal as ATLAS.

Conclusion: The LHC is briefly reviewed, from the goal of its construction through its design parameters to its four main detectors. In this thesis, the data used are obtained from the ATLAS detector, so in the next chapter it is be described in more details.

Chapter 5

ATLAS Detector

5.1 Coordinate system and nomenclature

The interaction point defines the origin of the coordinate system. The beam direction defines the z-axis and the x-y plane is the plane transverse to the beam direction. The positive x-axis and y-axis are pointing to the center of the LHC ring and upwards respectively. The transverse momentum p_T, the transverse energy E_T, and the missing transverse energy E_T^{miss} are defined in the x-y plane.

Cylindrical coordinates are also used, where the transverse plane is often described in term of the r-ϕ coordinates. The azimuthal angle ϕ is measured from the x-axis around the beam. The radial dimension r measures the distance from the beamline. The polar angle θ is defined as the angle from the positive z-axis, it's also given in term of pseudo-rapidity defined as $\eta = -\ln\tan(\theta/2)$. The distance ΔR in the pseudo-rapidity-azimuthal angle space is defined as $\Delta R = \sqrt{\Delta^2\eta + \Delta^2\phi}$.

The pseudo-rapidity is a massless approximation of the rapidity variable y. For particle with energy E, momentum $\boldsymbol{p}$ and longitudinal momentum $p_L = |\boldsymbol{p}|\sin\theta$ along the beam, y is defined as:

$$y = \frac{1}{2}\ln\frac{E + p_L}{E - p_L} \approx \eta = \frac{1}{2}\ln\frac{|\boldsymbol{p}| + p_L}{|\boldsymbol{p}| - p_L} = -\ln\tan\left(\frac{\theta}{2}\right). \tag{5.1}$$

In high energy physics the rapidity (or approximately pseudo-rapidity) is often used because it's invariant under Lorentz transformation.

It's also worth to mention the helix parametrization used in ATLAS since these variables will be used very often in this thesis. These helix parameters describe the trajectory of charged particles in an ideal magnetic field with all quantities measured at the point of the closest approach to the nominal beam axis $x = 0$, $y = 0$. In the x-y plane, the parameters are: $1/p_T$ which is the reciprocal of the transverse momentum with respect to the beam-axis, ϕ which is the azimuthal angle, and d_0 which is the transverse impact parameter. One defines d_0 as the transverse distance to the beam axis of a reconstructed track at the point of the closest approach. Its sign depends on the reconstructed angular momentum of the track about the axis. In the r-z plane, the parameters are $\cot\theta$ which is the cotangent of the polar angle defined by $\cot\theta = p_z/p_T$ and z_0 which is the longitudinal impact parameter defined as the z position of the track at the point of the closest approach.

5.2 ATLAS detector overview

Figure 5.1 shows the overall detector layout. It is nominally forward-backward

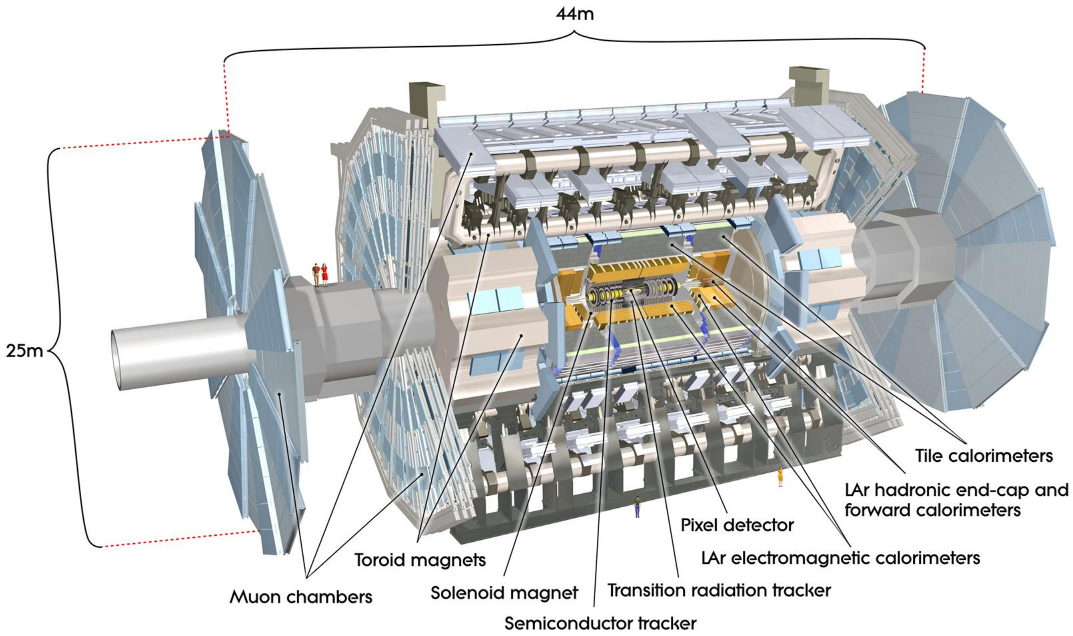

FIGURE 5.1: Cut-away view of the ATLAS detector. The dimensions of the detector are 25 m in height and 44 m in length. The overall weight of the detector is approximately 7000 tonnes. (Aad et al., 2008)

symmetric with respect to the interaction point. Before describing the ATLAS subsystems, let's briefly review them as listed in Figure 5.1. They mainly consist of:

- An inner thin superconducting solenoid surrounding the inner detector cavity and large superconducting air-core toroids consisting of independent coils arranged with an eight-fold symmetry outside the calorimeters. They are used for the dual inner solenoidal - outer toroidal magnetic configuration.

- A cylinder of 7 m and a radius of 1.15 m contains the Inner Detector (ID), surrounded by the solenoid magnetic field of 2 T. In the outer part of the ID, discrete, high-resolution semiconductor pixel and strip detectors in the inner part of the tracking volume, and straw-tube tracking detectors with the capability to generate and detect transition radiation are combined. This combination leads to a good pattern recognition, momentum and vertex measurements, and electron identification.

- The liquid-argon (LAr) electromagnetic sampling calorimetry covers the pseudo-rapidity range $|\eta| < 3.2$. Its technology is also used for the hadronic calorimeters, which share the cryostats with the EM end-caps, thus extend the pseudo-rapidity coverage of $|\eta| = 4.9$. It has a high granularity and a good performance in term of energy and position resolution, jet and E_T^{miss} reconstruction.

- The muon spectrometer surrounds the calorimeter and defines the overall dimension of the ATLAS detector. The outer chambers of the barrel are at radius of about 11 m. The length of the barrel toroid coils is about 25 m, and the third layer of the forward muon chambers, is located about 23 m from the

IP. Its strong bending power is generated by the air-core system with large magnets located at the barrel and end-caps. The trigger chamber in the muon system has a very fast time resolution which is in the order of 1.5-4 *ns*.

5.3 ATLAS subsystems

5.3.1 Magnet system

Figure 5.2 provides an illustration of the ATLAS magnet system. One of its goals is to bend charged particles in order to measure their momenta. The field integral $\int Bdl$, where B is the azimuthal field component, characterizes the performance in term of bending power which is lowered in the transition region where the two magnets overlap ($1.3 < |\eta| < 1.6$). The magnet system consists of a central solenoid

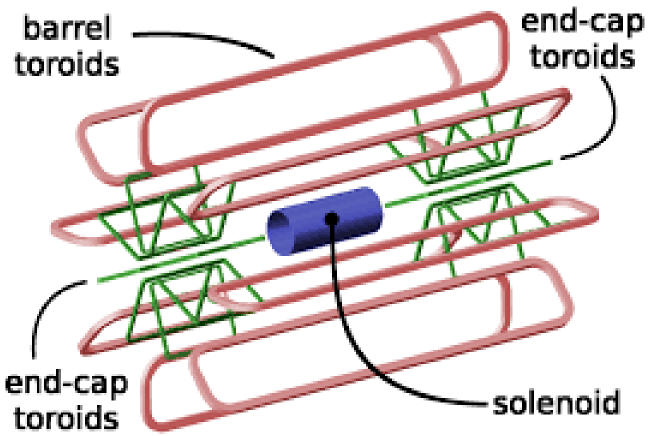

FIGURE 5.2: Geometry of the ATLAS magnet system.

(CS) which provides a $2T$ axial magnetic field for the Inner Detector (ID), a barrel toroid (BT) and two end-cap toroids (ECT). The peak magnetic field strength on the superconductors in the BT and the ECT are 3.9 and 4.1 T respectively. The overall dimensions of the magnet system are 26 m in length and 20 m in diameter. The ECT are inserted in the BT at each end and line up with the CS. They have a length of 5 m, an outer diameter of 10.7 m and an inner bore of 1.65 m. The CS extends over a length of 5.3 m and has a bore of 2.4 m. This complex configuration with such a large size make the magnet system very challenging and requires careful engineering.

The three toroids consists of eight coils assembled radially and symmetrically around the beam axis. In order to provide radial overlap and to optimize the bending power in the interface regions of both coil systems, the ECT coil system is rotated by 22.5° with respect to the BT coil system. A more detailed description of the magnet system can be found here (Aad et al., 2008).

5.3.2 Inner Detector

Figure 5.3 shows the layout of the Inner Detector. It lies within a cylindrical envelope of ± 3.51 m length and a radius of 1.15 m immersed in the 2 T magnetic field produced by the CS. It's designed to provide high precision measurement of the momentum of charged particles, primary and secondary vertex reconstruction within $|\eta| < 2.5$, and charged particle identification. These features are achieved

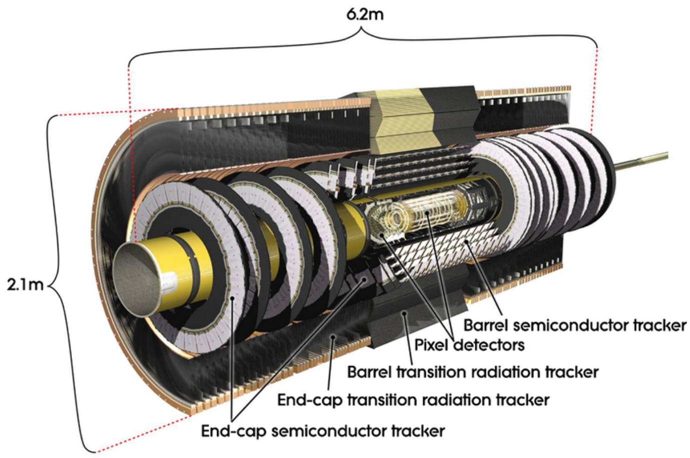

FIGURE 5.3: Cut-away view of the ATLAS inner detector. (Aad et al., 2008)

thanks to semiconductor tracking detectors, which use a silicon micro-strip (SCT) and pixel technologies.

For each track, three pixel layers and eight strip layers are crossed; that gives a very robust pattern recognition and high precision in both the ϕ and z coordinates. The straw tube tracker (TRT) provides a large number of precision tracking points whose hits at the outer radius contribute significantly to the momentum measurements. The high density of measurement in the outer part of the tracker is very important for the detection of photons conversion, which are an important element in the signature of CP violation in the B system. The detection of transition-radiation photons in the xenon-based gas mixture of the straw tubes enhances the electron identification.

Table 5.1 summarizes the parameters of the basic layout and the expected measurement resolutions

System	Position	Area (m^2)	Resolution $\sigma(\mu m)$	channels (10^6)	η coverage
Pixels	1 removable barrel layer (B-layer)	0.2	Rϕ = 12, z = 66	16	±2.5
	2 barrel layers	1.4	Rϕ = 12, z = 66	81	±1.7
	5 end-cap disks on each side	0.7	Rϕ = 12, z = 77	43	1.7-2.5
Silicon strips	4 barrel layers	34.4	Rϕ = 16, z = 580	3.2	±1.4
	9 end-cap wheels on each side	26.7	Rϕ = 16, z = 580	3.0	1.4-2.5
TRT	Axial barrel straws		170 (per straw)	0.1	±0.7
	Radial end-cap straws		170 (per straw)	0.32	0.7-2.5
	36 straws per track				

TABLE 5.1: Parameters of the Inner Detector. The resolutions quoted are typical values (the actual resolution in each detector depends on the impact angle) (Airapetian, 1999)

5.3.2.1 Pixel detector

The Pixel Detector is the nearest component of the ID to the beam pipe. It provides a very high-granularity, high-precision set of measurements as close to the IP as possible. It determines the d_0 resolution and the ability of the ID to find short-lived particles such as B hadrons and τ leptons. The system has three barrel layers which are concentric cylinders around the beam pipe in the barrel region, and two sets of three end-caps located perpendicular to the beam. It contains 1744 identical silicon pixel sensors. Each sensor consists of 47232 50 x 400 μm pixels resulting in a total of around 140 million silicon pixels which are very important for the task of pattern recognition for the various event types, given the number of bunch crossing per collision.

A charged particle from a collision will cross three of the pixel layer. This produces a series of electron-hole pairs within the silicon material of the pixels that are traversed. These pairs are separated by an electrical field leading to a pulse in the circuit which is readout by the electronics giving a hit signal on the pixel. The output signals are routed on the sensor surface to a hybrid module on top of the silicon chips, and from there to a separate clock-and-control integrated circuit. The measurement accuracies for each of the barrel layers and end-cap are 10 μm in the R-ϕ plane and 155 μm along the z-axis.

5.3.2.2 Silicon Tracker (SCT)

The SCT system contributes to the measurement of momentum, impact parameter and vertex position, and provides good pattern recognition based on high detector granularity. It provides eight precision measurements per track in the intermediate radial range. The SCT constitutes 61 cm^2 of silicon detectors, with 6.2 million readout channels. It has a very good spatial resolution which is 16 μm in R-ϕ and 580 μm in z and tracks can be distinguished if separated by more than $\sim$200 μm.

The SCT barrel has eight layers of silicon microstrip detectors. Each silicon detector is 6.36$\times$6.40 cm^2 with 768 readout strips of 80 μm pitch. Each module consists of 4 singlesided p-on-n silicon detectors and on each side of the module, two detectors are wire-bonded together to form 12.8 cm long strips. The readout chain consists of a front-end amplifier and discriminator, followed by a binary pipeline which stores the hits above threshold until the level-1 trigger decision.

The end-cap modules use tapered strips with either 12 cm (at the outer radii) or 6-7 cm length (at the innermost radius) to obtain optimal η-coverage across all end-cap wheels. The overall end-cap modules are very similar in construction to the ones in the barrel.

5.3.2.3 Transition radiation tracker (TRT)

The TRT is the outermost component of the ID. It uses gas filled straw detectors to provide further tracking of charged particles through the calorimeters. It is operated with a non-flammable gas mixture of 70% Xe, 20% CO2 and 10% CF4, with a total volume of 3 m^3. It provides electron identification by the use of xenon gas to detect transition-radiation photons created in a radiator between the straws. Each straw is 4 mm in diameter and equipped with a 30 μm diameter gold-plated W-Re wire, giving a fast response and good mechanical and electrical properties for a maximum straw length of 144 cm in the barrel.

The barrel contains about 50 000 straws, the end-cap contains 320 000 radial straws, and the total number of electronic channels is 420 000 giving a spatial resolution of 170 μm per straw, and two independent thresholds. These features allow the detectors to discriminate between tracking hits, which pass the lower threshold, and transition-radiation (TR) hits, which pass the higher one.

5.3.3 Calorimeters

Figure 5.4 present a view of the ATLAS calorimeter. It consists of an

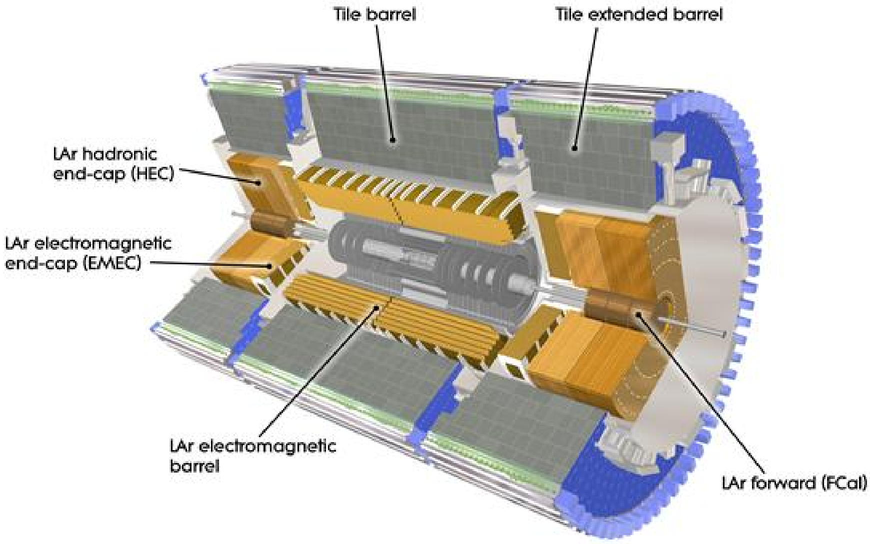

FIGURE 5.4: A cut-away view of the calorimeters. (Aad et al., 2008)

electromagnetic (EM) calorimeter covering the pseudorapidity region $|\eta| < 3.2$, a hadronic barrel calorimeter covering $|\eta| < 1.7$, a hadronic end-cap calorimeter covering $1.5 < |\eta| < 3.2$, and a forward calorimeter covering $3.1 < |\eta| < 4.9$. They are used to determine the energy and also the momentum direction of particles that are produced at the interaction points or decay products of other unstable particles. Both electromagnetic and hadronic calorimeters are built such that electromagnetic and hadronic showers are fully contained in the corresponding calorimeter material in order to optimize the energy resolution. In addition to the energy and direction measurement of particles, the calorimeters have also the functionality of trigger signal generation. They provide a fast signal response used for deciding if a collision event is interesting enough to be recorded for further data analysis.

5.3.3.1 Electromagnetic calorimeter

The EM calorimeter is divided into a barrel part ($|\eta| < 1.475$) and two end-caps ($1.375 < |\eta| < 3.2$). The barrel calorimeter consists of two identical half-barrels, separated by a small gap (6 mm) centered around the z-axis. Each end-cap calorimeter is divided into an outer wheel covering the region $1.375 < |\eta| < 2.5$, and an inner wheel covering the region $2.5 < |\eta| < 3.2$ which are coaxial. It uses sampling calorimeters with liquid argon (LAr) as active material and lead (Pb) or copper (Cu) as absorber. The accordion geometry as shown in Figure 5.5 provides complete ϕ symmetry without azimuthal cracks. The total thickness of the EM calorimeter in radiation length (X_0), for electron and photons, is $> 24\ X_0$ in the barrel and $> 26\ X_0$ in the end-caps ensure minimal leakage of electromagnetic energy.

In the region of $|\eta| < 2.5$ the EM calorimeter is segmented into longitudinal sections. For the end-cap inner wheel, it is segmented in two sections in depth and has a coarser lateral granularity than for the rest of the acceptance. In the region of

$|\eta| < 1.8$, a presampler detector is used to correct the energy lost by electrons and photons upstream of the calorimeter. The presampler consists of an active *LAr* layer with a thickness of 1.1 *cm* (0.5 *cm*) in the barrel (end-cap) region.

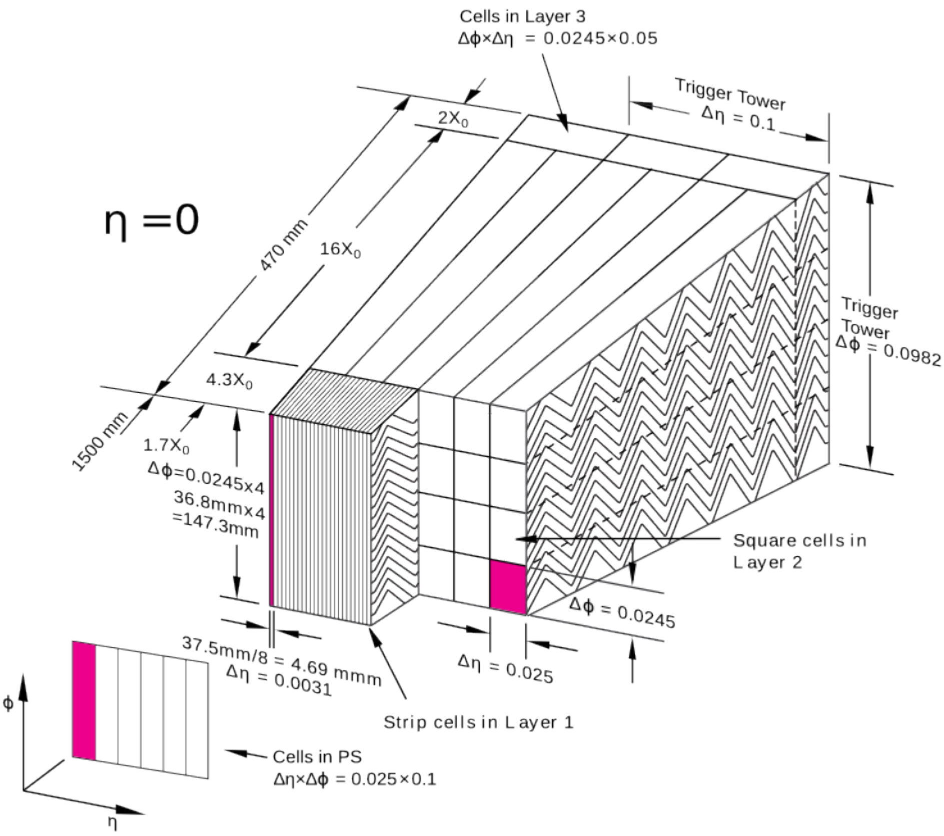

FIGURE 5.5: A sketch of the LAr geometry in an EMB module, showing the lateral and longitudinal segmentation in layers of radially coarser granularity. (Collaboration, 2020)

5.3.3.2 Hadronic calorimeters

The energy measurement of the EM calorimeters is complemented by the measurement of the hadronic calorimeters, which are designed as sampling devices. The measured hadrons may be produced in quark-initiated or gluon-initiated particle jets, decay of τ leptons, or single hadron decay. Therefore, a lead-scintillator tile calorimeter is installed, complemented by a hadronic end-cap calorimeter (HEC) and a forward calorimeter close to the beam-pipe.

Tile calorimeter. It's a sampling calorimeter using iron as an absorber and scintillating tiles as the active material. The tile calorimeter is placed directly outside the EM calorimeter envelope. The tiles are 3 *mm* thick and the total thickness of the iron plates in one period is 14 *mm*. Wavelength shifting (WLS) fibers divided into two separate photomultipliers (PMTs) are used to read out the two sides of the scintillating tiles. The tile calorimeter is composed of one barrel and two extended barrels, and radially extends from an inner radius of 2.28 *m* to an outer radius of 4.25 *m*. The barrel cylinder covers the region $|\eta| < 1.0$ and the extended barrel covers the region of 0.8 < | η | < 1.7.

LAr hadronic end-cap calorimeter . The *LAr* hadronic end-cap calorimeter is located behind the end-cap electromagnetic calorimeter and shares the same *LAr* cryostat. It consists of two independent wheels per end-cap, built out of 32 identical modules, assembled with fixtures at the periphery, and a central ring. The wheels closest to the interaction point are built from 25 *mm* parallel copper plates, while those further away use 50 *mm* copper plates. The outer and inner radius of the copper plates are respectively 2.03 and 0.475 *m*. Both of them are interleaved with 8.5 *mm LAr* gaps which provides its active medium.

Liquid-argon forward calorimeter. The forward calorimeter (FCAL) is integrated into the end-cap cryostat, with a front face at about 4.7 *m* from the interaction point. This provides clear benefits in terms of uniformity of the calorimetric coverage as well as reduced radiation background levels in the muon spectrometer. The front face of the FCAL is recessed by about 1.2 *m* with respect to the EM calorimeter front face in order to minimize the amount of neutron albedo in the ID cavity. The FCAL consists of one section made of cooper and optimized for electromagnetic measurements, and two others made out of tungsten which are new and challenging instead, and designed to predominantly measure the energy of hadronic interactions.

5.3.4 Muon spectrometer

The muon spectrometer is based on the magnetic deflection of muon tracks in the large superconducting air-core toroid magnets. It's designed with two sets of detectors; the trigger chambers with fast response time and precision chambers for good momentum resolution without loss of trigger efficiency. In the region of $|\eta| \leq 1.0$ the large barrel toroid provides the magnetic field for bending, in the region of 1.4 $\leq$ | η | $\leq$ 2.7, two smaller end-cap magnets inserted into both ends of the barrel toroid provide the magnetic field, and for the region over of 1.0 $\leq$ | η | $\leq$ 1.4 magnetic deflection is provided by a combination of barrel and end-cap fields. The magnetic field provided is orthogonal to the muon trajectories and minimize the degradation of resolution due to multiple scattering.

The precision tracking muon system is composed of two sub-detectors, the monitored drift tubes (MDT) and the cathode-strip chambers (CSC). Both detectors use a mixture of Ar and CO_2 gas inside the chambers as ionizing medium. The system has 70000 channels and provide a spatial resolution of 60 μm.

The MDT covers most of the solid angle, with three concentric layers in the barrel extending up to η = 2.7 with the end-cap. Thanks to the mechanical isolation of each sense wire from its neighbors, they provide a single-wire resolution of $\sim$80 μm when operated at high gas pressure (3 bar) together with robust and reliable operation. One MDT chamber consists of three to eight layers of gas filled drift tubes. In total about 355000 tubes cover an area of 3650 m^2, with a resolution of about 80 μm.

The Cathode-strip chambers (CSC) have high granularity and are used in the innermost plane over 2 < | η | < 2.7 to withstand the demanding rate and background conditions. Due to the small channel size, the CSC can function up to a counting rate of 1000Hz/cm^2 and therefore are better suited for higher particle fluxes at higher pseudo-rapidity. They have small electron drift times (30 *ns*), good time resolution (7 *ns*), good two-track resolution, and low neutron sensitivity.

The trigger chambers used for triggering are divided into two sub-detectors; the resistive-plate chambers in the barrel (RPC), and the thin-gap chambers (TGC) in the end-cap. They cover the pseudorapidity range of $\mid\eta\mid\leq$ 2.4 and serve a three-fold purpose: bunch crossing identification which requires a time resolution better than the LHC bunch spacing of 25 *ns*, a trigger with well-defined p_T cut-offs in moderate magnetic fields which requires a granularity of the order of 1 *cm* and the measurement of the second coordinate in a direction orthogonal to that measured by the precision chambers, with a typical resolution of 5-10 *mm*.

The RPC extend to $|\eta|$=1.05 with 380,000 channels. It has a good spatial and time resolution as well as adequate rate capability. The absence of wires in the RPC simplifies its construction and makes them less sensitive to small deviations from planarity if appropriate spacers are used to keep the gap width constant. It gives a sufficient trigger selectivity with moderate spatial resolution.

The TGC's cover the range of $1.05 < \mid\eta\mid < 2.4$, they are a multi-wire proportional chamber with a small wire-cathode gap and constitute 440,000 channels. It has two functions: the muon trigger capability and the determination of the second azimuthal coordinate to complement the measurement of the MDT's in the bending direction. With a good resolution and fine granularity, the TGC's tag the beam-crossing with an efficiency higher than 99% and provide a sufficiently sharp cut-off in the momentum of the triggering muon.

5.3.5 Trigger

With the large bunch-crossing rate at the LHC (40 *MHz*), and given the fact that the raw data volumes of the LHC detectors reach several hundred megabits per event, the storage of the complete raw data of the detectors is impossible. Most interesting physics processes have cross section several orders of magnitude smaller than the inelastic proton-proton cross section, so that a filtering of collisions is applied before data are written to permanent storage. This lowers the rate of storage to manageable proportions.

The trigger signature of ATLAS detector is mainly based on reconstructed physics objects such as electrons, photon, muons, hadronically decaying τ lepton and jets, which pass given thresholds in transverse momentum p_T. Events involving neutrinos which interact weakly are triggered by significant missing transverse energy E_T^{miss} above a certain threshold. Given the significant collision rate, a trigger strategy involving three levels is applied which uses information from several detector systems. Each trigger level refines the decisions made at the previous level and, if necessary, applies additional selection criteria.

The first trigger level (LVL1) is hardware based which includes the detector components with fast signal response. It has a trigger latency (or time response) of 2.5 μs, reducing the rate to about 75 *kHz*, during which the detector data remain stored in on-detector buffers. To select high transverse-momentum (high-pT) muons LVL1 uses information from the trigger chambers, RPCs in the barrel, and TGCs in the end-caps, while the selection of objects from the calorimeters is based on reduced-granularity information from all the calorimeters (EM and hadronic; barrel, end-cap and forward). The LVL1 defines also a region of interest (RoI), which includes information on the position (η, ϕ) and p_T of candidate objects and energy sums. This RoI is transferred to the second trigger level (LVL2).

The second level trigger (LVL2) is software based trigger. It makes use of RoI information provided by the LVL1 trigger over a dedicated data path and access to all of the event data (which became a few per cent of the full event data), if necessary with the full precision and granularity. LVL2 is designed to reduce the rate to approximately 3.5 kHz with an event processing time of about 40 ms, averaged over all events.

The last level is the event filter (EF), it reduces the event rate to roughly 200 Hz, and has four seconds of read out latency compared to 40 ms at LVL2 and 2.5 μs at LVL1.

Conclusion The ATLAS detector and its components have been briefly reviewed, but it's also important to mention that the detector regularly upgraded, and the descriptions in this chapter which are based mostly on the "Detector and physics performance technical design report" (Airapetian, 1999; Aad et al., 2008) can be slightly different from the latest version. In the next chapter the events and object reconstruction is reviewed.

Chapter 6

Event and Object Reconstruction

The final states measurement of physics objects, such as electrons, muons, jets ...etc, requires the combination of specifics signature from detectors and sub-detectors. Throughout this measurement, one of the important parts is the reconstruction and identification of individual physics objects and determination of their kinematic parameters for the results to be meaningful. The event reconstruction particle identification and kinematic parameter determination are done by converting the raw detector data to fundamental physics objects using a dedicated set of algorithms. The basic building blocks for constructing these objects are the particle trajectories (tracks) reconstructed from hits in the inner detector and muon spectrometer (in the case of muons), providing also an estimate of a particle's momentum, and topological clusters constructed from energy deposits in the calorimeters. The reconstruction of electrons and photons is done by using a second clustering to determine local energy deposits in the EM calorimeter. In this analysis, electrons and muons final states are considered, so the discussion in this chapter is restricted to the reconstruction of these objects.

6.1 Track Reconstruction

The inner detector track reconstruction software includes features covering the requirements of both the inner detector and muon spectrometer reconstructions. These features comprise a common event data model and detector description, which allow for standardized interfaces such as track extrapolation, track fitting including material corrections, and vertex fitting.

The tracking steps are as follows:

- When a charged particle traverses the detector, it induces electronic signals, known as hits, on sensitive detector elements. The first step is then to find segments of 3 silicon hits that meet basic p_T and spatial requirements. The collections of hits are then processed for seeding the track candidate search in the Inner Detector.
- The Kalman Filter (Frühwirth, 1987) algorithm with a pion track hypothesis is used to fit the track candidates from the pattern recognition. By applying quality cuts, outlier clusters are removed, ambiguities in the cluster-to-track association are resolved, and fake tracks are rejected.
- In order to resolve the left-right ambiguities, the selected tracks are extended into the TRT to associate drift circle information in a road around the extrapolation. The tracks are then refitted with the full information of all three detectors. To evaluate the quality of the fits, they are compared to the

silicon-only track candidates, and only the fitted tracks with good agreement are kept.

- A dedicated vertex finder is used to reconstruct primary vertices followed by algorithms dedicated to reconstruct photons conversion and secondary vertices.

6.2 Electron reconstruction and identification

6.2.1 Electron reconstruction

Electrons are excellent probes for physics analysis at the LHC. Given their low-background and their well-measured momenta, they become an indispensable tool for ATLAS precision electroweak measurements. Some BSM physics such as the benchmark models used in this thesis, have signatures that include electrons.

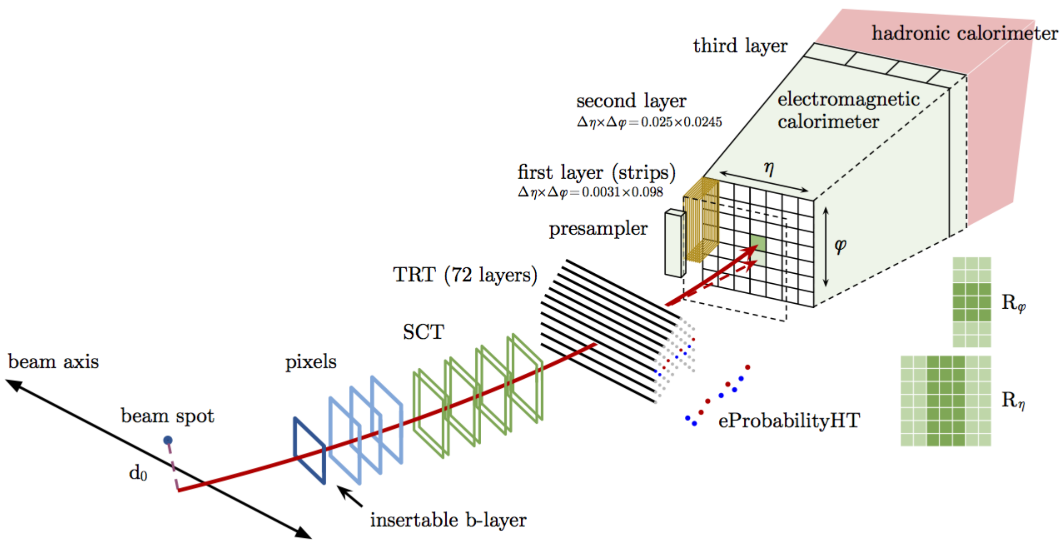

FIGURE 6.1: A schematic illustration of the path of an electron through the detector. The red trajectory shows the hypothetical path of an electron, which first traverses the tracking system (pixel detectors, then silicon-strip detectors and lastly the TRT) and then enters the electromagnetic calorimeter. The dashed red trajectory indicates the path of a photon produced by the interaction of the electron with the material in the tracking system (Aaboud, 2019b).

Figure 6.1 shows a depiction of an electron traversing some elements of the ATLAS detector. As it passes through the inner detector, an electron hits the IBL pixels layers, 3 pixel layers, 4 double-sided silicon strips, an average of around 30 straw hits in the TRT, a large number of which are high-threshold hits. After traversing the solenoid, it deposits its energy in four successive electromagnetic calorimeter layers: the presampler, then a layer finely segmented in η("strips"), followed by a layer of roughly 16 radiation lengths and a backplane layer. After this journey, only small amounts of the electron's energy reach the hadronic calorimeter.

The reconstruction of electron candidates within the kinematic region encompassed by the high-granularity electromagnetic calorimeter and the inner detector is based on three fundamental components characterizing the signature of electrons: Seed-cluster reconstruction which enables the localization of clusters of energy deposits found within the electromagnetic calorimeter, charged-particle tracks identified in the inner detector or track reconstruction (Sect. 6.1), and close matching in $\eta \times \phi$ space of the tracks to the clusters to form the final electron candidates.

6.2.2 Electron identification

The task of discriminating fundamental particles such as an electron (signal) from another (background) is mainly performed by the ATLAS tracking system, the calorimetry detectors and the software reconstruction algorithms. Here background objects include hadronic jets as well as electrons from photon conversions, Dalitz decays and semi-leptonic heavy-flavour hadron decays, and signals are referred to as prompt electrons.

Basically the standard identification for isolated high-pT electrons is based on cuts on variables related to the shower shapes, to the information from the reconstructed track and to the combined reconstruction. The cut-based selections commonly used are:

- Loose cuts: which consist of simple cuts on variables related to the shower-shape and to the matching between reconstructed track and calorimeter cluster;

- Medium cuts: which also consist of cuts on variables related to the shower-shape by using additional information contained in the first layer of the electromagnetic calorimeter. They also use track-quality cuts similar to the standard reconstruction cuts;

- Tight cuts: which require the track-matching criteria and the cut on the energy-to momentum ratio to be tighter. They also require the presence of a vertexing-layer hit on the track and a high ratio between high-threshold and low-threshold hits in the TRT.

The cut-based electron identification is a simple approach for identifying electron, it has been used by the ATLAS Collaboration for identifying electrons since the beginning of data-taking. However, according to ATLAS running conditions and for a better performance defined in terms of efficiency and background rejection, the cuts on the variables can vary, or even new variables can be added. For instance because of the significant pile-up (caused by the high luminosity), the variables most sensitive to pile-up were loosened, and a requirement on the f_3[1] variable was added, in 2012 for $\sqrt{s}$ = 8 TeV. A new selection called Multilepton was also added, optimized for the low-energy electrons in the $H \to ZZ* \to 4l$ ($l = e, \mu$) analysis; although if its efficiency is similar to the Loose selection, it provides a better background rejection. In comparison to the Loose selection, requirements on the shower shapes are loosened and more variables are added including those sensitive to bremsstrahlung effects. Moving beyond a cut-based selection, a likelihood (LH) identification menus can also be used, and additionally, further isolation of the electron may be required by using calorimeter energy isolation beyond the cluster itself.

[1] Ratio of the energy in the back layer to the total energy in the EM accordion calorimeter

A likelihood based (LH) identification can be used to identify electrons entering the central region of the detector ($|\eta| < 2.47$). The LH selection uses measurements from the tracking system, the calorimeter system, and quantities that combine both tracking and calorimeter information as inputs. It also makes use of signal and background probability density functions (pdfs, obtained from data) of the discriminating variables, treated as uncorrelated and from which an overall probability is calculated for the object to be signal or background. The likelihood discriminant $d_{\mathcal{L}}$ which combines the signal and background probabilities for a given electron candidate is defined as:

$$d_{\mathcal{L}} = \frac{\mathcal{L}_S}{\mathcal{L}_S + \mathcal{L}_B}, \quad \mathcal{L}_{S(B)}(\vec{x}) = \prod_{i=1}^{n} P_{S(B),i}(x_i), \tag{6.1}$$

where $\vec{x}$ is the vector of variable values and $P_{S,i}(x_i)$ and $P_{B,i}(x_i)$ are the values of the probability density function of the i^{th} variable evaluated at x_i for signal and background respectively. The LH identification includes variables sensitive to bremsstrahlung effects, and additionally variables with significant discriminating power but also a large overlap between signal and background that prevents explicit requirements (like Rϕ and f_1[2]) are included.
A corresponding selection to the cut-based identification are also designed (such as LooseLH, MediumLH, and VeryTightLH) which match roughly the same electron efficiencies but with a better rejection of light-flavour jets and conversions. The selection is done on the LH discriminant, made with a different set of variables by requiring some criteria. The LooseLH for instance, features variables most useful for discrimination against light-flavour jets. The MediumLH and VeryTightLH regimes, use additional variables to further reject heavy-flavour jets and conversions. Although different variables are used for the different selections, a sample of electrons selected using a tighter LH is a subset of the electron samples selected using the looser LH to a very good approximation. The LH for each selection consists of 9×6 sets of pdfs divided into 9 $|\eta|$ bins and 6 E$_T$ bins, which is coarser than the binning used for the cut-based selections. It is chosen to balance the available number of events with the variation of the pdf shapes in E$_T$ and $|\eta|$.

Isolation requirements can also be applied on the electrons in addition to the identification requirements, in order to further reject hadronic jets misidentified as electrons. Calorimeter and track isolation variables are the ones mainly used. $E_T^{cone\Delta R}$ is the calorimetric isolation variable which is the the sum of the transverse energy deposited in the calorimeter cells in a cone of size ΔR around the electron, excluding the contribution within $\Delta\eta \times \Delta\phi = 0.125 \times 0.175$ around the electron cluster barycenter. While the track isolation variable $p_T^{cone\Delta R}$ is the scalar sum of the transverse momentum of the tracks with p$_T$ > 0.4 GeV in a cone of ΔR around the electron, excluding the track of the electron itself.

6.2.3 Reconstruction efficiency for electrons

The tag-and-probe method is commonly used to evaluate the identification and reconstruction efficiency. Let's consider $Z \to ee$ and $J/\psi \to ee$ events from 2012 LHC proton–proton collision data at $\sqrt{s}$ = 13 TeV (The ATLAS Collaboration et al., 2017) which should satisfy data-quality criteria, in particular concerning the ID and the calorimeters, and at least one reconstructed primary vertex with at least three tracks present in the event. The tag electron is required to pass a strict selection

[2] Ratio of the energy in the strip layer to the total energy in the EM accordion calorimeter

criteria, the probe electron is used for efficiency measurement, and both tag-probe should also pass requirements on their reconstructed invariant mass.

The background contamination objects such as hadrons misidentified as electrons, electrons from semileptonic heavy flavour decays or from photon conversions, are estimated using either background template shapes or combined fits of background and signal analytical models to the data. The efficiencies are measured in data and in simulated $Z \rightarrow ee$ and $J/\psi \rightarrow ee$ samples, with the same criteria on the probe electron in order to compute efficiency Scale Factor (SF) $\epsilon^{Data}/\epsilon^{MC}$, used to evaluate the discrepancy between data and MC.

The identification efficiency is calculated as the ratio of the number of electrons passing a certain identification selection (numerator) to the number of electrons with a matching track satisfying the track quality requirements (denominator). The reconstruction efficiency is defined as the ratio of the number of electrons reconstructed as a cluster matched to a track satisfying the track quality criteria (numerator) to the number of clusters with or without a matching track.
Figure 6.2 shows the efficiencies of the reconstructed and identified electron combined, with respect to E_T (A) and η (B)

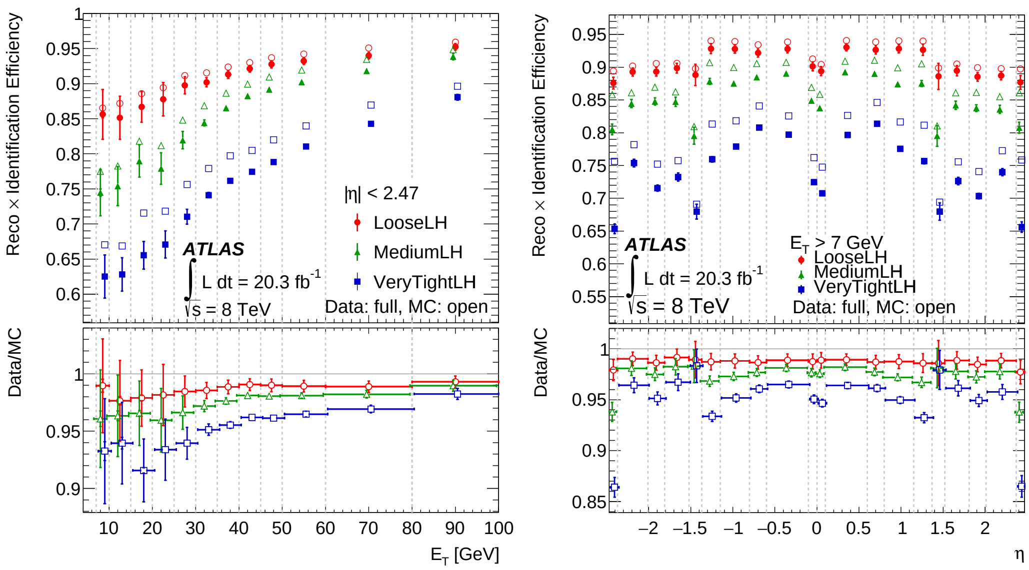

(A) (B)

FIGURE 6.2: Measured combined reconstruction and identification efficiency for the various cut-based and LH selections as a function of E_T (A) and η (B) for electrons. ratios. The panel at the bottom shows the efficiency ratio between Data and MC. (The ATLAS Collaboration et al., 2017)

6.3 Muon reconstruction and identification

6.3.1 Muon reconstruction

Muon reconstruction is performed by combining the information in the ID and MS to form the muons track that are used in physics analysis.

6.3.1.1 Muon reconstruction in the MS

The reconstruction of muons in the MS starts by forming segments from the hit patterns found in each muon chamber. The segments in the MDT are reconstructed by performing a straight-line fit to the hits found in each layer, and the ones in the CSC are built using a separate combinatorial search in the η and ϕ detector planes. Then the hits from segments in different layers are fitted together with a global χ^2 fit to build muon track candidates, and track candidate is considered only if the fit satisfies the selection criteria. Hits providing large contributions to the χ^2 are removed and the track fit is repeated. When additional hits are found which are consistent with the candidate trajectory, by using a recovery procedure, the fit is repeated. This task is performed by an algorithm which uses a segment-seeded combinatorial search that starts by using as seeds the segments generated in the middle layers of the detector where more trigger hits are available, and then extend the search to use the segments from the outer and inner layers as seeds. To build a track at least two matching segments are required, but in the barrel–endcap transition region where a single high-quality segment with η and ϕ information can be used to build a track.

6.3.1.2 Combined reconstruction

The information provided by the ID, MS, and calorimeters are used by various algorithms to perform the combined ID–MS muon reconstruction. Several methods can be used to reconstruct muons, depending on the instrumentation of the detector in the region traversed by the muon:

- Combined muons (CB): After track reconstruction is performed independently in the ID and MS, a combined track is formed with a global refit that uses the hits from both the ID and MS subdetectors. Some hits from the MS may be considered or not during the global fit in order to improve the fit quality. An outside-in pattern recognition is used for most of the muons reconstruction complemented by an inside-out combined reconstruction.

- Segment-tagged (ST) muons: If a track in the ID can be associated with at least one local track segment in the MDT or CSC chambers by extrapolation, it is considered as muon. Segment-tagged muons are used when muons cross only one layer of MS chambers.

- Calorimeter-tagged (CT) muons: If a track in the ID can be matched to an energy deposit in the calorimeter compatible with a minimum-ionizing particle, it is identifies as muon with $p_T > 15$ GeV. These type of muons cover an acceptance corresponding to $|\eta| < 0.1$ which has a very low purity and dedicated to ATLAS services.

- Extrapolated (Standalone) (ME) muons: a reconstructed muon is considered as standalone if its trajectory is reconstructed based only on the MS track and a loose requirement on compatibility with originating from the IP.

An overlap removal algorithm is used between different muon types before collecting the set of muons to be used for physics analysis.

6.3.2 Muons identification

In order to suppress background, mainly originating from pion and kaon decays, and increase the efficiency, quality requirements are applied to muon types. Four muon identification selections: Medium, Loose, Tight and High-p$_T$ are defined to meet the different requirements of the various physics analyses.

- Medium muons: Medium identification criteria required tracks with at least 3 hits in CB in at least two MDT layers, except for tracks in the $|\eta| < 0.1$ region, where tracks with at least one MDT layer but no more than one MDT hole layer are allowed. Tracks in the ME are also required with at least three MDT/CSC layers in the $2.5 < |\eta| < 2.7$ region. Medium selection is the default one in ATLAS and minimizes the systematic uncertainties associated with muon reconstruction and calibration.

- Loose muons: The Loose identification criteria maximizes the reconstruction efficiency providing good-quality tracks. This category is specifically included for reconstructing Higgs boson candidates in the four-lepton final state. It includes Medium requirements and all muons types with some restrictions according to the η regions considered.

- Tight muons: Though efficiency of the tight identification criteria is degraded, the muons which pass the selection are good quality, as only CB muons with hits in at least two stations of the MS and satisfying the Medium selection criteria are considered.

- High-p$_T$ muons: for the High-p$_T$ selection criteria only CB muons with high traverse momentum ($p_T > 20$ GeV) and muons passing the Medium selection and having at least three hits in three MS stations are selected, in order to maximize the momentum resolution for tracks. It is used specifically for searches for new high-mass resonances.

6.3.3 Reconstruction efficiency for muons

The reconstruction efficiency can be evaluated by checking how many times a muon identified in the ID matches to a muon identified in the MS and then combining the two efficiencies. The tag-and-probe (ATLAS Collaboration et al., 2016a) method is used to measure the efficiency of the muon identification selections based on the selection of an almost pure muon sample from $J/\Psi \to \mu\mu$ with low transverse momentum range $4.5 < p_T < 15$ GeV or $Z \to \mu\mu$ events with high $p_T < 110$ GeV.

The method requires one leg of the decay, denoted as tag to be identified as a Medium muon that fires the trigger. The second leg denoted as probe, has to be reconstructed by a system independent of the one being studied, and it is considered successfully reconstructed if the selected muon is found within a cone in the ($|\eta|$, ϕ) plane of size $\Delta R = \sqrt{\Delta\eta^2 + \Delta\phi^2} < 0.05$ around the probe track.

Muons pairs from Z events, are required to have invariant mass within 10 GeV of the Z boson mass and a transverse momentum of at least 10 GeV for the probe muon. The tag-probe pairs from J/Ψ are selected within the invariant mass window of 2.7-3.5 GeV, and are required to have a transverse momentum of at least 5 GeV for each muon.

MC simulation and data-driven techniques are used to subtract the background source in the $Z \to \mu\mu$. For J/Ψ events, simultaneous maximum-likelihood fit of two statistically independent distributions of the invariant mass; events in which the probe is or is not successfully matched to the selected muon, is used to estimate the background.

The methods are both applied on data and simulation, the ratio of two efficiencies $SF = \epsilon^{Data}/\epsilon^{MC}$ (efficiency Scale Factor) describes the discrepancy between data and MC, and is particularly relevant for physics analyses which use MC simulations that need to be corrected. The results are reported as a function of pseudorapidity (Figure 6.3) and probe transverse momentum (Figure 6.4). Figure 6.3 corresponds to Z events with respect to η where the muon reconstruction efficiency is almost 99% for Medium and Loose muons, and above 95% for Tight muons with all efficiencies in very good agreement with MC predictions. The main discrepancy between data and MC for Tight muons at $(\eta, \phi) \sim$ (-1.36, 1.6) is due to a poorly aligned MDT chamber. Further local inefficiencies in the barrel region are also linked to temporary faults during data taking. Figure 6.4 shows the reconstruction efficiency for medium muons with respect to p_T, with Z and J/Ψ events. The reconstruction efficiency remains high across a broad p_T spectrum with a good agreement between data and MC.

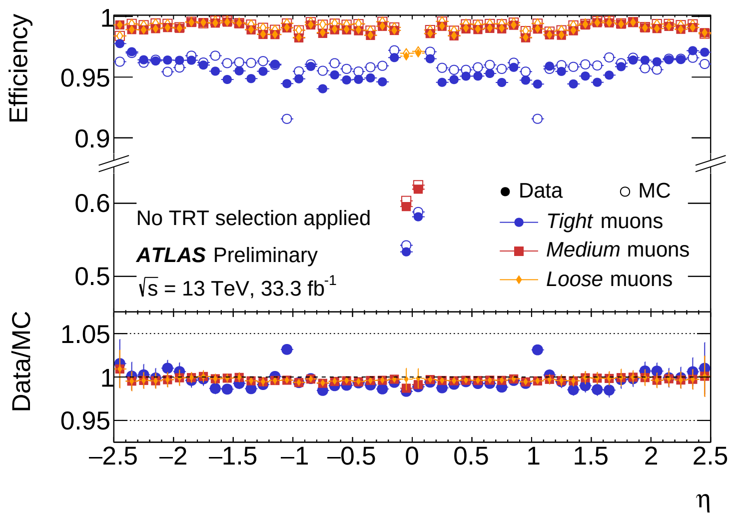

FIGURE 6.3: Muon reconstruction efficiencies for the Loose/Medium/Tight identification algorithms measured in $Z \to \mu\mu$ events as a function of the muon pseudorapidity for muons with $\mathrm{p}_T > 10$ GeV. The prediction by the detector simulation is depicted as open circles, while filled dots indicate the observation in collision data with statistical errors. The bottom panel shows the ratio between expected and observed efficiencies, the efficiency scale factor. The errors in the bottom panel show the quadratic sum of statistical and systematic uncertainty. (Marchese, 2017)

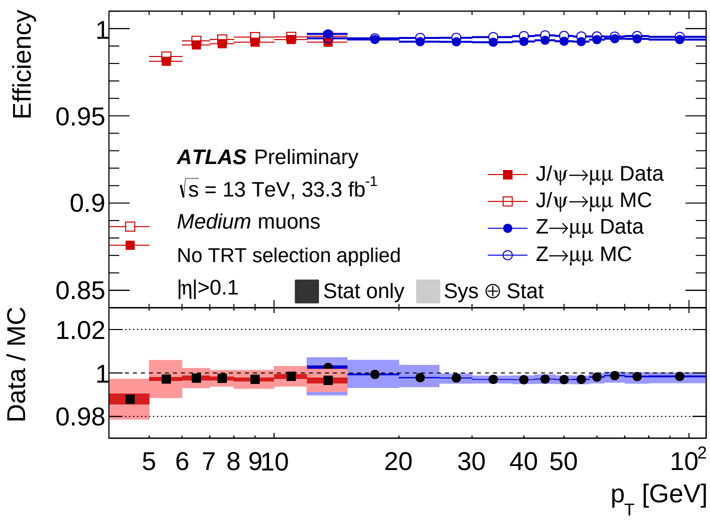

FIGURE 6.4: Muon reconstruction efficiencies for the Medium identification algorithm measured in $J/\Psi \to \mu\mu$ and $Z \to \mu\mu$ events as a function of the muon momentum. The prediction by the detector simulation is depicted as empty circles (squares), while the full circles (squares) indicate the observation in collision data. Only statistical errors are shown in the top panel. The bottom panel reports the efficiency scale factors. The darker error bands indicate the statistical uncertainty, while the lighter bands indicate the sum of the statistical and systematic uncertainties in quadrature (Marchese, 2017)

Conclusion. Events and object reconstruction such as electrons and muons are reviewed, the efficiencies of both objects using tag-and-probe method were also shown. The combined efficiency to reconstruct and identify an electron from $Z \to ee$ with E_T around 25 GeV is about 92% for the Loose cut-based identification and around 68% for the Tight cut-based identification as well as the VeryTightLH selection. The Muon reconstruction efficiencies are measured to be close to 99% for Medium and Loose muons and above 95% for Tight muons. Jets reconstruction is not reviewed since jets are not considered in this thesis, a detailed description of jet reconstruction can be found here (ATLAS Collaboration et al., 2017)

Part III

Analysis and interpretation

Chapter 7

Dark vector boson (Z_d) and pseudo-scalar (a) search with ATLAS detector in Run1 and Run2

7.1 Z_d search in Run1: Results

The search for a Z_d vector boson has been already performed in Run 1 with the ATLAS detector in proton-proton collision data at $\sqrt{s} = 8$ TeV with an integral luminosity of 20 fb^{-1}. The full analysis documentation which can be found here (Aad et al., 2015b) is not detailed in this thesis but the results are reviewed. This early search considers only the two processes: $H \to ZZ_d \to 4\ell$ and $H \to Z_dZ_d \to 4\ell$ corresponding to the two Feynman diagrams in left and right panel respectively of Figure 3.3. These two processes are also named ZX (X here stands for Z_d) channel and high mass (HM) channel respectively. The reconstructed mass of two di-lepton pairs are denoted as m_{12} and m_{34}, where m_{12} is the invariant mass of the di-lepton that is closer to the SM Z boson mass, and m_{34} is the invariant mass of the other di-lepton in the quadruplet.

ZX channel in the Run 1 analysis: The $H \to ZZ_d \to 4\ell$ search covers the exotic gauge boson mass range for $15 < m_{Z_d} < 55$ GeV. In this process m_{34} is the observable and it's expected to be consistent with a Z_d boson. The final states considered are: 4e, 2e2μ, 2μ2e and 4μ [1]. The m_{34} distribution is shown in figure 7.1, where no excess(es) or deviation from the SM expectations is observed. The observed and expected exclusion limit at 95% CL of the relative branching ratio $R_B = \frac{BR(H \to ZZ_d \to 4\ell)}{BR(H \to 4\ell)}$, and the branching ratio $BR(H \to ZZ_d \to 4\ell)$, for the combined final states are set, as shown in Figures 7.2a and 7.2b respectively. The branching ratio limit presents a range of $(1-9) \times 10^{-5}$, while the relative branching ratio has a range above 0.4 (observed) and 0.2 (expected). The HAHM benchmark model is used to set a limit on the kinetic mixing parameter ϵ (where ϵ is assumed to be $\gg$ κ for the $H \to ZZ_d \to 4\ell$ process) and the effective mass-mixing parameter $\delta^2 \times \mathcal{B}(Z_d \to \ell\ell)$ at the 95% CL, as shown in Figure 7.3a and 7.5 respectively. The respective limits on ϵ and $\delta^2 \times \mathcal{B}(Z_d \to \ell\ell)$ present a range of (4-17) $\times$ 10^{-2}, and (1.5 - 8.7) $\times 10^{-5}$ respectively.

[1] The distinction between $2e2\mu$ and $2\mu2e$ comes from the fact that the Z boson is reconstructed from $2e$ (which corresponds to the $2e2\mu$ notation) or 2μ (which corresponds to the $2\mu2e$ notation)

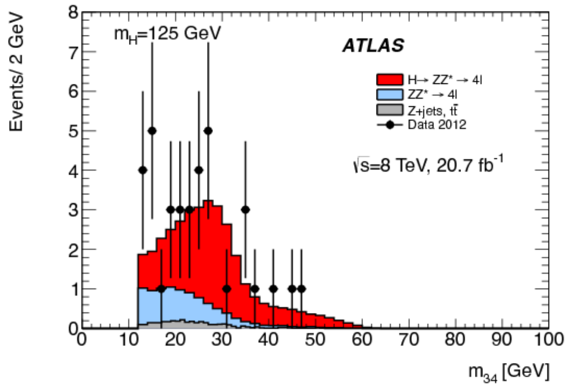

FIGURE 7.1: The distribution of the mass of the second lepton pair, m_{34}, of the $\sqrt{s}$= 8 TeV data (filled circles with error bars) and the expected (pre-fit) backgrounds. The $H \rightarrow ZZ* \rightarrow 4\ell\ell$ expected (pre-fit) normalization, for a mass hypothesis of mH=125 GeV, is set by subtracting the expected contributions of the $ZZ*$, Z+jets and $t\bar{t}$ backgrounds from the total number of observed 4′ events in the data (Aad et al., 2015b).

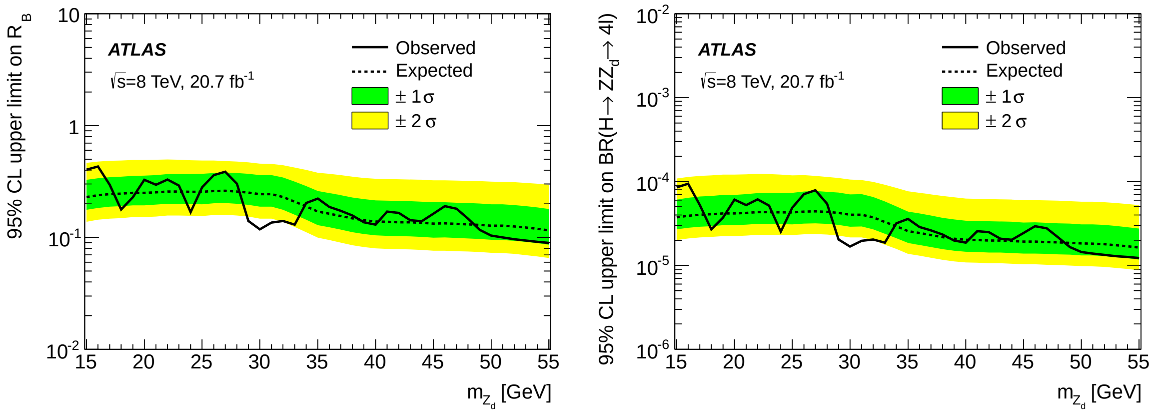

(A) (B)

FIGURE 7.2: A) The 95% CL upper limits on the relative branching ratio, $R_B = \frac{BR(H \rightarrow ZZ_d \rightarrow 4\ell)}{BR(H \rightarrow 4\ell)}$ as a function of m_{Z_d}. The $\pm\sigma$ and $\pm 2\sigma$ expected exclusion regions are indicated in green and yellow, respectively. B) The 95% CL upper limits on the branching ratio of $H \rightarrow ZZ_d \rightarrow 4\ell$ as a function of m_{Z_d} using the combined upper limit on R_B and the SM branching ratio of $H \rightarrow ZZ^* \rightarrow 4\ell$ (Aad et al., 2015b).

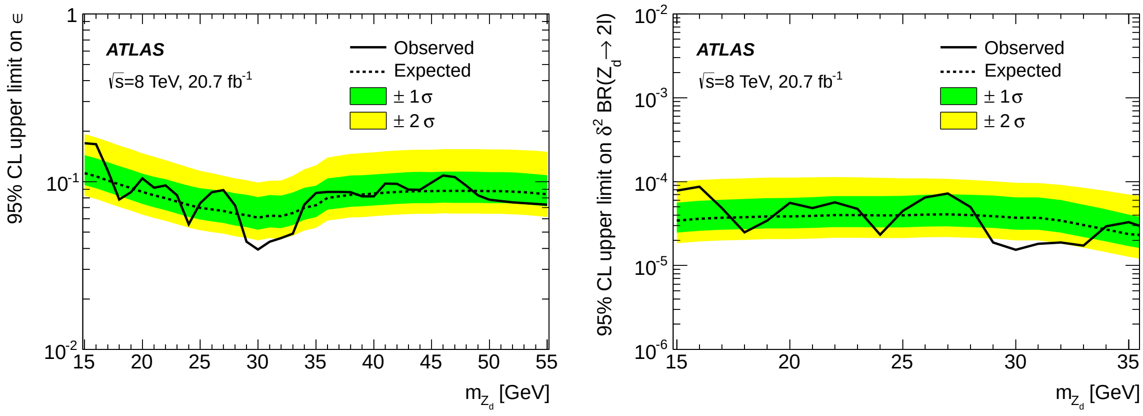

(A) (B)

FIGURE 7.3: A) The 95% CL upper limits on the gauge kinetic mixing parameter ϵ as a function of m_{Z_d} using the combined upper limit on the branching ratio of $H \to ZZ_d \to 4\ell$ and Table 2 of Ref.(Curtin et al., 2015).B) The 95% CL upper limits on the product of the mass-mixing parameter δ and the branching ratio of Z_d decays to two leptons (electrons, or muons), $\delta^2 \times \mathcal{B}(Z_d \to \ell\ell)$, as a function of m_{Z_d} using the combined upper limit on the relative branching ratio of $H \to ZZ_d \to 4\ell\ell$ and the partial width of $H \to ZZ_d$ (Aad et al., 2015b).

HM channel in the Run 1 analysis: The $H \to Z_d Z_d \to 4\ell$ search covers the exotic gauge boson mass range $15 < m_{4\ell} < 60$ GeV. The final states considered are: 4e, 2e2μ and 4μ. The average di-lepton mass $\langle m_{\ell\ell} \rangle = \frac{m_{12}+m_{34}}{2}$ is the observable. The signal region cut of this channel depends on the mass point hypothesis of the Z_d boson, so only the results of two hypothetical mass points where excesses were observed are presented in Table 7.1 and 7.2. One event is observed in the 4e final

Process	$4e$	4μ	$2e2\mu$
$H \to ZZ^* \to 4\ell$	$(1.5 \pm 0.3 \pm 0.2) \times 10^{-2}$	$(1.0 \pm 0.3 \pm 0.3) \times 10^{-2}$	$(2.9 \pm 1.0 \pm 2.0) \times 10^{-3}$
$ZZ^* \to 4\ell$	$(7.1 \pm 3.6 \pm 0.5) \times 10^{-4}$	$(8.4 \pm 3.8 \pm 0.5) \times 10^{-3}$	$(9.1 \pm 3.6 \pm 0.6) \times 10^{-3}$
WW, WZ	$< 0.7 \times 10^{-2}$	$< 0.7 \times 10^{-2}$	$< 0.7 \times 10^{-2}$
$t\bar{t}$	$< 3.0 \times 10^{-2}$	$< 3.0 \times 10^{-2}$	$< 3.0 \times 10^{-2}$
$Zbb, Z + jets$	$< 0.2 \times 10^{-2}$	$< 0.2 \times 10^{-2}$	$< 0.2 \times 10^{-2}$
$ZJ/\Psi, ZY$	$< 2.3 \times 10^{-2}$	$< 2.3 \times 10^{-2}$	$< 2.3 \times 10^{-2}$
Total background	$< 5.6 \times 10^{-2}$	$< 5.9 \times 10^{-2}$	$< 5.3 \times 10^{-2}$
Data	1	0	0

TABLE 7.1: Expected and observed events for mass $m_{Zd} = 25\,GeV$ (Aad et al., 2015b)

state as shown in Table 7.1. It has di-lepton invariant masses of 21.8 GeV and 28.1 GeV and is consistent with a Z_d mass in the $23.5 < m_{Z_d} < 26.5$ GeV range. The corresponding local significance is about 1.6 σ. Another event is observed in the 4μ final state (Table 7.1). This event has di-lepton invariant masses of 23.2 GeV and 18.0 GeV and is compatible with a Z_d mass in the $20.5 < m_{Zd} < 21.0$ GeV range. The corresponding local significance is about 1.8 σ. For both events the expected background is negligible ($< 5.6 \times 10^{-2}$). These two events are not statistically significant, so limits are set at 95% CL on the signal strength $\mu_d = \frac{\sigma \times BR(H \to Z_d Z_d \to 4\ell)}{\sigma \times BR(H \to ZZ^* \to 4\ell)}$

Process	$4e$	4μ	$2e2\mu$
$H \to ZZ^* \to 4\ell$	$(1.2 \pm 0.3 \pm 0.2) \times 10^{-2}$	$(5.8 \pm 2.0 \pm 2.0) \times 10^{-3}$	$(2.6 \pm 1.0 \pm .2) \times 10^{-3}$
$ZZ^* \to 4\ell$	$(3.5 \pm 2.0 \pm 0.2) \times 10^{-3}$	$(4.1 \pm 2.7 \pm 0.2) \times 10^{-3}$	$(2.0 \pm 0.6 \pm 0.1) \times 10^{-3}$
WW, WZ	$< 0.7 \times 10^{-2}$	$< 0.7 \times 10^{-2}$	$< 0.7 \times 10^{-2}$
$t\bar{t}$	$< 3.0 \times 10^{-2}$	$< 3.0 \times 10^{-2}$	$< 3.0 \times 10^{-2}$
$Zbb, Z + jets$	$< 0.2 \times 10^{-2}$	$< 0.2 \times 10^{-2}$	$< 0.2 \times 10^{-2}$
$ZJ/\Psi, ZY$	$< 2.3 \times 10^{-2}$	$< 2.3 \times 10^{-2}$	$< 2.3 \times 10^{-2}$
Total background	$< 5.3 \times 10^{-2}$	$< 5.1 \times 10^{-2}$	$< 6.4 \times 10^{-2}$
Data	1	0	0

TABLE 7.2: Expected and observed events for mass $m_{Zd} = 20.5\,GeV$ (Aad et al., 2015b)

and on the branching ratio assuming the SM Higgs cross section, for all the combined final states, as shown in Figure 7.4a and 7.4b respectively. Using the HAHM as benchmark model, an exclusion limit at 95% CL is set on the Higgs portal coupling parameter κ, as shown in Figure 7.5. The limits on the branching ratio and on κ show a range of (2-3) $\times 10^{-5}$ and (1-10) $\times$ 10^{-4} respectively.

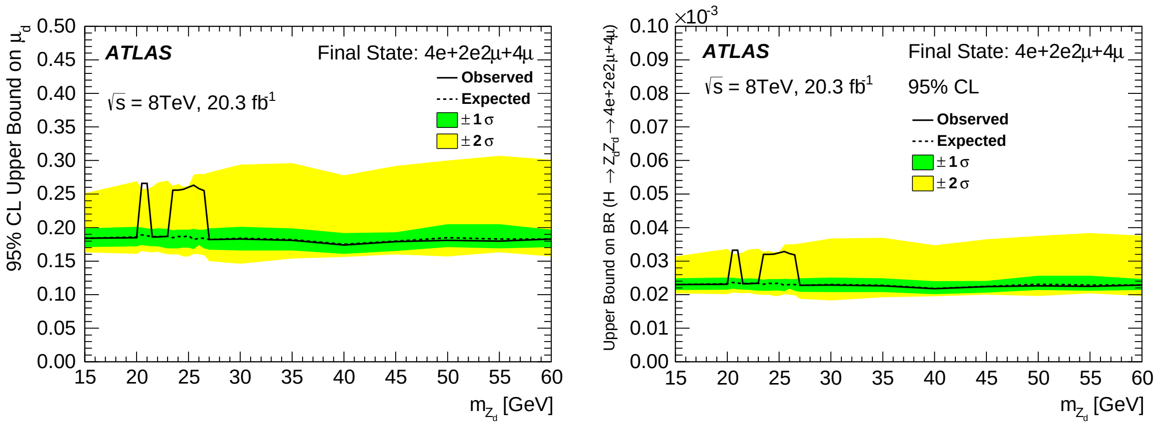

(A) (B)

FIGURE 7.4: A) The 95% confidence level upper bound on the signal strength $\mu_d = \frac{\sigma \times BR(H \to Z_d Z_d \to 4\ell)}{\sigma \times BR(H \to ZZ^* \to 4\ell)}$ in the combined 4e, 2e2μ, 4μ final state, for m_H = 125 GeV. The $\pm\sigma$ and $\pm 2\sigma$ expected exclusion regions are indicated in green and yellow, respectively. B) The 95% CL upper limits on the branching ratio of $H \to Z_d Z_d \to 4\ell$as a function of m_{Z_d} in the combined 4e, 2e2μ, 4μ final state, for m_H = 125 GeV The $\pm\sigma$ and $\pm 2\sigma$ expected exclusion regions are indicated in green and yellow, respectively (Aad et al., 2015b).

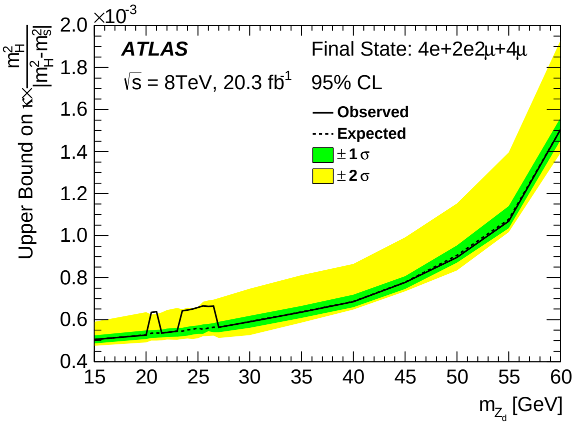

FIGURE 7.5: The 95% confidence level upper bound on the Higgs mixing parameter $\kappa \times m_H^2 |m_H^2 - m_S^2|$ as a function of m_{Z_d} in the combined 4e, 2e2μ, 4μ final state, for m_H = 125 GeV. The $\pm\sigma$ and $\pm 2\sigma$ expected exclusion regions are indicated in green and yellow, respectively (Aad et al., 2015b).

7.2 Z_d and a search in Run 2: Results

In the Run 2 analysis the search for the dark vector boson already performed in Run 1 is carried out with several improvements in some cases and also extended to the search for a pseudo-scalar a, with the ATLAS detector in proton-proton collisions data at $\sqrt{s}$ = 13 TeV with an integral luminosity of 36.1 fb^{-1}. The new channel ($H \to aa \to 4\mu$) in this iteration, named as the Low Mass channel (LM), uses the 2HDM+S as benchmark model and considers only 4μ as final state. X is used again in the Higgs decay process ($H \to XX \to 4\ell$) and stands for Z_d or a depending on the mass range and the benchmark model considered as already described in Chapter 3. As in the previous section, only the results are summarized here, the full analysis can be found in this reference (The ATLAS collaboration et al., 2018).

ZX channel in the Run 2 analysis: The search strategy is the same between Run 1 and Run 2, for the ZX channel. The m_{34} distribution is shown in Figure 7.6, the results are also presented in the Table 7.3.

Process	$2\ell 2\mu$	$2\ell 2e$	Total
$H \to ZZ^* \to 4\ell$	34.3 ± 3.6	21.4 ± 3.0	55.7 ± 6.3
$ZZ^* \to 4\ell$	16.9 ± 1.2	9.0 ± 1.1	25.9 ± 2.0
Reducible background	2.1 ± 0.6	2.7 ± 0.7	4.8 ± 1.1
$VVV, t\bar{t} + V$	0.20 ± 0.05	0.20 ± 0.04	0.40 ± 0.06
Total expected	53.5 ± 4.3	33.3 ± 3.4	86.8 ± 7.5
Observed	65	37	102

TABLE 7.3: Expected and observed of events at $36.1 fb^{-1}$ (The ATLAS collaboration et al., 2018).

As in the Run 1 no significant excess(es) is observed also in the Run 2 search, so limits are set on the branching ratio of the $H \to ZX$ process (Figure 7.7a), and on the

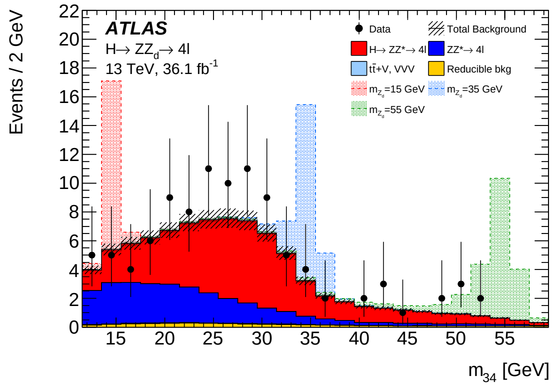

FIGURE 7.6: Distribution of m_{34} for data and background events in the mass range $m_{4\ell} \in [115, 130]$ GeV after the $H \rightarrow ZX \rightarrow 4\ell$ selection. Three signal points for the $H \rightarrow ZZ_d \rightarrow 4\ell$ model are shown. The signal strength corresponds to a branching ratio $\mathcal{B}(H \rightarrow ZZ_d \rightarrow 4\ell) = \frac{1}{3}\mathcal{B}(H \rightarrow ZZ^* \rightarrow 4\ell)$ (with $\mathcal{B}(H \rightarrow ZZ^* \rightarrow 4\ell)$ corresponding to the SM prediction (Dittmaier, 2012)). The uncertainties include statistical and systematic contributions (The ATLAS collaboration et al., 2018).

same parameters at 95% CL such as: the kinetic mixing parameter ϵ (Figure 7.7b), and the effective mass mixing parameter δ (Figure 7.8).

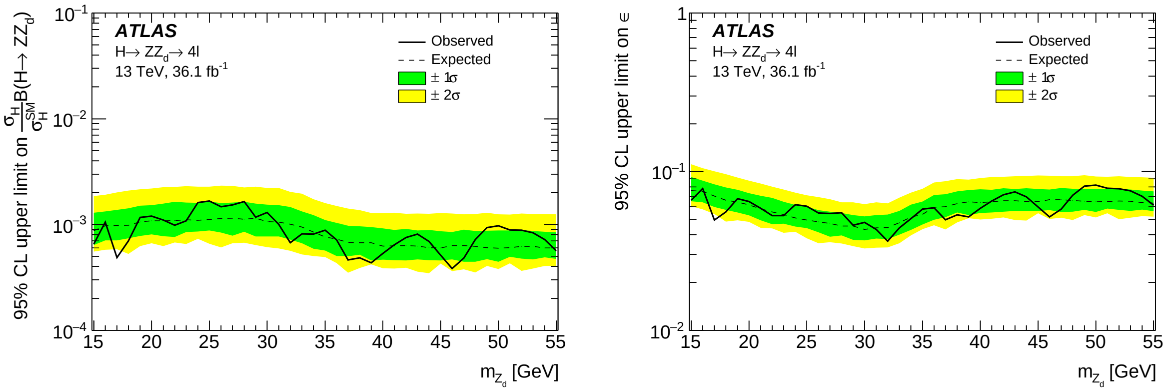

(A) (B)

FIGURE 7.7: (A) Upper limit at 95% CL on the branching ratio for the $H \rightarrow ZZ_d$ process. (B) Upper limits on the kinetic mixing parameter, ϵ, between the SM Z boson and Z_d. The limits on ϵ are obtained directly from the $BR(H \rightarrow ZZ_d \rightarrow 4\ell)$ (The ATLAS collaboration et al., 2018).

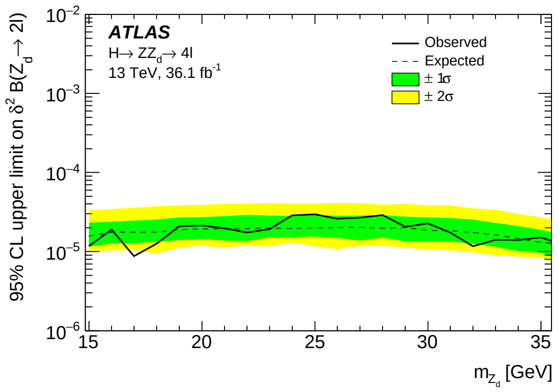

FIGURE 7.8: The branching ratio and the partial width of $H \to ZZd$ can be used to constrain as well the mass-mixing parameter, δ, of the model described, where the mass mixing between the Z_d and the SM Z boson is introduced. The limits are valid in the region where $m_{Z_d} < m_H - m_Z$, and are set on the product $\delta^2 \times B(Z_d \to 2\ell)$ since both δ and $B(Z_d \to 2\ell)$ are model-dependent (The ATLAS collaboration et al., 2018).

HM channel in the Run 2 analysis: In the Run 2 search the signal region cut of the HM channel is optimized in such a way it's now independent of the hypothetical Z_d mass point. The average di-lepton mass $\langle m_{\ell\ell} \rangle$ distribution, in Figure 7.9, shows the results of this channel. The results are also presented in Table 7.4. Six events are observed; 3 in the 2e2μ final state and 3 in the 4μ final state, where the expected background is only 3.9±0.3. The biggest deviation from the Standard Model expectation is from a single event at $\langle m_{\ell\ell} \rangle \approx 20$ GeV, with a local significance of 3.2 σ. The corresponding global significance is approximately 1.9 σ. These excesses do not show any significant deviation from the SM expectations, so the results are interpreted in term of limit. An upper limit at 95% CL is set on the branching ratio of the process $H \to Z_d Z_d$ and on the Higgs mixing parameter κ as shown in Figure 7.10a and 7.10b respectively.

Process	Yield
$ZZ^* \to 4l$	0.8 ± 0.1
$H \to ZZ* \to 4l$	2.6 ± 0.3
VVV/VBS	0.51 ± 0.18
$Z + (t\bar{t}/J/\Psi) \to 4\ell$	0.004 ± 0.004
Other Reducible Background	Negligible
Total	3.9 ± 0.3
Data	6

TABLE 7.4: Expected and observed of events at $36.1 fb^-1$ (The ATLAS collaboration et al., 2018) .

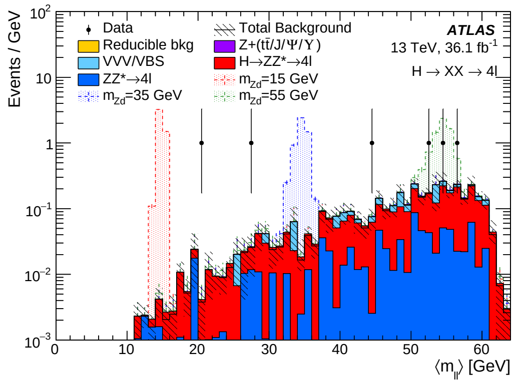

FIGURE 7.9: Distribution of (a) $\langle m_{\ell\ell} \rangle = \frac{1}{2}(m_{12} + m_{34})$ and (b) m_{34} vs m_{12}, for events selected in the $H \to XX \to 4\ell$ ($15 < m_X < 60$ GeV) analysis. The example signal distributions in (a) correspond to the expected yield normalized with $\sigma(pp \to H \to Z_d Z_d \to 4\ell) = \frac{1}{10}\sigma_{\mathrm{SM}}(pp \to) H \to ZZ^* \to 4\ell$(The ATLAS collaboration et al., 2018).

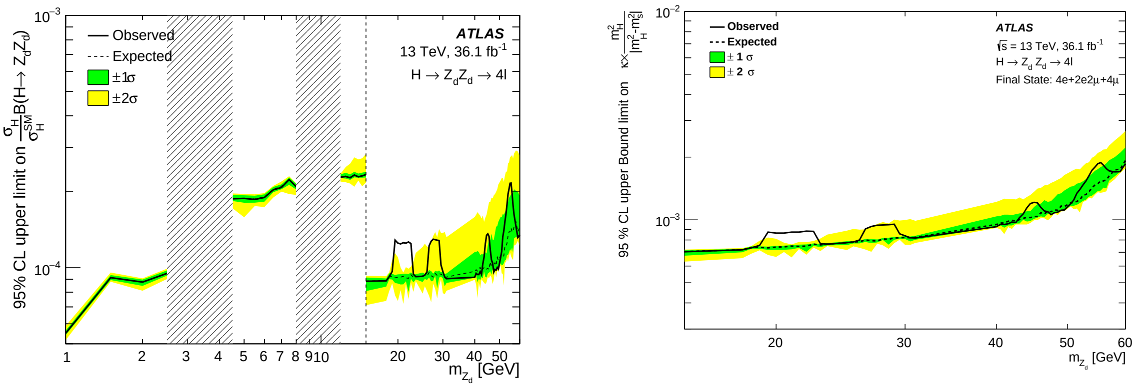

(A) (B)

FIGURE 7.10: (A) Upper limit at 95% CL on the branching ratios for processes $H \to Z_d Z_d$. The step change at the $m_X = 15$ GeV boundary is due to the addition of sensitivity to 4e and $2e2\mu$ final states (lowering the limit). The shaded areas are the quarkonia veto regions. (B) The $H \to Z_d Z_d$ decay can be used to obtain the 95% CL upper bound on the effective Higgs mixing parameter $\kappa' = \kappa \times m_H^2/|m_H^2 - m_S^2|$ as a function of m_{Z_d}, for $m_H/2 < m_S < 2m_H$. κ is the size of the Higgs portal coupling and m_S is the mass of the dark Higgs boson, the relation can be achieved by using the partial width of $H \to Z_d Z_d$ as given in terms of κ. The limit is valid in the regime where the Higgs mixing parameter dominates ($\kappa \gg \epsilon$), $m_S > m_H/2, m_{Z_d} < m_H/2$ and $H \to Z_d Z* \to 4\ell$ is negligible. This would correspond to an upper bound on the Higgs portal coupling in the range $\kappa \sim (1 - 10) \times 10^{-4}$ (The ATLAS collaboration et al., 2018).

LM channel in the Run 2 analysis: The $H \to aa \to 4\mu$ search covers the exotic gauge boson mass range for $1 < m_a < 10$ GeV. It also uses the average di-lepton mass $\langle m_{\ell\ell} \rangle$ as observable. Figure 7.11a and Table 7.5 show the results obtained with the low mass channel. No events were observed which also is compatible with background expectation, so limits are set at 95% CL on the branching ratio for the process $H \to aa$ using the 2HDM+S as benchmark model, as shown in Figure 7.11b.

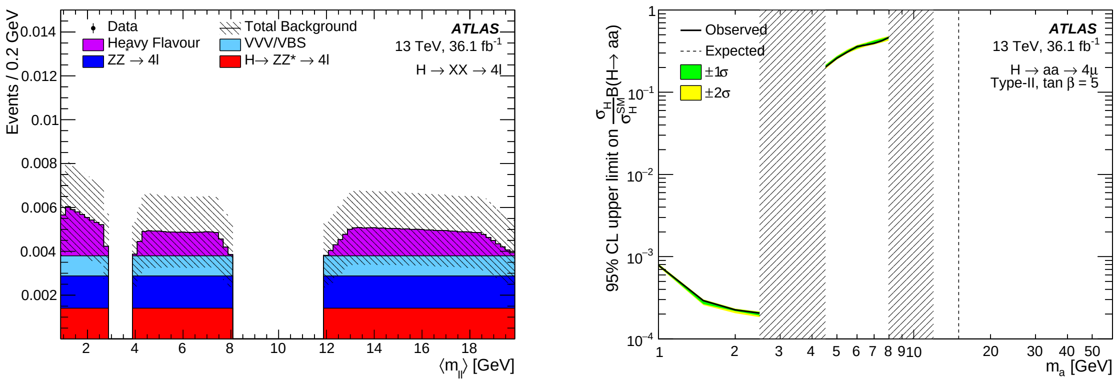

(A)

(B)

FIGURE 7.11: (A) Distribution of $\langle m_{\ell\ell} \rangle = \frac{1}{2}(m_{12} + m_{34})$, for events selected in the $H \to XX \to 4\mu(1 < m_X < 15$ GeV) analysis. (B) Upper limit at 95% CL on the branching ratios for processes $H \to aa$, for the 2HDM+S bench mark model studied. The limit is greater than 1 for $m_a > 15$ GeV. The shaded areas are the quarkonia veto regions (The ATLAS collaboration et al., 2018).

Process	Yield
$ZZ^* \to 4l$	0.10 ± 0.01
$H \to ZZ* \to 4l$	0.1 ± 0.1
VVV/VBS	0.06 ± 0.03
Heavy flavour	0.07 ± 0.04
Total	0.4 ± 0.1
Data	0

TABLE 7.5: Expected and observed events at $36.1 fb^{-1}$ (The ATLAS collaboration et al., 2018).

7.3 Conclusion

The first iteration of the Z_d search was carried out in Run 1, where only two channels were considered: $H \to ZZ_d \to 4\ell$ and $H \to ZdZ_d \to 4\ell$. No statistical significant evidence of a deviation from the SM expectations were observed for both searches, hence limits are set on the branching ratio of the two processes, on the kinetic mixing (ϵ), the Higgs mixing (κ) and the mass mixing (δ) parameters using the HAHM as bench mark model. In the Run 2, the Z_d search is performed again and extended to the pseudo-scalar a search which uses 2HDM+S as benchmark model. No evidence of deviation from the SM expectations were also observed for the three channels, limits were set at 95% on the same parameters as in Run 1, and on the branching ratio of the three processes. However, The limit on the branching ratio for $H \to ZdZ_d \to 4\ell$ in Run 1 was improved in Run 2 by about a factor of four, which corresponds to the increase in both luminosity and Higgs boson production cross-section between Run 1 and Run 2.

In the full Run 2 data set corresponding to a luminosity of 139.1 fb^{-1} the Z_d and a search is carried out again, also with several improvements implemented, and also extended to the search for an additional scalar S decaying to 4ℓ via two Z_d. The full Run 2 analysis is discussed in the next chapter.

Chapter 8

Dark vector boson (Z_d), pseudo-scalar (a) and dark Higgs (S) search with the ATLAS detector in full Run2

The full Run 2 analysis uses data 15, 16, 17 and 18 with a total luminosity of 139.1 fb^{-1}. The ZX, HM and LM channels performed in Run 2 (The ATLAS collaboration et al., 2018), are also carried out in the full Run 2 search, plus a new channel called Additional Scalar (AS). The AS channel considers a dark Higgs boson S outside the Higgs window [1] ($m_S \in [20, 115[\cup]130, 750]$GeV) GeV decaying to 4ℓ via two Z_d bosons: $S \to XX \to 4\ell$[2]. The theory which motivates these BSM searches is described in detail in Chapter 3. Recently the IBL (Insertable B-Layer) has been installed between the pixel detector and a new smaller radius beam-pipe. It provides robust tracking and improved precision for vertexing and tagging for the full Run 2. A better performance of the trigger has also been observed in the full Run 2. A new release (21) of the analysis software has been used in the full Run 2 which provides a lot of improvement in term of robustness. The strategy, the background estimation as well as the signal region (SR) selection used in the full Run 2 search for ZX, and LM channels are the same as in the Run 2 search already published (The ATLAS collaboration et al., 2018). For the HM channel the differences between the full Run 2 and the Run 2 searches, are the SR re-optimization (described in Appendix A.2), the definition of new validation regions to avoid overlaps with the signal region of other channels, and the new methods used to estimate the reducible backgrounds, which are the ABCD and the fake factor methods. This chapter will focus on the AS channel which is the new channel and the one I contributed the most. Without repeating the strategies of the others channels, their results in the full Run 2 will be showed. An improvement in the limit setting is expected, with a higher Higgs production cross section and a higher luminosity (from 36.1 fb^{-1} in Run 2 to 140.0 fb^{-1}) in full Run 2.

8.1 Object and event reconstruction

The following steps define the event selection:

- Event preselection,

[1] The Higgs window is defined in the previous iterations as $115 < m_{4l} < 130$ GeV.

[2] The same notation for X is used here; it stands for Z_d or a according to the mass range and the benchmark model used.

- Baseline e selection,
- Baseline μ selection,
- Dilepton and quadruplet formation,
- Quadruplet selection and ranking,
- Event selection.

The Event preselections are detailed in Section 8.1.1 and baseline lepton selections are detailed in Section 8.1.2.

8.1.1 Event preselection

At the preselection stage, all events must pass the Good Run Lists (GRL) requirement. GRL is a dedicated list of data quality criteria containing all valid physics runs and luminosity block[3]. Then, they should pass the cleaning requirements (ATLAS Collaboration et al., 2015) designed to reject events with excessive noise in the calorimeters. It requires all the events to not contain errors from any detectors or sub-detectors (`LArError`, `TileError`, `SCTError`, or `CoreError`). Events are considered if they only fire at least one of the triggers listed in Table 8.1, and contain at least one primary vertex (ATLAS Collaboration, 2015) reconstructed with two or more associated tracks with $p_T = 400$ MeV. Since we are looking for at least one quadruplet, only event with at least four leptons are considered.

8.1.1.1 Trigger

As shown in Table 8.1, single lepton, di-lepton or tri-lepton unprescaled triggers (Aaboud, 2017) are used to preselect the events with the following thresholds:

- From 24 GeV - 26 GeV for single-lepton,
- From 2×12 GeV - 2×24 GeV for di-electron,
- From 2×10 GeV - $22, 8$ GeV for di-muon,
- $17, 9, 9$ GeV for tri-electron,
- 3×6 GeV for tri-muon.

When running on MC, the random run and luminosity block numbers as provided by the `PileupReweightingTool`[4] (Buttinger, 2015) are used to decide which triggers are applied.

[3] A luminosity block is defined as a unit of time for data taking

[4] A PileupReweightingTool is an analysis tool which calculates the weights that correct MC and data for differences between instantaneous luminosity distributions and triggers prescales

ℓ	Trigger name	2015	2016	2017	2018
e	HLT_e24_lhmedium_L1EM20VH	✓			
	HLT_e24_lhmedium_iloose_L1EM18VH				
	HLT_e24_lhtight_nod0_ivarloose		✓		
	HLT_e26_lhtight_nod0				✓
	HLT_e26_lhtight_nod0_ivarloose		✓	✓	✓
	HLT_e60_lhmedium	✓	✓		
	HLT_e60_lhmedium_nod0		✓	✓	✓
	HLT_e60_medium				
ee	HLT_2e12_lhloose_L12EM10VH	✓			
	HLT_2e15_lhvloose_nod0_L12EM13VH		✓		
	HLT_2e17_lhvloose_nod0		✓		
	HLT_2e17_lhvloose_nod0_L12EM15VHI			✓	✓
	HLT_2e24_lhvloose_nod0			✓	✓
μ	HLT_mu20_iloose_L1MU15	✓			
	HLT_mu26_ivarmedium		✓	✓	✓
	HLT_mu50	✓	✓	✓	✓
	HLT_mu60_0eta105_msonly	✓	✓	✓	✓
$\mu\mu$	HLT_mu18_mu8noL1	✓			
	HLT_mu22_mu8noL1		✓	✓	✓
	HLT_2mu10	✓	✓		
	HLT_2mu14		✓	✓	✓
$e\mu$	HLT_e17_lhloose_mu14	✓			
	HLT_e17_lhloose_nod0_mu14		✓	✓	✓
	HLT_e24_lhmedium_nod0_L1EM20VHI_mu8noL1		✓		
	HLT_e26_lhmedium_nod0_mu8noL1			✓	✓
	HLT_e7_lhmedium_mu24	✓			
	HLT_e7_lhmedium_nod0_mu24		✓	✓	✓
$e\mu\mu$	HLT_e12_lhloose_2mu10	✓			
	HLT_e12_lhloose_nod0_2mu10		✓	✓	✓
$ee\mu$	HLT_2e12_lhloose_mu10	✓			
	HLT_2e12_lhloose_nod0_mu10		✓	✓	✓
eee	HLT_e17_lhloose_2e9_lhloose	✓			
	HLT_e17_lhloose_nod0_2e9_lhloose_nod0		✓		
	HLT_e17_lhloose_nod0_2e10_lhloose_nod0_L1EM15VH_3EM8VH		✓		
	HLT_e24_lhvloose_nod0_2e12_lhvloose_nod0_L1EM20VH_3EM10VH			✓	✓
$\mu\mu\mu$	HLT_mu18_2mu4noL1	✓			
	HLT_mu20_2mu4noL1		✓	✓	✓
	HLT_3mu4			✓	
	HLT_3mu6	✓	✓	✓	✓
	HLT_3mu6_msonly	✓	✓	✓	✓

TABLE 8.1: Triggers used in the 2015–8 analysis. Triggers are only used when they are unprescaled. Prescaled triggers are not included because of their low thresholds.

8.1.2 Baseline lepton selection

Electrons and muons are required to pass some baseline selection cuts before they can be used to form the quadruplets. For electrons only the region $|\eta| < 2.47$ is considered with $p_T > 7$ GeV and a longitudinal impact parameter $|z_0 \sin\theta| < 0.5$ mm. The electrons also should pass `Loose` likelihood identification cut, and the quality object cut, which require them not to originate from a bad cluster. For muons, the region where $|\eta| < 2.5$ is considered. Muons should have $p_T > 5$ GeV (> 15 GeV if calo-tagged), an impact parameter $|z_0 \sin\theta| < 0.5$ mm and $d_0 < 1$ mm (both are not applied to standalone muons as they do not have an ID track). They also should pass `Loose` identification cut (discussed in Chapter 6), and can be combined, standalone, calo-tagged, or silicon-associated forward muons.

8.1.3 Selection and ranking of quadruplets

After the baseline lepton selection, quadruplet is formed if the events contain at least four leptons. The quadruplet should pass some requirements otherwise the event is discarded. The quadruplet must have leptons of the same flavor and opposite sign (SFOS). The leptons inside the quadruplets are ranked by p_T and then ordered where the first, second and third lepton should have $p_T^1 > 20$ GeV , $p_T^2 > 15$ GeV and $p_T^3 > 10$ GeV respectively. The quadruplet should also pass the trigger matching requirement which imposes the condition that the leptons in the quadruplet must be responsible for firing at least one trigger (for multi-lepton triggers, all leptons of the trigger must match to leptons of the quadruplet). For a quadruplet containing muons, more than one cannot be a calo-tagged muon or standalone muon. In order to separate the di-leptons, the distance in the pseudorapidity–azimuthal-angle space ΔR should > 0.10 (0.20) for same-flavour (different-flavour) leptons in the quadruplet. This requirement is not applied in the LM search since low-mass bosons are more boosted and thus the resulting muons are less separated. An overlap removal algorithm is also applied to avoid identifying the same detector signature as multiple electrons or muons. In case more than quadruplet passes these requirements, the one with the smallest $\Delta m_{\ell\ell}$ [5] is selected.

8.2 Event selection

In the event selection stage, further requirements on the leptons of the quadruplet, including isolation, electron quality, and impact parameter significance are applied. The quadruplet should also be originated from a common vertex. Some kinematic requirements are also applied to the kinematics variables, in the two signal regions defined as: signal region 1 (SR1) which requires $m_{4\ell} > 130$ GeV and signal region (SR2) which requires $m_{4\ell} < 115$ GeV.

8.2.1 Invariant mass kinematic variables

The invariant masses of the two di-leptons that make up a quadruplet are denoted as m_{ab} and m_{cd} where $m_{ab} > m_{cd}$. Thus, m_{ab} and m_{cd} are the leading and sub-leading di-lepton pairs respectively. In the case of $4e$ or 4μ final states, it may happen that the di-leptons are mis-paired, so the alternative pairing with same flavor opposite sign (SFOS) is also defined and denoted as m_{ad} and m_{bc}.

[5] $\Delta m_{\ell\ell}$ is defined as $\equiv |m_{ab} - m_{cd}|$

8.2.2 The E'_{ab} variable

E'_{ab}/m_{4l} is a kinematic variable defined as the energy component of the lepton pair's four-momentum in the center of momentum frame (CMF), expressed by the equation:

$$E'_{ab}/m_{4l} = \frac{1}{2} \times [1 + (m_{ab}^2 - m_{cd}^2)/m_{4l}^2]. \tag{8.1}$$

It's distribution is given in Figure 8.1, and its derivation is discussed in Appendix A.3.

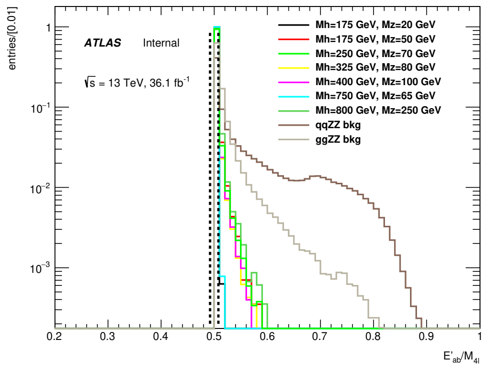

FIGURE 8.1: E'_{ab}/M_{4l} distributions for additional scalar signal hypotheses and the two leading SM background processes (normalized to unity). The dotted lines delimit the cut applied using this variable.

8.2.3 Requirements on leptons in the event selection

At the first stage of the event selection, all leptons are required to pass isolation cuts: `FCLoose` [6] for electrons (Aaboud, 2019b) and `FCLoose_FixedRad` [7] for muons (Aad, 2016), each with close-by corrections. In addition, electrons should pass the `Loose` likelihood identification. And finally only electrons (muons) with a transverse impact parameter calculated relative to the beam line in the range $d_0^{\mathrm{BL}}\mathrm{Sig.} < 3$ (< 5) are considered.

8.2.4 Kinematic requirements in event selection

In the second stage of the event selection, some kinematic cuts are applied on the di-lepton and the quadruplet invariant masses:

- H veto cut for SR1 $m_{4l} > 130$ GeV
- H veto cut for SR2 $m_{4l} < 115$ GeV
- Z boson veto in SR1: m_{ab} and m_{cd} $\notin$ $[83.2, 99.2]$ GeV, m_{ad} and m_{cb} $\notin$ $[87.2, 95.2]$ GeV. It is defined by the optimization procedure discussed in Appendix A.1.

[6] `FCLoose` is an isolation cut on electron which required $p_T^{iso}/p_T > 0.15$ and $E_T^{iso}/p_T > 0.2$
[7] `FCLoose_FixedRad` is an isolation cut on electron which required $p_T^{iso}/p_T > 0.15$ and $E_T^{iso}/p_T > 0.3$

- Z boson veto in SR2: $m_{ab} \notin [50, 106]$ GeV. It is defined to be orthogonal to the Z boson acceptance window defined in the ZX search, in order to avoid overlap between SR2 and the ZX validation region.

- Low mass veto cut: It requires $m_{ab,cd,ad,cb} > 5$, this requirement is to avoid discrepancies between data and MC observed in validation plots.

- Quarkonia veto around J/Ψ, $\Upsilon(2S)$, $\Upsilon(1S)$, and $\Upsilon(3S)$: event is rejected if either (or both) $(m_{J/\Psi} - 0.25\text{ GeV}) < m_{ab,cd,ad,cb} < (m_{\Psi(2S)} + 0.30\text{ GeV})$, $(m_{\Upsilon(1S)} - 0.70\text{ GeV}) < m_{ab,cd,ad,cb} < (m_{\Upsilon(3S)} + 0.75\text{ GeV})$.

- Medium SR: This is a requirement on the compatibility of the di-lepton invariant masses. In the previous iteration (Run 2 search) it was defined as $m_{34}/m_{12} > 0.85$ for HM and LM channels. This cut is optimized for HM in the full Run 2 iteration and used also for AS channel. The optimized cut is defined as $m_{cd} > 0.85m_{ab} - 0.075f(m_{ab})m_{ab}$, where $f(m_{ab})$ is a modulating function with constants, it's derivation is discussed in Appendix A.2.

- Tight SR cut: It is applied on the kinematic variable $E'_{ab}/m_{4\ell}$ in both SR1 and SR2.

Table 8.2 summarizes the event selection of the AS channel. Table 8.3 gives the cut-flow selection in SR1 and SR2, for the mass points $((m_{Zd}, m_S) = (70, 250)$ and $((m_{Zd}, m_S) = (35, 80)$ GeV , and their efficiencies respectively.

	cuts	SR1	SR2
Baseline Electrons	p_T	> 7 GeV	same
	η	$\lvert\eta\rvert < 2.47$	same
	ID	Silicon and Pixel Hits requirements of LooseLH working point	same
	OQ	Not from a bad cluster	same
	$z_0 \sin\theta$	$< 0.5 mm$	same
Baseline Muons	p_T	> 6GeV (15 GeV if calo-tagged)	same
	η	$\lvert\eta\rvert < 2.7$	same
	ID	Loose	same
	$z_0 \sin\theta$	$< 0.5 mm$	same
	$\lvert d_0\rvert$	$< 1 mm$ if muon is not StandAlone	same
Quadruplet formation	Quadruplet	At least one quadruplet formed from two SFOS dilepton pairs.	same
Quadruplet Selection	Overlap removal	No overlap-removed e or μ	same
	p_T	$p_T^1 > 20$ GeV, $p_T^2 > 15$ GeV, $p_T^3 > 10$ GeV	same
	Trigger matched	Leptons in quadruplet responsible for firing at least one trigger	same
	ΔR	> 0.1 between same-flavor leptons, > 0.2 between different-flavor	same
	Muon Quality	Number of StandAlone or CaloTagged$\mu < 2$	same
Quadruplet Ranking	Minimal Δm	Select quadruplet with smallest $\Delta m = \lvert m_{ab} - m_{cd}\rvert$	same
Event Selection	Electron ID	All e in quadruplet pass LooseLH working point	same
	Isolation	All leptons in quadruplet pass FixedCutLoose working point	
	Impact Parameter	$\lvert d_0^{BL} Sig.\rvert < 5(3)$ for $e(\mu)$ in quadruplet	same
	Quarkonia Veto	$(m_{J/\psi} - 0.25GeV) < m_{ab}, m_{cd}, m_{ad}, m_{cb} < (m_{\psi(2S)} + 0.30GeV)$ or, $(m_{\Upsilon/(1S)} - 0.70GeV) < m_{ab}, m_{cd}, m_{ad}, m_{cb} < (m_{\Upsilon(3S)} + 0.75$ GeV$)$	same
	LowMass Veto	$(m_{ab}, m_{cd}, m_{ad}, m_{cb}) > 5$ GeV	same
	ZVeto	m_{ab} and $m_{cd} \notin [83.2, 99.2]$ GeV, m_{ad} and $m_{cb} \notin [87.2, 95.2]$ GeV	$m_{ab} \notin [50, 106]$ GeV
	LooseSR	$(m_{ab}, m_{cd}) > 10\, GeV$	same
	H Veto	$m_{4\ell} > 130$GeV	$m_{4\ell} < 115$ GeV
	MediumSR	new SR	same
	TightSR	$\lvert E'_{ab}/M_{4l} - 0.5\rvert < 0.008$	same

TABLE 8.2: Summary of the event selection of SR1 and SR2 for the AS search.

Systematic	$(m_{Zd}, m_S) = (70, 250)$ GeV		$(m_{Zd}, m_S) = (35, 80)$ GeV	
	all channel	efficiency (%)	all channel	efficiency (%)
All	50000.00	100.00	50000.00	100.00
Pre_OverlapEvent	50000.00	100.00	50000.00	100.00
Pre_Cleaning	50000.00	100.00	50000.00	100.00
Pre_PrimaryVertex	50000.00	100.00	50000.00	100.00
Pre_Trigger	49079.27	98.16	32231.09	64.46
SFOS	33385.49	66.77	18774.15	37.55
NotOverlaps	33368.56	66.74	18768.65	37.54
Kinematic	33157.24	66.31	15841.53	31.68
TriggerMatched	33146.95	66.29	15816.81	31.63
DeltaR	32830.58	65.66	15366.09	30.73
MuQuality	32809.54	65.62	15360.08	30.72
Isolation	25804.63	51.61	10717.87	21.44
ElectronID	22940.71	45.88	9277.09	18.55
ImpactParameter	22526.83	45.05	9017.44	18.03
QVeto	22508.92	45.02	8652.09	17.3
LowMassVeto	22506.36	45.01	8579.16	17.16
HWinHM	22504.43	45.01	8579.16	17.16
ZVeto	20831.63	41.66	8579.16	17.16
LooseSR	20831.63	41.66	8576.15	17.15
MediumSR	20103.65	40.21	8342.28	16.68
TightSR	19409.33	38.82	5757.81	11.52

TABLE 8.3: Cut-flow two in SR1 and SR2 for the mass points $((m_{Zd}, m_S) = (70, 250)$ and $((m_{Zd}, m_S) = (35, 80)$ GeV , and their efficiencies respectively.

8.3 Monte Carlo simulation

8.3.1 Background and signal simulation

The background processes considered consist of:

$\mathbf{ZZ^* \to 4\ell}$: The non-resonant SM $ZZ \to 4\ell$ process is the main background of the additional scalar channel.

$\mathbf{H \to ZZ^* \to 4\ell}$: The Higgs boson production through ggF (Hamilton et al., 2013), vector-boson fusion (VBF) (Nason and Oleari, 2010), and in association with a vector boson (VH) (Luisoni et al., 2013), became a sub-dominant background in the AS channel, by requiring $m_{4\ell} > 130$ GeV or $m_{4\ell} < 115$ GeV in SR1 and SR2 respectively.

$\mathbf{VVV, t\bar{t} + V}$: The triboson backgrounds ZZZ, WZZ, and WWZ with four or more leptons originating from the hard scatter.

Reducible background: Processes like $Z + jets$, $t\bar{t}$ and WZ, produce less than four prompt leptons but can contribute to the selection through jets misidentified as leptons.

The simulation and modeling of the backgrounds are the same as our previous analysis (The ATLAS collaboration et al., 2018), with some updated softwares and the extensions to new campaigns.

For the signal simulation, samples of events with $S \to Z_d Z_d \to 4\ell$, are produced in the gluon–gluon fusion mode (ggF), using the Hidden Abelian Higgs Model (HAHM) (Wells, 2008; Gopalakrishna, Jung, and Wells, 2008). The event generator MADGRAPH5_AM@NLO v2.2.3 (Alwall et al., 2014) with the NNPDF23 (Ball et al., 2013) parton distribution functions (PDFs) at leading order (LO) is used. PYTHIA8 (Mrenna and Skands, 2008) (v8.170) with the A14 parameter set (ATLAS Collaboration et al., 2014) was used for the modeling of the parton shower, harmonization and underlying event. Ten samples were generated in the signal region 1 ($m_{4\ell} > 130$ GeV) and 8 in the signal region 2 (($m_{4\ell} < 115$ GeV)) with different Z_d and S hypothetical masses as shown in Table 8.4. The model parameters ϵ and κ were adjusted so that only $S \to Z_d Z_d \to 4\ell$ decays were generated ($\kappa \gg \epsilon$). The samples were normalized using the SM Higgs boson production cross-section $\sigma_{SM}(ggF) = 48.58$ pb and the $\mathcal{BR}(H \to ZZ^* \to 4\ell)= 1.25 \times 10^{-4}$ taken from the reference (Andersen, 2013), as this branching ratio corresponds approximately to the upper limit set in this reference (Aad et al., 2015b). The width of the dark Higgs is computed with respect to the dark Higgs mass (m_S) as reported in the reference (Contino et al., 2014) and shown in Figure 8.2.

S mass (GeV)	Z_d mass (GeV)	S width (GeV)
	SR1	
175	20	0.5
175	50	0.5
250	70	4.05
250	70	0.41e−2
325	80	11.46
400	50	29.16
400	100	29.16
750	65	246.0
750	150	246.0
800	250	302.1
	SR2	
30	15	0.86×10^{-3}
40	15	0.11×10^{-2}
50	20	0.13×10^{-2}
60	25	0.15×10^{-2}
70	30	0.18×10^{-2}
80	35	0.20×10^{-2}
90	40	0.22×10^{-2}
100	45	0.25×10^{-2}

TABLE 8.4: Signal samples generated for the AS channel, with variation of the dark Higgs mass (m_S) , the dark vector boson mass (m_{Z_d}) and the dark Higgs width (Γ) with respect to the dark Higgs mass (m_S).

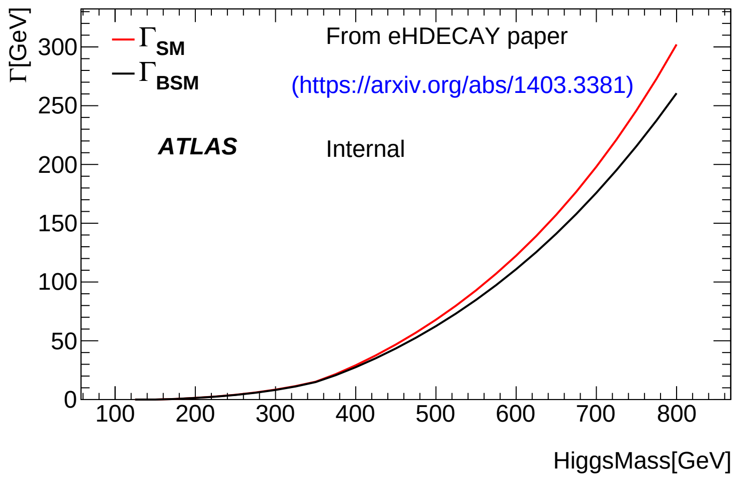

FIGURE 8.2: Width of dark Higgs mass (m_S) w.r.t to m_S. This plot is produced using the code available in (Contino et al., 2014)

8.4 Background estimation

8.4.1 Estimation of irreducible backgrounds

A validation region is an acceptance window orthogonal to the signal region, where data and Monte Carlo (MC) can be plotted in order to assess the MC simulation based on their agreement. One validation region named (VR1) is used which is defined by inverting the "medium SR" $m_{cd} > 0.85 m_{ab} - 0.075 f(m_{ab}) m_{ab}$ cut and the Higgs window cut ($115 < m_{4l} < 130$ GeV). The average di-lepton mass distribution $m_{\ell\ell} = \frac{m_{ab}+m_{cd}}{2}$ in VR1 is shown in Figure 8.3 for the three final states and all final states combined, all MC campaigns are also considered (mc16a, mc16d and mc16e). The Monte Carlo campaigns are defined by their different integrated luminosities. For instance, mc16a, mc16d and mc16e campaigns corresponds to an integrated luminosity of 36.1, 44.3 and 59.9 fb^{-1}. Their numbers of events also may be different. The yields of VR1 are tabulated in Table 8.5. The VR1 shows a good agreement between MC and data.

Campaign	Luminosity (fb^{-1})	VR1	
		Expected	Observed
2015-6 (mc16a)	36.2	132.7 ± 1.3	125 ± 12
2017 (mc16d)	43.3	144.2 ± 0.9	144 ± 13
2018 (mc16e)	59.9	196.9 ± 1.5	193 ± 15
2015-8	140	473.8 ± 2.2	462 ± 23

TABLE 8.5: The total expected and the total observed number of events in the validation regions. The uncertainties on the total expected number of events include only MC-statistical components. The predictions do not include Z+jets, because of the unreliability of the MC prediction (negative event yields).

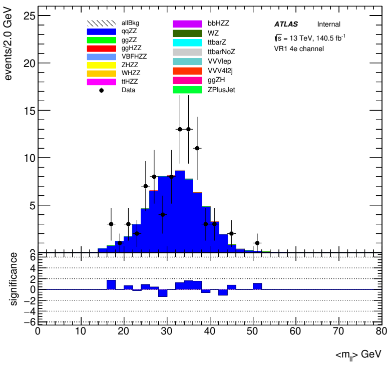

(A) $4e$

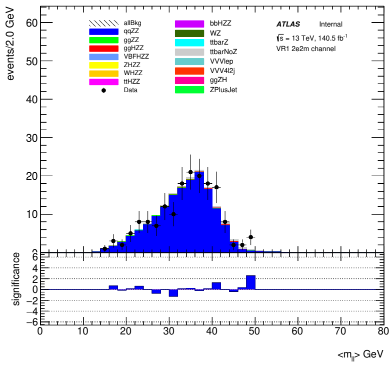

(B) $2e2\mu$

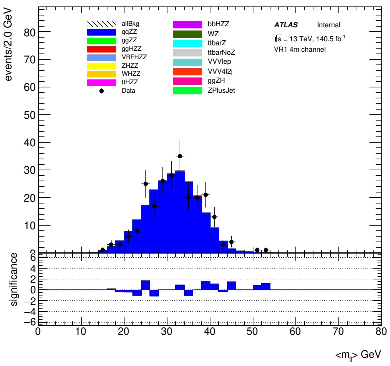

(C) $4m$

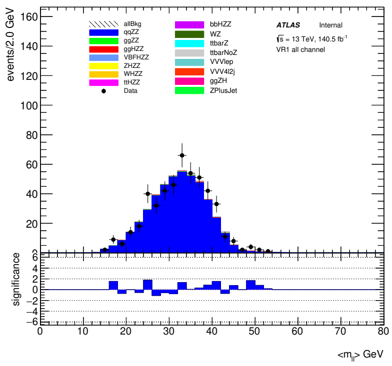

(D) all

FIGURE 8.3: The average di-lepton mass distribution $m_{\ell\ell} = \frac{m_{ab}+m_{cd}}{2}$ in VR1 is shown in Figure 8.3 for the three final states and all final states combined, all MC campaigns are also considered (mc16a, mc16d and mc16e). .

8.4.2 Estimation of reducible backgrounds

In this section the ABCD method used to estimate the $t\bar{t}$ and the Z+ jets backgrounds is discussed. To carry out the ABCD method we use the isolation and the impact parameters as discriminating variables, since they are the most uncorrelated variables compared to others. From the two variables four regions A, B, C and D are defined in quadrants in the 2D space. For the $t\bar{t}$ case, the cuts on the discriminating variables are applied on the two least p_T leptons while the leading and sub-leading leptons are supposed to always pass the cuts. The regions are defined as follows:

- Region A: all leptons in the quadruplet pass the isolation cut and the impact parameter cut;
- Region B: the two least p_T leptons in the quadruplet pass the isolation cut and at least one of them fails the impact parameter cut;
- Region C: the two least p_T leptons in the quadruplet pass the impact parameter cut and at least one of them fails the isolation cut;
- Region D: at least one of the two least p_T leptons fails the isolation cut and the impact parameter cut.

For Z + Jets case, the cuts are applied on the di-lepton which has its mass more distant from the Z mass while the two other leptons are supposed to always pass the cuts. The regions are defined as follows:

- Region A: all leptons in the quadruplet pass the isolation cut and the impact parameter cut;
- Region B: the di-lepton which has its mass more distant from the Z mass pass the isolation cut and at least one of them fails the impact parameter cut;
- Region C: the di-lepton which has its mass more distant from the Z mass pass the impact parameter cut and at least one of them fails the isolation cut;
- Region D: at least one of the di-lepton which has its mass more distant from the Z mass fails the isolation cut and the impact parameter cut.

Figure 8.4 shows graphically the four regions A, B, C and D. As required by the ABCD method these two variables are supposed to be uncorrelated which we have checked *a* priori by computing the correlation coefficient r from the variables as defined by Equation 8.2

$$r = \frac{A \times D - B \times C}{\sqrt{(A+C) \times (B+D) \times (A+B) \times (C+D)}} \tag{8.2}$$

The result of the correlation coefficient r is shown in Table 8.6, where we observe for the 4e and 2e2μ channels the two test variables are nearly uncorrelated. However, there is a higher correlation for the 4μ channel. As in Run 1 the correlation coefficient will be taken into account as a systematic error in the final results. In order to have enough statistics, the study is done at the level of the quarkonia veto cut, also electron ID cut is not applied. The steps of the method are as follows:

- All the background contributions are considered except X_{bkg}, where X_{bkg} is the background we want to estimate, either $t\bar{t}$ or Z + Jets in our case, then we count the events in region B_{bkg}, C_{bkg} and D_{bkg}.

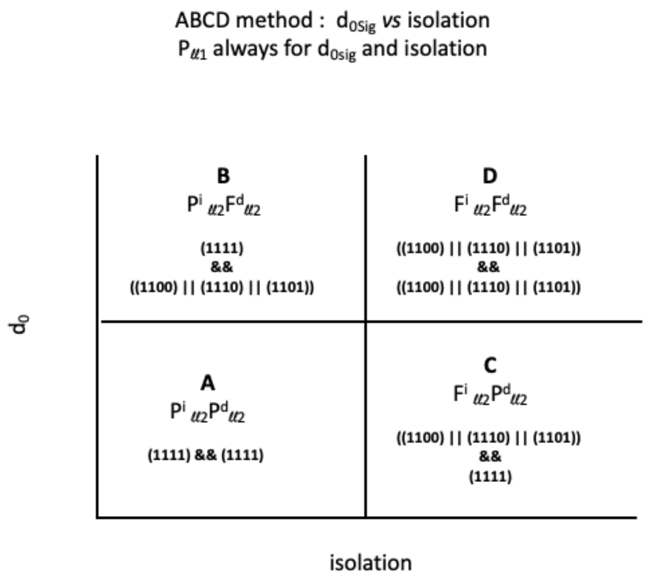

FIGURE 8.4: The A, B, C, D regions defined by specific regions in the 2D plane of the two discriminating variables; the impact parameter d^0 (in the Y axis) and the isolation variable (on the X axis).

TABLE 8.6: The correlation coefficient for the isolation and the impact parameter variables of the different channels, 4e, 2e2μ, 4μ for data1516 and data17

Corr Coef (r) at Q Veto level	data1516			data17		
	$4e$	$2e2\mu$	4μ	$4e$	$2e2\mu$	4μ
r	0.02	0.02	0.58	0.02	0.02	0.59

- We consider the data and count the events in B_{data}, C_{data} and D_{data}.
- We subtract data from background region by region: $(B_{data} - B_{bkg})$, $(C_{data} - C_{bkg})$, $(D_{data} - D_{bkg})$.
- X_{bkg} in the signal region A is estimated as: $\epsilon \times \frac{(B_{data}-B_{bkg})\times(C_{data}-C_{bkg})}{(D_{data}-D_{bkg})}$ where ϵ is the efficiency of the remaining cuts.

Tables 8.7 and 8.8 show the results of each step and the estimated $t\bar{t}$ and $Z+$jets backgrounds for the HM and also the AS channels, where 2015-16-17 data are used. The 2018 data is not considered since the ABCD method required the data to be unblinded (through the calculation of ϵ) which is not the case yet for 2018 data. As expected, these backgrounds are negligible.

Yields data	2015–16 data			2017 data		
	$4e$	$2e2\mu$	4μ	$4e$	$2e2\mu$	4μ
A	4144	5475	720	4728	6459	817
B	374	548	66	415	673	64
C	388373	449204	567	456758	532380	652
D	60527	81798	1515	71218	98821	1850
Yields bkg without $t\bar{t}$	mc16a			mc16d		
A	3803.38	4805.01	535.015	4898.73	6236.65	627.53
B	284.44	331.91	46.27	369.85	456.94	60.24
C	331567	379154	322.17	480865	557488	407.15
D	30111.8	34514.1	598.31	44644.9	52338	908.39
(data)−(bkg without $t\bar{t}$)	(data)−(mc16a)			(data)−(mc16d)		
A	340.62	669.99	184.99	-170.73	222.35	189.47
B	89.56	216.09	19.72	45.15	216.06	3.76
C	56805.8	70050.3	244.83	-24107.3	-25107.7	244.86
D	30415.2	47283.9	916.69	26573.1	46483	941.61
–	AS (SR1)			AS (SR1)		
efficiency (ϵ)	$(9.29 \pm 3.52) \times 10^{-6}$	$(2.40 \pm 0.31) \times 10^{-5}$	0.03 ± 0.00	$(1.50 \pm 0.41) \times 10^{-5}$	$(3.10 \pm 0.31) \times 10^{-5}$	0.03 ± 0.00
$t\bar{t}$ estimates	0.00 ± 0.00	0.01 ± 0.00	0.16 ± 0.13	0.00 ± 0.00	0.00 ± 0.00	0.03 ± 0.11
Estimates including systematics	0.00 ± 0.01	0.00 ± 0.00	0.16 ± 0.13	0.00 ± 0.00	0.00 ± 0.00	0.03 ± 0.13
–	AS (SR2)			AS (SR2)		
efficiency (ϵ)	$(2.65 \pm 1.88) \times 10^{-6}$	$(1.56 \pm 0.24) \times 10^{-5}$	0.02 ± 0.00	$(6.96 \pm 2.84) \times 10^{-6}$	$(1.78 \pm 0.24) \times 10^{-5}$	0.03 ± 0.00
$t\bar{t}$ estimates	0.00 ± 0.00	0.00 ± 0.00	0.11 ± 0.09	0.00 ± 0.00	0.00 ± 0.00	0.02 ± 0.08
Estimates including systematics	0.00 ± 0.00	0.00 ± 0.00	0.11 ± 0.10	0.00 ± 0.00	0.00 ± 0.00	0.02 ± 0.09
–	HM			HM		
efficiency (ϵ)	$(2.66 \pm 1.88) \times 10^{-6}$	$(1.15 \pm 0.21) \times 10^{-5}$	0.01 ± 0.00	$(1.16 \pm 1.16) \times 10^{-6}$	$(1.39 \pm 0.21) \times 10^{-5}$	0.01 ± 0.01
$t\bar{t}$ estimates	0.00 ± 0.00	0.00 ± 0.00	0.04 ± 0.04	0.00 ± 0.00	0.00 ± 0.00	0.01 ± 0.03
Estimates including systematics	0.00 ± 0.00	0.00 ± 0.00	0.04 ± 0.06	0.00 ± 0.00	0.00 ± 0.00	0.01 ± 0.02

TABLE 8.7: Estimation of the $t\bar{t}$ background in HM and AS search for the 2015–16 data (with mc16a MC) and the 2017 data (with mc16d MC), by channel.

Yields data	2015–16 data			2017 data		
	$4e$	$2e2\mu$	4μ	$4e$	$2e2\mu$	4μ
A	4144	5471	720	4728	6435	817
B	314	616	48	356	747	48
C	388373	449430	567	456758	532637	652
D	40634	65440	865	47790	78757	1034
Yields bkg without $Z+$jets	mc16a			mc16d		
A	492.50	1013.92	537.35	577.6	1185.12	619.36
B	51.92	102.675	19.14	61.63	109.31	22.28
C	36011.5	38902.9	227.41	41431.5	46012.8	297.97
D	14537.1	22026.2	399.98	16726.4	26037	481.45
(data)−(bkg without $Z+$jets)	(data)−(mc16a)			(data)−(mc16d)		
A	3651.5	4457.08	182.65	4150.4	5249.88	197.64
B	262.08	513.33	28.86	294.37	637.69	25.72
C	352361	410527	339.59	415326	486624	354.04
D	26096.9	43413.8	465.02	31063.6	52720	552.55
–	AS (SR1)			AS (SR1)		
efficiency (ϵ)	$(9.29 \pm 3.52) \times 10^{-6}$	$(2.41 \pm 0.30) \times 10^{-5}$	0.03 ± 0.00	$(1.51 \pm 0.42) \times 10^{-5}$	$(3.10 \pm 0.32) \times 10^{-5}$	0.03 ± 0.00
Z+ jets estimates	0.03 ± 0.01	0.12 ± 0.02	0.63 ± 0.33	0.06 ± 0.02	0.18 ± 0.03	0.55 ± 0.31
Estimates including systematics	0.03 ± 0.01	0.12 ± 0.02	0.63 ± 0.37	0.06 ± 0.02	0.18 ± 0.03	0.55 ± 0.35
–	AS (SR2)			AS (SR2)		
efficiency ϵ	$(2.65 \pm 0.19) \times 10^{-6}$	$(1.56 \pm 0.24) \times 10^{-5}$	0.02 ± 0.00	$(6.96 \pm 2.85) \times 10^{-6}$	$(1.78 \pm 0.24) \times 10^{-5}$	0.03 ± 0.00
Z+ jets estimates	0.01 ± 0.01	0.08 ± 0.02	0.44 ± 0.24	0.03 ± 0.01	0.10 ± 0.02	0.41 ± 0.23
Estimates including systematics	0.01 ± 0.01	0.08 ± 0.02	0.44 ± 0.28	0.03 ± 0.01	0.10 ± 0.02	0.41 ± 0.26
–	HM			HM		
efficiency (ϵ)	$(2.66 \pm 1.88) \times 10^{-6}$	$(1.15 \pm 0.21) \times 10^{-5}$	0.01 ± 0.00	$(1.16 \pm 1.16) \times 10^{-6}$	$(1.39 \pm 0.21) \times 10^{-5}$	0.01 ± 0.01
Z+jets estimates	0.01 ± 0.01	0.06 ± 0.01	0.18 ± 0.11	0.00 ± 0.00	0.08 ± 0.02	0.11 ± 0.07
Estimates including systematics	0.01 ± 0.01	0.06 ± 0.01	0.18 ± 0.13	0.00 ± 0.00	0.08 ± 0.02	0.11 ± 0.08

TABLE 8.8: Estimation of the $Z+$jets background in HM and AS search for the 2015–16 data (with mc16a MC) and the 2017 data (with mc16d MC), by channel.

8.5 Systematics uncertainties

The systematic uncertainties play an important role in the high energy physics measurement. They are related to the experiment itself, the calibration and also the theory or model used by the experimenter.

8.5.1 Experimental systematic uncertainties

The experimental systematics are mostly scale factors used to correct MC simulation with respect to the data. For electrons and muons the uncertainties that are considered are on the following quantities:

- Quantities related to the reconstruction and isolation of leptons;
- The kinematic smearing parameter: it is used to simulate detector resolution for MC samples by pseudorandomly modifying the kinematics of the object according to assumed process.
- The calibration coefficients: they are transfer factors from detector raw hit value to energy in the case of electrons and momentum in the case of muons.
- `The luminosity`: the preliminary uncertainty of the integrated luminosity on the combined 2015+2016 is ~ 3.2 % . It is derived following a methodology similar to that detailed in (ATLAS Collaboration, 2019), from a preliminary calibration of the luminosity scale using x-y beam-separation scans performed in August 2015 and May 2016. This uncertainty is applied on all the processes modeled with MC simulations.
- `The pileup reweighting` factor: this uncertainty covers the discrepancy seen between the predicted and the measured inelastic cross-section in the fiducial volume defined by $M_X > 13$ GeV, where M_X is the mass of the non-diffractive hadronic system. The Monte Carlo modeling of the various physics processes involves some parametrization, and these are optimized in a process known as tuning. A discrepancy arises because of mismodeling of the central activity by the Monte Carlo tune (Siegert, 2011), so it can be incorporated into the analysis as an uncertainty on the signal strength $< \mu >$ that a given MC event corresponds to.

8.5.2 Theoretical systematic uncerainties

The theoretical systematics uncertainties for the signal are taken from the ATLAS yellow report, and consist of the quantum chromodynamic (QCD) and the Parton Distribution Function (PDF) uncertainties. The gluon-gluon fusion processes are considered depending on the signal mass point. The QCD and PDF uncertainties for ZZ^* background are taken from this reference (Aaboud et al., 2018a). Table 8.9 reports the highest QCD and PDF uncertainties for signals and ZZ^* background which is the main background for the additional scalar channel.

The relative systematics uncertainties on the signals are given in Table 8.10 and 8.11 for SR1 and SR2 respectively. The mass points considered for SR1 are $(m_{Zd}, m_S) = (20, 175), (70, 250), (150, 750)$ GeV and the ones for SR2 are $(m_{Zd}, m_S) = (35, 90), (40, 90), (45, 100)$. Tables 8.12 and 8.13 correspond to the relative systematics uncertainties of the $ZZ* \rightarrow 4l$ for both SR1 and SR2 respectively. The convention used is: in cases where the UP and DOWN variations

QCD and PDF uncertainties		
	QCD (%)	**PDF (%)**
Signal	$^{+18.5}_{-15.6}$	± 4.2
ZZ^*	$^{+5.2}_{-4.7}$	$^{+2.7}_{-1.7}$

TABLE 8.9: Highest QCD and PDF uncertainties of signals and our main background ZZ^*.

Systematic	$(m_{Zd}, m_S) = (20, 175)$ GeV			$(m_{Zd}, m_S) = (70, 250)$ GeV			$(m_{Zd}, m_S) = (150, 750)$ GeV		
	$4e$	$2e2\mu$	4μ	$4e$	$2e2\mu$	4μ	$4e$	$2e2\mu$	4μ
EG_RESOLUTION_ALL	$^{+0.32}_{0.00}$	$^{+0.07}_{-0.01}$	$^{0.00}_{+0.12}$	$^{-0.16}_{+0.23}$	$^{-0.40}_{0.00}$	$^{0.00}_{-0.06}$	$^{-1.02}_{+0.98}$	$^{-0.07}_{+0.04}$	$^{0.00}_{-0.04}$
EG_SCALE_AF2	–	–	–	–	–	–	–	–	–
EG_SCALE_ALL	$^{+0.38}_{-0.54}$	± 0.15	$^{0.00}_{+0.06}$	$^{-0.44}_{+0.43}$	$^{+0.00}_{-0.16}$	$^{-0.02}_{+0.00}$	$^{-0.23}_{+0.292}$	$^{-0.24}_{+0.25}$	0.00
EL_EFF_ID_TOTAL_1NPCOR_PLUS_UNCOR	$^{+13.8}_{-12.7}$	$^{+6.27}_{-6.14}$	–	$^{+8.39}_{-7.93}$	$^{+4.05}_{-3.99}$	–	$^{+6.57}_{-6.25}$	$^{+3.25}_{-3.2}$	–
EL_EFF_Iso_TOTAL_1NPCOR_PLUS_UNCOR	$^{+0.95}_{-0.94}$	± 0.42	–	± 0.55	± 0.27	–	$^{+5.12}_{-4.92}$	$^{+2.47}_{-2.44}$	–
EL_EFF_Reco_TOTAL_1NPCOR_PLUS_UNCOR	$^{+2.03}_{-2.}$	± 0.92	–	$^{+1.19}_{-1.18}$	± 0.59	–	$^{+0.77}_{-0.76}$	± 0.39	–
MUONS_ID	–	$^{+0.04}_{-0.00}$	$^{0.00}_{+0.23}$	–	$^{-0.12}_{+0.04}$	$^{-0.03}_{+0.08}$	–	$^{-0.17}_{+0.22}$	$^{-0.32}_{+0.40}$
MUONS_MS	–	$^{-0.05}_{+0.03}$	$^{0.00}_{+0.56}$	–	$^{-0.16}_{+0.03}$	$^{-0.06}_{+0.36}$	–	$^{-0.08}_{+0.09}$	$^{-0.19}_{+0.04}$
MUONS_SAGITTA_RESBIAS	–	–	–	–	–	–	–	–	–
MUONS_SAGITTA_RHO	–	–	–	–	–	–	–	–	–
MUONS_SCALE	–	$^{-0.06}_{+0.05}$	$^{-0.00}_{+0.11}$	–	$^{+0.00}_{+0.03}$	$^{-0.02}_{+0.09}$	–	$^{-0.05}_{+0.05}$	$^{0.00}_{+0.08}$
MUON_EFF_ISO_STAT	–	± 0.13	± 0.28	–	± 0.07	± 0.15	–	± 0.06	± 0.13
MUON_EFF_ISO_SYS	–	± 0.52	$^{+1.06}_{-1.05}$	–	± 0.45	$^{+0.92}_{-0.91}$	–	$^{+0.405}_{-0.40}$	± 0.81
MUON_EFF_RECO_STAT	–	± 0.15	± 0.29	–	± 0.17	± 0.33	–	± 0.17	± 0.33
MUON_EFF_RECO_STAT_LOWPT	–	± 0.06	± 0.12	–	± 0.02	± 0.05	–	–	–
MUON_EFF_RECO_SYS	–	± 0.59	$^{+1.16}_{-1.15}$	–	$^{+0.65}_{-0.64}$	$^{+1.28}_{-1.27}$	–	$^{+1.3}_{-1.28}$	$^{+2.59}_{-2.52}$
MUON_EFF_RECO_SYS_LOWPT	–	± 0.15	± 0.33	–	± 0.06	± 0.13	–	–	± 0.01
MUON_EFF_TTVA_STAT	–	± 0.06	± 0.11	–	± 0.05	± 0.11	–	± 0.05	± 0.1
MUON_EFF_TTVA_SYS	–	± 0.05	± 0.09	–	± 0.03	± 0.07	–	± 0.02	± 0.04
PileupWeight	$^{-1.3}_{+0.66}$	$^{-0.73}_{+0.78}$	$^{-0.35}_{+0.36}$	$^{-0.53}_{+0.49}$	$^{-0.2}_{+0.27}$	$^{-0.41}_{+0.05}$	$^{-0.50}_{+0.38}$	$^{-0.16}_{+0.13}$	$^{-0.54}_{+0.39}$

TABLE 8.10: AS search: Relative systematic uncertainties in percent on the yield for mc16a signal in SR1 for the mass points $(m_{Zd}, m_S) = (20, 175)$, $(70, 250)$, and $(150, 750)$ GeV.

result in uncertainties with different signs, the sign has been preserved, with the uncertainty in the upper (lower) position corresponding to the UP (DOWN) variation. If they are equal in magnitude, one number is shown, with the upper (lower) sign corresponding to the UP (DOWN) variation. In cases where both variations result in uncertainties that are both positive (negative), the larger (smaller) of the two is shown with the sign preserved in the upper (lower) position. The other position is set to zero.

Systematic	$(m_{Zd}, m_S) = (35, 80)$ GeV			$(m_{Zd}, m_S) = (40, 90)$ GeV			$(m_{Zd}, m_S) = (45, 100)$ GeV		
	$4e$	$2e2\mu$	4μ	$4e$	$2e2\mu$	4μ	$4e$	$2e2\mu$	4μ
EG_RESOLUTION_ALL	$^{-1.35}_{+0.06}$	$^{-1.21}_{+0.80}$	$^{+0.03}_{-0.04}$	$^{-2.04}_{+1.32}$	$^{-1.81}_{+0.84}$	$^{+0.07}_{-0.06}$	$^{-1.79}_{+0.48}$	$^{-1.49}_{+0.46}$	$^{-0.05}_{0.00}$
EG_SCALE_AF2	–	–	–	–	–	–	–	–	–
EG_SCALE_ALL	$^{+0.95}_{-0.40}$	$^{0.00}_{-0.44}$	–	$^{0.00}_{-1.14}$	$^{+0.00}_{-0.73}$	$^{-0.04}_{+0.00}$	$^{0.00}_{-0.30}$	$^{0.00}_{-0.58}$	$^{-0.09}_{0.07}$
EL_EFF_ID_TOTAL_1NPCOR_PLUS_UNCOR	$^{+33}_{-26.3}$	$^{+15.5}_{-14.4}$	–	$^{+29.3}_{-24}$	$^{+14.2}_{-13.3}$	–	$^{+27}_{-22.5}$	$^{+12.7}_{-12.1}$	–
EL_EFF_Iso_TOTAL_1NPCOR_PLUS_UNCOR	$^{+1.8}_{-1.78}$	$^{+0.88}_{-0.88}$	–	$^{+1.48}_{-1.47}$	± 0.73	–	$^{+1.18}_{-1.17}$	± 0.54	–
EL_EFF_Reco_TOTAL_1NPCOR_PLUS_UNCOR	$^{+4.67}_{-4.52}$	$^{+2.36}_{-2.34}$	–	$^{+4.1}_{-3.99}$	$^{+2.04}_{-2.03}$	–	$^{+3.52}_{-3.44}$	$^{+1.77}_{-1.76}$	–
MUONS_ID	–	$^{-0.37}_{+0.00}$	$^{-0.97}_{+0.80}$	–	$^{-0.35}_{+0.15}$	$^{-0.97}_{+1.01}$	–	$^{-0.48}_{+0.13}$	$^{-1.21}_{+0.93}$
MUONS_MS	–	$^{-0.87}_{+0.81}$	$^{-2.52}_{+2.31}$	–	$^{-1.02}_{+0.22}$	$^{-2.07}_{+1.59}$	–	$^{-0.91}_{+0.97}$	$^{-2.61}_{+1.85}$
MUONS_SAGITTA_RESBIAS	–	$^{+0.42}_{0.00}$	$^{+1.35}_{0.00}$	–	$^{+0.55}_{0.00}$	$^{0.00}_{1.58}$	–	$^{0.00}_{+0.39}$	$^{0.00}_{+0.28}$
MUONS_SAGITTA_RHO	–	± 0.41	± 1.49	–	± 0.63	± 1.66	–	± 0.11	± 1.52
MUONS_SCALE	–	$^{-0.6}_{+0.38}$	$^{-0.79}_{+0.44}$	–	$^{-0.43}_{0.00}$	$^{0.00}_{+0.26}$	–	$^{-0.71}_{+0.00}$	$^{-0.57}_{+0.30}$
MUON_EFF_ISO_STAT	–	± 0.35	$^{+0.71}_{-0.70}$	–	± 2.99	± 0.58	–	± 0.25	± 0.48
MUON_EFF_ISO_SYS	–	$^{+2.16}_{-2.14}$	$^{+4.41}_{-4.28}$	–	$^{+2.09}_{-2.07}$	$^{+4.1}_{-3.98}$	–	$^{+1.87}_{-1.86}$	$^{+3.7}_{3.61}$
MUON_EFF_RECO_STAT	–	± 0.14	$^{+0.30}_{-0.31}$	–	± 0.16	± 0.33	–	± 0.17	± 0.37
MUON_EFF_RECO_STAT_LOWPT	–	± 0.22	± 0.38	–	± 0.16	± 0.32	–	± 0.11	± 0.24
MUON_EFF_RECO_SYS	–	$^{+0.40}_{-0.38}$	$^{+0.86}_{-0.82}$	–	$^{+0.45}_{-0.42}$	$^{+0.92}_{-0.88}$	–	$^{+0.47}_{-0.46}$	$^{+1.01}_{-0.96}$
MUON_EFF_RECO_SYS_LOWPT	–	± 0.53	± 0.99	–	± 0.40	± 0.78	–	± 0.29	± 0.59
MUON_EFF_TTVA_STAT	–	$^{+0.19}_{-0.21}$	$^{+0.39}_{-0.43}$	–	$^{+0.16}_{-0.18}$	$^{+0.32}_{-0.34}$	–	$^{+0.14}_{-0.15}$	$^{+0.27}_{-0.28}$
MUON_EFF_TTVA_SYS	–	$^{+0.04}_{-0.03}$	$^{+0.08}_{-0.06}$	–	$^{+0.03}_{-0.03}$	$^{+0.06}_{-0.05}$	–	$^{+0.03}_{-0.02}$	$^{+0.06}_{-0.04}$
PileupWeight	$^{-2.88}_{+2.19}$	$^{-0.72}_{+0.61}$	$^{-1.31}_{+1.33}$	$^{-1.75}_{+1.67}$	$^{-1.11}_{+0.96}$	$^{-0.31}_{+0.47}$	$^{-1.87}_{+1.54}$	$^{-0.99}_{+0.84}$	$^{-0.78}_{+0.60}$

TABLE 8.11: AS search: Relative systematic uncertainties in percent on the yield for mc16a signal in SR2 for the mass points $(m_{Zd}, m_S) = (35, 80)$, $(40, 90)$, and $(45, 100)$ GeV.

Systematic	$ZZ^* \to 4\ell$		
	$4e$	$2e2\mu$	4μ
EG_RESOLUTION_ALL	$^{-0.32}_{0}$	$^{-0.25}_{+0.02}$	$^{+0.01}_{-0.00}$
EG_SCALE_AF2	–	–	
EG_SCALE_ALL	$^{+1.59}_{-1.18}$	$^{+1.23}_{-0.82}$	$^{+0.00}_{-0.01}$
EL_EFF_ID_TOTAL_1NPCOR_PLUS_UNCOR	$^{+7.54}_{-7.08}$	$^{+3.73}_{-3.67}$	–
EL_EFF_Iso_TOTAL_1NPCOR_PLUS_UNCOR	$^{+0.813}_{-0.806}$	± 0.39	–
EL_EFF_Reco_TOTAL_1NPCOR_PLUS_UNCOR	$^{+1.8}_{-1.78}$	± 0.89	–
MUONS_ID	–	$^{0.00}_{+0.16}$	$^{-0.04}_{+0.81}$
MUONS_MS	–	± 0.15	± 0.46
MUONS_SAGITTA_RESBIAS	–	–	–
MUONS_SAGITTA_RHO	–	–	–
MUONS_SCALE	–	$^{-0.35}_{+0.60}$	$^{-0.32}_{+0.65}$
MUON_EFF_ISO_STAT	–	± 0.11	± 0.27
MUON_EFF_ISO_SYS	–	± 0.58	$^{+1.2}_{-1.19}$
MUON_EFF_RECO_STAT	–	± 0.18	± 0.35
MUON_EFF_RECO_STAT_LOWPT	–	± 0.04	± 0.09
MUON_EFF_RECO_SYS	–	$^{+0.81}_{-0.81}$	$^{+1.63}_{-1.6}$
MUON_EFF_RECO_SYS_LOWPT	–	± 0.11	± 0.26
MUON_EFF_TTVA_STAT	–	± 0.07	± 0.13
MUON_EFF_TTVA_SYS	–	± 0.05	± 0.11
PileupWeight	$^{-1.1}_{+1.06}$	$^{-0.49}_{+0.45}$	$^{-0.16}_{+0.20}$

TABLE 8.12: AS search: Relative systematic uncertainties in percent on the yield for the $ZZ^* \to 4\ell$ backgrounds in SR1 for mc16a+d+e (2015–8) simulation.

Systematic	$ZZ^* \to 4\ell$		
	$4e$	$2e2\mu$	4μ
EG_RESOLUTION_ALL	$^{+1.71}_{0}$	$^{0}_{-0.64}$	$^{-0.02}_{0.01}$
EG_SCALE_AF2	–	–	
EG_SCALE_ALL	$^{-1.44}_{+0.88}$	$^{-0.56}_{+0.17}$	$^{+0.00}_{-0.01}$
EL_EFF_ID_TOTAL_1NPCOR_PLUS_UNCOR	$^{+16.6}_{-14.3}$	$^{+7.54}_{-7.23}$	–
EL_EFF_Iso_TOTAL_1NPCOR_PLUS_UNCOR	$^{+2.65}_{-2.62}$	± 1.1	–
EL_EFF_Reco_TOTAL_1NPCOR_PLUS_UNCOR	$^{+4.86}_{-4.72}$	± 2.36	–
MUONS_ID	–	$^{0.00}_{+0.18}$	$^{-0.35}_{0.00}$
MUONS_MS	–	± 0.49	± 0.66
MUONS_SAGITTA_RESBIAS	–	–	–
MUONS_SAGITTA_RHO	–	–	–
MUONS_SCALE	–	$^{+0.34}_{-0.01}$	$^{+0.35}_{-0.2}$
MUON_EFF_ISO_STAT	–	± 0.44	± 0.98
MUON_EFF_ISO_SYS	–	± 0.99	$^{+2.02}_{-1.99}$
MUON_EFF_RECO_STAT	–	± 0.13	± 0.24
MUON_EFF_RECO_STAT_LOWPT	–	± 0.2	± 0.38
MUON_EFF_RECO_SYS	–	± 0.60	$^{+1.07}_{-1.06}$
MUON_EFF_RECO_SYS_LOWPT	–	± 0.53	± 1.05
MUON_EFF_TTVA_STAT	–	± 0.08	± 0.16
MUON_EFF_TTVA_SYS	–	± 0.12	± 0.25
PileupWeight	$^{-1.91}_{+1.81}$	$^{-0.89}_{+0.71}$	$^{-0.76}_{+0.57}$

TABLE 8.13: AS search: Relative systematic uncertainties in percent on the yield for the $ZZ^* \to 4\ell$ backgrounds in SR2 for mc16a+d+e (2015–8) simulation.

8.6 Results

8.6.1 Additional Scalar results

Figures 8.6 and 8.7 show the $\langle m_{\ell\ell} \rangle$ distribution in SR1 and SR2 of the AS channel for the full MC campaigns merged. Figures 8.8 and 8.9 show the $m_{4\ell}$ distribution with the distribution of the dark Higgs mass (m_S) superimposed. The signal distributions are normalized using the SM Higgs boson production cross-section. The yields in both SR1 and SR2 of the background are shown in Table 8.14.

In the SR1 only the main background, $ZZ* \to 4\ell$, is significant. The $H \to ZZ* \to 4\ell$ background is reduced by requiring $m_{4\ell} > 130$ GeV. The gap around 91.2 GeV is because of the Z veto cut applied.

In the SR2, $ZZ* \to 4\ell$ is once again the dominant background, the $H \to ZZ* \to 4\ell$ background is suppressed by requiring $m_{4\ell} < 115$ GeV. The cut at 50 GeV corresponds to the Z veto cut, it is applied in order to avoid overlap with the signal region acceptance of the ZX channel. The m_{4l} distribution in SR2 shows also that this region is mostly dominated by the $Z* \to 4\ell$ decay as shown in Figure 8.5, with a peak around 91.2 GeV.

The hypothetical signal mass points in both SR1 and SR2 are well simulated and show peaks around their respective dark vector boson masses (m_{Z_d}) as shown in Figure 8.6 and 8.7 and their respective dark Higgs masses ($m_{4\ell}$) as shown in Figures 8.8 and 8.9. Their widths indicate the performance of the ATLAS detector, as intrinsic resolution, rather than the natural line width for this process which is very narrow.

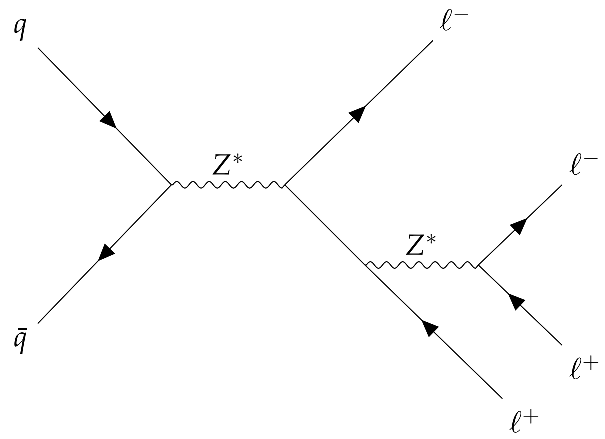

FIGURE 8.5: Feynman diagram of $Z^* \to 4\ell$ decay.

background yields in SR of AS channel, full MC (mc16a+mc16d+mc16e)							
SR1				SR2			
$4e$	$2e2\mu$	4μ	all	$4e$	$2e2\mu$	4μ	all
15.18 $\pm$ 0.35	24.48 $\pm$ 0.40	26.56$\pm$ 0.37	66.22$\pm$ 0.65	8.98 $\pm$ 0.30	5.98 $\pm$ 0.23	25.21$\pm$ 0.41	40.17$\pm$ 0.58

TABLE 8.14: Background yields in SR1 and SR2 of the AS channel with the full MC campaign merged, mc16a+mc16d+mc16e

8.6.2 ZX results

Figure 8.10 shows the m_{34} distribution of the main backgrounds and some hypothetical signal mass points, in the signal region. The data are blinded, all final states are combined and the full MC campaigns are considered (mc16a+mc16d+mc16e). The two main backgrounds ($H \to ZZ^* \to 4\ell$ and $ZZ* \to 4\ell$) show peaks around the Z^* mass [8] as expected. The hypothetical signal mass points are well simulated and show peaks around their respective dark vector boson masses (m_{Z_d}).

8.6.3 High mass results

Figure 8.11 shows the distributions of the average di-lepton mass $\langle m_{\ell\ell}\rangle = \frac{1}{2}(m_{12} + m_{34})$ on a channel-by-channel basis in 2015–8 MC with the unblinded data. The two main backgrounds ($H \to ZZ^* \to 4\ell$ and $ZZ* \to 4\ell$) show peaks around the Z mass as expected. The shift from the Z mass (91.2 GeV) is because by averaging the di-leptons masses a Z^* mass ($<$ 91.2 GeV) and a Z mass ($\sim$ 91.2 GeV) are used. The hypothetical signal mass points are well simulated and show peaks around their respective dark vector boson masses (m_{Z_d}). They were normalized using the SM Higgs boson production cross-section $\sigma_{SM(ggF)}$ = 48.58 pb. The data events observed are 4 in the $4e$ channel, 7 in the 4μ channel and 8 in the 2e2μ channel. Hence, by combining the 3 channels 19 data events are observed where 14 were predicted. In overall, the data are consistent with the MC prediction.

8.6.4 Low mass results

The LM channel results are shown in Figure 8.12 as a function of $\langle m_{\ell\ell}\rangle$. The gaps between 2-4 GeV , and 9-11 correspond to the quarkonia veto cut. Only backgrounds

[8]As a remider m_{34} is the most distant di-lepton mass from the Z boson mass

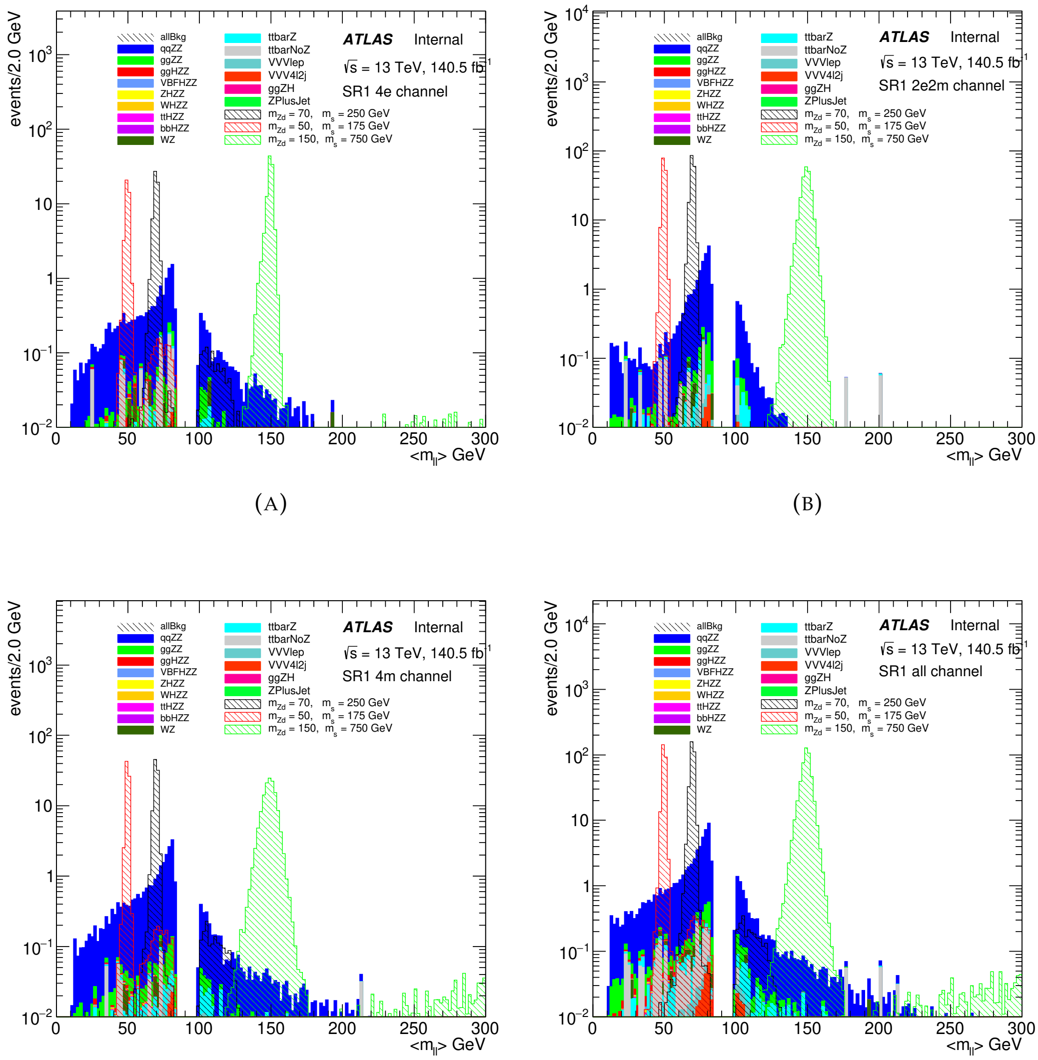

(A) (B) (C) (D)

FIGURE 8.6: a), b), c) and d) are respectively the distributions of the average leading di-lepton mass $\langle m_{\ell\ell} \rangle$ for the $4e$, $2e2\mu$, 4μ, and combined channels in SR1 of the AS channel. The full MC campaigns are merged (mc16a+mc16d+mc16e). The signals are normalized by the gluon-gluon fusion Higgs cross-section.

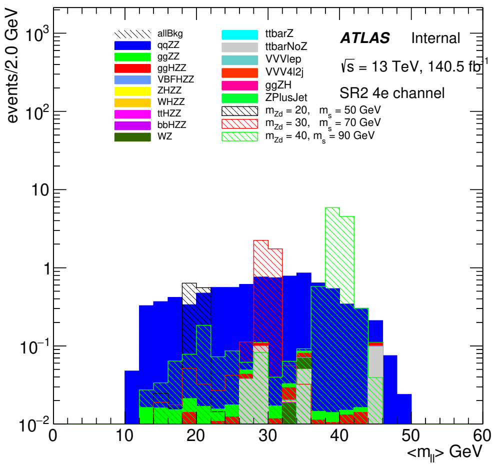

(A)

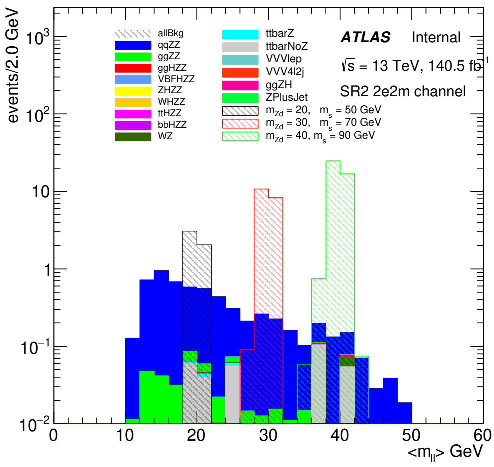

(B)

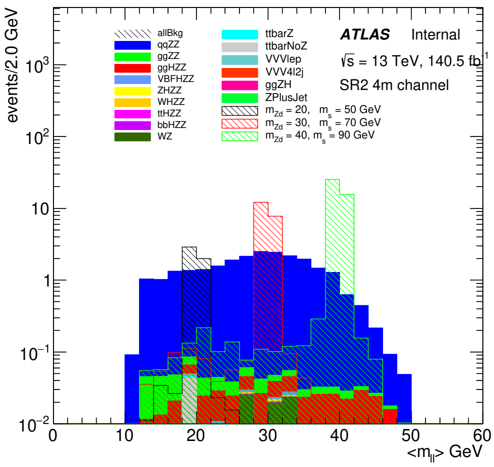

(C)

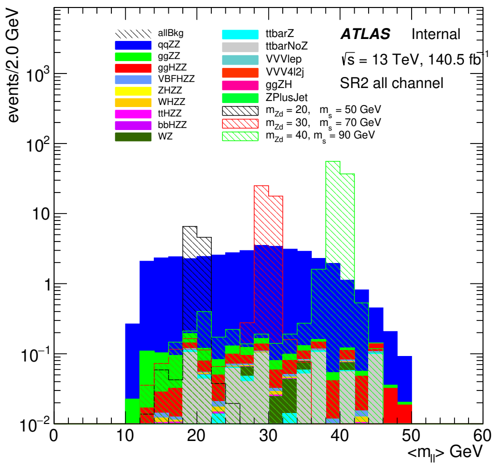

(D)

FIGURE 8.7: a), b), c) and d) are respectively the distributions of the average leading di-lepton mass $\langle m_{\ell\ell} \rangle$ for the $4e$, $2e2\mu$, 4μ, and combined channels in SR2 of the AS channel. The full MC campaigns are merged (mc16a+mc16d+mc16e). The signals are normalized by the gluon-gluon fusion Higgs cross-section.

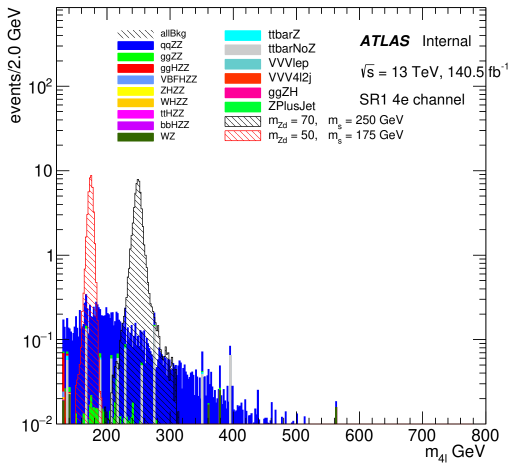

(A)

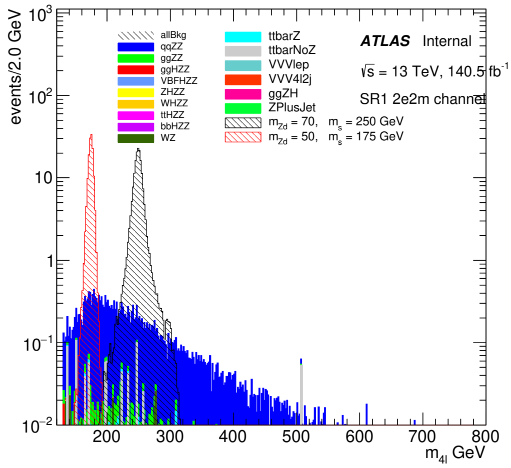

(B)

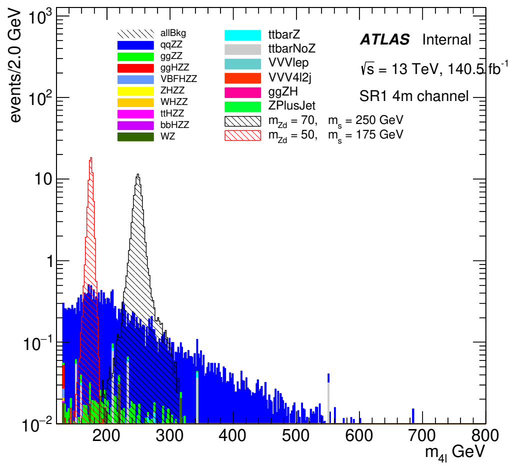

(C)

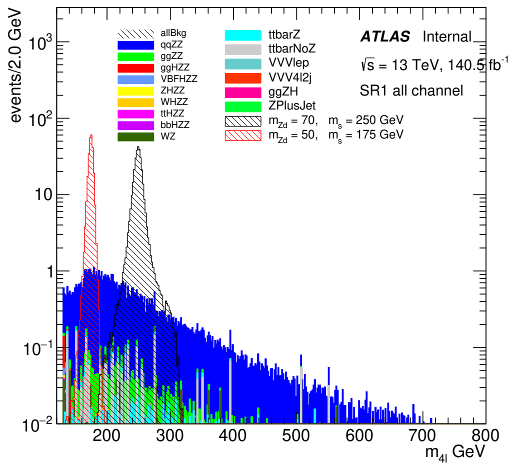

(D)

FIGURE 8.8: a), b), c) and d) are respectively the distributions of the scalar mass m_S $\langle m_{\ell\ell} \rangle$ for the $4e$, $2e2\mu$, 4μ, and combined channels in SR1 of the AS search from full MC merged (mc16a+mc16d+mc16e). The signals are normalized by the gluon-gluon fusion Higgs cross-section.

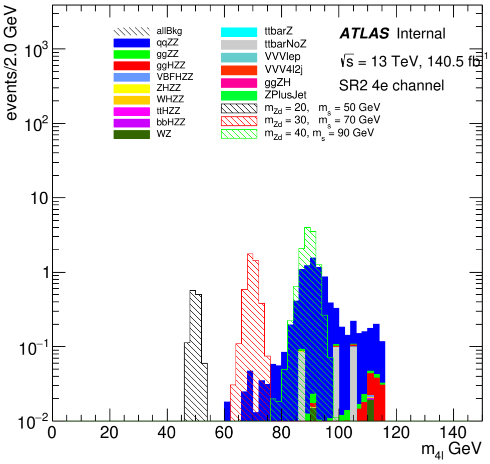

(A)

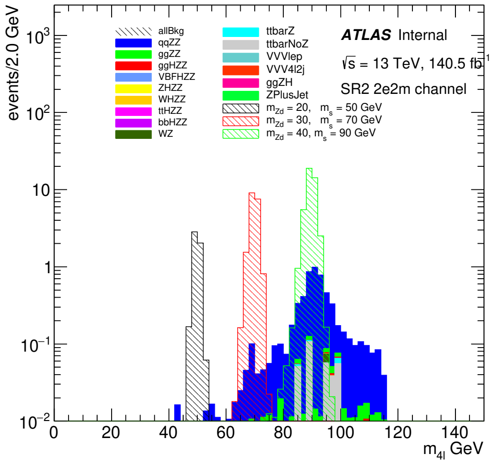

(B)

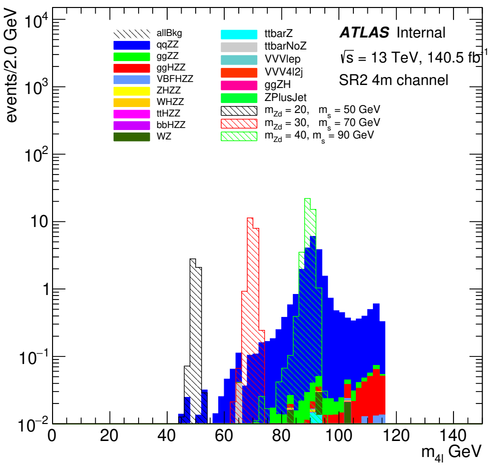

(C)

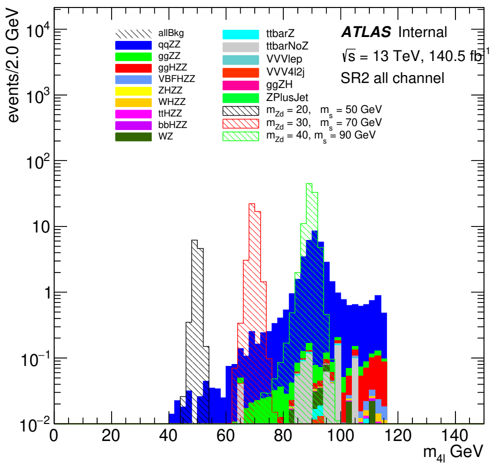

(D)

FIGURE 8.9: a), b), c) and d) are respectively the distributions of the the scalar mass m_S $\langle m_{\ell\ell} \rangle$ for the $4e$, $2e2\mu$, 4μ, and combined channels in SR2 of the AS search from full MC merged (mc16a+mc16d+mc16e). The signals are normalized by the gluon-gluon fusion Higgs cross-section.

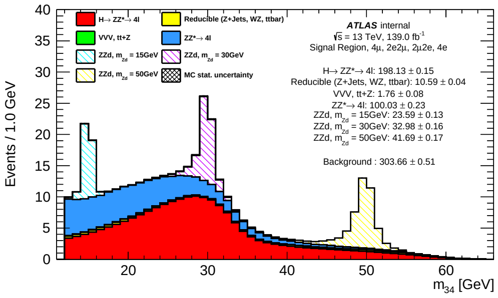

FIGURE 8.10: Expected background m_{34} distribution in the ZX channel signal region with $H \to ZZ_d \to 4\ell$ signal templates. The kinematic variable m_{34} aims to reconstruct m_{Z_d} in the $H \to ZZ_d \to 4\ell$ process, and signal templates are shown for Z_d masses of $m_{Z_d} = 15, 30, 55\,\text{GeV}$. The cross sections of the signal templates here are set to 1 fb.

are shown, the data is blinded. The total expected yields per background category are summarized in Table 8.15. Here, on top of the two main backgrounds ($H \to ZZ* \to 4\ell$ and $ZZ* \to 4\ell$), the heavy flavor background is also quite significant.

Process	Expected yields
$H \to ZZ \to 4\mu$	0.42±0.01
$ZZ \to 4\mu$	1.05±0.02
EWK6 $\to 4\ell + 2X$	0.04±0.00
Fakes	0.29 ± 0.08

TABLE 8.15: The total expected background yields in the low mass signal region for the full Run 2 luminosity.

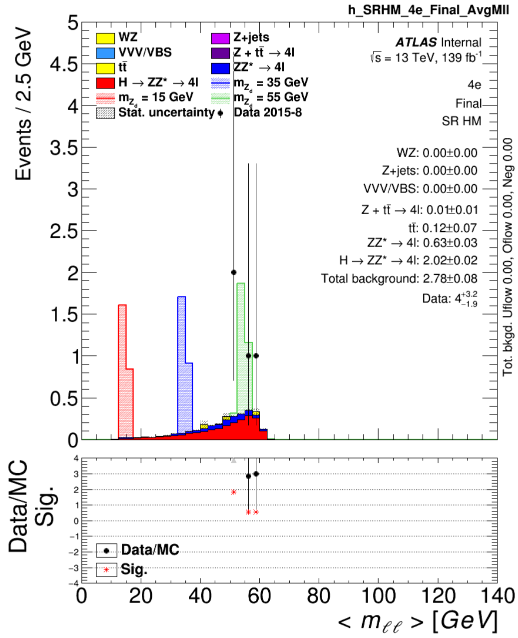

(A) 2015–8 $4e$

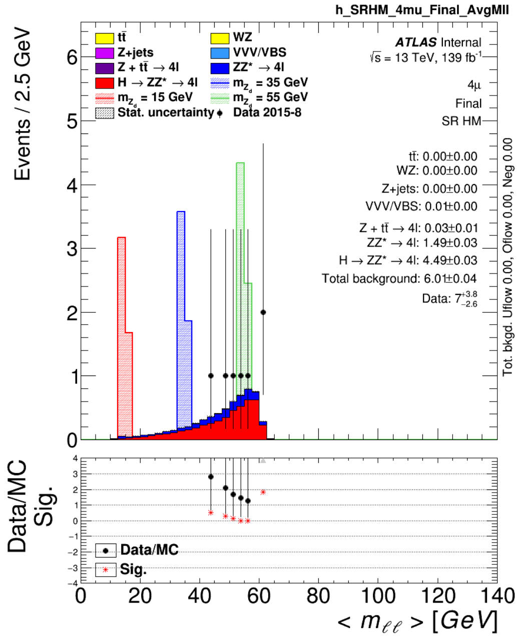

(B) 2015–8 4μ

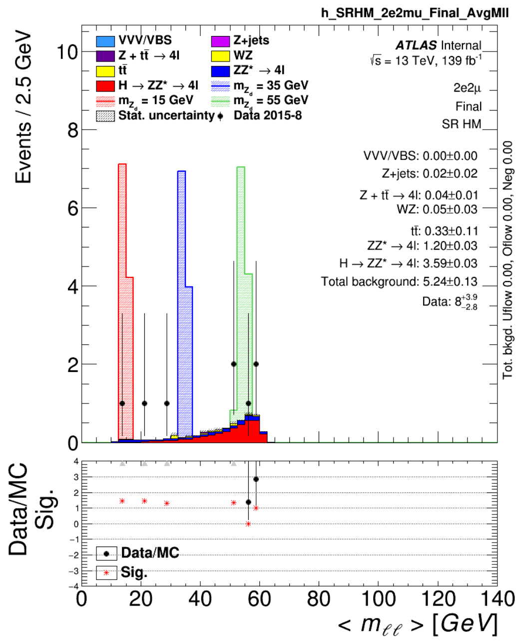

(C) 2015–8 $2e2\mu$

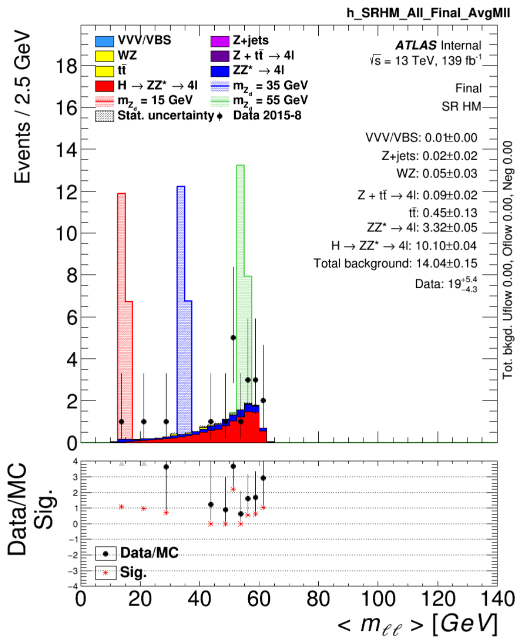

(D) 2015–8 all channels

FIGURE 8.11: HM search: 2015–8 with new Medium SR: distributions of $\langle m_{\ell\ell} \rangle$ in the signal region with the $4e$, 4μ, and $2e2\mu$ channels shown separately and combined. The predictions have been scaled separately to the integrated luminosity of each data-taken campaign and then combined. The total integrated luminosity is 140 fb^{-1}. The example signal distributions correspond to the expected yield normalized with $\sigma(pp \to H \to Z_d Z_d \to 4\ell) = \frac{1}{10}\sigma_{SM}(pp \to H \to ZZ^* \to 4\ell)$.

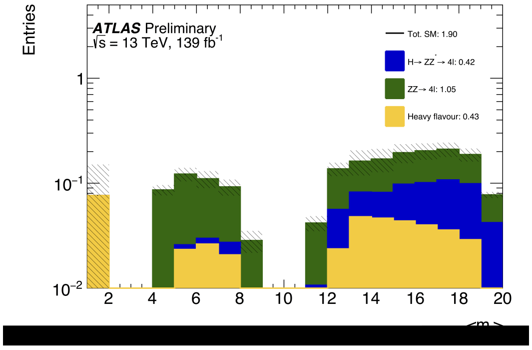

FIGURE 8.12: The total background expectation in low mass signal region as a function of $\langle m_{\ell\ell} \rangle$. The error band includes the systematic uncertainty on the heavy flavour background estimate and the statistical uncertainty.

8.7 Interpretation

8.7.1 Fiducial volume definition

The results of this analysis, in the no-discovery scenario, are to be used to set limits on a cross-section in a fiducial volume defined such that the limit is suitably model-independent. For this analysis, the fiducial volume was defined to mirror the selection applied in the analysis: cuts were added until the corresponding reconstruction efficiency was compatible between the $H \rightarrow Z_d Z_d \rightarrow 4\ell$ and aa signal samples. Unfortunately, it was found necessary to define separate fiducial volumes for the low and high mass selections, in order to obtain the desired model-independence.

The fiducial volume definition is summarized in Table 8.16. This is appropriate for processes of the form $H(125) \rightarrow XX \rightarrow 4\ell$ where X is an on-shell, narrow resonance. The efficiencies are provided in Appendix C.0.2 parameterized by the X boson mass. Fiducial events contain at least four prompt electrons and/or muons. The four-momenta of all prompt photons within $\Delta R = \sqrt{(\Delta\eta)^2 + (\Delta\phi)^2} = 0.1$ of a lepton are added to the four-momentum of the closest lepton. This dressing is done to emulate the effects of quasi-collinear electromagnetic radiation off the charged leptons on their experimental reconstruction in the detector (The ATLAS Collaboration et al., 2015).

8.7.2 Statistical model used for limit setting

Given the wide range of searches conducted in this compound analysis, different statistical methods are constructed to interpret the results according to the two benchmark models mentioned in Chapter 3. Across sub-analyses, the standard approach is performed using the maximum likelihood fit to the yields in the signal regions following the CL_S modified frequentist formalism (Read, 2002) with a profiled likelihood-ratio test statistic (Cowan et al., 2011) is used. Expected signal and background probability distributions are mostly determined from MC predictions or data-driven methods as mentioned in Section 8.4 with the exception of using Gaussian signal modelling instead in the "$H \rightarrow XX$" analyses as described in Appendix C. All nuisance parameters are constrained with Gaussians, except for the statistical uncertainties which use Poisson constraints. The HISTFACTORY

Object	**High-mass fiducial (for $15 < m_X < 60$ GeV)**	**Low-mass fiducial (for $1 < m_X < 15$ GeV)**
Electrons	Dressed with prompt photons within $\Delta R = 0.1$. $pt > 5$ GeV. $\|\eta\| < 2.5$.	
Muons	Dressed with prompt photons within $\Delta R = 0.1$. $pt > 7$ GeV. $\|\eta\| < 2.7$.	
Quadruplet	Three leading-pt leptons satisfy $pt > 20$ GeV, 15 GeV, 10 GeV.	
	Reject event if either of: $(m_{J/\Psi} - 0.25\text{ GeV}) < m_{12,34,14,23} < (m_{\Psi(2S)} + 0.30\ GeV)$, $(m_{\Upsilon(1S)} - 0.70\text{ GeV}) < m_{12,34,14,23} < (m_{\Upsilon(3S)} + 0.75\ GeV)$.	
	$m_{34}/m_{12} > 0.85$	
	$10 < m_{12,34} < 64$ GeV. $\Delta R > 0.1$ (0.2) between all same-flavor (different-flavor) leptons. $5 < m_{32,14} < 75$ GeV if $4e$ or 4μ.	$0.88 < m_{12,34} < 20$ GeV.

TABLE 8.16: Summary of the fiducial definitions used in this analysis, appropriate for processes of the form $H(125) \to XX \to 4\ell$ where X is a promptly-decaying, on-shell, narrow resonance.

(Cranmer et al., 2012) [9] model-building tool is used to construct the model from the input histograms. Experimental systematics are treated as correlated in all samples.

In the case of no significant excess(es) being observed after unblinding the data, 95% CL upper limits are to be set on different parameters of interest. This is the case for instance for the high mass channel which is now unblinded. Firstly, a model-independent fiducial cross section is considered for the "$H \to XX$" as described in Section 8.7.3. Secondly, a model-dependent total cross section is calculated in all the sub-analyses (in the second half of Section 8.7.3), then deduced into limits on BR ($H \to XX/ZX$) and theoretical model parameters (section 8.7.4). Section 8.7.5 describes the $H \to ZX$ specific statistical analysis in which normalizations of signal and background are connected. Section 8.7.6 shows specific differences in the AS channel.

With the same method of model building, one can easily switch to performing discovery tests (for instance, to estimate the local and global p_0-value, one can use the same tools as in the exclusion limit case, the Higgs tool StandardHypoTestInv package or the SUSY tool HISTFITTER).

8.7.3 Fiducial and total cross section limits

Limits on the fiducial cross section for the "$H \to XX$" analysis are computed with the model-independent efficiencies (described in Appendix C.0.2) and Gaussian signal observables (described in Appendix C.0.1). The efficiencies ϵ_c and Gaussian signal shape parameters ($\overline{\langle m_{\ell\ell}\rangle}_c$ and $\sigma^c_{\langle m_{\ell\ell}\rangle}$) are computed for the generated m_{Zd} (m_a) mass points and then linearly interpolated over the considered mass range in

[9] some sub-analyses use HISTFITTER (Baak et al., 2015), which ultimately incorporates HISTFACTORY This two software frameworks are specific tools used by ATLAS for statistical data analysis.

0.5 GeV steps.[10] These efficiencies and shape parameters are used to generate binned histograms (1 GeV bins except for the LM search, which uses 0.1 GeV) according to the final term of Equation (8.3). These histograms and similar ones for the background are the inputs to limit setting. Therefore, an extended likelihood model is constructed in the observable $\langle m_{\ell\ell} \rangle$, where the expectation in each channel as a function of $\langle m_{\ell\ell} \rangle$, $N^c_{\text{exp.}}(\langle m_{\ell\ell} \rangle)$ is given by:

$$N^c_{\text{exp.}}(\langle m_{\ell\ell} \rangle) = N^c_{\text{bkg}} + \sigma^c_{\text{fid}} \times \mathcal{L}\text{umi} \times \epsilon_c \times \text{Gaus}\left(\langle m_{\ell\ell} \rangle, \overline{\langle m_{\ell\ell} \rangle}_c, \sigma^c_{\langle m_{\ell\ell} \rangle}\right). \tag{8.3}$$

where σ^c_{fid} is the parameter of interest. See Appendix C.0.4 for the mathematical derivation.

Given the low number of events, a toy Monte Carlo approach is used for the limit setting in each of the final states, and also for their combination. The expected upper bounds on σ^c_{fid} at 95% confidence level (CL) for the 139 fb^{-1} unblinded data-set are shown in Figure 8.13.

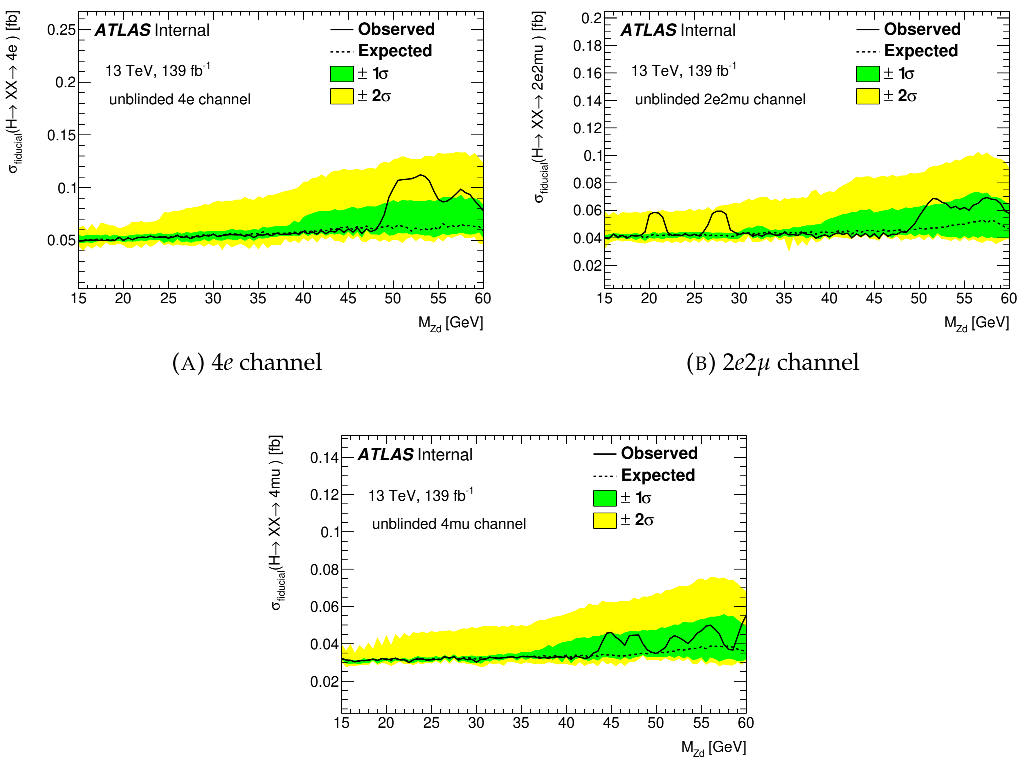

(A) $4e$ channel

(B) $2e2\mu$ channel

(C) 4μ channel

FIGURE 8.13: 95% *CL* upper bounds on the model-independent fiducial cross-sections corresponding to the fiducial phase spaces defined in Table 8.16 (separate phase spaces are defined for m_X above and below 15 GeV).

Figure 8.14 shows the limit on the cross section in the fiducial volume for LM channel with the 139 fb^{-1} dataset (all campaigns with the data blinded). The LM

[10] Moment morphing (Baak et al., 2014) of the reco-level signal distribution was also tested. These distributions from morphing (at every 0.5 GeV in m_{Z_d}) were given directly to the limit setting instead of Gaussians constructed at the same mass points from interpolated Gaussian parameters. Both approaches produce identical limits.

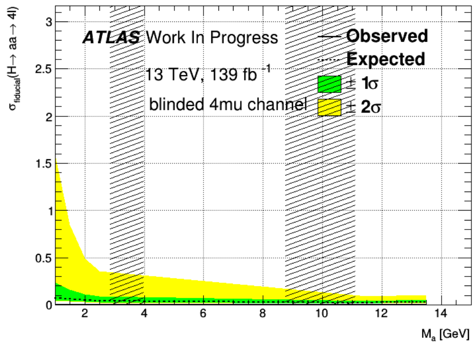

FIGURE 8.14: Expected 95% CL upper bounds on $\sigma_{fid}(H \to aa \to 4\ell)$ vs m_a for the LM search using the 2015–8 blinded 139 fb^{-1} dataset. The shaded areas are the quarkonia veto regions.

results are obtained using the asymptotic formulae since the data is not yet unblinded.

The acceptances α_c^X (derived in Section C.0.3) can be used to set model-dependent limits on the total cross section covered by the phase space of the decay modes generated in each benchmark model $\sigma^{tot}(H \to XX \to 4\ell)$ (where $XX \to 4\ell$ is either $Z_dZ_d \to 4\ell$ or $aa \to 4\mu$). The model in each channel takes the form:

$$\begin{aligned} N^c_{\text{X,exp.}}\left(\langle m_{\ell\ell}\rangle\right) =& N^c_{\text{X,bkg}}\left(\langle m_{\ell\ell}\rangle\right) + \\ & \sigma^{tot}(H \to XX \to 4\ell) \times \mathcal{L}\text{umi} \\ & \times \frac{\Gamma^c_X}{\Gamma^{4\ell}_X} \times \alpha^X_c \times \epsilon_c \times \text{Gaus}\left(\langle m_{\ell\ell}\rangle, \overline{\langle m_{\ell\ell}\rangle}_c, \sigma^c_{\langle m_{\ell\ell}\rangle}\right). \end{aligned} \tag{8.4}$$

where $\sigma^{tot}(H \to XX \to 4\ell)$ [11] is the parameter of interest. See Appendix C.0.5 for the mathematical derivation. The approach used to generate the inputs for setting limits on the total cross section is similar to the approach used for the fiducial cross section limits. The partial fraction ratios $\Gamma^c_X/\Gamma^{4\ell}_X$, are defined as the decay width ratios. When the partial fraction ratio is zero, that particular channel is not included in the model (i.e. the aa model only includes the 4μ channel in the high-mass region). The resulting limits for the HM channel ($H \to Z_dZ_d \to 4\ell$) are shown in Figure 8.15. Limits for 139.0 fb^{-1} in the form of limits on the Higgs branching ratio are shown in Section 8.7.4.

8.7.4 Limits on Higgs branching ratios and model parameters

Once a limit on the total production cross section of the process $H \to ZX/XX \to 4\ell$ is obtained from the method described in Section 8.7.3, a limit on the branching ratio BR($H \to XX/ZX$) can be calculated by taking into account the theoretical benchmark model assumptions on branching ratio BR($X \to 2\ell$). The section below describes how it can be done for the $H \to XX \to 4\ell$ analysis. While with not much difference, can be applied for other analyses as well.

[11] For narrow width approximation, $\sigma^{tot}(H \to XX \to 4\ell)$ can be written as $\sigma_H \times \text{BR}(H \to XX \to 4\ell)$

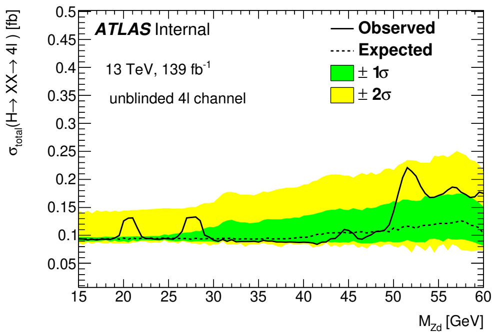

FIGURE 8.15: The expected and observed 95% confidence level upper bound on the total cross-section for the phase spaces covered by the benchmark models, $\sigma_H \mathrm{BR}(H \to XX \to 4\ell)$.

8.7.4.1 Setting a limit on BR(H → XX) HM and LM

The mathematical derivation of the branching ratio BR($H \to XX$) from the total production cross section of the process $H \to XX \to 4\ell$ to BR($H \to XX$), using Narrow Width Approximation (NWA) is:

$$BR(H \to XX \to 4\ell) = \frac{\sigma^{tot}(H \to XX \to 4\ell)}{\sigma_H} \tag{8.5}$$

We then consider the definition of the branching ratio

$$BR(H \to XX) = \frac{BR(H \to XX \to 4\ell)}{\sum_{all\ channels}[BR(X \to 2\ell)]^2}. \tag{8.6}$$

We factorize the branching ratio and use the two previous results to find $BR(H \to Z_d Z_d)$ and $BR(H \to aa)$ which comes:

$$BR(H \to Z_d Z_d) = \frac{BR(H \to Z_d Z_d \to 4\ell)}{4[BR(Z_d \to 2\ell)]^2} \tag{8.7}$$

$$BR(H \to aa) = \frac{BR(H \to aa \to 4\ell)}{[BR(a \to 2\mu)]^2} \tag{8.8}$$

where σ_H is the SM Higgs production cross-section (taken as 48.58 pb at 13 TeV at N3LO from (Andersen, 2013)), and $BR(X \to 2\ell)$ is the branching ratio to one flavour of $\ell\ell$, for our benchmark models (Curtin et al., 2015). For the HM analysis $H \to Z_d Z_d \to 4\ell$, the branching ratio $BR(Z_d \to 2\mu) + BR(Z_d \to 2e)$ are given in (Curtin et al., 2015) for different m_{Z_d}, thus are divided by 2 to plug into the above calculation.

Figure 8.16 shows the expected branching ratio limit on $H \to Z_d Z_d$ for the high-mass channel using the 2015–8 139 fb^{-1} data set (unblinded). The limits were produced with the true signal distribution at the generated m_{Z_d} mass points (separated 5 GeV apart) instead of a Gaussian signal observable. For the production of the expected limit, ten thousand toy distributions were generated at each mass point. For the production of the observed limit, ten thousand toy distributions of $\tilde{q_\mu}$ were generated for μ ranging from 0 to 0.2 in 40 stepswhere the latter is the conditional MLE based on observed data[12]. The weaker bound at higher m_{Z_d} is due

[12] see the Frequentist Limit Recommendation document (forum, 2011) supplied by the ATLAS Statistics Forum for more details.

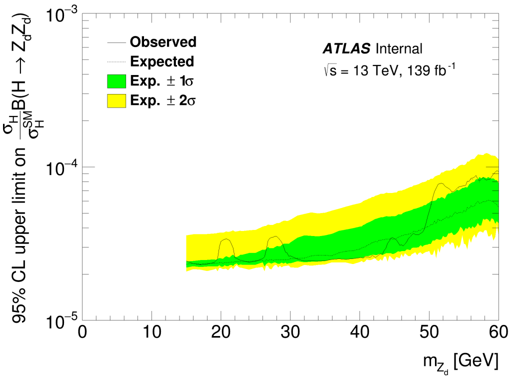

FIGURE 8.16: HM search: Observed and expected branching ratio limits on $H \to Z_dZ_d$ for the high-mass channel using the 2015–8 unblinded 140 fb^{-1} data set.

to the fact that the branching ratio $Z_d \to \ell\ell$ drops slightly at higher m_{Z_d} (Curtin et al., 2015) as other decay channels are opened. Using the model dependent prediction on BR($a \to \mu\mu$) (Curtin et al., 2015), the limit on BR($H \to aa$) can be obtained using Equation 8.7.

8.7.4.2 The limit on the Higgs mixing parameter κ

The $H \to Z_dZ_d$ decay can be used to obtain a m_{Z_d}-dependent limit on a reduced Higgs mixing parameter κ' Curtin et al., 2014:

$$\kappa' = \kappa \times \frac{m_H^2}{|m_H^2 - m_S^2|}, \tag{8.9}$$

where κ is the size of the Higgs mixing parameter and m_S is the mass of the dark Higgs boson. The partial width of $H \to Z_dZ_d$ is given in terms of κ (Curtin et al., 2015). In the regime where the Higgs mixing parameter dominates ($\kappa \gg \epsilon$), $m_S > m_H/2$ and $m_{Z_d} < m_H/2$, so $H \to Z_dZ^* \to 4\ell$ is negligible, and the only relevant decay is $H \to Z_dZ_d$. Therefore, the partial width $\Gamma(H \to Z_dZ_d)$ can be written as:

$$\Gamma(H \to Z_dZ_d) = \Gamma_{\text{SM}} \frac{\text{BR}(H \to Z_dZ_d)}{1 - \text{BR}(H \to Z_dZ_d)}. \tag{8.10}$$

The reduced Higgs mixing parameter κ' is obtained using Eq. (53) of Ref. (Curtin et al., 2014) or Table 2 of Ref. (Curtin et al., 2015):

$$\kappa'^2 = \frac{\Gamma_{\text{SM}}}{f(m_{Z_d})} \frac{\text{BR}(H \to Z_dZ_d)}{1 - \text{BR}(H \to Z_dZ_d)}, \tag{8.11}$$

where

$$f(m_{Z_d}) = \frac{v^2}{32\pi m_H} \sqrt{1 - \frac{4m_{Z_d}^2}{m_H^2}} \times \frac{\left(m_H^2 + 2m_{Z_d}^2\right)^2 - 8\left(m_H^2 - m_{Z_d}^2\right) m_{Z_d}^2}{m_H^4}. \tag{8.12}$$

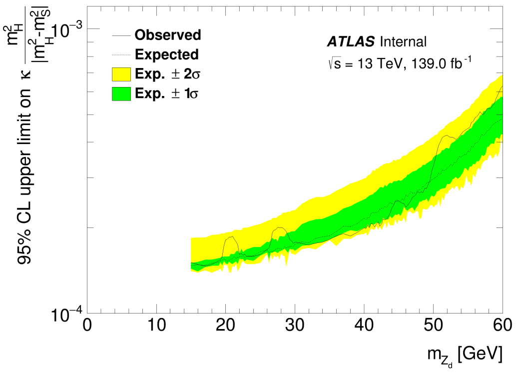

FIGURE 8.17: HM search: Observed and expected κ' limits on $H \to Z_dZ_d$ for the high-mass channel using the 2015–8 unblinded 140 fb^{-1} data set.

Figure 8.17 shows the expected and observed limit at 95% CL on κ'. As expected, the trend is similar to the one published in Run 2 (Figure 7.10b) but the result is improved as the luminosity and the statistics increased. An interpretation for $H \to Z_dZ_d$ is not done for the Z-Z_d mass mixing scenario described in Refs. (Davoudiasl et al., 2013; Davoudiasl, Lee, and Marciano, 2012) since in this model the rate of $H \to Z_dZ_d$ is highly suppressed relative to that of $H \to ZZ_d$.

8.7.5 Limits in the ZX search

In the ZX channel, HISTFACTORY (Cranmer et al., 2012) and ROOSTATS (Moneta et al., 2010) frameworks are used for limit setting. The following likelihood expression is used:

$$\mathcal{L}(\sigma_{ZZd}, \mu, \vec{\theta}|\vec{n}) = e^{-\frac{(1-\mu)^2}{2\cdot\delta_\mu^2}} \prod_j e^{-\frac{1}{2}\theta_j^2} \cdot \prod_i \mathcal{L}_i\Big(\mu(Z_i(\theta_j) + \lambda H_i(\theta_j) + \sigma_Z ZdS_i(\theta_j))|N_i\Big)$$

- μ is the luminosity strength parameter that scales the Monte Carlo signal region event rates, and $\delta_\mu = 1.7\,\%$ is the uncertainty on μ
- θ_j are the systematic parameters which interpolate between the up, nominal, and down variations of the Monte Carlo derived m_{34} distributions for the detector and theoretical systematics as well as account for statistical uncertainties.
- $\mathcal{L}_i(n_i^{\text{exp}}, N_i)$ is the Poisson Likelihood of finding N_i events in bin i given an expectation of n_i^{exp} events.

Figure 8.18 shows the limit on the total cross section σ_{ZZd} of the $H \to ZZ_d \to 4\ell$ process which is derived from a binned maximum likelihood fit of background and signal expectations to the observed data, and by profiling the associated likelihood ratio.

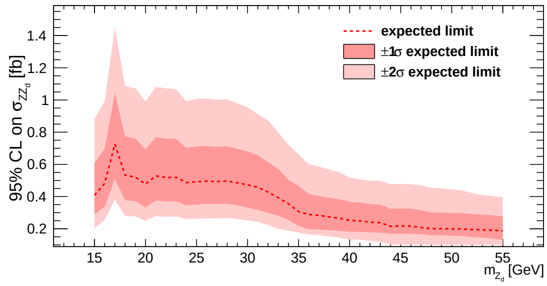

FIGURE 8.18: Expected upper 95 % confidence level limits on σ_{ZZd} with the 139 fb^{-1} dataset. The limits are based on a binned maximum likelihood fit to 5000 background only Monte Carlo toys samples of the ZX signal region.

8.7.6 Limits in the AS search

Following the same approach as in the "$H \rightarrow XX$" analysis, Gaussian signal modeling is used. A limit on the total cross section ratio $= \frac{\sigma^{tot}_{(S\rightarrow Z_d Z_d \rightarrow 4l)}}{(\sigma_{(ggFH)} \times BR(H\rightarrow ZZ^* \rightarrow 4l))_{SM}}$ of the $S \rightarrow Z_d Z_d \rightarrow 4\ell$ and $H \rightarrow Z_d Z^* \rightarrow 4\ell$ processes is calculated using 139 fb $^{-1}$. No interpolation over the generated mass point hypotheses is done. The results in SR1 and SR2 are presented in Tables 8.17 and 8.18 respectively. In SR1 the best limit corresponds to the higher m_{Z_d} masses: m_{Z_d} = 150 GeV and m_S = 250 GeV, this can be interpreted by the fact that less backgrounds and more signal statistics are observed in those regions (see Figure 8.6). The worst limit are the mass points: m_{Z_d} = 80 GeV and m_{Z_d} = 80 GeV. Those mass points are much more affected by the Z veto cut which degrades theirs statistics. In the SR2, the limit increases with respect to the m_{Z_d} and m_S mass points. This can be explained by the increase of the efficiency as m_{Z_d} and m_S increase, as shown in Figure 8.19.

Limit on XS ratio with 139.0 fb^{-1}, SR1					
(m_{Z_d}, m_S)	-2σ	-1σ	Expected	$+1\sigma$	$+2\sigma$
(100, 400)	0.018	0.025	0.035	0.053	0.085
(150, 750)	0.003	0.004	0.006	0.009	0.016
(20, 175)	0.005	0.007	0.009	0.015	0.026
(250, 800)	0.003	0.004	0.005	0.008	0.015
(50, 175)	0.008	0.011	0.015	0.023	0.039
(50, 400)	0.005	0.006	0.009	0.014	0.022
(65, 750)	0.006	0.008	0.011	0.017	0.027
(70, 250)	0.011	0.014	0.019	0.029	0.047
(80, 325)	0.017	0.022	0.031	0.046	0.069

TABLE 8.17: Limit setting on the total cross section ratio of $S \rightarrow Z_d Z_d \rightarrow 4\ell$ and $H \rightarrow Z_d Z^* \rightarrow 4\ell$ processes XS ratio $= \frac{\sigma^{tot}_{(S\rightarrow Z_d Z_d \rightarrow 4l)}}{(\sigma_{(ggFH)} \times BR(H\rightarrow ZZ^* \rightarrow 4l))_{SM}}$

Finally pull plots were also produced for all of the 4 channels presented in this thesis. Figure 8.20 is an example of pull plot which corresponds to the mass point (m_{Z_d}, m_S) = (40, 90) GeV. As expected the highest impacts are the dominant systematics.

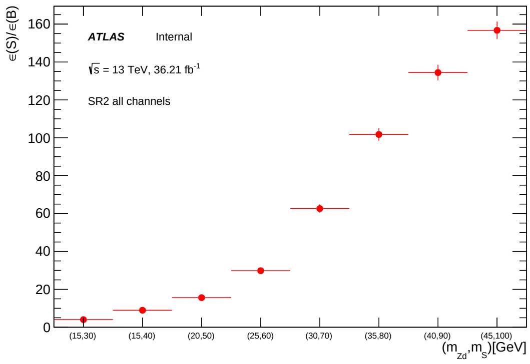

FIGURE 8.19: Signal-background efficiency versus (m_S, m_{Z_d}) in SR2

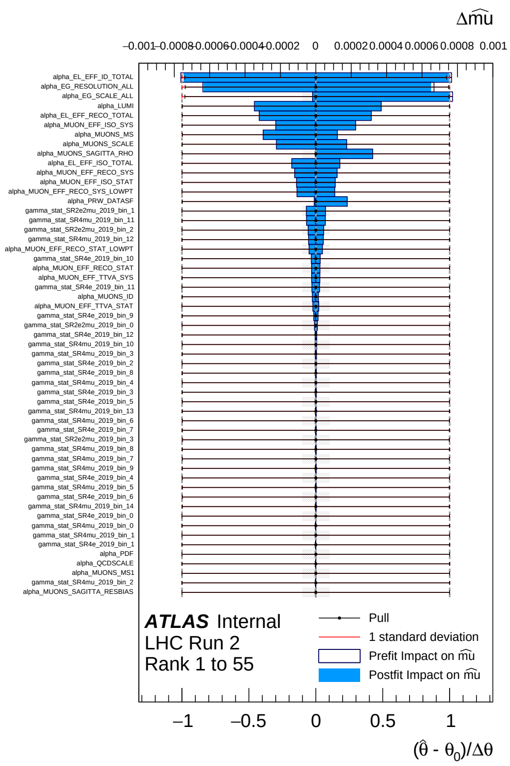

FIGURE 8.20: Signal-background efficiency versus (m_S, m_{Z_d}) in SR2

Limit on XS ratio with 139.0 fb^{-1}, SR2					
(m_{Z_d}, m_S)	-2σ	-1σ	Expected	$+1\sigma$	$+2\sigma$
(15, 30)	0.376	0.505	0.700	1.239	–
(15, 40)	0.143	0.192	0.267	0.450	1.147
(20, 50)	0.083	0.111	0.154	0.253	0.572
(25, 60)	0.081	0.108	0.150	0.246	0.485
(30, 70)	0.048	0.065	0.089	0.144	0.268
(35, 80)	0.025	0.034	0.047	0.076	0.139
(40, 90)	0.021	0.029	0.040	0.063	0.112
(45, 100)	0.017	0.023	0.033	0.051	0.091

TABLE 8.18: Limit setting on the total cross section ratio of $S \rightarrow Z_d Z_d \rightarrow 4\ell$ and $H \rightarrow Z_d Z^* \rightarrow 4\ell$ processes XS ratio = $\frac{\sigma^{tot}_{(S\rightarrow Z_d Z_d \rightarrow 4l)}}{(\sigma_{(ggFH)} \times BR(H\rightarrow ZZ^*\rightarrow 4l))_{SM}}$

Chapter 9

Conclusion

In this Thesis, a search for new dark particles is described. The motivation arises from shortcomings of the Standard Model. Therefore, as context, some successes of the Standard Model have been reviewed, that establish it as a very powerful description of nature. However, many physics phenomena can't be explained by the SM, which suggest that new physics, known as Beyond Standard Model, need to be explored. Amongst the BSM theories, two of them have been considered in this thesis as benchmark models; these are the HAHM and the 2HDM+S. These two models predict the Higgs boson decaying to intermediate states which could be two dark vector bosons, Z_d, or two pseudo scalars a. These then decay to four leptons. These two particles, the Z_d or the a, could be candidates or force carriers of dark matter. The dark sector Lagrangian could also include fermions so that the full dark sector could explain the astrophysical observations of position excesses and other possible signatures of cold dark matter. The benchmark model is only used to optimize the search algorithms and to extract a model dependent interpretation. Nonetheless, the search for a Z_d and the dark Higgs (S) considered in this thesis is somewhat model independent and the results can be presented as a generic fiducial cross section.

The Large Hadron Collider and the ATLAS detector has also been described, since they are the experimental facilities used in the Z_d, S and a searches.

The dark vector boson (Z_d) search that originates from the discovered SM Higgs boson decaying ultimately into four-lepton events using pp collision data corresponding to an integrated luminosity of about 20 fb^{-1} at the center-of-mass energy of $\sqrt{s}$ = 8 TeV recorded with the ATLAS detector has been performed. Two processes have been considered; $H \to ZZ_d \to 4\ell$ (ZX channel) and $H \to Z_dZ_d \to 4\ell$ (High Mass channel). The results reviewed in this thesis do not show any evidence of deviation from the SM expectation. In the $H \to ZZ_d \to 4\ell$ an expected and observed limits above 0.4 and 0.2 respectively are set at 95% CL on the relative branching ratio for the entire Z_d mass range considered in this search. An Upper bound limit at 95% CL is also set on the branching ratio of $H \to ZZ_d \to 4\ell$ in the range of (1-9)$\times 10^{-9}$ assuming the SM branching ratio of $H \to ZZ^* \to 4\ell$. By using the HAHM as benchmark model, an upper bond limit at 95% CLs is set on the kinetic mixing parameter ϵ and on the effective mass mixing parameter δ. In the $H \to Z_dZ_d \to 4\ell$ search, 2 data events are observed, one in the 4e channel and another one in the 4μ channel. The one in the 4e (4μ) channel has a di-lepton invariant masses of 21.8 GeV and 28.1 (23.2 GeV and 18.0) GeV and it's consistent with a Z_d mass in the range of 23.5 < m_{Z_d} < 26.5 GeV (20.5 < m_{Z_d} < 21.0 GeV). These two events are not statistically significant, an upper bond limit at 95% CL on the signal strength (μ_d) is set in the entire Z_d mass range for the 3 combined final states. Using the HAHM model, an upper bound limit at 95% is set on the Higgs mixing parameter κ. The dark vector boson search has been carried out again in the Run 2 search, and extended to the search of a pseudo-scalar a in the low mass regime ($H \to aa \to 4\mu$ (LM channel) with $a \in [1;10]$ GeV).

In the Run 2 search, the integrated luminosity increased to 36.1 fb^{-1} and the center of mass energy to 13 TeV. No deviation from the SM expectation or excess(es) has been observed for the ZX and low mass channels. An Upper bond limit is set on the branching ratio of the Higgs boson to ZZ_d and aa corresponding to $\mathcal{B}(H \to ZZ_d) \approx 0.1\%$ and $\mathcal{B}(H \to aa) \approx 0.1\%$ respectively. An upper bond limit is also set at 95% CLs on the kinetic mixing and the mass mixing parameters. For the HM channel, 6 data events have been observed where the background prediction is only 3.9$\pm$0.3. The biggest deviation from the Standard Model expectation is from a single event at $\langle m_{\ell\ell} \rangle \approx 20$ GeV, with a local significance of 3.2 σ. The corresponding global significance is approximately 1.9 σ. These events are not statistically significant. An upper bond limit is set at 95% CL on the branching ratio of the Higgs boson to $Z_d Z_d$ ($\mathcal{B}(H \to ZZ_d) \approx 0.01\%$) as well as on the Higgs mixing parameter κ. From Run 1 to Run 2, the limit on the branching ratio of the HM channel improved by a factor of four which corresponds to the increase in both luminosity and Higgs boson production cross-section between the two Runs.

In the full Run 2, corresponding to an integrated luminosity of 139.1 fb $^{-1}$, these 3 searches (ZX, LM and HM) are performed again plus a new channel named additional scalar (AS) which searches for a dark Higgs (S) boson decaying to four leptons via two Z_d bosons. For now, only the high mass channel has been unblinded. Nineteen data events are observed where 14 are predicted. The results show that the data are consistent with the MC prediction and no deviation from the SM expectation is observed. Hence, limits have been set at 95% CL on the branching ratio $H \to ZdZ_d \to 4\ell$ ($\mathcal{B}(H \to Z_d Z_d)$) and also on the Higgs mixing parameter κ'. These results compared to the Run 2 ones show a lot of improvements in the same trend as the luminosity and the statistics increased. Recently CMS published its results regarding the high mass search and it turns out that both results from CMS and ATLAS are very similar even if the comparison is not straightforward. For instance the limit on $\mathcal{B}(H \to Z_d Z_d)$ set by CMS in Figure 4.b of this reference (CMS-Collaboration, 2020) is very similar to our limit as shown in Figure 8.16. Our current limits on the $\mathcal{B}(H \to Z_d Z_d)$ of some mass points such as the ones for $m_{Z_d} = 20, 30$ and 40 GeV are around (2.1, 1.9, 2.1)$\times 10^{-6}$ respectively while in CMS they are (1.7, 1.8, 2.2)$\times 10^{-6}$ which bolster the conclusion about the similarity. The number of data events observed are also very similar. In the high mass channel, a bump at around 20 GeV was observed in Run 1 and more significantly in Run 2 with a local significance of around 3.2σ in the 2e2μ channel. In the full Run 2 analysis this little bump appears to be less significant, with a local significance of about 1.5σ. However, in CMS the bump appears at exactly around the same place ($\sim$ 20 GeV) with a higher local significance as shown in Figure 5.b of this reference(CMS-Collaboration, 2020). This is a very interesting result and sparks our motivation to pursue this analysis in the Run 3 round where more data are expected. The other channels (ZZ_d, LM, and AS) are not unblinded yet, but they already proceeded to an unblinding approval meeting and need to address some follow-up tasks before being able to unblind the Signal Region of the data. However, for ZX and LM channels, limits have been at 95% on their respective branching ratios based on Assimov data. The results show some improvement which correspond to the statistics and the luminosity increase in the full Run 2 search compared to the Run 2 one. For the AS channel, the limits are set at 95% CL on the cross section ratio using Assimov data in both SR1 and SR2. The best limit in SR1 corresponds to the higher m_{Z_d} masses. This can be interpreted by the fact that less backgrounds and more signal statistics are observed in those regions. The worst limits are the mass points close to the SM Z mass pole. Those mass points are much more affected by the Z veto cut which degrades theirs statistics. In the SR2, the limit increases with respect to the m_{Z_d} and m_S mass points. This can be explained by the increase of the efficiency as m_{Z_d} and m_S increase.

This thesis has therefore described several searches. In particular, for the AS search, there is the design and validation of a completely new search which goes beyond the previous searches in many respects. Firstly the full Run 2 version, has an improved reducible background estimation. This will make the extracted limits more robust and reliable. Secondly the signal region has been re-optimized to take advantage of the low background in the low mass region. This will improve the discovery potential for a possibly broader Z_d without any loss of sensitivity. New validation regions have been explored in order to make sure there is no overlap between VR and SR of any search channels. Finally, we have opened the dark Higgs Portal, as a novel search channel. This means that one may not only discover the Z_d, but also the dark Higgs S itself. This is therefore a more powerful search and simultaneously a much broader search. In addition, the search is done with several significant improvements to the ATLAS detector and the reconstruction algorithms. Most significantly, the Insertable B-Layer (IBL) has been brought into operation. This allows additional tracking capacity closer to the Interaction Point. The effect of this is to reduce reducible background arising from jets decaying leptons.

It can therefore be seen that the expected limits presented are the strongest ever in any previous version of the analysis. At the time of writing, the data have not yet been unblinded (except the HM channel), so only Asimov data is used for the limit setting, on their respective branching ratios. The full analysis presented in this thesis has been validated by the oversight mechanisms of the collaboration.

The full Run 2 analysis is expected to be decisive on the matter of the deviations seen in the previous analysis versions. It brings improved algorithms, better performance of the detector and reconstruction of the physics objects and substantially improved statistics. It is therefore very exciting and impactful, given the discovery potential it offers.

Since all the remaining channels (ZX, LM, and AS) went already through an unblinding approval meeting and only some follow-ups need to be addressed before being able to unblind the data, the future of the analyses have been already discussed amongst the analysis team. Hence, it's planed to pursue the analyses in Run 3 by including Machine Learning (ML) algorithmic approaches such as supervised (or unsupervised) and an anomaly detection ML algorithms where a significant improvement of the signal background efficiency is expected. So far the dark vector boson (Z_d) is supposed to be prompt but including a long-lived Z_d particle will be considered for the next round. The mass of the two Z_d coming from a Higgs (H) or a dark Higgs (S) decays are supposed to be compatible in term of mass in our current analysis, however, a scenario where the 2 Z_d are different will also be considered. One could imagine the processes $H \rightarrow Z_{d1}Z_{d1} \rightarrow 4\ell$ and $H \rightarrow Z_{d2}Z_{d2} \rightarrow 4\ell$. There is an SM analogy with the Z and W except for the charge difference. It apparently is not ruled out theoretically that one can build a model with 2 $U(1)$d and 2 dark Higgs's that mix with the SM Higgs.

Part IV

Appendix

Appendix A

Definition and derivation of cuts

A.1 The Z veto cut definition for AS

The Z veto cut was investigated in Run 2 based on Run 1 results by observing the di-lepton mass distribution and varying cuts to maximize the approximated total signal significance by the formula.

$$\sigma = \sqrt{2.((S+B)\ln\left(1+\frac{S}{B}\right) - S)}. \tag{A.1}$$

S stands for signal yield and B stands for background yield. All the backgrounds are considered and normalized proportionally to their theoretical cross-sections, and the signal mass points considered are similarly normalized using the SM Higgs boson production cross-section. Only signal samples where the mass points which are are expected to be more affected by a Z-veto cut are considered ($m_{Z_d} = 70\,\text{GeV}$, $m_{Z_d} = 80\,\text{GeV}$, $m_{Z_d} = 100\,\text{GeV}$). However some other mass points ($m_{Z_d} = 50\,\text{GeV}$, $m_{Z_d} = 150\,\text{GeV}$) where we expect less effect are also added. The study proceeded after applying all the cuts of the AS channel cut-flow.

Samples (GeV)
m_s= 175 , m_{Z_d}= 20
m_s= 175 , m_{Z_d}= 50
m_s= 750, m_{Z_d}= 65
m_s= 250, m_{Z_d}= 70
m_s= 325, m_{Z_d}= 80
m_s= 400, m_{Z_d}= 100
m_s= 400, m_{Z_d}= 50
m_s= 750, m_{Z_d}= 150

TABLE A.1: Additional scalar scalar signal samples

Figure A.1 shows the distributions of the leading (m_{ab}) and sub-leading (m_{cd}) di-leptons, and the alternative leading (m_{ad}) and sub-leading (m_{cb}) di-lepton, after applying all cuts except the Z veto cut. From these distributions we defined a set of ten Z veto cut hypotheses where m_{ab} and m_{cd} are excluded in a given mass range as shown in Table A.2.

The same set of Z veto cut hypotheses is performed on the alternative di-lepton pairs (m_{ad} and m_{cb}). Figures A.2 and A.3 show the signal-background distribution of the leading and sub-leading di-lepton mass respectively, when each of Z veto cut hypothesis is applied, Figure A.4 and A.5 are the plots for the corresponding

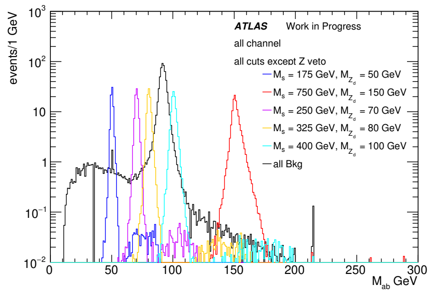

(A)

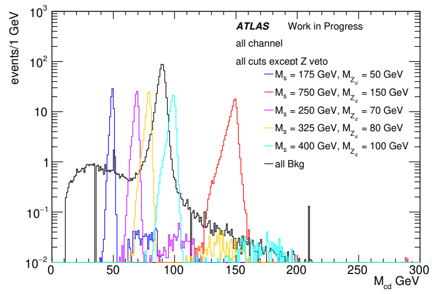

(B)

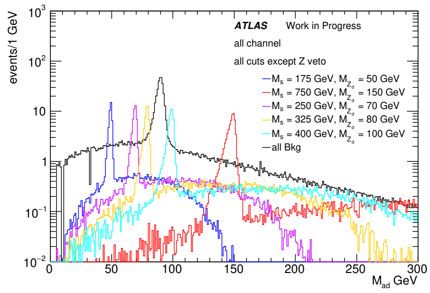

(C)

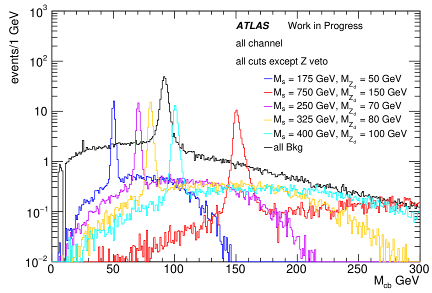

(D)

FIGURE A.1: a) and b) are respectively the distributions of the leading (m_{ab}) and sub-leading (m_{cd}) di-leptons, c) and d) the distributions of the alternative leading (m_{ad}) and sub-leading (m_{cb}) di-lepton. All cuts are applied except Z-veto cut. Backgrounds are normalized by the theoretical cross section and signal by the SM Higgs boson production cross-section.

m_{ab}, m_{cd} $\notin$ **in the ranges (GeV):**
$[71.2, 111.2]$
$[73.2, 109.2]$
$[75.2, 107.2]$
$[77.2, 105.2]$
$[79.2, 103.2]$
$[81.2, 101.2]$
$[83.2, 99.2]$
$[85.2, 97.2]$
$[87.2, 95.2]$
$[89.2, 93.2]$

TABLE A.2: The ten Z veto cut hypothesis

alternative di-lepton pairs. For each Z-veto cut hypotheses the significance of the signal compared to the background is calculated from equation A.1.

Figure A.6 shows this significance for each Z veto cut hypothesis a) when the cuts are performed on the di-lepton pair and b) when the cuts are performed on the alternative di-lepton pairs, where we can conclude from a) that a best Z veto cut on the di-lepton pairs would be m_{ab} and m_{cd} $\notin]85.2, 97.2[$ GeV and from b) m_{ad} and m_{cb} $\notin]87.2, 95.2[$ GeV would be the best Z veto for the alternative di-lepton pairs.

A.2 Signal region re-optimization

The medium signal region (MSR) cut of the $H \to XX \to 4\ell$ channel in the Run 2 analysis was the $m_{34}/m_{12} > 0.85$ "wedge" cut. This cut assumes the Z_d width is narrow as in the HAHM (Wells, 2008; Gopalakrishna, Jung, and Wells, 2008), so that the observed width is determined by detector performance. The detector performance is then modeled with a linear function in the reconstructed di-lepton mass leading to a wedge shape in (m_{34}, m_{12}) plane.

This section motivates the broadening of the MSR cut considering the di-lepton mass dependence of the background distribution and the possibility of other theoretical models where the Z_d width may be broader, while still optimizing the signal exclusion / discovery sensitivity for the local di-lepton mass region.

We first review the justification of the previous wedge cut. The HAHM relates the Z_d width to the kinetic mixing parameter with a scaling $\Gamma_{Z_d} \sim \epsilon^2$, and in particular, the point $(\epsilon, \Gamma_{Z_d}) = (10^{-4}, 2.7 \times 10^{-9}\text{GeV})$ is mentioned for $m_{Z_d} = 20$ GeV (Gopalakrishna, Jung, and Wells, 2008). In order to get a prompt decay (displaced by $< 10\mu$m) when $(10 \text{ GeV} < m_{Z_d} < 50 \text{ GeV})$, we see from Figure 2 in reference (Curtin et al., 2014) that $\epsilon > 10^{-5}$. Then to accommodate the largest degree of kinetic mixing consistent with precision electroweak observables, we must expect from the same paper in Figure 4 that $\epsilon < 0.03$ in the same region of m_{Z_d}. Using the scaling law above, we then find the broadest expectation for the Z_d width is $\Gamma_{Z_d} < 0.25$ MeV. This is indeed very narrow, and the observed width of this search must therefore be constrained by the detector performance. The detector resolution has been investigated in detail for electrons and muons in the references (ATLAS Collaboration et al., 2016b; Aaboud et al., 2019a) respectively. Considering the region of interest for the leptons in this study, we select the general value of $\Delta E_e \sim 3.5\%$ and $\Delta E_\mu \sim 3.8\%$ respectively. It would be reasonable to select

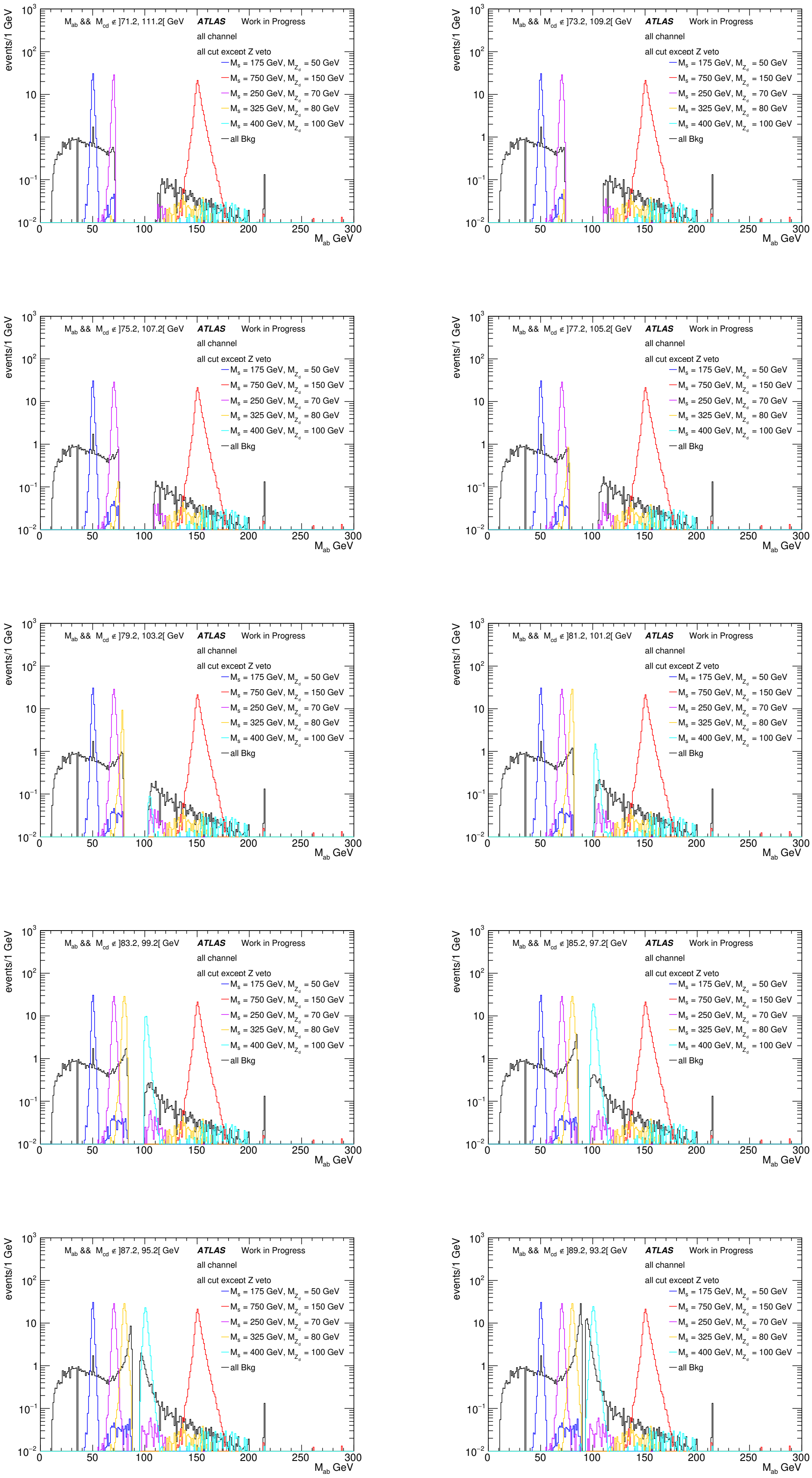

FIGURE A.2: leading di-lepton (m_{ab}) distribution for each of the ten Z veto cut hypothesis

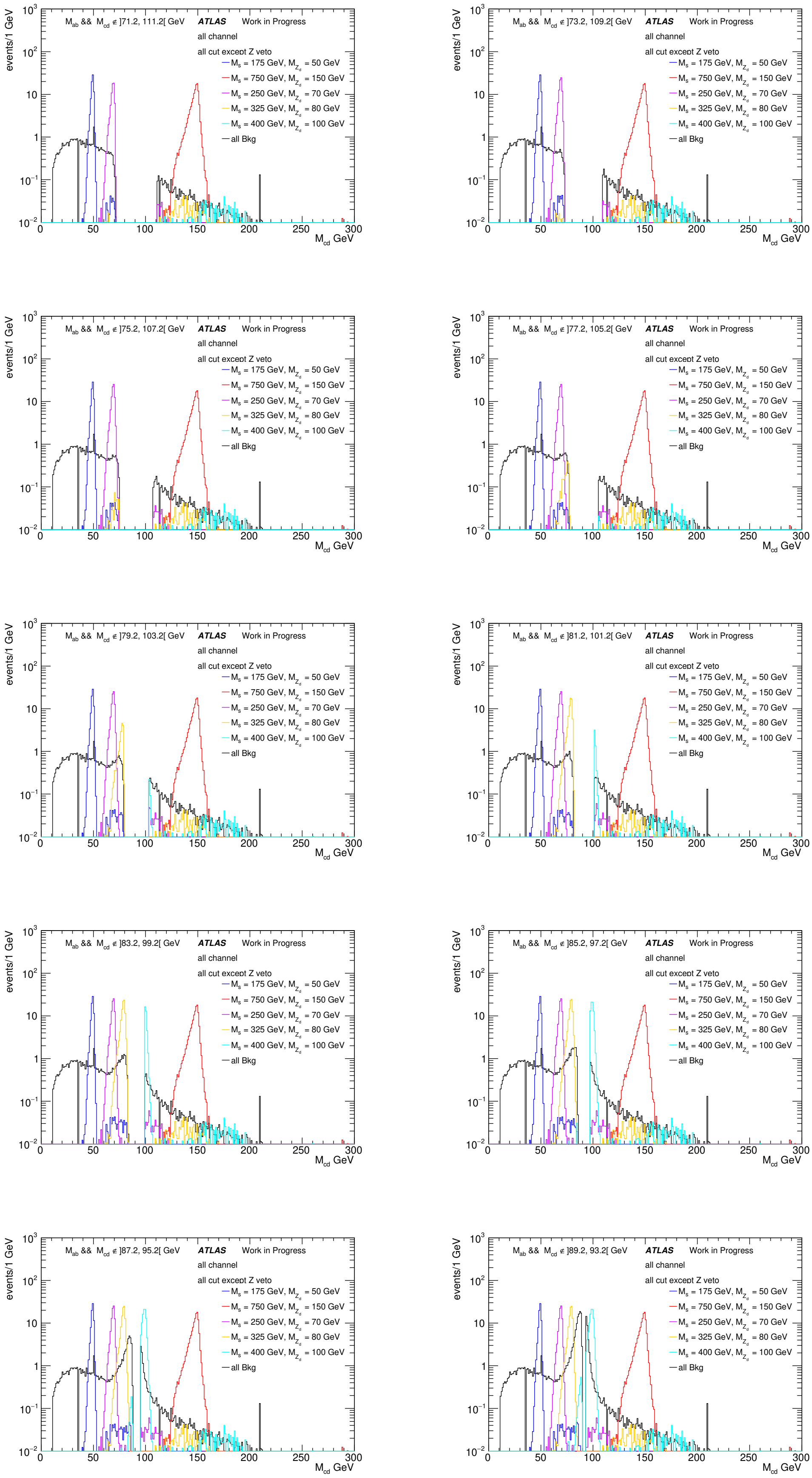

FIGURE A.3: sub-leading di-lepton (m_{cd}) distribution for each of the ten Z veto cut hypothesis

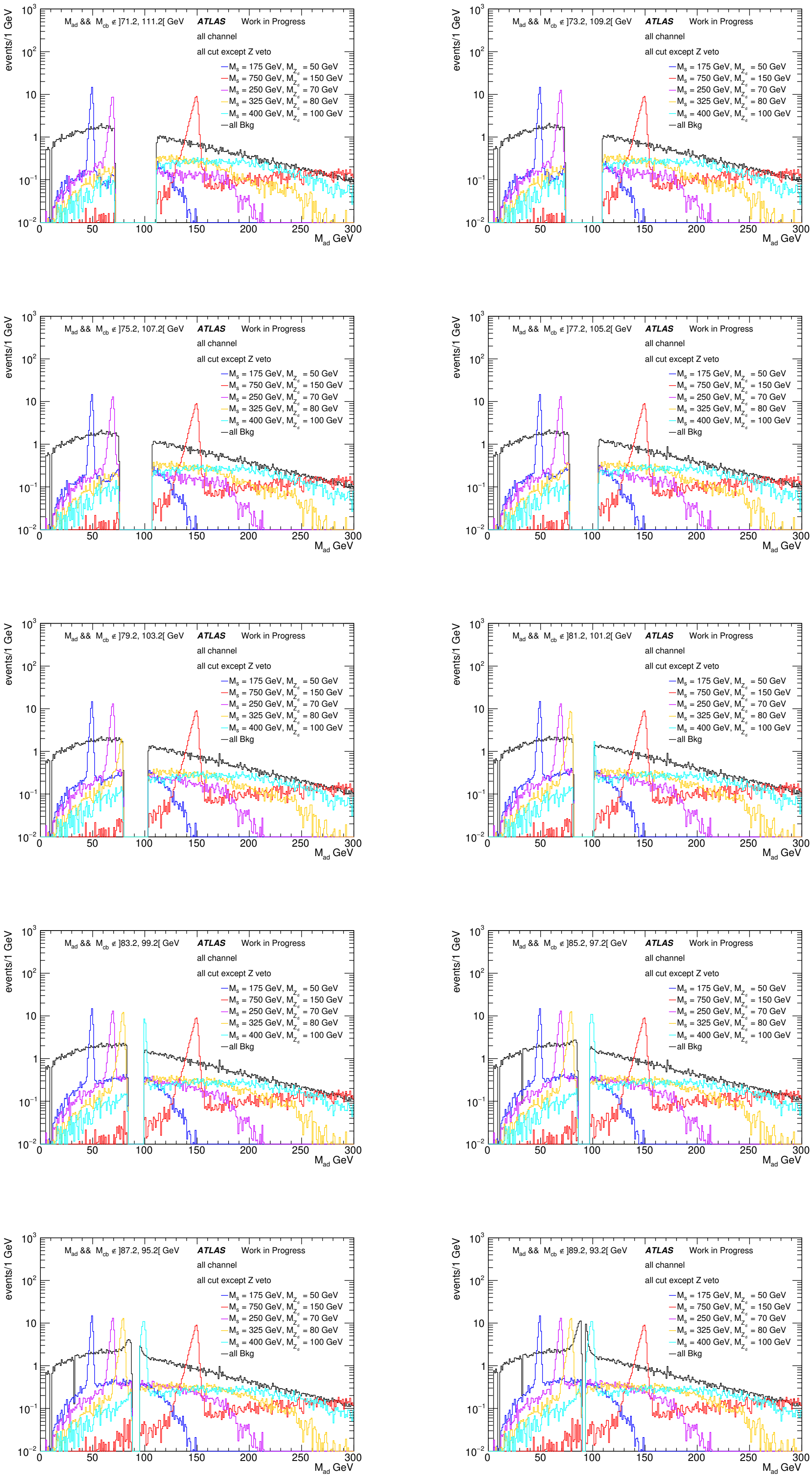

FIGURE A.4: leading di-lepton (m_{ad}) distribution for each of the ten Z veto cut hypothesis

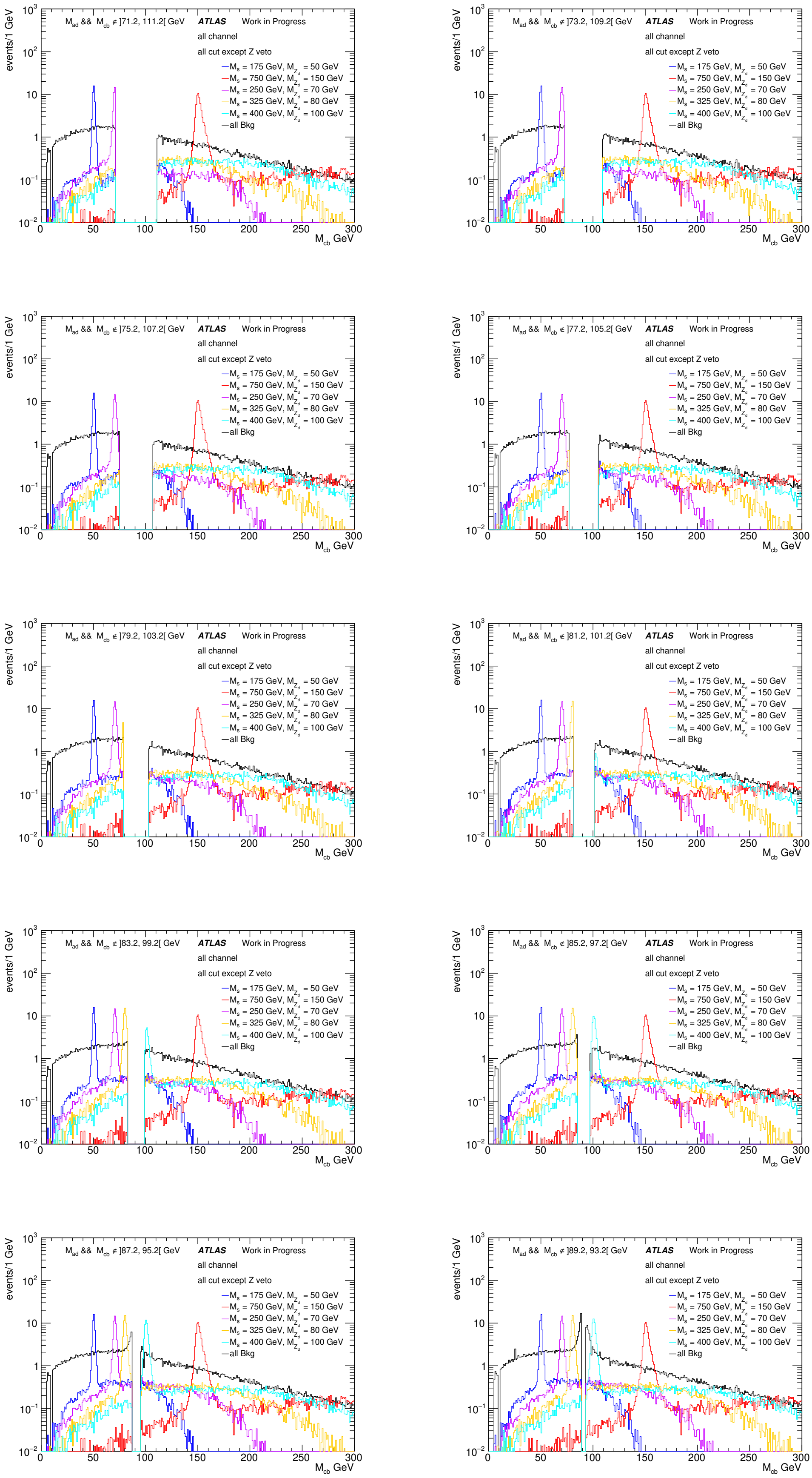

FIGURE A.5: leading di-lepton (m_{cb}) distribution for each of the ten Z-veto cut hypothesis

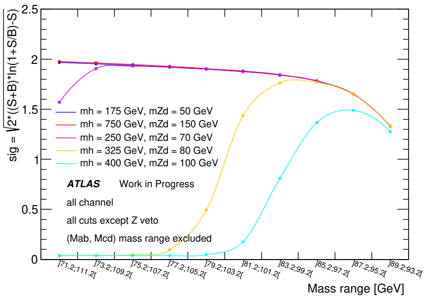

(A)

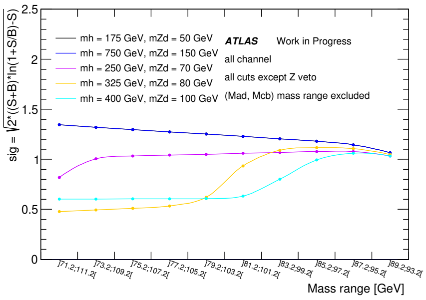

(B)

FIGURE A.6: Significance vs Z veto cut hypothesis a) when the cuts are performed on the di-leptons pair and b) when the cuts are performed on the alternative di-lepton pairs.

a $\pm 2\sigma$ window, and this would then be 13 GeV for electrons and 10 GeV for muons which is 14% for electrons and 11.2% for muons respectively. In terms of the wedge cut definition, $m_{34}/m_{12} > 0.85$, a value of 15% was selected for both muons and electrons in the reconstruction of the di-lepton mass. This cut was re-examined in the context of broadening the MSR, and it was found that indeed it was optimized for its context, that of the very narrow HAHM prediction for the Z_d width. This is therefore consistent with the $\pm 2\sigma$ consideration, which would have 95.45% of the events.

Now we can return to the question of possibly broadening the MSR definition. The two previous versions of the analysis, Run 1 and Run 2 described in Chapter. 7, both showed the expected background in the MSR or SR has vanishingly few events. The analysis for this current study could look, in addition, at the possible shape of that background distribution in the di-lepton mass parameter. Figure A.7 shows the expected background distribution histogrammed as a function of di-lepton mass using Monte Carlo (MC) data. This study includes all the appropriate backgrounds for the $H \rightarrow XX \rightarrow 4\ell$ HM case. We present the shape of the background at the stage of the cut flow where all cuts are applied up to and not including the MSR cut of $m_{34}/m_{12} > 0.85$. Superimposed are signals from the HAHM model at several steps of di-lepton mass, reconstructing the Z_d mass, m_{Z_d}. The MC backgrounds are normalized to apply to ATLAS Run 2 (data 15+16) conditions with 36 fb^{-1} of 13 TeV data. The signal MC events are appropriate for the same position in the cut flow but where the HAHM cross section is set equal to the equivalent SM process of $H \rightarrow ZZ^* \rightarrow 4\ell$. One notes that the background is very small in low m_{Z_d} region (from 10 to 35 GeV) and increases from 40 GeV to 60 GeV.

The suggestion is that the MSR could be broadened, anticipating an alternative model to the HAHM, where the Z_d width is broader, or simply model independent. The very low background of especially the lower end of the di-lepton mass spectrum could be exploited to allow this broadening of the MSR with very little effect on the sensitivity of the analysis. Theoreticians have suggested that a broad Z_d, which could have a width of 3-4 GeV with a mean mass around 25 GeV, could appear in models of compositeness. The goal of the study in this section is to optimize the MSR by using a varying width cut as a function of the di-lepton mass.

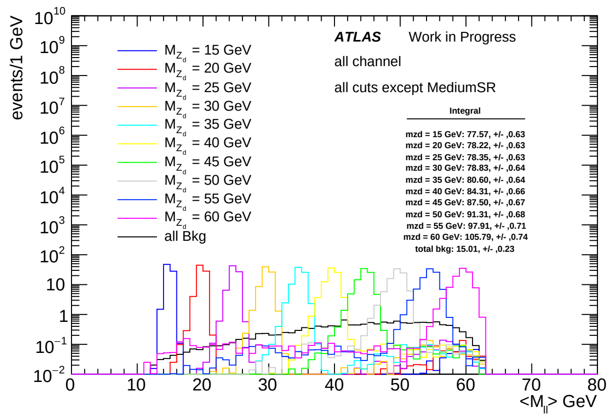

FIGURE A.7: Average di-lepton mass of the signal and background MCs, all cuts are applied except the MSR cut.

The following exercise is implemented using the HAHM width for the Z_d. A tested MSR cut is defined around each signal mass point by:

$$m_0 \times (1 - r \times \sigma) < \frac{(m_{12} + m_{34})}{2} < m_0 \times (1 + r \times \sigma)$$

where m_0 is the mass point considered, and r varies from 1 to 3.5 in steps of 0.5, and σ is 3.5% corresponding to the electron energy resolution performance of the detector. Keep in mind that for the 2σ point the ratio $\frac{(1-2\times\sigma)}{(1+2\times\sigma)} = 0.86$, which corresponds well to the previous MSR cut of $m_{34}/m_{12} < 0.85$.

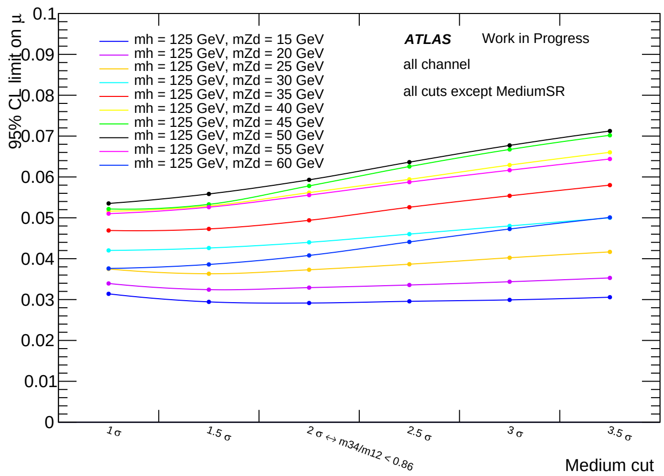

FIGURE A.8: 95% CL on μ_d for different signal mass points versus the size of the tested MSR cut.

Table A.3 and A.4 show that moving the MSR cut from 2σ (the previous MSR cut) to 3.5σ for the mass point $m_{Z_d} = 15$ GeV will increase the signal quite significantly compared to the background, while for the signal mass point $m_{Z_d} = 60$ GeV the

Number of events vs σ						
signal samples	1σ	1.5σ	2σ	2.5σ	3σ	3.5σ
$M_{Z_d} = 15$	67.0±0.6	73.5±0.6	75.7±0.6	76.6±0.6	76.9±0.6	77.1±0.6
$M_{Z_d} = 20$	67.0±0.6	73.5±0.6	75.9±0.6	76.9±0.6	77.2±0.6	77.0±0.6
$M_{Z_d} = 25$	66.9±0.6	73.6±0.6	76.0±0.6	76.8±0.6	77.1±0.6	77.3±0.6
$M_{Z_d} = 30$	67.2±0.6	73.9±0.6	76.3±0.6	77.1±0.6	77.5±0.6	77.7±0.6
$M_{Z_d} = 35$	68.7±0.6	75.5±0.6	77.9±0.6	78.9±0.6	79.2±0.6	79.4±0.6
$M_{Z_d} = 40$	71.1±0.6	78.5±0.6	81.3.0±0.6	82.3±0.6	82.6±0.6	82.8±0.6
$M_{Z_d} = 45$	74.2±0.6	81.8±0.6	84.7±0.7	85.8±0.7	86.2±0.7	86.5±0.7
$M_{Z_d} = 50$	77.1±0.6	85.1±0.7	88.1±0.7	89.3±0.7	89.8±0.7	89.9±0.7
$M_{Z_d} = 55$	82.6±0.6	91.2±0.7	94.5±0.7	95.7±0.7	96.1±0.7	96.3±0.7
$M_{Z_d} = 60$	89.7±0.7	97.9±0.7	101.2±0.7	102.3±0.7	102.6±0.7	102.7±0.7

TABLE A.3: Statistics of the signal MC events for different signal mass points with respect to the tested MSR cut.

Number of events vs σ						
bkgs sample	1σ	1.5σ	2σ	2.5σ	3σ	3.5σ
bkg for $M_{Z_d} = 15$	0.04±0.00	0.06±0.00	0.08±0.00	0.10±0.00	0.12±0.00	0.14±0.00
bkg for $M_{Z_d} = 20$	0.10±0.00	0.16±0.00	0.21±0.01	0.27±0.01	0.32±0.01	0.37±0.01
bkg for $M_{Z_d} = 25$	0.23±0.01	0.34±0.01	0.46±0.01	0.56±0.02	0.67±0.02	0.77±0.02
bkg for $M_{Z_d} = 30$	0.45±0.05	0.70±0.08	0.91±0.08	1.12±0.08	0.33±0.08	1.54±0.08
bkg for $M_{Z_d} = 35$	0.78±0.05	1.14±0.06	1.50±0.06	1.93±0.08	2.31±0.08	2.64±0.09
bkg for $M_{Z_d} = 40$	1.27±0.10	1.94±0.13	2.58±0.15	3.12±0.15	3.71±0.16	4.26±0.16
bkg for $M_{Z_d} = 45$	1.52±0.05	2.26±0.06	3.14±0.12	4.05±0.15	4.88±1.17	5.63±0.18
bkg for $M_{Z_d} = 50$	1.89±0.08	2.88±0.10	3.76±0.11	4.71±0.12	5.65±0.13	6.50±0.14
bkg for $M_{Z_d} = 55$	2.02±0.07	2.96±0.75	3.81±0.08	4.59±0.08	5.28±0.09	5.96±0.11
bkg for $M_{Z_d} = 60$	0.92±0.18	1.40±0.03	1.90±0.03	2.49±0.06	3.06±0.07	3.61±0.07

TABLE A.4: Statistics of the background MC events differentially with respect to bins in di-lepton mass with respect to the tested MSR cut.

background increases quite significantly compared to the signal. In the foregoing, one can consider that if there was an actual Z_d width that was somewhat wider than the 3.5% performance of the detector, then the effect of broadening the MSR would favor the growth of the statistics of the signal yet more strongly that of the background. Using the HAHM signal model is therefore a worst case scenario in terms of assessing any adverse effect on the analysis for the exercise of testing any loss of sensitivity of the analysis due to broadening the MSR.

We can now proceed to testing the sensitivity to the signal strength μ_d in the context of limit setting, at a 95%CL for the different MSR cut hypotheses. Figure A.8 shows the local significance limit has a very weak (flat) dependence on the MSR width for low m_{Z_d}. The local significance limit develops a stronger dependence on the MSR width for $m_{Z_d} > 35$ GeV. This suggests we should use a MSR that is modulated by the shape of the background. It would be increased to a 3.5σ window at the lowest $m_{Zd} = 10$ GeV, but it would decrease as the background increases so that it reverts to the previous MSR cut of the 2.0σ window where the background is largest. In terms of the previous MSR terminology, the MSR cut has $m_{34}/m_{12} > 0.77$ at the di-lepton mass $m_{12} = 10$ GeV and $m_{34}/m_{12} > 0.85$ at $m_{12} = 64$ GeV, but the MSR modulation decreases as m_{Z_d} increases in linear step with the increasing background.

Figure A.9 shows the distribution of the total background after applying all the cuts except the MSR cut ($m_{34}/m_{12} > 0.85$). The distribution is well modeled phenomenologically by an exponential tail which is smoothly attached to the left hand side of a Gaussian peak. Such a compound function is used in the context of asymmetric peaks and has the form of equation A.2 (Medhat et al., 2005):

$$F(x_i) = \begin{cases} B_1 + B_2(x_i - X) + h \times e^{\frac{-(x_i-X)^2}{2\times\sigma^2}}, & x_i > X - T \\ B_1 + B_2(x_i - X) + h \times e^{\frac{T(2\times x_i - 2\times X + T)}{2\times\sigma^2}}, & x_i < X - T \end{cases} \tag{A.2}$$

where x_i corresponds to the average mass distribution $< m_{ll} >$, B_1 and B_2 are the two coefficients for a linear model of a compensating "background" to this skew peak shape, h is the height of the peak, X is the peak centroid, σ is the width of the Gaussian function, and T is the smooth matching point of the exponential tail to the Gaussian expressed as a positional offset from the peak centroid. All the parameters are extracted from a fit:

- Gaussian height $h = 3.73/2\text{GeV}$
- Gaussian centroid $X = 51.6$ GeV
- Gaussian width $\sigma = 16.6$ GeV
- Constant term in the background $B_1 = -2.62/2\text{GeV}$
- Linear term in the background $B_2 = -0.0266/(2\text{GeV})^2$
- Matching point offset from peak $T = 6.39$ GeV

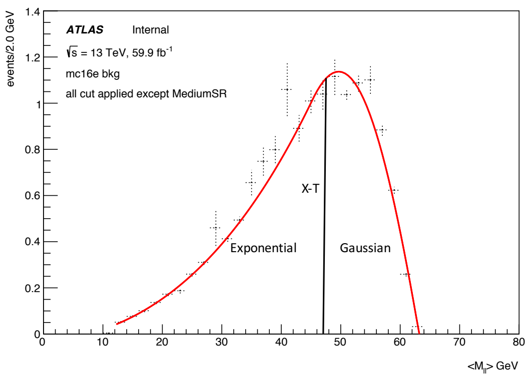

FIGURE A.9: $< m_{ll} >$ distribution of the total background

This background shape is then converted to a modulating function $f(m_{12})$ that will be normalized to a fraction varying from 100% to 0% as the background itself varies from its minimum to its maximum, as in Equation A.3.

$$f(m_{12}) = 1 - \frac{F(m_{12}) - F(10)}{F(49.64) - F(10)} \tag{A.3}$$

$f(m_{12})$ should verify:

$$f(m_{12}) = \begin{cases} f(m_{12}) = 1, & \text{if} \quad m_{12} = 10\text{GeV} \\ f(m_{12}) = 0, & \text{if} \quad m_{12} = 51.6\text{GeV} \end{cases} \tag{A.4}$$

Figure A.10 shows the shows the resulting shape of modulating function $f(m_{12})$. It is chosen to maintain the modulating function at 0% in the higher di-lepton mass region, after the background has reached its peak. This is done even though this shape of the background does actually decrease after the peak due to physical rather than systematic reasons. This is the conservative approach.

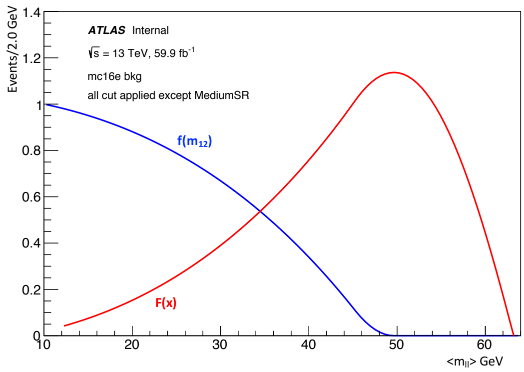

FIGURE A.10: $< m_{ll} >$ distribution of the total background and modulating function

Hence the new signal region is defined by:

$$m_{34} > 0.85 \times m_{12} - 0.1125 \times f(m_{12}) \times m_{12} \tag{A.5}$$

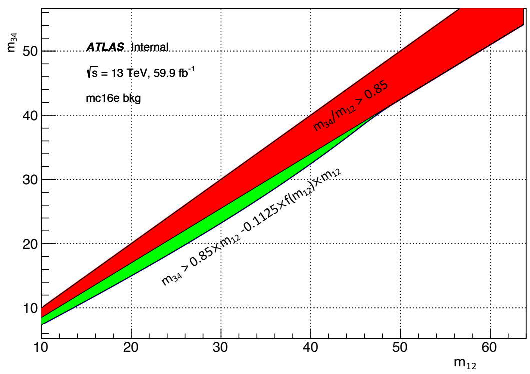

FIGURE A.11: New and old signal region

Finally, this modulating function is shown in the 2D plane of $(m_{34}\ ,\ m_{12})$ in Figure A.11. The old and the new MSR are indicated, as a red area and a red+green area respectively. Hence the cut $m_{34}/m_{12} > 0.85$ was replaced by the $m_{34} > 0.85 \times m_{12} - 0.1125 \times f(m_{12}) \times m_{12}$ for $m_{Z_d} < 49.65$ GeV, where f is a modulation function whose constants are obtained from optimization, for $m_{Z_d} > 49.65$ GeV the former medium signal region cut ($m_{34}/m_{12} > 0.85$) is used.

A.3 E'_{ab}/m_{4l} variable

The tight SR cut applied for both SR1 and SR2 use the kinematic variable E'_{ab}/m_{4l} which is defined as the energy component of the lepton pair's four-momentum in the center of momentum frame (CMF in units of the progenitor mass). It can be derived mathematically as follows:

- Consider $H \to Z_d Z_d \to 4\ell$, in the center of momentum frame (CMF) for the produced $Z_d Z_d$ (aka H rest frame), i.e:
  - $\vec{P}_{ab} + \vec{P}_{cd} = \vec{0} \Longrightarrow \vec{P}_{ab} \cdot \vec{P}_{cd} = -|\vec{P}_{ab}|^2 = -(E'_{ab})^2 + m^2_{ab}$
  - $E'_{ab} + E'_{cd} = m_{4\ell}$ [1]
- Some algebra with the relativistic energy-momentum conservation law:

$$(p'_{12} + p'_{34})^2 = m^2_{4\ell} \tag{A.6}$$
$$m^2_{12} + m^2_{34} + 2 \times (E'_{12}E'_{34} - \vec{P}'_{12}\vec{P}'_{34}) = m^2_{4\ell} \tag{A.7}$$
$$m^2_{12} + m^2_{34} + 2 \times [E'_{12}E'_{34} + (E'_{12})^2 - m^2_{12}] = m^2_{4\ell} \tag{A.8}$$
$$-m^2_{12} + m^2_{34} + 2 \times E'_{12}(E'_{12} + E'_{34}) = m^2_{4\ell} \tag{A.9}$$
$$-m^2_{12} + m^2_{34} + 2 \times E'_{12}(E'_{12} m_{4\ell}) = m^2_{4\ell} \tag{A.10}$$
$$\Longrightarrow E'_{12}/m_{4\ell} = \frac{1}{2}\left(1 + \frac{m^2_{12} - m^2_{34}}{m^2_{m4\ell}}\right) \tag{A.11}$$

- Equation A.11 shows that $\lim\limits_{\substack{(m_{ab}-m_{cd})\to 0 \\ m_{4\ell}\to\infty}} E'_{ab}/m_{4\ell} = \frac{1}{2}$.

The distribution of $E'_{ab}/m_{4\ell}$ is shown in Figure A.12 where we can observe the peak around 0.5.

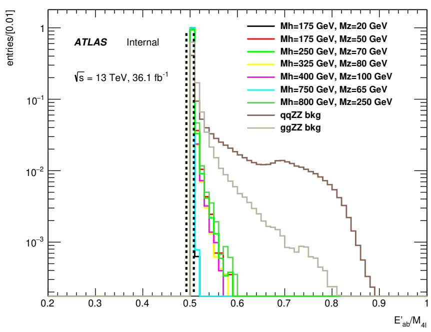

FIGURE A.12: E'_{ab}/m_{4l} signal and background distributions. The dotted line indicates the cut applied using this variable.

[1] prime (′) means for CMF

A dedicated study has been made on the correlation between the new variable E'_{ab}/m_{4l} and m_{cd}/m_{ab}, Figure A.13 is a scatter plot of E'_{ab}/m_{4l} vs m_{cd}/m_{ab}, where the mass of the Z_d dark boson is set to 50 GeV and the mass of the dark Higgs S is varied from 150 to 800 GeV. It shows some correlation between the two variables which can also be derived from Equation A.11 as following.

$$E'_{ab}/m_{4\ell} = -\frac{m_{ab} \times m_{cd}}{2 \times m_{4\ell}^2} \times (\frac{m_{cd}}{m_{ab}}) + 1/2 + \frac{m_{ab}^2}{2 \times m_{4\ell}^2} \tag{A.12}$$

Where the term $-\frac{m_{ab} \times m_{cd}}{2 \times m_{4\ell}^2}$ can be interpreted as the negative slope observed in Figure.A.13. The figure shows also the larger is the mass of the parent particle, the more E'_{ab}/M_{tot} is centered around 1/2 as expected. Table A.5 shows the ratio of efficiencies $(\epsilon_{(S)}/\epsilon_{(B)})$ between signal and background computed by applying either m_{cd}/m_{ab} or $E'_{ab}/m_{4\ell}$. This study is done at the level of quarkonia veto cut where different signal mass points, $(m_S, m_{Z_d}) = (125, 50), (400, 50)$ and $(755, 65)$ GeV were considered and the two main backgrounds gluon-gluon fusion (ggF) and SM $ZZ*$ to 4ℓ. The signal region cut is defined by $m_{cd}/m_{ab} > 0.85$ (before optimization) so for every signal mass point, an equivalent cut on E'_{ab}/m_{4l} was applied derived from Equation A.12. For instance for the mass point $(m_S, m_{Z_d}) = (125, 50)$ GeV, $m_{cd}/m_{ab} > 0.85$ is equivalent to $E'_{ab}/m_{4l} < 0.522$. Table A.5a and A.5b where the dark Higgs is much heavier than SM Higgs, shows a cut on $E'_{ab}/m_{4\ell}$ gives a better efficiency than a cut on $m_{34}/m12$, while in Table A.5a a better efficiency is observed with m_{cd}/m_{ab}.

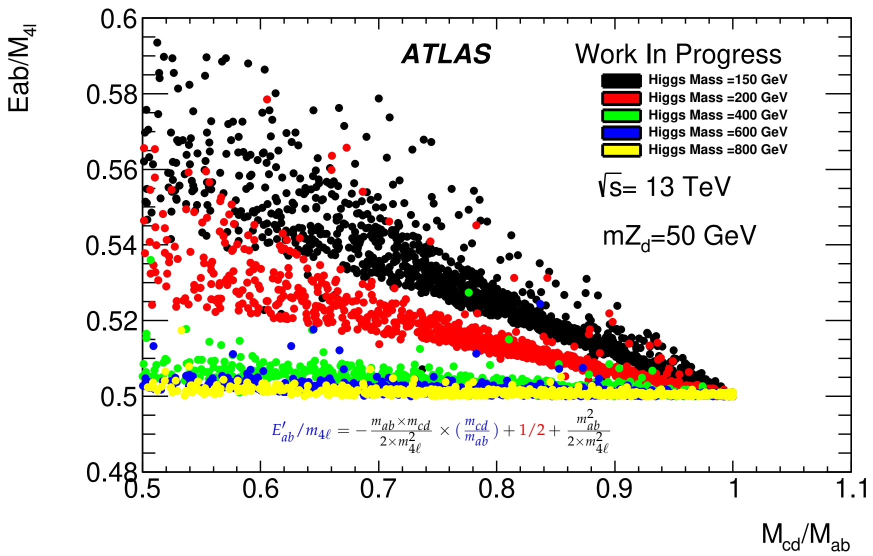

FIGURE A.13: E'_{ab}/m_{4l} vs m_{cd}/m_{ab}. The mass of the Z_d is set to 50 GeV and the mass of the dark Higgs S varied from 150 to 800 GeV

Given the correlation of the two variables, it appears to be necessary to check if it worth while to apply both of them. Table A.6 shows the number of events which survive from the $E'_{ab}/m_{4\ell}$ after applying m_{cd}/m_{ab} cuts. Different signal mass points are considered and the two main backgrounds gluon-gluon fusion (ggF) and SM $ZZ*$ to 4ℓ. The combination of all channels is also considered ($4e$, $2e2\mu$, 4μ). One can observe that adding the cut on $E'_{ab}/m_{4\ell}$ reduces the background by almost a factor of 2 while losing only few percent in signal efficiency, which remains above 90% (and close to 95%) in most cases.

$m_s = 125$ and $m_{Z_d} = 50$ GeV				
Cuts Applied	Signal	ggZZ	qqZZ	$\epsilon_{(S)}/\epsilon_{(B)}$
QVeto	1.352×10^4	1.007×10^5	1.914×10^6	—
Applying cuts on: m_{cd}/m_{ab} or $E'_{ab}/m_{4\ell}$				
$m_{cd}/m_{ab} > 0.85$	1.307×10^4	8.104×10^4	8.813×10^5	2.024 ± 0.008
$E'_{ab}/m_{4\ell} < 0.522$	1.294×10^4	8.232×10^4	9.929×10^5	1.793 ± 0.009

(A)

$m_s = 400$ and $m_{Z_d} = 50$ GeV				
Cuts Applied	Signal	ggZZ	qqZZ	$\epsilon_{(S)}/\epsilon_{(B)}$
QVeto	2.836×10^4	1.007×10^5	1.914×10^6	—
Applying cuts on: m_{cd}/m_{ab} or $E'_{ab}/m_{4\ell}$				
$m_{cd}/m_{ab} > 0.85$	2.748×10^4	8.104×10^4	8.813×10^5	2.028 ± 0.006
$E'_{ab}/m_{4\ell} < 0.522$	2.71×10^4	2.118×10^4	3.23×10^5	5.594 ± 0.002

(B)

$m_s = 750$ and $m_{Z_d} = 65$ GeV				
Cuts Applied	Signal	ggZZ	qqZZ	$\epsilon_{(S)}/\epsilon_{(B)}$
QVeto	3.182×10^4	1.007×10^5	1.914×10^6	—
Applying cuts on: m_{cd}/m_{ab} or $E'_{ab}/m_{4\ell}$				
$m_{cd}/m_{ab} > 0.85$	3.072×10^4	8.104×10^4	8.813×10^5	2.021 ± 0.006
$E'_{ab}/m_{4\ell} < 0.522$	3.027×10^4	2.118×10^4	3.23×10^5	9.778 ± 0.001

(C)

TABLE A.5: Ratio of efficiencies between signal and background computed by applying either m_{cd}/m_{ab} or $E'_{ab}/m_{4\ell}$ for different signal mass points, $(m_S, m_{Z_d}) = (125, 50), (400, 50)$ and $(755, 65)$

Surviving Events (Efficiency)			
Samples (GeV)	**all channels**	$\mathbf{M_{cd}/M_{ab}}$	$\mathbf{E'_{ab}/M_{4l}}$
M_s= 175 , M_{Z_d}= 20	20314(100%)	19747(97.21%)	19737(97.16%)
M_s= 175 , M_{Z_d}= 50	20149(100%)	19415(96.36%)	18487(91.75%)
M_s= 250, M_{Z_d}= 70	24128(100%)	23217(96.22%)	22352(92.64%)
M_s= 250, M_{Z_d}= 70 [2]	23926(100%)	23037(96.28%)	22113(92.42%)
M_s= 325, M_{Z_d}= 80	26306(100%)	25329(96.26%)	24942(94.81%)
M_s= 400, M_{Z_d}= 100	28243(100%)	27122(95.21)	26689(94.50%)
M_s= 750, M_{Z_d}= 65	31750(100%)	30600(96.38%)	30586(96.33%)
M_s= 800, M_{Z_d}= 250	32881(100%)	31104(93.20)	28992(88.17%)
ggFh background	86462(100%)	17375(20.04%)	8911(10.30%)
SM $ZZ*$ **to** 4ℓ **background**	$1.44e^6$(100%)	622126(42.73%)	402869(27.98%)

TABLE A.6: Events surviving from m_{cd}/m_{ab} or E'_{ab}/m_{ab} cuts, for different signal mass point hypothesis and the two main backgrounds, gluon-gluon fusion (ggF) and SM $ZZ*$ to 4ℓ.

.

Appendix B

m_{ab}, m_{cd} labeling used in additional scalar channel

For the high mass, Low mass and ZX channels m_{12}, and m_{34} labeling is used where m_{12} is the mass of the di-lepton closer to the mass of the Z boson. In the additional scalar channel, E'_{12}/m_{4l} vs m_{34}/m_{12} distribution in Figure B.1 and B.2 shows that this labeling causes a migration of the signal pattern from one frame to another, according to the child particle mass whether it is larger or smaller than the Z mass boson. To avoid this migration some other labeling system are tested:

- m_{ab}, m_{cd}; where m_{ab} is the higher mass of the two dileptons masses ($m_{ab} > m_{cd}$).
- m_{ld}, m_{nl}; where m_{ld} is the mass of the di-lepton which has the highest p_T.
- m_{ee}, $m_{\mu\mu}$; for the $2e2\mu$ channel.

Figure B.3 and B.4 show the $E'_{l_1 l_2}/m_{4l}$ vs m_{34}/m_{12} distribution, where the child particle mass is under the Z boson mass (Z_d = 20 GeV) for the SMZZ and the gluon-gluon fusion (ggF) background, for different labeling schemes as defined above. For the m_{ld}, m_{nl} and the m_{ee}, $m_{\mu\mu}$ labeling schemes, most of the signal is located in opposite diagonal quadrants, for the m_{12}, m_{34} labeling schemes most of the signal is located in the upper frame and for the m_{ab}, m_{cd} labeling scheme most of the signal is located in one quadrant. In Figure B.5 and B.6 the same conclusion can be drawn for the other labeling schemes except for the m_{12}, m_{34} case where most of the signal populates the lower quadrant.

Comparing these 4 types of labeling schemes it turns out that the m_{ab}, m_{cd} labeling scheme is the one more appropriate for the additional scalar analysis in the sense that it populates only one frame whatever the child particle mass is compared to the m_{ld}, m_{nl} labeling scheme, and also it can be generalized to all the three channels compared to the m_{nl} , m_{ee} labeling scheme which is appropriate only for $2e2\mu$. Actually the m_{ab}, m_{cd} labeling scheme is just a generalization of the m_{12}, m_{34} labeling scheme because m_{12} is defined as the mass of the di-lepton closer to the mass of the Z boson, in the high mass, low mass and ZX channels, which is the same as defining $m_{12} > m_{34}$ because of the kinematic constraint ($m_{Z_d} < m_H/2$) of these channels.

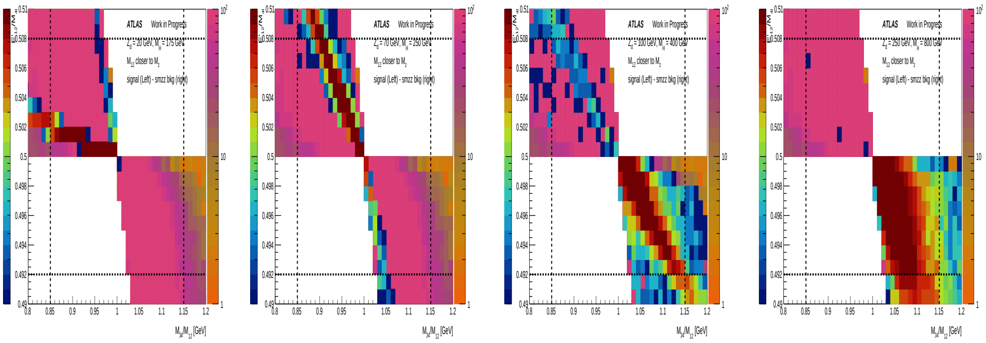

FIGURE B.1: $E'_{l_1 l_2}/m_{4l}$ vs m_{34}/m_{12} for different mass points: s = 175 GeV, Z_d = 20 GeV, s = 250 GeV, Z_d = 70 GeV, s = 400 GeV, Z_d = 100 GeV,s = 800 GeV, Z_d = 250 GeV, the intensity bar on left hand refers to the signal, and the one on the right hand refers to the SMZZ background

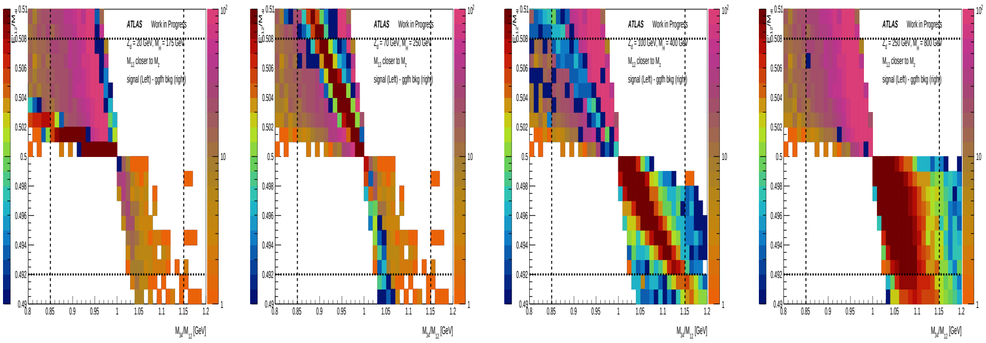

FIGURE B.2: $E'_{l_1 l_2}/m_{4l}$ vs m_{34}/M_{12} for different mass points: s = 175 GeV, Z_d = 20 GeV, s = 250 GeV, Z_d = 70 GeV, s = 400 GeV, Z_d = 100 GeV,s = 800 GeV, Z_d = 250 GeV, the intensity bar on left hand refers to the signal, and the one on the right hand refers to the ggfh background

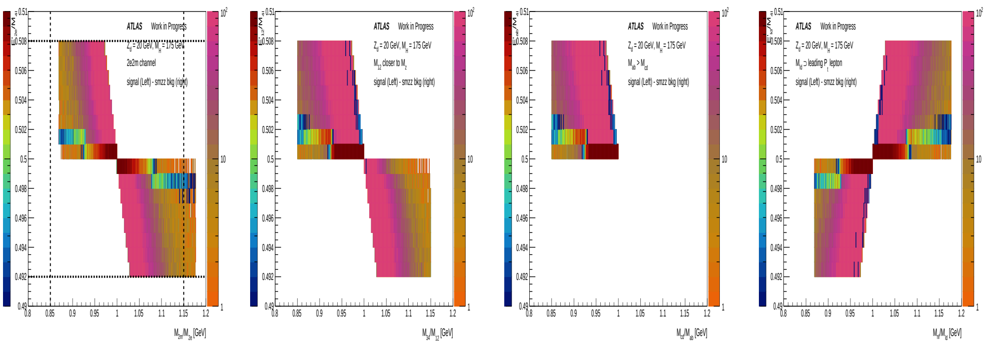

FIGURE B.3: $E'_{l_1 l_2}/m_{4l}$ vs m_{34}/m_{12} for different labeling with a child particle under Z boson mass: s = 175 GeV, Z_d = 20 GeV, the intensity bar on left hand refers to the signal, and the one on the right hand refers to the SMZZ background

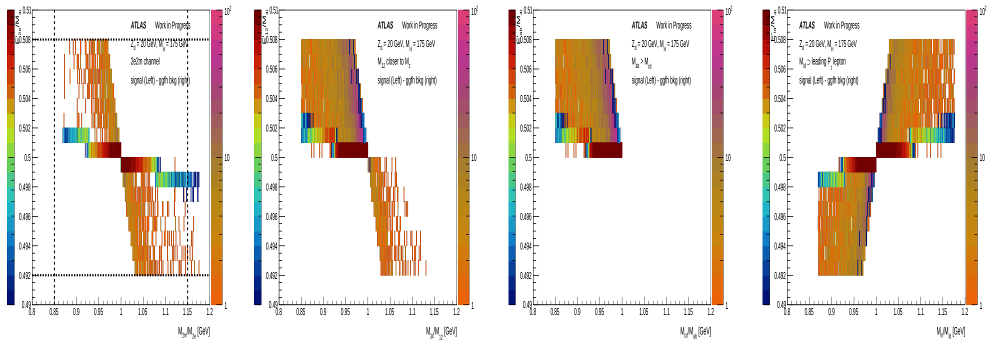

FIGURE B.4: $E'_{l_1 l_2}/m_{4l}$ vs M_{34}/m_{12} for different labeling with a child particle under Z boson mass: s = 175 GeV, Z_d = 20 GeV, the intensity bar on left hand refers to the signal, and the one on the right hand refers to the ggfh background

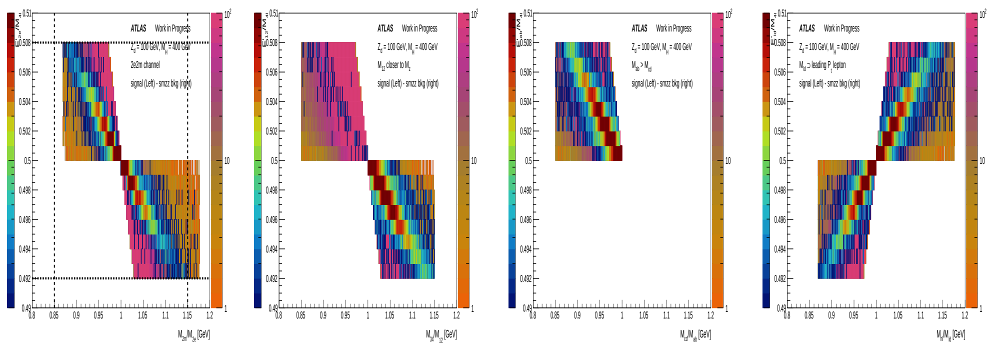

FIGURE B.5: $E'_{l_1 l_2}/M_{4l}$ vs M_{34}/M_{12} for different labeling with a child particle above Z boson mass: s = 400 GeV, Z_d = 100 GeV, the intensity bar on left hand refers to the signal, and the one on the right hand refers to the SMZZ background

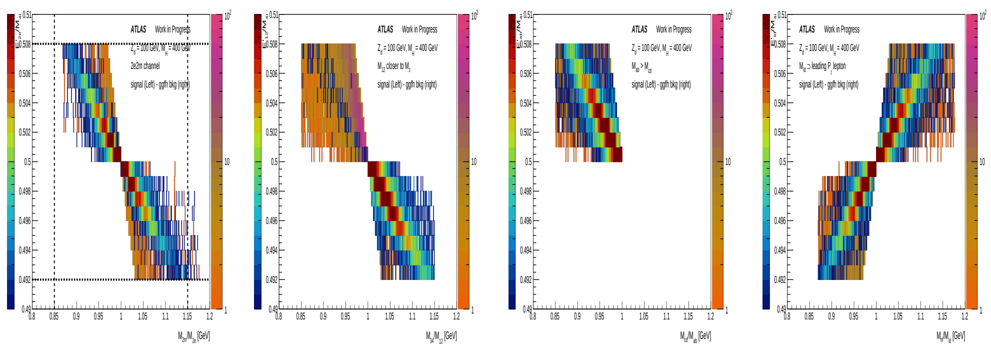

FIGURE B.6: $E'_{l_1 l_2}/M_{4l}$ vs M_{34}/M_{12} for different labeling with a child particle above Z boson mass: s = 400 GeV, Z_d = 100 GeV, the intensity bar on left hand refers to the signal, and the one on the right hand refers to the ggfh background

Appendix C

Signal Modeling

C.0.1 Shape of the $\langle m_{\ell\ell} \rangle$ observable for signal

This analysis follows closely the statistical method presented in the previous paper which used 36 fb^{-1} of data at 13 TeV (The ATLAS collaboration et al., 2018). The signal is modelled by a Gaussian distribution of the $\langle m_{\ell\ell} \rangle$ observable, with mean and standard deviation dependent on the true boson mass. For the HAHM and 2HDM+a models, the hypothetical bosons have negligible mass width, so the aforementioned parameters depend only on the mass scale and resolution of the detector and are thus model-independent. Figure C.1 shows some example Gaussian fits to generated signal samples. It is seen that there is a scale miscalibration of approximately -2% for ee dileptons, and -0.5% for $\mu\mu$ dileptons. The narrower mass resolution in the 4μ channel also makes the radiative losses more apparent. The shaded regions in Figure C.1(d) indicate the regions where the loose SR and quarkonia veto cuts suppress the signal yield. The signal model shape must be truncated to exclude these regions. These regions were estimated to be bounded by $\langle m_{\ell\ell} \rangle$ of 1.0, 2.6 to 4.3, and 8.1 to 11.8.

Figure C.2 shows the result of the Gaussian fits as a function of the true boson mass. The mean, standard deviation, and goodness of fit are shown. The mean and standard deviation have been divided by the true boson mass (and the mean is also shifted, to show deviations from the mean=m_{Zd} parameterization), and both have been scaled by a factor of 100.

C.0.2 Model-independent efficiency

The efficiency in a given channel c is defined as:

$$\epsilon_c = \frac{N^c_{\text{reco}}}{N^c_{\text{fid}}}, \tag{C.1}$$

where N^c_{reco} is the expected yield in the medium SR in channel c, computed using all reweighting and efficiency scale factors, and N^c_{fid} is the expected yield in the fiducial volume, computed using just generator-level event weights. This definition of efficiency therefore includes impurities: contributions to the numerator from events outside of the fiducial volume. For the selections and fiducial definition in this analysis, the impurity level was checked and found to be negligible.

Figure C.3 shows a comparison of the efficiencies measured using the two benchmark models of this analysis. Only the 4μ channel can be compared. While there is a small bias towards lower efficiency in the aa model, the efficiencies are compatible within the statistical uncertainties.

The model-independent efficiencies are shown in Figure C.4 as a function of the boson mass, m_X. The efficiencies were estimated using the $H \to Z_d Z_d \to 4\ell$ signal

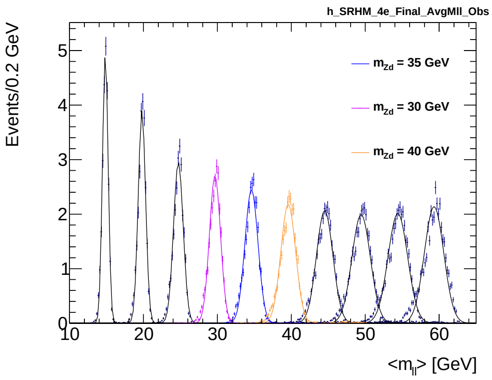

(A) $4e$ channel

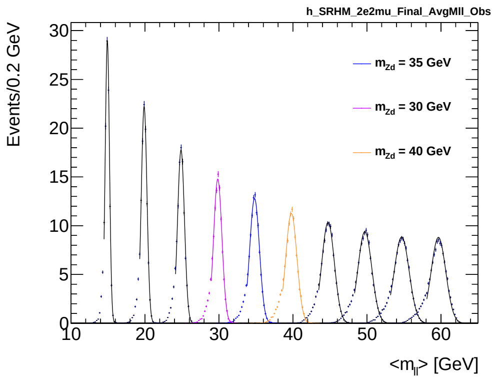

(B) $2e2\mu$ channel

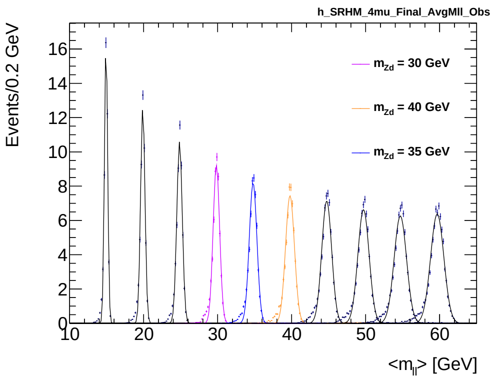

(C) 4μ channel

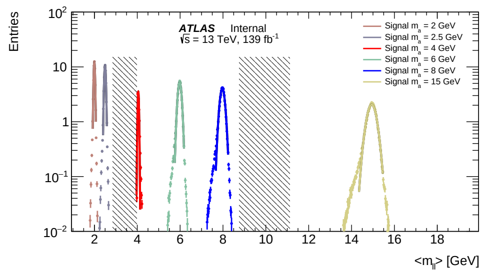

(D) 4μ low-mass channel

FIGURE C.1: Examples of Gaussian fits to the generated $H \to Z_d Z_d \to 4\ell$ signal samples in the medium SR (figure a, b, and c), and with the low-mass selection after the impact parameter requirement (figure d). The shaded regions in figure d indicate the regions where the loose SR and quarkonia veto cuts come into play and reduce the signal yield to zero. The signal model shape must be suppressed in these regions.

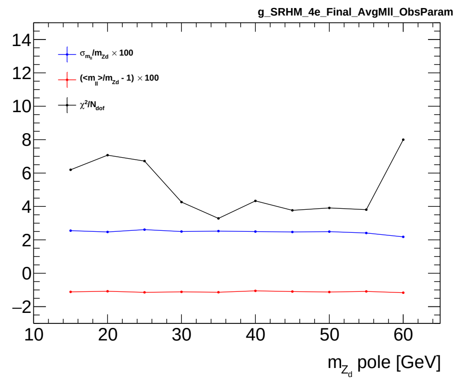

(A) $4e$ channel

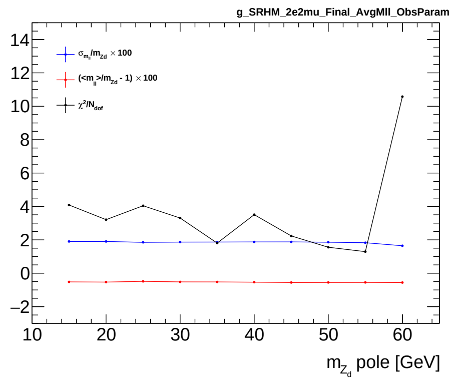

(B) $2e2\mu$ channel

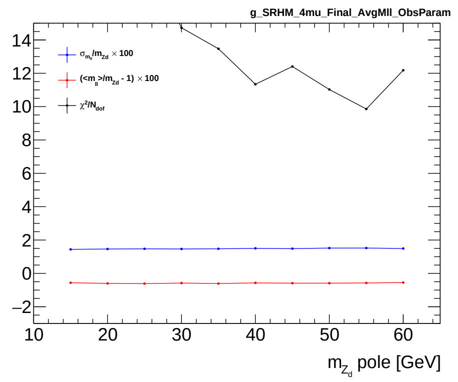

(C) 4μ channel

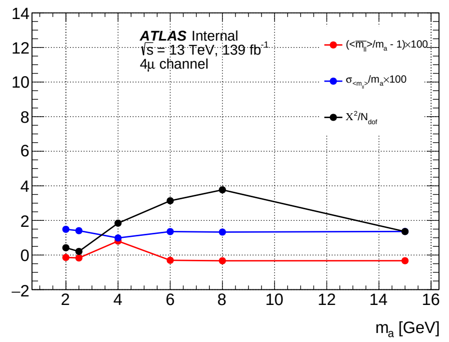

(D) 4μ low-mass channel

FIGURE C.2: Parameters for a Gaussian signal model in the $\langle m_{ll} \rangle$ observable, $\langle \bar{m}_{ll} \rangle_c$ and $\sigma^c_{\langle m_{ll} \rangle}$, based on Gaussian fits to the generated $H \rightarrow Z_d Z_d \rightarrow 4\ell$ signal samples in the medium SR (figure a,b,c) and after the impact parameter cut low the low-mass selection (figure d). These extracted model parameters are assumed to be model independent for any narrow-width resonance model. The red line shows the relative mean of the fitted Gaussian: i.e. the mass scale is slightly miscalibrated (approximately 0.5% in the $\mu\mu$ channel and 2% in the ee channel, primarily due to final state radiative losses). The blue line shows the relative standard deviation of the fitted Gaussian (scaled by a factor of 100), which is consistent with $\frac{1}{2}\sqrt{\sigma^2_{ll1} + \sigma^2_{ll2}}$, where $\sigma_{ll1,2}$ are the mass resolutions in each dilepton channel (approximately 1.9% for $\mu\mu$ and 3.5% for ee). The effect of the constant term in the mass resolution can be seen by the rise is resolution for the smallest masses in figure d. The black line shows the goodness-of-fit for the Gaussian - while a Crystal Ball would be expected to provide a better model than a Gaussian, the Gaussian model is judged to be sufficient for the purposes for limit setting.

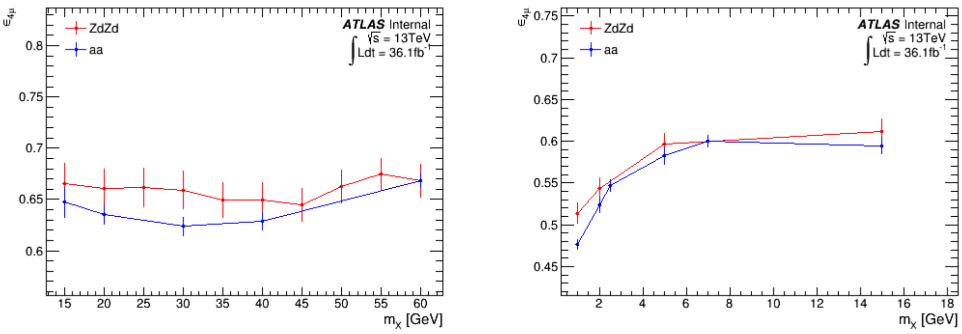

(A) High mass 4μ channel

(B) Low mass 4μ channel

FIGURE C.3: Comparison of the efficiencies as measured with the two benchmark models used in this analysis. TODO: update this figure to release 21, currently use rel 20.7 old plots.

samples. Linear interpolation is used to extrapolate between the generated mass points.

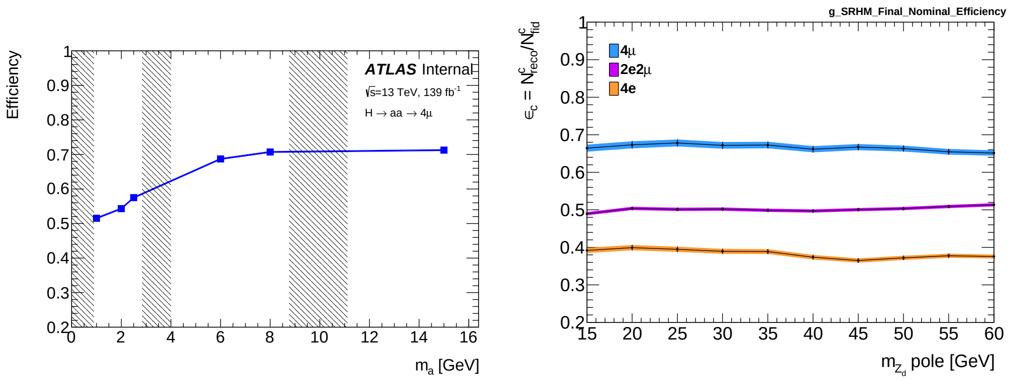

(A) All channels

(B) All channels

FIGURE C.4: Efficiency with respect to the fiducial volumes defined in section 8.7.1: separate fiducial volumes are defined above and below $m_X = 15\text{GeV}$. The inner band of each curve is the MC-statistical uncertainty, and the outer band is the systematic uncertainty. The shaded regions in the low-mass region correspond to where the efficiency will drop to zero due to the quarkonia veto. The step-change in the 4μ efficiency at the $m_X = 15\text{GeV}$ boundary is due to the differences in the fiducial volume definitions in the high and low mass regions: the additional ΔR requirement improves the signal efficiency.

C.0.3 Model-dependent acceptances

The acceptance in a given channel c for a given model for Higgs boson decay to light bosons X is defined as:

$$\alpha_c^X = \frac{N_{\text{fid}}^{Xc}}{N_{\text{tot}}^{Xc}}, \tag{C.2}$$

where N_{tot}^{Xc} is the signal yield in channel c across the full phase space for that particular model, and N_{fid}^{Xc} is the yield of that particular model in the fiducial volume. Note that the denominator does not depend on the channel, they are simply total generated truth yields which are the same for all channels; α_c^X therefore incorporates the branching fraction for that specific channel[1]. By defining acceptance in this way, the statistical analysis performed in Section 8.7 can extract a model-dependent *total cross-section*, $\sigma_H \text{BR}(H \to XX \to 4\ell)$, by using the following expression in the model for each channel:

$$\begin{aligned} N_{\text{expected}}^{c}\left(\langle m_{\ell\ell}\rangle\right) = N_{\text{bkg}}^{c}\left(\langle m_{\ell\ell}\rangle\right) + \sigma_H \text{BR}(H \to XX \to 4\ell) \\ \times \mathcal{L}\frac{\Gamma_X^c}{\Gamma_X^{4\ell}}\alpha_c^X \epsilon_c \text{Gaus}\left(\langle m_{\ell\ell}\rangle, \langle \bar{m}_{\ell\ell}\rangle_c, \sigma_{\langle m_{\ell\ell}\rangle}^c\right), \end{aligned} \tag{C.3}$$

where $\Gamma_X^c / \Gamma_X^{4\ell}$ is the partial fraction for decays of X across the three channels with respect to the partial fraction for any 4ℓ decay. In the $H \to Z_d Z_d \to 4\ell$ model, these fractions are 0.25:0.5:0.25 for the $4e$: $2e2\mu$: 4μ channels, and 0:0:1 for the aa model. The statistical model for a given limit combines all channels where the partial fraction ratio is not zero (i.e. the $4e$ and $2e2\mu$ channels are not part of the statistical model when setting limits for the aa benchmark model). The model-dependent acceptances for the two benchmark models ($H \to Z_d Z_d \to 4\ell$ and $H \to aa$) studied in this analysis are shown in Figure C.5.

C.0.4 Mathematical derivation for the relation between fiducial cross section and efficiency

All the mathematical formulae used for fiducial and total cross section calculation are derived in this section and the next. The efficiency for a given channel c is

$$\epsilon_c = \frac{N_{\text{reco}}^c}{N_{\text{fid}}^c}, \tag{C.4}$$

where N_{reco}^c is the **reconstructed** yield in the **medium SR**, and N_{fid}^c is the **truth** yield in the **fiducial volume**.

At reconstructed level in the Signal Region, pure yield:

$$N_{\text{exp.}}^c\left(\langle m_{\ell\ell}\rangle\right) = N_{\text{bkg}}^c + N_{\text{reco-signal}}^c \tag{C.5}$$

$$= N_{\text{bkg}}^c + N_{\text{fid-signal}}^c \times \frac{N_{\text{reco-signal}}^c}{N_{\text{fid-signal}}^c} \tag{C.6}$$

$$= N_{\text{bkg}}^c + N_{\text{fid-signal}}^c \times \epsilon_c \tag{C.7}$$

[1] This is really the fraction of the total sample that fell in the given channel. In the $H \to Z_d Z_d \to 4\ell$ model, these fractions will be approximately 0.25:0.5:0.25 for the $4e$:$2e2\mu$:4μ channels, but for the aa model there is negligible branching to electrons, so the fractions are effectively 0:0:1.

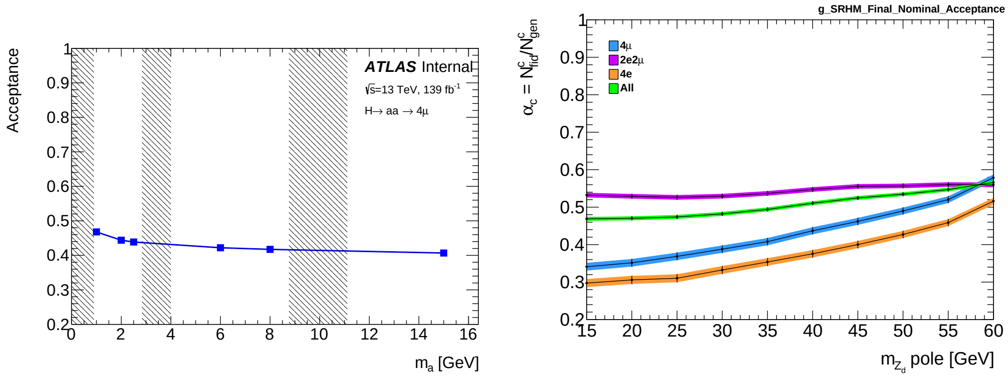

(A) All channels (B) All channels

FIGURE C.5: Acceptance of each model into the fiducial volumes defined in section 8.7.1: separate fiducial volumes are defined above and below $m_X = 15$GeV. The shaded regions indicate where the effect of the quarkonia veto (which is part of the low-mass fiducial volume definition) invalidates the interpolated acceptance. The change in acceptance at 15 GeV is due to the change of fiducial phase space, with additional cuts applied above 15 GeV. The steep rise in acceptance in the high-mass selection in the 4μ and 4ℓ channels is due to the Z Veto, which is cutting on the alternative mass pairings m_{32} and m_{14}. This cut is not applicable to the $2e2\mu$ channel, which therefore has a higher acceptance.

At reconstructed level in the Signal Region, with shape:

$$N^c_{\text{exp.}}\left(\langle m_{\ell\ell}\rangle\right) = N^c_{\text{bkg}} + \sigma^c_{\text{fid}} \times \mathcal{L}\text{umi} \times \epsilon_c \times \text{Gaus}\left(\langle m_{\ell\ell}\rangle, \bar{\langle m_{\ell\ell}\rangle}_c, \sigma^c_{\langle m_{\ell\ell}\rangle}\right) \tag{C.8}$$

C.0.5 Mathematical derivation for the relation between total cross section and efficiency and acceptance

To derive acceptance and total cross section for a specific model, we need the acceptance in a given channel c for Higgs boson decays to light bosons, X:

$$\alpha^X_c = \frac{N^{Xc}_{\text{fid}}}{N^{Xc}_{\text{tot}}}, \tag{C.9}$$

where N^{Xc}_{tot} is the truth yield in the full phase space in channel c **(all truth events)**, and N^{Xc}_{fid} is the truth yield in the fiducial volume in channel c.

At reconstructed level, in Signal Region, pure yield ("X" is omitted below for convenience)

$$N_{\text{exp.}}\left(\langle m_{\ell\ell}\rangle\right) = N_{\text{bkg}}\left(\langle m_{\ell\ell}\rangle\right) + N_{\text{reco-signal}}, \text{ where} \tag{C.10}$$

$$N_{\text{reco-signal}} = N_{\text{tot}} \times \frac{N_{\text{reco}}}{N_{\text{tot}}}, \text{ and} \tag{C.11}$$

$$N_{\text{tot}} = \sigma^{\text{tot}}_{(H\to XX\to 4\ell)} \times \mathcal{L}\text{umi} \tag{C.12}$$

$$
\begin{aligned}
\frac{N_{\text{reco}}}{N_{\text{tot}}} &= \frac{1}{N_{\text{tot}}} \times \sum_c N_{\text{reco}}^c = \frac{1}{N_{\text{tot}}} \times \sum_c \left[N_{\text{fid}}^c \times \frac{N_{\text{reco}}^c}{N_{\text{fid}}^c} \right] \\
&= \sum_c \left[\frac{N_{\text{fid}}^c}{N_{\text{tot}}} \times \frac{N_{\text{reco}}^c}{N_{\text{fid}}^c} \right] = \sum_c \left[\frac{N_{\text{tot}}^{\text{c}}}{N_{\text{tot}}} \times \frac{N_{\text{fid}}^c}{N_{\text{tot}}^{\text{c}}} \times \epsilon_c \right] \\
&= \sum_c \left[\frac{\Gamma_X^c}{\Gamma_X^{4\ell}} \times \alpha_c^X \times \epsilon_c \right], \text{where}
\end{aligned}
$$

$$
\frac{N_{\text{tot}}^{\text{c}}}{N_{\text{tot}}} = \frac{\sigma^{\text{c,tot}}_{(H \to XX \to 4\ell(c))} \times \mathcal{L}\text{umi}}{\sigma^{\text{tot}}_{(H \to XX \to 4\ell)} \times \mathcal{L}\text{umi}} \tag{C.13}
$$

$$
= \frac{\sigma_H \times BR(H \to XX \to 4\ell(c))}{\sigma_H \times BR(H \to XX \to 4\ell)} \tag{C.14}
$$

$$
= \frac{\Gamma_{H \to XX \to 4\ell(c)}}{\Gamma_{H \to XX \to 4\ell}} = \frac{\Gamma_X^c}{\Gamma_X^{4\ell}} \tag{C.15}
$$

At reconstructed level, in Signal Region, with shape

$$
\begin{aligned}
N_{\text{exp.}}\left(\langle m_{\ell\ell} \rangle\right) = N_{\text{bkg}}\left(\langle m_{\ell\ell} \rangle\right) + \sigma^{\text{tot}}_{(H \to XX \to 4\ell)} \times \mathcal{L}\text{umi} \\
\times \sum_c \left[\frac{\Gamma_X^c}{\Gamma_X^{4\ell}} \times \alpha_c^X \times \epsilon_c \times \text{Gaus}\left(\langle m_{\ell\ell} \rangle, \langle \bar{m}_{\ell\ell} \rangle_c, \sigma^c_{\langle m_{\ell\ell} \rangle} \right) \right]
\end{aligned} \tag{C.16}
$$

Appendix D

kappa derivation

$$\mu_d = \frac{\Gamma(H \to Z_d Z_d).BR(Z_d \to ll).BR(Z_d \to ll)}{[\Gamma_{SM} + \Gamma(H \to Z_d Z_d)].[BR(H \to ZZ^* \to 4l)]_{SM}} \tag{D.1}$$

Let Q, T, U be:

$$Q = \Gamma(H \to Z_d Z_d) \tag{D.2}$$

$$T = BR(Z_d \to ll) \tag{D.3}$$

$$U = BR(H \to ZZ^* \to 4l) \tag{D.4}$$

So μ_d becomes

$$\mu_d = \frac{Q.T.T}{[\Gamma_{SM} + Q].U} \tag{D.5}$$

And Q:

$$Q = \frac{\Gamma_{SM} - U\mu_d}{T.T - U\mu_d} \tag{D.6}$$

$$Q = \Gamma(H \to Z_d Z_d) = \frac{K^2 v^2}{32\pi m_h}\sqrt{1 - \frac{4m_{Z_d}^2}{m_h^2}}\frac{(m_h^2 + 2m_{Z_d}^2)^2 - 8(m_h^2 - m_{Z_d}^2)m_{Z_d}^2}{(m_h^2 - m_s^2)^2} \tag{D.7}$$

K' is defined as following:

$$K'^2 = \frac{(Km_h^2)^2}{(m_h^2 - m_s^2)^2} \Rightarrow (m_h^2 - m_s^2)^2 = \frac{(Km_h^2)^2}{K'^2} \tag{D.8}$$

Hence Q becomes:

$$Q = \frac{v^2}{32\pi m_h}\sqrt{1 - \frac{4m_{Z_d}^2}{m_h^2}}\frac{(m_h^2 + 2m_{Z_d}^2)^2 - 8(m_h^2 - m_{Z_d}^2)m_{Z_d}^2}{m_h^4}K'^2 \tag{D.9}$$

if we say (6)=(9), it comes:

$$\frac{\Gamma_{SM} - U\mu_d}{T.T - U\mu_d} = \frac{v^2}{32\pi}\sqrt{1 - \frac{4m_{Z_d}^2}{m_h^2}}\frac{(m_h^2 + 2m_{Z_d}^2)^2 - 8(m_h^2 - m_{Z_d}^2)m_{Z_d}^2}{m_h^5}K'^2 \tag{D.10}$$

And then K' becomes:

$$K'^2 = \frac{\Gamma_{SM} - U\mu_d}{T.T - U\mu_d} \frac{32\pi m_h^5}{v^2[(m_h^2 - 2m_{Z_d}^2)^2 - 8(m_h^2 - m_{Z_d}^2)m_{Z_d}^2]} \frac{1}{\sqrt{1 - \frac{4m_{Z_d}^2}{m_h^2}}} \tag{D.11}$$

Or Just

$$K'^2 = \Gamma(H \to Z_d Z_d) \frac{32\pi m_h^5}{v^2[(m_h^2 - 2m_{Z_d}^2)^2 - 8(m_h^2 - m_{Z_d}^2)m_{Z_d}^2]} \frac{1}{\sqrt{1 - \frac{4m_{Z_d}^2}{m_h^2}}} \tag{D.12}$$

Appendix E

Report on my qualification task

E.1 Introduction

As part of my PhD study, I undertook a scientific analysis whose subject is "the search for a dark vector boson and a new scalar with the ATLAS detector". In parallel, I carried out a qualification task in the New Small Wheel which is mandatory for any physicist to become an Author in ATLAS. The NSW is a huge detector component that is being developed and built. Sub-components are being manufactured all over the world by institutes and companies. For instance, some of its components have been developed at INFN (Italy), Germany, Saclay (France), Dubna (Russia), Thessaloniki (Greece), CERN etc... During my qualification task, I had the opportunity to be part of this huge project under the supervision of Paolo Iengo whose I acknowledged already his help and devotion during all my service task.
The scientific search, its motivation, the experimental setups used to carry it out, the methodology and technique used as well as the results are described in the main thesis, from Chapter 1 to 9. In this report, my qualification task is described. It starts with:

- an overview of the New Small Wheel project in Section E.2;
- a description of the Micromegas Detector technology in Section E.3;
- a description of the shifts that I have been taking on the Micromegas in Section E.4;
- a description of a software tool that I developed to further inspect some components of the Micromegas detector in Section E.5.

Then the conclusion in Section E.6.

E.2 The New Small Wheel (NSW) project

Since 2018 the LHC entered a long shutdown for the phase I upgrade. The High-Luminosity LHC (HL-LHC) expected is around 2-3$\times 10^{-34}$cm^{-2}s^{-1} corresponding to 55-80 mean interaction per bunch crossing and 100 fb^{-1} of data collection. This comes along with innovative technologies that are being developed in the ATLAS experiment to take advantage of this high luminosity ever reached. The upgrade will focus mainly on the Level-1 (LV1) trigger to maintain a high trigger efficiency in a condition of high luminosity that the current equipment couldn't handle. In this context, the forward muon-tracking region known as the Small Wheel and located in

the Muons Spectrometer (MS) will be replaced by the New the Small Wheel (NSW). It will be installed in the forward region $1.3 < |\eta| < 2.7$ of the ATLAS detector.
The NSW is designed to operate in a high background radiation environment with a good real-time spatial and resolution. It needs about 2200 boards of size up to 0.5x2 m^2 for a total active surface of 1200 m^2. It is an unprecedented project for a micro-patter gaseous detector like micromegas. It will enable both tracking and triggering with high precision. For these purposes, two technologies are being developed; the small-strip Thin Gap Chambers (sTGC) and the Micromegas (MM) detector planes. The primary role of the sTGC is for triggering with an angular resolution of 1 mrad and a response time within 1μs. The MM is devoted for tracking with a spatial resolution less than 100 μm. However, these two technologies complement each other. For instance, in addition to the sTGC, the MM will also contribute for triggering which improves the redundancy, the robustness and the coverage of the forward trigger.
Figure E.1 gives an overview of the NSW. It consists of 16 detectors planes (or sectors) in 2 multilayers, 8 larges and 8 smalls. Four sTGC and four MM constitute each multilayers arranged in sandwich such as sTGC – MM – MM – sTGC. This arrangement enables to maximize the distance between the sTGCs of the two multilayers.

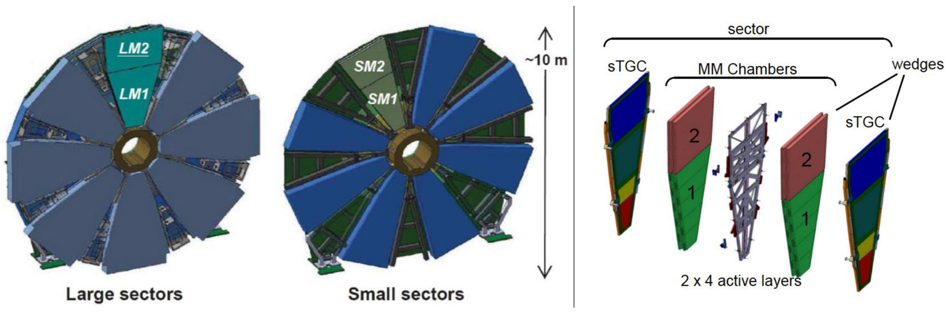

FIGURE E.1: Overall view of the New Small Wheel. Left: Views of the wheel highlighting the modules of the large sectors (LM1 and LM2) and the modules of the small ones (SM1 and SM2). Right: Enlarged view of a Large sector with two small-strip Thin Gap Chambers and two Micromegas quadruplets on both sides of the spacer frame (Manthos et al., 2019).

E.3 Micromegas detector technology

My qualification task was on the Micromegas Read Out (RO) Printed Circuit Boards (PCBs) so in this section, a short description is given to this key component of the NSW detector. As shown in Figure E.2, the MM consists of PCB containing the readout electrodes strips of 17 μm with 300 μm width. A kapton foil insulator of 50 μm separates the readout electrodes from the resistive strips. Sparks[1] are very dangerous for the detectors and can even damage the readout electronics hence, these resistive strips will act as spark protection. On top of the resistive strips'

[1] When the total number of electrons in the avalanche reaches a few 10^7, sparks can be experienced.

surface are deposited the pillars. The nominal height of the pillars is 128 μm [2] with a diameter of 230 μm. They are separated by a distance of 7.0 mm. On top of the pillars, there is a thin metallic mesh at 100-150 μm from the readout strips. It has a thickness of few millimeters and serves as conversion and drift region. The role of the pillars are very important since they define the amplification gap between the PCBs and the drift cathode once the electrically grounded metallic mesh is applied. These technologies being built by different companies and institutes need some quality control, investigations and inspections before the assembly. These tasks are crucial for the project and require high-quality person power. Hence, After a dedicating training, I joined the shift crew taking regular quality control/quality assurance (QCQA) shifts that's described in the following section.

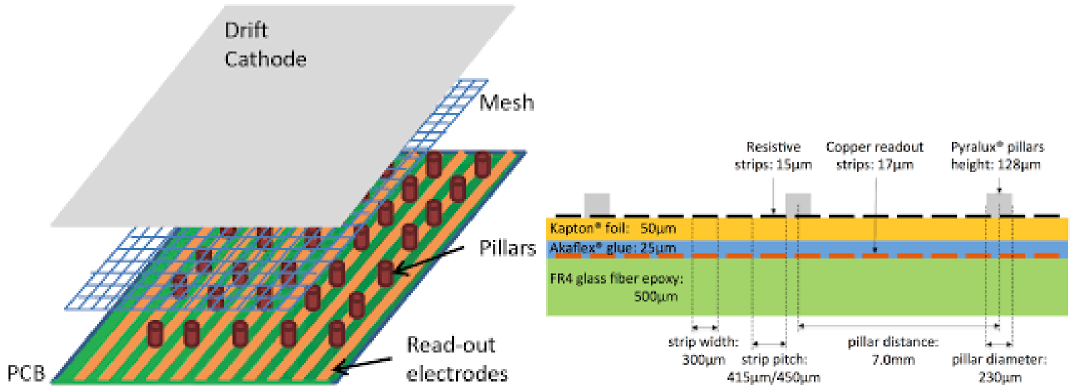

FIGURE E.2: Left: Operating principle of a Micromegas detector (Alexopoulos et al., 2010). Right: Schematic of the New Small Wheel Micromegas anode board layers and dimensions of its main structures (Kuger, F. and Iengo, P., 2018).

E.4 The quality control and quality assurance shifts

During the shift a lot of checks, inspections and verifications of the PCBs have to be carried out. The first step during the shift is to register the PCB ID using the logistic installed in the Lab to keep track of the board. Then a visualization for any possible defects on the board such as bubbles, bumps, dirt, scratches has to be done. A magnifying glasses or the Leica Stereo Microscope can be used to further inspect any suspicious feature. After this general inspection of the board more specific checks need be done.

A toplight inspection: The board is put on a table which is under bright lights and the following checks have to be carried out:

- the kapton foil: the kapton foil is located between the resistive strips and the readout strips. Its accuracy should be checked and also if it's correctly stacked with the glue foil and well glued. The distance between the position where the readout strips make their first kink and the end of the kapton foil should be measured. It should be ± 1.5 mm otherwise it has to be reported.

[2]This nominal value turns out to be 120 μm (2×60 μm) instead. The boards are produced by two different companies using different processes, so a difference of $\sim 1-2\mu$ m can be observed between boards coming from different companies.

- the coverlay: the coverlay on top of the silver lines[3] should be checked if it is free from any bubbles or spikes. This check is done using the Leica Stereo Microscope. Finding a bubble (if it exists) is very important, it avoids fatal short circuit even after months of normal detector operation.
- the connector: at this step, the quality of the copper strip etching needs to be estimated using the USB microscope.

High Voltage (HV) connector checks: This step presents a checklist containing all the checks that need to be done on the HV connector. It starts with an inspection of the silver line; if it's covered by the coverlay and also if it ends before the end of the thick black resistive line. Then the following checks have to be performed:

- Resistivity between HV supply point and resistive foil: A Fluke Multimeter device is available for the measurement of the resistivity for all five contacts and the values between 0.3 MΩ and 2MΩ are expected.
- Coverlay insulation: the coverlay has to be checked if it's well insulated. At 1kV a resistivity of 30GΩ has to be reached.
- Resistive to copper pattern insulation: check if the insulation between readout strips and resistive layer reaches a value higher than 3GΩ within approximately 60 seconds. For this, all readout strips need to be interconnected with the second-long contact on the HV template.

A backlight inspection: The board is put on a table light underneath and the following checks need to be done:

- Alignment Between Resistive and Copper Pattern: The alignment targets are checked both on the left and the right side of the board.
- Number of dark-bright transitions: By eye and using the reflection of the light, one sees some transitions between dark and bright. The number of transitions needs to be counted and reported since this gives some information about a rotation of the resistive to copper pattern and about a scaling between the two patterns.
- Edge inspection: the edges of the boards have to be cut cleanly and this needs to be checked by eye and also using the magnifying glass. They also need to be measured if they are in the correct position.
- Mechanical holes: some boards contain holes (which is normal) if so, they need to be checked if they are centered within the circle, symmetric and clean.
- Interconnection holes: the holes should be centered with respect to the copper strips bending the holes, by calculating the displacement.

The pillars inspection: The pillar's inspection starts with:

- A search for missing pillars: The missing pillars are checked by lifting the board on one side and look the pillar pattern. In this way, it's easy to spot a missing pillar. Less than 10 missing pillars are not critical if none of them are consecutive. However, if two or more neighboring pillars are missing it should be reported in the QC form.

[3] The silver line enables to maintain a low impedance connection, it's deposited to the end of each strip

- The pillar attachment test: the pillars should be checked if they are well attached. For that, a 30 cm piece kapton tape is used; put it on top of the pillars and then pull it off. Then re-inspect the pillar pattern on the board in the respective region and check if all pillars are still there. If any pillar is removed by this test, it should be reported to be repaired by the company.

Dimensions and Accuracy: at this step, the dimensions of the board are measured with a precision of $\sim$20μm.
Pillar height mapping: the pillar heights should also be measured. An automated pillar heights measuring tool which is connected to a computer is used . The expected value of the pillar heights is around 120μm $\pm$ 3μm
Resistivity Mapping: the resistive pattern is measured and a resistivity map is produced using the resistivity tool.
Strip Capacitance Measurement: By simple visualization, it's almost impossible to identify interrupted readout strips instead, so the capacitance of each readout strips is measured with respect to the HV silver line.
Finishing the Board: At this step all the checks have been done and the board should be covered and marked as "done".

In parallel, I developed a software tool to perform a statistical analysis of the measurements performed during the QCQA shifts which include in particular statistics for the pillar heights measurement and the board dimension measurements.

FIGURE E.3: Taking shift at CERN building 188, this step corresponds to the pillar heights measurement.

E.5 Pillar height measurements

In this second part of my qualification task I developed a software tool to compute the pillar heights and sort them into histograms, fit the distributions with a Gaussian, extract the mean and the standard deviation for each board. The software is also able to check the left-right symmetry or any trend on the Y-axis of the board. Figure E.4 shows the pillar heights of each LS7 board superimposed.

Most of the plots are centered around 120 μm as expected. Figure E.5 shows each LS7 board fitted with a Gaussian. The mean of each board is around 120 μm which is very close to the expected value (120μm $\pm$ 3 μm). The mean and the standard deviation of each board from the fit are shown in Figure E.6. Figure E.7 considers the pillar heights of all the LS7 board fitted with a Gaussian. The results are also consistent with the expected value (around 120 μm).

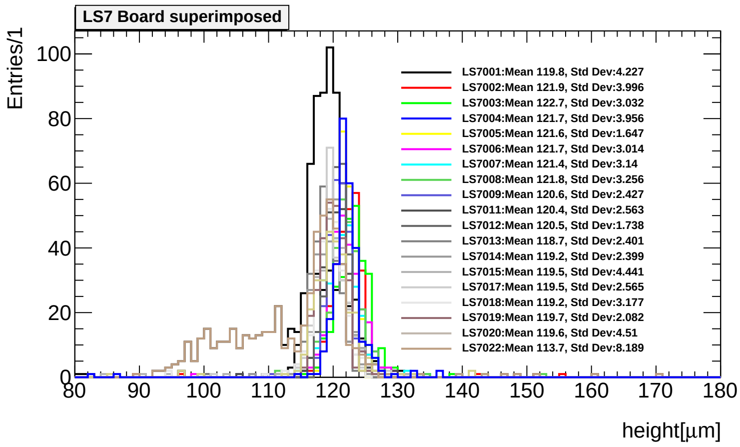

FIGURE E.4: Pillar heights of each LS7 board superimposed.

With the software, a left-right symmetry study is carried out by dividing the board into 2 equal parts (as shown in Figure E.8) along the Y-axis. The pillar heights of each side are around the expected value as shown in Figure E.9. No sizeable left-right asymmetry is observed. Figure E.10 considers the pillar heights of each side of all the boards and the same conclusion can be drawn.

One last check proceeded using the software which was to make four slices along the Y-axis of the board (see Figure E.11) and plot the pillar heights of each slice in order to check any trend along the Y-axis. Figure E.12 shows the average pillar heights of each slice for the LS7 boards. Most of the plots show a flat trend as expected.

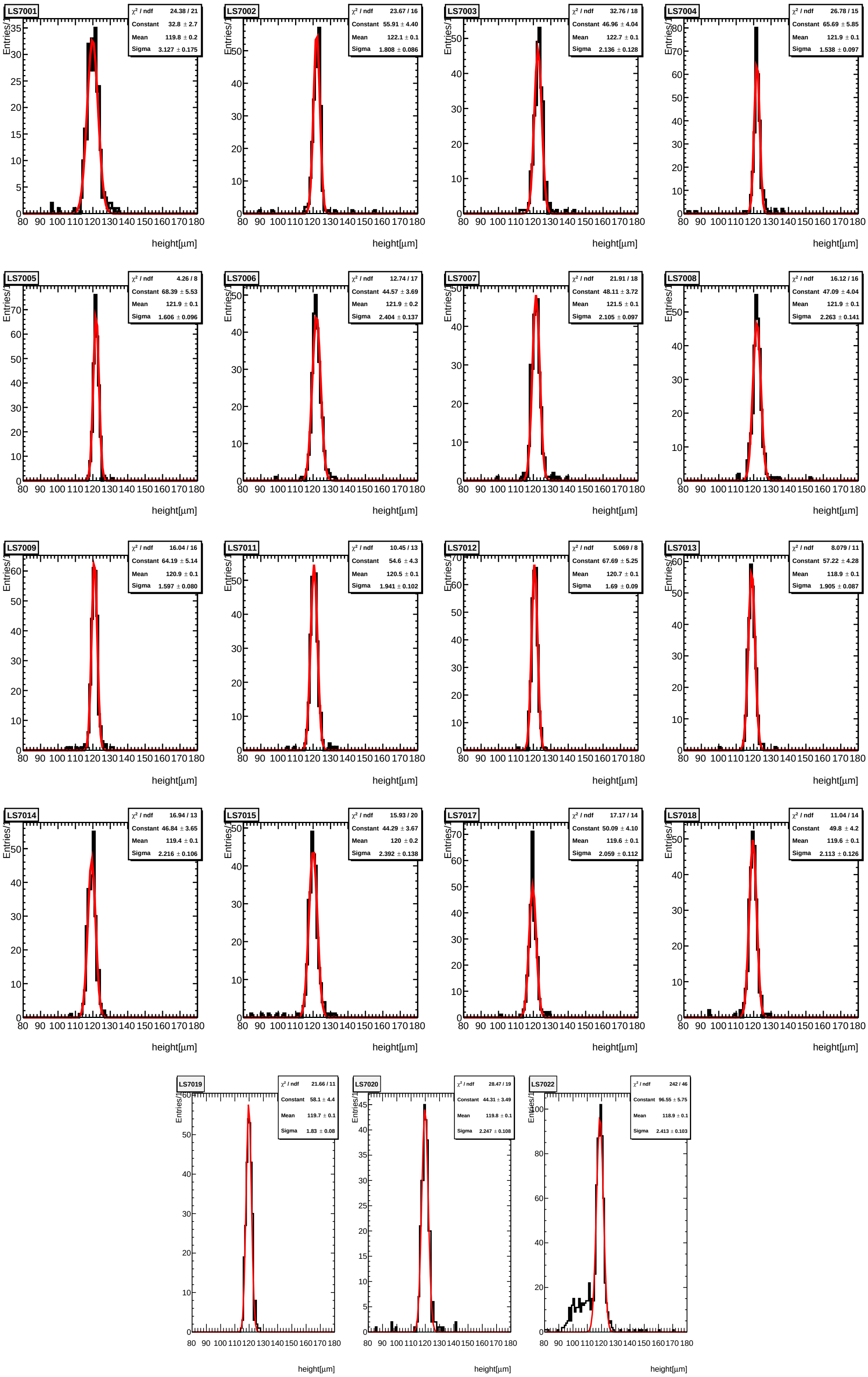

FIGURE E.5: Pillar heights of all LS7 boards.

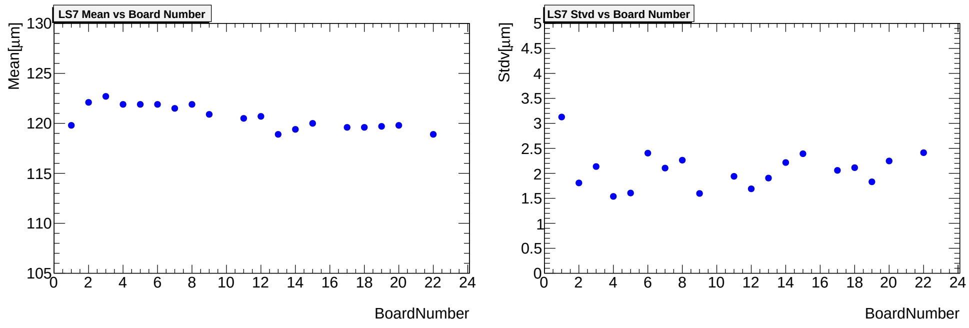

FIGURE E.6: Mean and standard deviation from the fit of each board.

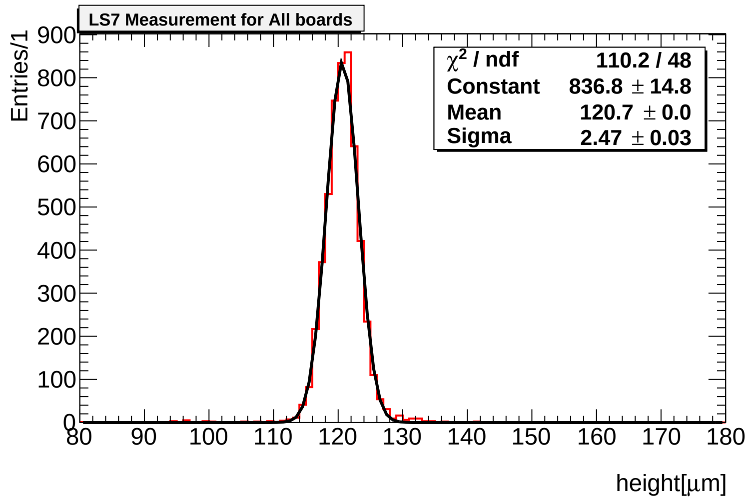

FIGURE E.7: Pillar heights of all LS7 boards.

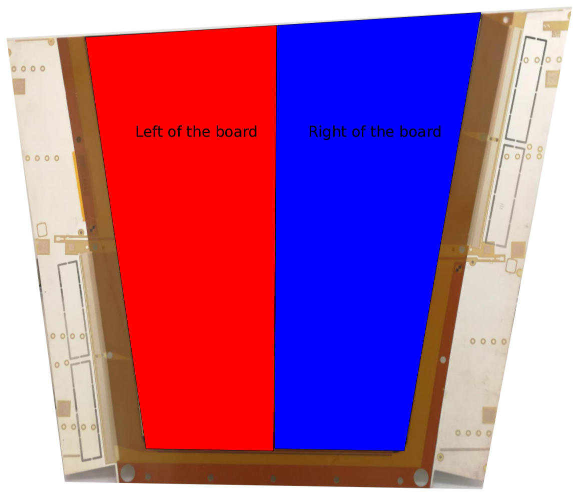

FIGURE E.8: Dividing the board in 2 equal parts, left and right in order to check any possible asymmetry regarding the pillar heights.

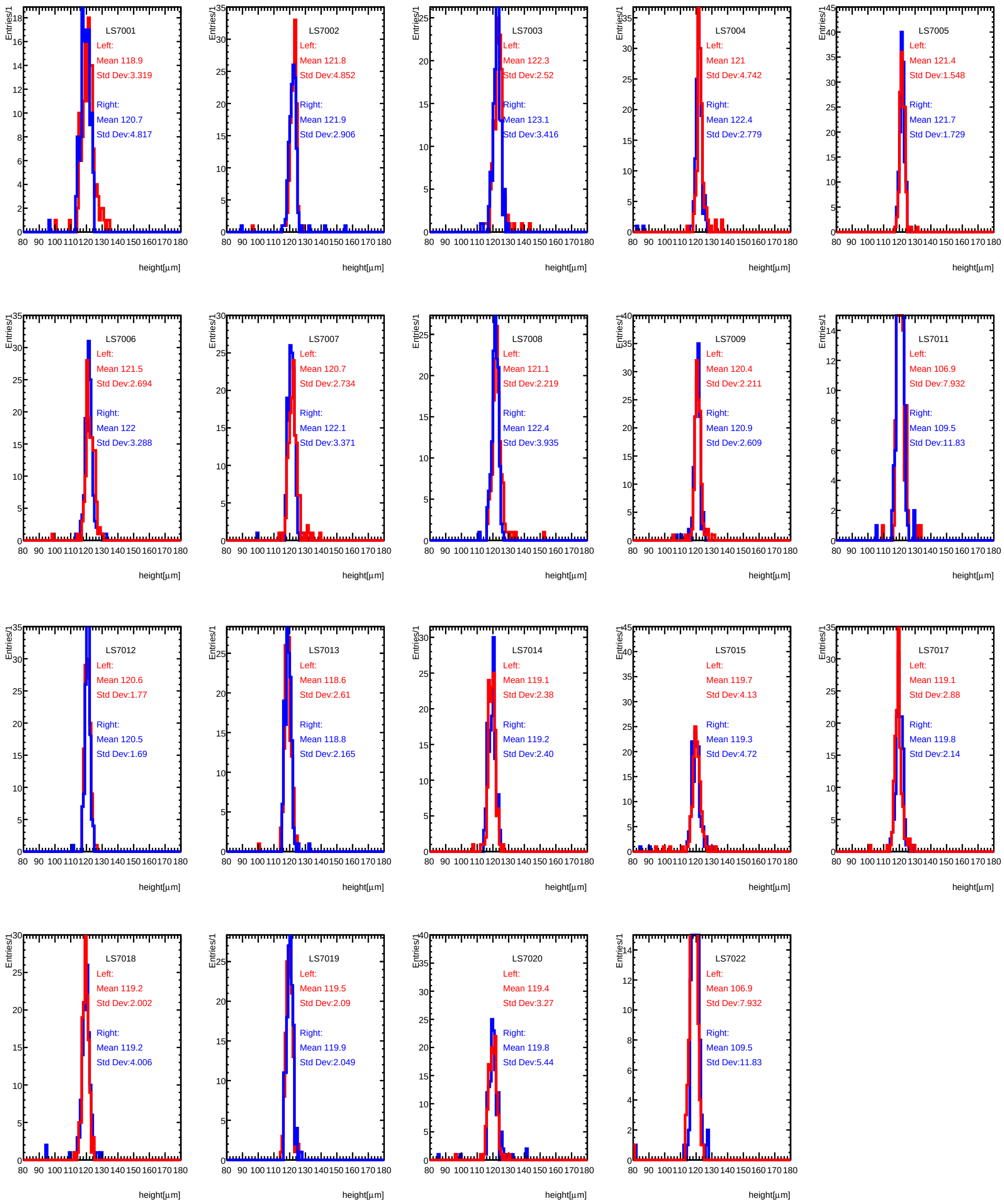

FIGURE E.9: Pillar heights of all LS7 boards.

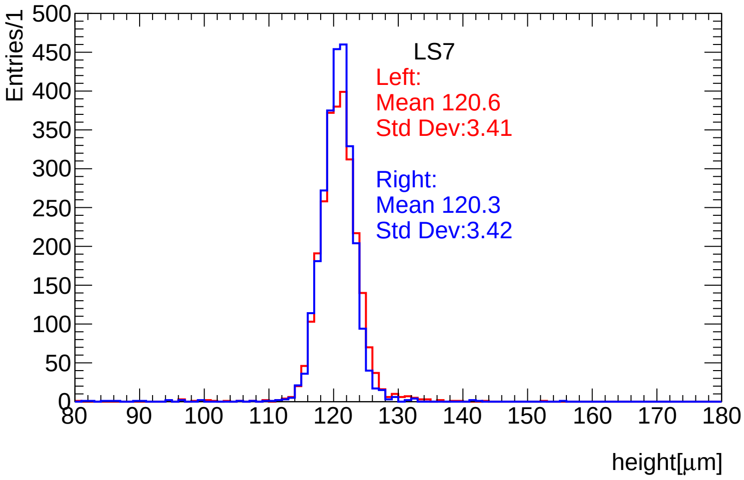

FIGURE E.10: Left and right pillar heights superimposed. As expected no significant asymmetry is observed.

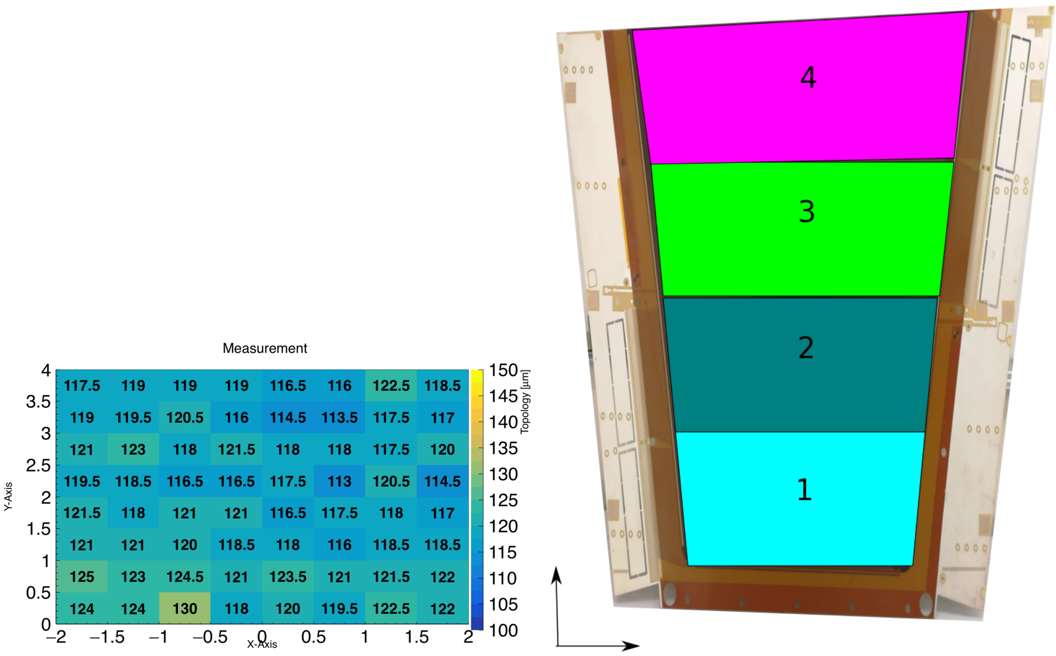

FIGURE E.11: Left: Pillar heights map of a given LS7 board. Right: Slices that I defined for checking any possible trend along the Y axis.

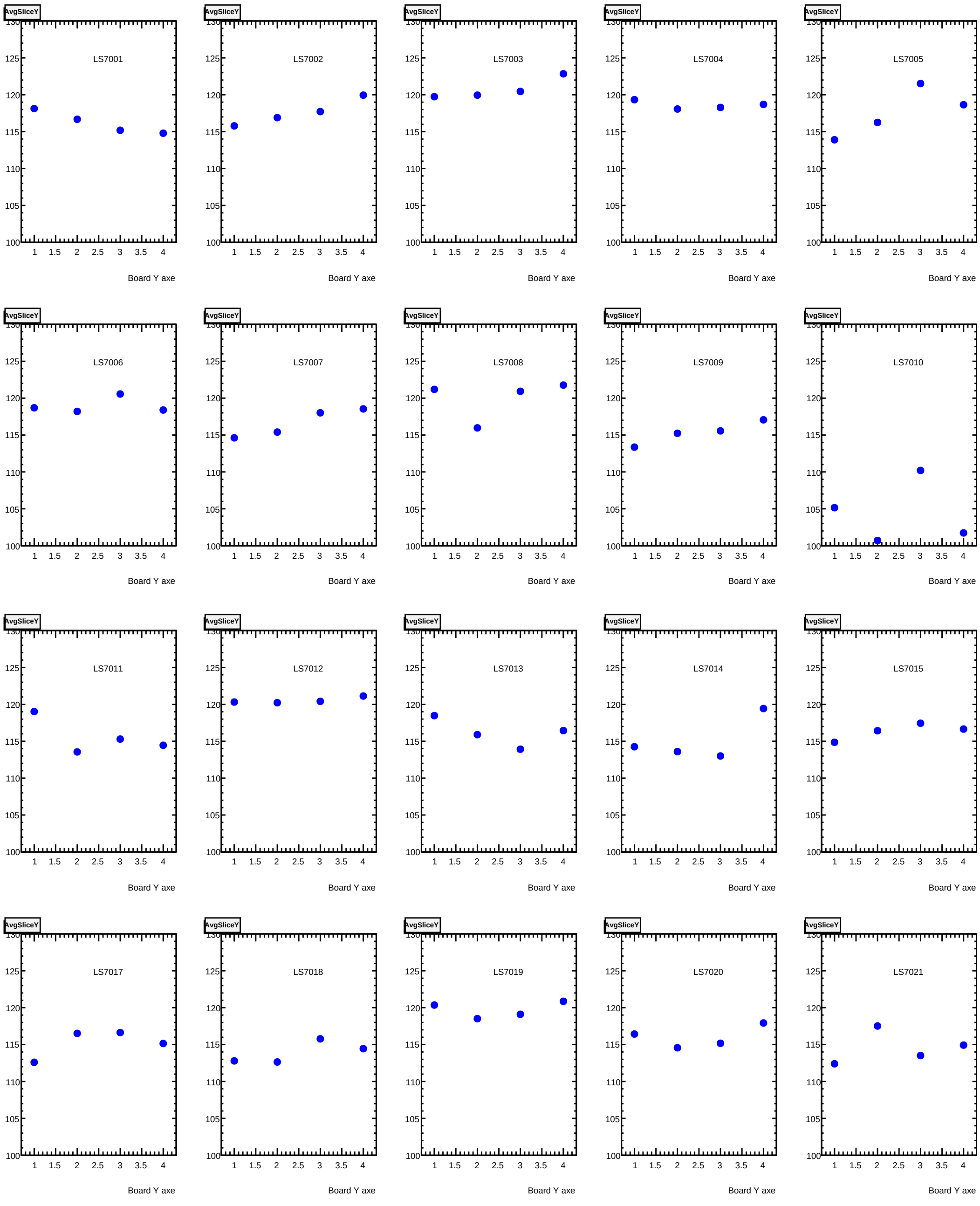

FIGURE E.12: Average of pillar heights vs slices. Most of the plots are flat which means no trend along th Y axis is observed.

E.6 Conclusion

The service task enabled me to contribute to the ATLAS experiment both in hardware and software aspects. In the hardware part, I was taking regular shifts for the QCQA of the boards where I gained a lot of expertise and knowledge in term of electronics at a deep level. In the software part, I designed a tool to further exploit the data taken from the shifts, especially for the pillar height measurements which are key components of the PCBs. Most of the results from the software show that the boards behave as expected. However, some board results look suspicious, in that case, the board is re-investigated to detect the reason. Sometimes it can be related to some dust present on the board when proceeding to the measurement or sometimes it's related to the board itself which requires, in this case, some repair. The results showed here consider only one sample of board (LS7) but the study is also extended to the other samples.

Bibliography

ATLAS Collaboration (2019). *Measurement of Differential Cross Sections for Single Diffractive Dissociation in $\sqrt{s}$ = 8TeV pp collisions using the ATLAS ALFA Spectrometer*. Tech. rep. ATLAS-CONF-2019-012. Geneva: CERN. URL: https://cds.cern.ch/record/2670978.

Aaboud, M. et al. (2018a). "$ZZ \to \ell^+\ell^-\ell'^+\ell'^-$ cross-section measurements and search for anomalous triple gauge couplings in 13 TeV pp collisions with the ATLAS detector". In: *Phys. Rev. D* 97 (3), p. 032005. DOI: 10 . 1103 / PhysRevD . 97 . 032005. URL: https://link.aps.org/doi/10.1103/PhysRevD.97.032005.

Aaboud, M. et al. (2019a). "Electron reconstruction and identification in the ATLAS experiment using the 2015 and 2016 LHC proton–proton collision data at $\sqrt{s}$ = 13 TeV". In: *The European Physical Journal C* 79.8, p. 639. DOI: 10.1140/epjc/s10052-019-7140-6. URL: https://doi.org/10.1140/epjc/s10052-019-7140-6.

Aaboud, Morad et al. (2017). "Performance of the ATLAS Trigger System in 2015". In: *Eur. Phys. J.* C77.5, p. 317. DOI: 10.1140/epjc/s10052-017-4852-3. arXiv: 1611.09661 [hep-ex].

— (2018b). "Measurement of the W-boson mass in pp collisions at $\sqrt{s} = 7$ TeV with the ATLAS detector". In: *Eur. Phys. J.* C78.2. [Erratum: Eur. Phys. J.C78,no.11,898(2018)], p. 110. DOI: 10.1140/epjc/s10052-018-6354-3,10.1140/epjc/s10052-017-5475-4. arXiv: 1701.07240 [hep-ex].

— (2019b). "Electron reconstruction and identification in the ATLAS experiment using the 2015 and 2016 LHC proton-proton collision data at $\sqrt{s}$ = 13 TeV". In: *Eur. Phys. J.* C79.8, p. 639. DOI: 10.1140/epjc/s10052-019-7140-6. arXiv: 1902.04655 [physics.ins-det].

Aad, G et al. (2008). "The ATLAS Experiment at the CERN Large Hadron Collider". In: *JINST* 3. Also published by CERN Geneva in 2010, S08003. 437 p. DOI: 10.1088/1748-0221/3/08/S08003. URL: https://cds.cern.ch/record/1129811.

Aad, G. et al. (2015a). "Search for Higgs bosons decaying to aa in the $\mu\mu\tau\tau$ final state in pp collisions at $\sqrt{s} = 8$ TeV with the ATLAS experiment". In: *Phys. Rev. D* 92 (5), p. 052002. DOI: 10.1103/PhysRevD.92.052002. URL: https://link.aps.org/doi/10.1103/PhysRevD.92.052002.

Aad, G. et al. (2015b). "Search for new light gauge bosons in Higgs boson decays to four-lepton final states in pp collisions at $\sqrt{s} = 8$ TeV with the ATLAS detector at the LHC". In: *Phys. Rev. D* 92 (9), p. 092001. DOI: 10.1103/PhysRevD.92.092001. URL: https://link.aps.org/doi/10.1103/PhysRevD.92.092001.

Aad, Georges et al. (2012). "Observation of a new particle in the search for the Standard Model Higgs boson with the ATLAS detector at the LHC". In: *Phys. Lett.* B716, pp. 1–29. DOI: 10.1016/j.physletb.2012.08.020. arXiv: 1207.7214 [hep-ex].

— (2016). "Muon reconstruction performance of the ATLAS detector in proton–proton collision data at $\sqrt{s}$ =13 TeV". In: *Eur. Phys. J.* C76.5, p. 292. DOI: 10.1140/epjc/s10052-016-4120-y. arXiv: 1603.05598 [hep-ex].

Abazov, V. M. et al. (2009). "Search for Next-to-Minimal Supersymmetric Higgs Bosons in the $h \to aa \to \mu\mu\mu\mu$, $\mu\mu\tau\tau$ Channels Using $p\bar{p}$ Collisions at $\sqrt{s} = 1.96$ TeV". In: *Phys. Rev. Lett.* 103 (6), p. 061801. DOI: 10.1103/PhysRevLett.103.061801. URL: https://link.aps.org/doi/10.1103/PhysRevLett.103.061801.

Abel, S.A. and B.W. Schofield (2004). "Brane anti brane kinetic mixing, millicharged particles and SUSY breaking". In: *Nuclear Physics B* 685.1, pp. 150 –170. ISSN: 0550-3213. DOI: https://doi.org/10.1016/j.nuclphysb.2004.02.037. URL: http://www.sciencedirect.com/science/article/pii/S0550321304001543.

Adriani, Oscar et al. (2009). "An anomalous positron abundance in cosmic rays with energies 1.5-100 GeV". In: *Nature* 458, pp. 607–609. DOI: 10.1038/nature07942. arXiv: 0810.4995 [astro-ph].

Aguilar, M. et al. (2013). "First Result from the Alpha Magnetic Spectrometer on the International Space Station: Precision Measurement of the Positron Fraction in Primary Cosmic Rays of 0.5–350 GeV". In: *Phys. Rev. Lett.* 110 (14), p. 141102. DOI: 10.1103/PhysRevLett.110.141102. URL: https://link.aps.org/doi/10.1103/PhysRevLett.110.141102.

Airapetian, A. et al. (1999). "ATLAS: Detector and physics performance technical design report. Volume 1". In:

Alexopoulos, T. et al. (2010). "Development of large size Micromegas detector for the upgrade of the ATLAS Muon system". In: *Nuclear Instruments and Methods in Physics Research Section A: Accelerators, Spectrometers, Detectors and Associated Equipment* 617.1. 11th Pisa Meeting on Advanced Detectors, pp. 161 –165. ISSN: 0168-9002. DOI: https://doi.org/10.1016/j.nima.2009.06.113. URL: http://www.sciencedirect.com/science/article/pii/S0168900209013485.

Alwall, J. et al. (2014). "The automated computation of tree-level and next-to-leading order differential cross sections, and their matching to parton shower simulations". In: *Journal of High Energy Physics* 2014.7, p. 79. ISSN: 1029-8479. DOI: 10.1007/JHEP07(2014)079. URL: https://doi.org/10.1007/JHEP07(2014)079.

Andersen, J R et al. (2013). "Handbook of LHC Higgs Cross Sections: 3. Higgs Properties". In: ed. by S Heinemeyer et al. DOI: 10.5170/CERN-2013-004. arXiv: 1307.1347 [hep-ph].

Arnison, G. et al. (1983). "Experimental observation of isolated large transverse energy electrons with associated missing energy at s=540 GeV". In: *Physics Letters B* 122.1, pp. 103 –116. ISSN: 0370-2693. DOI: https://doi.org/10.1016/0370-2693(83)91177-2. URL: http://www.sciencedirect.com/science/article/pii/0370269383911772.

ATLAS Collaboration (2015). *Vertex Reconstruction Performance of the ATLAS Detector at $\sqrt{s}$ = 13 TeV*. Tech. rep. ATL-PHYS-PUB-2015-026. Geneva: CERN. URL: https://cds.cern.ch/record/2037717.

ATLAS Collaboration et al. (2014). *ATLAS Run 1 Pythia8 tunes*. Tech. rep. ATL-PHYS-PUB-2014-021. Geneva: CERN. URL: https://cds.cern.ch/record/1966419.

ATLAS Collaboration et al. (2015). *Selection of jets produced in 13TeV proton-proton collisions with the ATLAS detector*. Tech. rep. ATLAS-CONF-2015-029. Geneva: CERN. URL: https://cds.cern.ch/record/2037702.

ATLAS Collaboration et al. (2016a). "Muon reconstruction performance of the ATLAS detector in proton–proton collision data at s=13 TeV". In: *The European Physical Journal C* 76.5, p. 292. ISSN: 1434-6052. DOI: 10.1140/epjc/s10052-016-4120-y. URL: https://doi.org/10.1140/epjc/s10052-016-4120-y.

ATLAS Collaboration et al. (2016b). “Muon reconstruction performance of the ATLAS detector in proton–proton collision data at $\sqrt{s}$=13 TeV”. In: *The European Physical Journal C* 76.5, p. 292. DOI: 10.1140/epjc/s10052-016-4120-y. URL: https://doi.org/10.1140/epjc/s10052-016-4120-y.

ATLAS Collaboration et al. (2017). “Jet reconstruction and performance using particle flow with the ATLAS Detector”. In: *The European Physical Journal C* 77.7, p. 466. ISSN: 1434-6052. DOI: 10.1140/epjc/s10052-017-5031-2. URL: https://doi.org/10.1140/epjc/s10052-017-5031-2.

Baak, M. et al. (2015). “HistFitter software framework for statistical data analysis”. In: *Eur. Phys. J.* C75, p. 153. DOI: 10.1140/epjc/s10052-015-3327-7. arXiv: 1410.1280 [hep-ex].

Baak, Max et al. (2014). *Interpolation between multi-dimensional histograms using a new non-linear moment morphing method*. Tech. rep. CERN-OPEN-2014-050. NIMA57112. Geneva: CERN. URL: https://cds.cern.ch/record/1957587.

Ball, Richard D. et al. (2013). “Parton distributions with LHC data”. In: *Nuclear Physics B* 867.2, pp. 244 –289. ISSN: 0550-3213. DOI: https://doi.org/10.1016/j.nuclphysb.2012.10.003. URL: http://www.sciencedirect.com/science/article/pii/S0550321312005500.

Banner, M. et al. (1983). “Observation of single isolated electrons of high transverse momentum in events with missing transverse energy at the CERN pp collider”. In: *Physics Letters B* 122.5, pp. 476 –485. ISSN: 0370-2693. DOI: https://doi.org/10.1016/0370-2693(83)91605-2. URL: http://www.sciencedirect.com/science/article/pii/0370269383916052.

Bélanger, G. et al. (2013). “Global fit to Higgs signal strengths and couplings and implications for extended Higgs sectors”. In: *Phys. Rev. D* 88 (7), p. 075008. DOI: 10.1103/PhysRevD.88.075008. URL: https://link.aps.org/doi/10.1103/PhysRevD.88.075008.

Bell, J.S. and H. Ruegg (1975). “Dirac equations with an exact higher symmetry”. In: *Nuclear Physics B* 98.1, pp. 151 –153. ISSN: 0550-3213. DOI: https://doi.org/10.1016/0550-3213(75)90206-0. URL: http://www.sciencedirect.com/science/article/pii/0550321375902060.

Berryman, Sylvia (2016). “Democritus”. In: *The Stanford Encyclopedia of Philosophy*. Ed. by Edward N. Zalta. Winter 2016. Metaphysics Research Lab, Stanford University.

Boye, D and X Mapekula (2019). “Search for a Higgs boson decaying through Zd to 4 leptons”. In: *Journal of Physics: Conference Series* 1271, p. 012005. DOI: 10.1088/1742-6596/1271/1/012005. URL: https://doi.org/10.1088%2F1742-6596%2F1271%2F1%2F012005.

Brown, Laurie M. and Helmut Rechenberg (1988). “Nuclear structure and beta decay (19321933)”. In: *American Journal of Physics* 56.11, pp. 982–988. DOI: 10.1119/1.15352. eprint: https://doi.org/10.1119/1.15352. URL: https://doi.org/10.1119/1.15352.

Butterfield, J. (1984). “Relationism and Possible Worlds”. In: *The British Journal for the Philosophy of Science* 35.2, pp. 101–113. ISSN: 00070882, 14643537. URL: http://www.jstor.org/stable/686961.

Buttinger, William (2015). *Using Event Weights to account for differences in Instantaneous Luminosity and Trigger Prescale in Monte Carlo and Data*. Tech. rep. ATL-COM-SOFT-2015-119. Geneva: CERN. URL: https://cds.cern.ch/record/2014726.

Chang, Jin et al. (Dec. 2008). “An excess of cosmic ray electrons at energies of 300–800 GeV”. In: *Nature* 456, pp. 362–5. DOI: 10.1038/nature07477.

Chatrchyan, Serguei et al. (2012). “Observation of a New Boson at a Mass of 125 GeV with the CMS Experiment at the LHC”. In: *Phys. Lett.* B716, pp. 30–61. DOI: 10.1016/j.physletb.2012.08.021. arXiv: 1207.7235 [hep-ex].

Chilton, D. (1964). “Clerk Maxwell and Modern Science. Six commemorative lectures by SirEdward V. Appleton, E. G. Bowen, C. A. Coulson, R. E. Peierls, SirJohn Randall, and R. A. Smith. Edited by C. Domb. Pp. x 118, frontis., 5 plates and numerous text figures. University of London, The Athlone Press. 1963. Price 25s. net.” In: *The British Journal for the History of Science* 2.1, 76–76. DOI: 10.1017/S0007087400001886.

Clowe, Douglas et al. (2006). “A Direct Empirical Proof of the Existence of Dark Matter”. In: *The Astrophysical Journal* 648.2, pp. L109–L113. DOI: 10.1086/508162. URL: https://doi.org/10.1086%2F508162.

CMS-Collaboration (2020). *Search for a low-mass dilepton resonance in Higgs boson decays to four-lepton final states at* $\sqrt{s} = 13$ TeV. Tech. rep. CMS-PAS-HIG-19-007. Geneva: CERN. URL: https://cds.cern.ch/record/2718976.

Collaboration, ATLAS (2020). “Public Liquid-Argon Calorimeter Plots on Detector Status.” In: URL: https://twiki.cern.ch/twiki/bin/view/AtlasPublic/LArCaloPublicResultsDetStatus.

Contino, Roberto et al. (2014). “eHDECAY: An implementation of the Higgs effective Lagrangian into HDECAY”. In: *Computer Physics Communications* 185.12, 3412–3423. ISSN: 0010-4655. DOI: 10.1016/j.cpc.2014.06.028. URL: http://dx.doi.org/10.1016/j.cpc.2014.06.028.

Cottingham, W. N. and D. A. Greenwood (2007). *An Introduction to the Standard Model of Particle Physics*. 2nd ed. Cambridge University Press. DOI: 10.1017/CBO9780511791406.

Cowan, Glen et al. (2011). “Asymptotic formulae for likelihood-based tests of new physics”. In: *Eur. Phys. J.* C71. [Erratum: Eur. Phys. J.C73,2501(2013)], p. 1554. DOI: 10.1140/epjc/s10052-011-1554-0,10.1140/epjc/s10052-013-2501-z. arXiv: 1007.1727 [physics.data-an].

Cranmer, Kyle et al. (2012). *HistFactory: A tool for creating statistical models for use with RooFit and RooStats*. Tech. rep. CERN-OPEN-2012-016. New York: New York U. URL: https://cds.cern.ch/record/1456844.

Curtin et al. (Feb. 2015). “Illuminating dark photons with high-energy colliders”. In: *Journal of High Energy Physics* 2015.157, pp. 1–45. URL: https://link.springer.com/article/10.1007/JHEP02(2015)157.

Curtin, David et al. (2014). “Exotic decays of the 125 GeV Higgs boson”. In: *Phys. Rev. D* 90 (7), p. 075004. DOI: 10.1103/PhysRevD.90.075004. URL: https://link.aps.org/doi/10.1103/PhysRevD.90.075004.

Davoudiasl, Hooman, Hye-Sung Lee, and William J. Marciano (2012). ““Dark” Z implications for parity violation, rare meson decays, and Higgs physics”. In: *Phys. Rev. D* 85 (11), p. 115019. DOI: 10.1103/PhysRevD.85.115019. URL: https://link.aps.org/doi/10.1103/PhysRevD.85.115019.

Davoudiasl, Hooman et al. (2013). “Higgs decays as a window into the dark sector”. In: *Phys. Rev. D* 88 (1), p. 015022. DOI: 10.1103/PhysRevD.88.015022. URL: https://link.aps.org/doi/10.1103/PhysRevD.88.015022.

Dittmaier, S. et al. (2012). “Handbook of LHC Higgs Cross Sections: 2. Differential Distributions”. In: DOI: 10.5170/CERN-2012-002. arXiv: 1201.3084 [hep-ph].

Eidelman, S. et al. (2004). “Review of Particle Physics”. In: *Physics Letters B* 592.1. Review of Particle Physics, pp. 1 –5. ISSN: 0370-2693. DOI: https://doi.org/10.1016/j.physletb.2004.06.001. URL: http://www.sciencedirect.com/science/article/pii/S0370269304007579.

Einstein, A., B. Podolsky, and N. Rosen (1935). "Can Quantum-Mechanical Description of Physical Reality Be Considered Complete?" In: *Phys. Rev.* 47 (10), pp. 777–780. DOI: 10 . 1103 / PhysRev . 47 . 777. URL: https://link.aps.org/doi/10.1103/PhysRev.47.777.

Ellwanger, Ulrich, Cyril Hugonie, and Ana M. Teixeira (2010). "The Next-to-Minimal Supersymmetric Standard Model". In: *Physics Reports* 496.1, pp. 1 –77. ISSN: 0370-1573. DOI: https://doi.org/10.1016/j.physrep.2010.07.001. URL: http://www.sciencedirect.com/science/article/pii/S0370157310001614.

Englert, F. and R. Brout (1964). "Broken Symmetry and the Mass of Gauge Vector Mesons". In: *Phys. Rev. Lett.* 13 (9), pp. 321–323. DOI: 10.1103/PhysRevLett.13.321. URL: https://link.aps.org/doi/10.1103/PhysRevLett.13.321.

Essig, Rouven et al. (2013). "Working Group Report: New Light Weakly Coupled Particles". In: *Proceedings, 2013 Community Summer Study on the Future of U.S. Particle Physics: Snowmass on the Mississippi (CSS2013): Minneapolis, MN, USA, July 29-August 6, 2013*. arXiv: 1311.0029 [hep-ph]. URL: http://www.slac.stanford.edu/econf/C1307292/docs/IntensityFrontier/NewLight-17.pdf.

forum, ATLAS statistics (2011). *Frequentist Limit Recommendation*. https://indico.cern.ch/event/126652/contributions/1343592/attachments/80222/115004/Frequentist_Limit_Recommendation.pdf. [Online; accessed 12-February-2020].

Fritzsch and Gell-Mann (1972). "Current algebra: Quarks and what else?" In: *eConf* C720906V2, pp. 135–165. arXiv: hep-ph/0208010 [hep-ph].

Frontline (2009). *INDIA'S NATIONAL MAGAZINE from the publishers of THE HINDU*. https://frontline.thehindu.com/static/html/fl2602/stories/20090130260208900.htm. [Online; accessed 13-January-2020].

Frühwirth, R. (1987). "Application of Kalman filtering to track and vertex fitting". In: *Nuclear Instruments and Methods in Physics Research Section A: Accelerators, Spectrometers, Detectors and Associated Equipment* 262.2, pp. 444 –450. ISSN: 0168-9002. DOI: https://doi.org/10.1016/0168-9002(87)90887-4. URL: http://www.sciencedirect.com/science/article/pii/0168900287908874.

Gaillard et al. (1999). "The standard model of particle physics". In: *Rev. Mod. Phys.* 71 (2), S96–S111. DOI: 10.1103/RevModPhys.71.S96. URL: https://link.aps.org/doi/10.1103/RevModPhys.71.S96.

Gopalakrishna, Shrihari, Sunghoon Jung, and James D. Wells (2008). "Higgs boson decays to four fermions through an Abelian hidden sector". In: *Phys. Rev. D* 78 (5), p. 055002. DOI: 10.1103/PhysRevD.78.055002. URL: https://link.aps.org/doi/10.1103/PhysRevD.78.055002.

Gross, D. J. (2005). "The discovery of asymptotic freedom and the emergence of QCD". In: *Proc. Nat. Acad. Sci.* 102. [Int. J. Mod. Phys.A20,5717(2005); Rev. Mod. Phys.77,837(2005)], pp. 9099–9108. DOI: 10.1142/S0217751X05029009,10.1073/pnas.0503831102,10.1103/RevModPhys.77.837.

Gunion, J. F. et al. (1997). "Limits from LEP Data on CP-Violating Nonminimal Higgs Sectors". In: *Phys. Rev. Lett.* 79 (6), pp. 982–985. DOI: 10.1103/PhysRevLett.79.982. URL: https://link.aps.org/doi/10.1103/PhysRevLett.79.982.

Haber, H.E. and G.L. Kane (1985). "The search for supersymmetry: Probing physics beyond the standard model". In: *Physics Reports* 117.2, pp. 75 –263. ISSN: 0370-1573. DOI: https://doi.org/10.1016/0370-1573(85)90051-1. URL: http://www.sciencedirect.com/science/article/pii/0370157385900511.

Hamilton, Keith et al. (2013). "NNLOPS simulation of Higgs boson production". In: *Journal of High Energy Physics* 2013.10, p. 222. ISSN: 1029-8479. DOI: 10.1007/JHEP10(2013)222. URL: https://doi.org/10.1007/JHEP10(2013)222.

Fundamental Physics at the Intensity Frontier (2012). DOI: 10.2172/1042577. arXiv: 1205.2671 [hep-ex]. URL: http://lss.fnal.gov/archive/preprint/fermilab-conf-12-879-ppd.shtml.

Holdom, Bob (1986). "Two U(1)'s and ϵ charge shifts". In: *Physics Letters B* 166.2, pp. 196–198. ISSN: 0370-2693. DOI: https://doi.org/10.1016/0370-2693(86)91377-8. URL: http://www.sciencedirect.com/science/article/pii/0370269386913778.

Hollik, W. (2010). "Quantum field theory and the Standard Model". In: *High-energy physics. Proceedings, 17th European School, ESHEP 2009, Bautzen, Germany, June 14-27, 2009*. arXiv: 1012.3883 [hep-ph].

Hubble, E., Humason, and M L. (July 1931). "The Velocity-Distance Relation among Extra-Galactic Nebulae". In: *apj* 74, p. 43. DOI: 10.1086/143323.

Jaeckel, Joerg and Andreas Ringwald (2010). "The Low-Energy Frontier of Particle Physics". In: *Annual Review of Nuclear and Particle Science* 60.1, pp. 405–437. DOI: 10.1146/annurev.nucl.012809.104433. eprint: https://doi.org/10.1146/annurev.nucl.012809.104433. URL: https://doi.org/10.1146/annurev.nucl.012809.104433.

Khachatryan, V. et al. (2016). "A search for pair production of new light bosons decaying into muons". In: *Physics Letters B* 752, pp. 146–168. ISSN: 0370-2693. DOI: https://doi.org/10.1016/j.physletb.2015.10.067. URL: http://www.sciencedirect.com/science/article/pii/S0370269315008266.

Khare, Avinash (1999). "The November J / psi revolution: Twenty five years later". In: *Curr. Sci.* 77, p. 1210. arXiv: hep-ph/9910468 [hep-ph].

Kim, Jihn E. (1987). "Light pseudoscalars, particle physics and cosmology". In: *Physics Reports* 150.1, pp. 1–177. ISSN: 0370-1573. DOI: https://doi.org/10.1016/0370-1573(87)90017-2. URL: http://www.sciencedirect.com/science/article/pii/0370157387900172.

Kuger, F. and Iengo, P. (2018). "Design, construction and quality control of resistive-Micromegas anode boards for the ATLAS experiment". In: *EPJ Web Conf.* 174, p. 01013. DOI: 10.1051/epjconf/201817401013. URL: https://doi.org/10.1051/epjconf/201817401013.

Langacker, Paul (2009). "The physics of heavy $Z^{'}$ gauge bosons". In: *Rev. Mod. Phys.* 81 (3), pp. 1199–1228. DOI: 10.1103/RevModPhys.81.1199. URL: https://link.aps.org/doi/10.1103/RevModPhys.81.1199.

Luisoni, Gionata et al. (2013). "HW/HZ + 0 and 1 jet at NLO with the POWHEG BOX interfaced to GoSam and their merging within MiNLO". In: *Journal of High Energy Physics* 2013.10, p. 83. ISSN: 1029-8479. DOI: 10.1007/JHEP10(2013)083. URL: https://doi.org/10.1007/JHEP10(2013)083.

Lütkebohle, Ingo (1969). *The Nobel Prize in Physics 1969*. https://www.nobelprize.org/prizes/physics/1969/summary/. [Online; accessed 28-Feb-2020].

Manthos, I. et al. (2019). "The Micromegas Project for the ATLAS New Small Wheel". In: *AIP Conf. Proc.* 2075.arXiv:1901.03160. 1. 7 pages, 8 figures, 10th Jubilee Conference of the Balkan Physical Union, 080010. 7 p. DOI: 10.1063/1.5091211. URL: https://cds.cern.ch/record/2654941.

Marchese, Luigi (2017). *Muon reconstruction performance of the ATLAS detector in 2016*. Tech. rep. ATL-PHYS-PROC-2017-246. Geneva: CERN. DOI: 10.1051/epjconf/201818203008. URL: https://cds.cern.ch/record/2292925.

Medhat, M. E. et al. (2005). "A package for gamma-ray spectrum analysis and routine neutron activation analysis". In: *Pramana* 65.2, pp. 245–258. ISSN: 0973-7111. DOI: 10.1007/BF02898613. URL: https://doi.org/10.1007/BF02898613.

Moneta, Lorenzo et al. (2010). "The RooStats Project". In:

Mrenna, Stephen and Peter Skands (2008). "A brief introduction to PYTHIA 8.1". In: *Computer Physics Communications* 178.11, pp. 852 –867. ISSN: 0010-4655. DOI: https://doi.org/10.1016/j.cpc.2008.01.036. URL: http://www.sciencedirect.com/science/article/pii/S0010465508000441.

Nagashima, Yorikiyo (2009). *Elementary Particle Physics, volume 1: Quantum Field Theory and Particles. The Science of Microfabrication*. Wiley.

Nason, Paolo and Carlo Oleari (2010). "NLO Higgs boson production via vector-boson fusion matched with shower in POWHEG". In: *Journal of High Energy Physics* 2010.2, p. 37. ISSN: 1029-8479. DOI: 10.1007/JHEP02(2010)037. URL: https://doi.org/10.1007/JHEP02(2010)037.

Peccei, R. D. and Helen R. Quinn (1977). "CP Conservation in the Presence of Pseudoparticles". In: *Phys. Rev. Lett.* 38 (25), pp. 1440–1443. DOI: 10.1103/PhysRevLett.38.1440. URL: https://link.aps.org/doi/10.1103/PhysRevLett.38.1440.

Perl, Martin L. (2004). "The Discovery of the Tau Lepton and the Changes in Elementary-Particle Physics in Forty Years". In: *Physics in Perspective* 6.4, pp. 401–427. ISSN: 1422-6960. DOI: 10.1007/s00016-003-0218-3. URL: https://doi.org/10.1007/s00016-003-0218-3.

Pitt, Joseph C. (1988). "Galileo, Rationality and Explanation". In: 55, pp. 87–103. ISSN: 00318248, 1539767X. URL: http://www.jstor.org/stable/187822.

Read, A L (2002). "Presentation of search results: theCLstechnique". In: *Journal of Physics G: Nuclear and Particle Physics* 28.10, pp. 2693–2704. DOI: 10.1088/0954-3899/28/10/313. URL: https://doi.org/10.1088%2F0954-3899%2F28%2F10%2F313.

Rende Steerenberg, by (2017). "LHC Report: 100 inverse femtobarns and counting..." In: URL: https://cds.cern.ch/record/2291281.

Rubin, V. C. and Ford (Feb. 1970). "Rotation of the Andromeda Nebula from a Spectroscopic Survey of Emission Regions". In: *apj* 159, p. 379. DOI: 10.1086/150317.

Schael, S. et al. (2006). "Precision electroweak measurements on the Z resonance". In: *Phys. Rept.* 427, pp. 257–454. DOI: 10.1016/j.physrep.2005.12.006. arXiv: hep-ex/0509008 [hep-ex].

Siegert, F (2011). "Monte Carlo Tuning with ATLAS Data". In: URL: https://cds.cern.ch/record/1352158.

The ATLAS Collaboration et al. (2015). *Proposal for truth particle observable definitions in physics measurements*. Tech. rep. ATL-PHYS-PUB-2015-013. Geneva: CERN. URL: https://cds.cern.ch/record/2022743.

The ATLAS Collaboration et al. (2017). "Electron efficiency measurements with the ATLAS detector using 2012 LHC proton–proton collision data". In: *The European Physical Journal C* 77.3, p. 195. ISSN: 1434-6052. DOI: 10.1140/epjc/s10052-017-4756-2. URL: https://doi.org/10.1140/epjc/s10052-017-4756-2.

The ATLAS collaboration et al. (2018). "Search for Higgs boson decays to beyond-the-Standard-Model light bosons in four-lepton events with the ATLAS detector at $\sqrt{s}$ 13 TeV". In: *Journal of High Energy Physics* 2018.6, p. 166. ISSN: 1029-8479. DOI: 10.1007/JHEP06(2018)166. URL: https://doi.org/10.1007/JHEP06(2018)166.

The CMS collaboration et al. (2017). "Search for light bosons in decays of the 125 GeV Higgs boson in proton-proton collisions at $\sqrt{s} = 8TeV$". In: *Journal of High Energy Physics* 2017.10, p. 76. ISSN: 1029-8479. DOI: 10.1007/JHEP10(2017)076. URL: https://doi.org/10.1007/JHEP10(2017)076.

Todd, N P M (2012). "The 1961 Rutherford Jubilee Conference: Perspectives from 2011". In: *Journal of Physics: Conference Series* 381, p. 012127. DOI: 10.1088/1742-6596/381/1/012127. URL: https://doi.org/10.1088%2F1742-6596%2F381%2F1%2F012127.

Trodden, Mark (1998). *Electroweak Baryogenesis: A Brief Review*. arXiv: hep-ph/9805252 [hep-ph].

Weinberg, Steven (1967). "A Model of Leptons". In: *Phys. Rev. Lett.* 19 (21), pp. 1264–1266. DOI: 10.1103/PhysRevLett.19.1264. URL: https://link.aps.org/doi/10.1103/PhysRevLett.19.1264.

Wells, James D. (2008). *How to Find a Hidden World at the Large Hadron Collider*. arXiv: 0803.1243 [hep-ph].

Wikipedia (2019a). *Galaxy rotation curve*. https://en.wikipedia.org/wiki/Galaxy_rotation_curve. [Online; accessed 13-January-2020].

— (2019b). *Proton Synchrotron Booster*. https://en.wikipedia.org/wiki/Proton_Synchrotron_Booster. [Online; accessed 13-January-2020].

Wikiwand (2020). *Particle accelerator*. https://www.wikiwand.com/en/Particle_accelerator. [Online; accessed 13-January-2020].

Wolfgang and Pauli (1955). *Niels Bohr and the development of physics : essays dedicated to Niels Bohr on the occasion of his seventieth birthday*. English. Includes bibliographies. Oxford : Pergamon Press.

Yukawa, Hideki (1935). "On the Interaction of Elementary Particles I". In: *Proc. Phys. Math. Soc. Jap.* 17. [Prog. Theor. Phys. Suppl.1,1(1935)], pp. 48–57. DOI: 10.1143/PTPS.1.1.